Synthesis and Properties of Macroporous Thin Films – Towards Multifunctional Photonic Crystals

Catherine Christine Ann Barron

Thesis submitted in fulfilment of the requirements for the degree of Doctor of Philosophy of Imperial College London.

November 2006

©Catherine Christine Ann Barron, 2006

This thesis is dedicated to the memory of my late granda, Tony. I hope it would have made you proud.

Author's Declaration

This thesis is the result of the work I have carried out in the Department of Materials, Imperial College London. The work described herein is my own with the exception of the following. The contact angle measurements presented in chapter 5 were conducted by Niall Thompson. The XRD data presented in chapter 7 was collected by Richard Sweeny and Dr Caroline Kirk (Natural History Museum). The FIB work presented in chapter 7 was assisted by Dr Martyn McLachlan and Dr John Walker (SciVenture). Finally the zeta potential measurements (chapter 3) and the Raman data (chapter 7) were conducted at the University of Strathclyde by Dr Rachael Littleford and Mr Dale Cunningham respectively.

The results contained within this thesis have not previously been submitted for a higher degree. Some results have been presented at various conferences and have been published in:

Barron, C.C.A., McLachlan, M.A., Zhang, Q., Whatmore, R.W. and McComb, D.W., Ferroelectric Three-Dimensionally Ordered Macroporous Thin Films, *Proceedings of the 5th Materials Research Conference*, 2006

Barron, C.C.A., McLachlan, M., Zhang, Q., McComb, D.W., Ferroelectric Three-Dimensionally Ordered Macroporous Thin Films, submitted to *Ferroelectrics* 2006

Abstract

In this thesis the results of an investigation into the synthesis and characterisation of three-dimensionally ordered macroporous (3-DOM) films from 3-D photonic crystal (PC) thin film templates is presented. Extensive characterisation of all the films formed has been carried out using a range of spectroscopic and microscopic techniques.

Thin film PCs with stop-bands in the visible and near infra-red spectral regions have been formed using colloidal self-assembly of sub-micron polystyrene spheres. By optimising the growth process large area, well ordered, low defect density thin films of controllable thickness have been fabricated.

One objective of this project was to obtain a greater understanding of the self-assembly growth process, in particular to try and minimise the cracking present in the thin films. Through analysis of the growth rate at different conditions the most important growth parameter was found to be temperature. The results presented show that cracking cannot be eliminated using the self-assembly growth process alone and can only be minimised. Through investigating the phenomenon of cracking a model for thin film growth is proposed highlighting the importance of the flow of solvent from the semi-ordered regions of spheres.

Another objective was the use of the 3-D PC films as templates for the formation of ferroelectric 3-DOM thin films. The structure and properties of macroporous films produced using the sol-gel precursor for the ferroelectric perovskite lead zirconate titanate (PZT) for the potential use as a tunable, or multifunctional, PCs is reported. The 3-DOM PZT films are supported on flat substrates to provide both mechanical stability and a method for forming electrical contacts.

Characterisation of the 3-DOM PZT has shown that the PZT is in the desirable tetragonal, ferroelectric, phase and is chemically homogeneous. Ferroelectric materials can through the electro-optic effect change their refractive index under an applied voltage. Initial results are reported for investigating the electro-optic effect of the 3-DOM PZT films towards forming a multifunctional PC.

Contents

Author's Declaration 3
Abstract 4
Acknowledgements 17
Definitions/Abbreviations 19
1 Introduction 20
1.1 Initial concept 20
1.2 Propagation of light 21
1.3 A complete band gap 24
1.4 Structures 26
1.5 Natural photonic crystals 28
1.6 Evidence of the fcc structure 29
1.7 Synthetic opal 32
1.8 Inverse opal 33
1.9 Multifunctional photonic crystals 33
1.10 Basics of Ferroelectricity 34
1.11 Theory of light diffraction 36
1.11.1 Derivation of the Bragg/Snell law 37
1.12 Characterisation by reflectance spectroscopy 40
1.12.1 Information gained from spectra 42
1.13 Structure of thesis 44
2 Instrumentation 45
2.1 Optical Microscopy 45
2.2 Electron Microscopy 46
2.2.1 Scanning Electron Microscopy (SEM) 46
2.2.2 Transmission Electron Microscopy (TEM) 52
2.3 Optical Spectroscopy 54
2.3.1 Instrumentation 55
2.3.2 Experiments 57
3 Polymerisation 61
3.1 Introduction 61
3.2 Polymerisation Technique 62
3.2.1 Initiation 62
3.2.2 Propagation 63
3.2.3 Termination 64
3.3 Polymerisation Mechanism 64
3.3.1 Emulsion polymerisation 64
3.3.2 Emulsifier-free Emulsion Polymerisation 65
3.3.3 Surface Chemistry 66
3.4 Size control 66
3.4.1 Synthesis Temperature 67
3.4.2 Monomer concentration 67
3.4.3 Initiator concentration 68
3.4.4 Agitation 68
3.5 Styrene Polymerisation 68
3.6 Sizing Method 70
3.7 Synthesis results 72
3.7.1 Initial polymerisation reactions 72
3.7.2 Subsequent syntheses 73
3.8 Zeta potential 75
3.8.1 Zeta potential measurement 76

3.9 Conclusions 77
4 Sizing Methods 78
4.1 Introduction 78
4.2 Dynamic Light Scattering 78
4.2.1 Theory 78
4.2.2 Experimental procedure 82
4.2.3 Results 83
4.2.4 Conclusions 86
4.3 Low Angle Laser Light Scattering 86
4.3.1 Theory 86
4.3.2 Experimental procedure 88
4.3.3 Results 88
4.3.4 Conclusions 90
4.4 Overall Conclusions 90
5 Thin Film Growth 91
5.1 Colloidal Crystallisation Methods 91
5.1.1 Sedimentation 92
5.1.2 Langmuir-Blodgett 93
5.1.3 Vertical Deposition 93
5.2 Variables associated with vertical deposition 95
5.2.1 Temperature 95
5.2.2 Relative Humidity 96
5.2.3 Colloidal Concentration 97
5.2.4 Sphere Diameter 98
5.3 Experimental procedure 98
5.4 Analysis 100
5.4.1 Optical Microscopy 101
5.4.2 Reflectance Spectroscopy 101
5.4.3 Scanning Electron Microscopy 107
5.4.4 Thickness 110
5.5 Growth on other substrates 118
5.6 Conclusions 121
6 Towards a Model for Thin Film Growth 123
6.1 Introduction 123
6.2 Experimental procedure 124
6.2.1 Temperature 125
6.2.2 Relative Humidity (R.H.) 127
6.2.3 Colloidal concentration 131
6.2.4 Overall growth rate 132
6.3 Activation energy 133
6.4 Reflectance spectroscopy 135
6.5 SEM 136
6.5.1 Domain widths 136
6.6 Film thickness 140
6.7 Why do cracks form? 142
6.8 Mechanism for cracking 146
6.8.1 Hydrodynamic model 147
6.8.2 Other models 150
6.9 Conclusions 150
7 Three-Dimensionally Ordered Macroporous Films 152
7.1 Introduction 152
7.2 Applications 153

7.3 Literature associated with the formation of 3-DOM materials 153
7.4 Reported experimental methods 155
7.4.1 Before infiltration 156
7.4.2 Infiltration methods 156
7.4.3 Sphere removal 159
7.5 Precursor Material 161
7.6 Experimental methods 162
7.6.1 Characterisation of PZT sol 162
7.6.2 Template Film Growth 164
7.6.3 Heat treatment of the polystyrene template 164
7.6.4 Infiltration of the PZT sol 164
7.6.5 Calcination conditions 165
7.6.6 Analysis of the 3-DOM PZT films 166
7.7 Characterisation of the PZT sol 166
7.7.1 Thermal analysis 166
7.7.2 XRD 167
7.7.3 EDX 170
7.7.4 Raman Spectroscopy 172
7.8 Formation of 3-DOM PZT films 175
7.8.1 Polystyrene template 175
7.8.2 Methods of infiltration 178
7.8.3 Calcination conditions 181
7.9 Characterisation of the 3-DOM PZT films 182
7.9.1 XRD 182
7.9.2 EDX 187
7.9.3 Optical spectroscopy 188
7.9.4 Shrinkage 191
7.9.5 Volume fraction 194
7.10 Optimisation of the infiltration process 196
7.10.1 Infiltration process 196
7.10.2 Calcination conditions 199
7.10.3 Optimum formation conditions 201
7.11 Conclusions 201
8 Towards a Multifunctional 3-DOM Material 203
8.1 Introduction 203
8.2 Birefringence 204
8.3 Electro-optic Effect 207
8.3.1 Electro-optic Coefficient for PZT 210
8.4 Experimental methodology 213
8.5 Multiple domain 215
8.5.1 Gold coat 215
8.5.2 Sandwich Films 216
8.5.3 Electrical Testing 219
8.6 Single domain 228
8.7 Conclusions 235
9 Conclusions 236
9.1 Outline of chapter 236
9.2 Conclusions 236
9.2.1 Thin film growth 236
9.2.2 Towards a method for thin film growth 237
9.2.3 3-D macroporous films 238
9.2.4 Towards multifunctional PCs 238

9.3 Possibilities for further work 239
Appendix 1 244
Appendix 2 246
Appendix 3 247
References 248

List of tables

Table 1.1 Position of reflection peaks for the spectra shown in figure 1.12 42
Table 2.1 Bragg peak positions along the x direction of the sample as a function of incident angle 58
Table 2.2 Bragg peak positions along the y direction of the sample as a function of incident angle 58
Table 2.3 Bragg peak positions and errors at different angles of incidence 59
Table 3.1 Zeta potential measurements for the polystyrene colloids detailed in figure 3.9 76
Table 4.1 Summary of the Zav-10% and the number data for the different techniques investigated with the HPPS 84
Table 4.2 Summary of the D[1,0] and Av. size for the different techniques investigated with the Mastersizer 89
Table 5.1 Wavelengths of Bragg reflection peaks for reflectance and transmission spectra for a film composed of 254 nm spheres 102
Table 5.2 Data calculated from the modified Bragg law for thin films of varying diameter 104
Table 5.3 Comparison of the wavelength position and $\Delta E/E_c$ for spectra gathered with different spot sizes 106
Table 5.4 Wavelength of Fabry-Perot fringes from reflectance spectra of a thin film composed grown at 0.036 vol% and calculated film thickness 114
Table 5.5 Comparison of the thickness calculated by three different methods for films grown with 200 nm spheres at concentrations in the range 0.012-0.036 vol% 117
Table 5.6 Comparison of sphere diameter and n_{eff} calculated for films grown at the same colloidal concentration on glass and ITO substrates 120
Table 6.1 Calculated growth rates at the seven temperatures investigated 126
Table 6.2 Calculated growth rates at the three R.H.values investigated 130
Table 6.3 Calculated growth rates at the three colloidal concentrations investigated 131
Table 6.4 Smallest measurable size from DigitalMicrograph 137
Table 6.5 Average domain widths and crack widths calculated by both methods for the films investigated. Each entry represents an average of 200 measurements 138
Table 6.6 Thickness measurements for films grown at different temperatures 141
Table 6.7 Water-air surface tension and solvent viscosity at increasing temperature 148
Table 7.1 Summary of the five initial methods investigated for infiltration 164
Table 7.2 Summary of the intensities of the Zr and Ti peaks and the corresponding percentages of each element in the PZT sample 172
Table 7.3 Approximate frequencies of the Raman active phonon modes for PZT(30/70) (168) 174
Table 7.4 Mass absorption coefficients for the elements of PZT 184
Table 7.5 Summary of the intensities of the Zr and Ti peaks and the corresponding percentages of each element in the 3-DOM PZT sample 187
Table 7.6 Measure of the stop-band width for three template films and the 3-DOM PZT films formed from them 190
Table 7.7 Interplanar spacing and n_{eff} calculated from the spectra shown in figure 7.24 191
Table 7.8 Summary of sphere diameter and n_{eff} of three template films and their corresponding 3-DOM films 192

Table 7.9 Volume fraction of PZT back calculated from reflectance data using equations 7.8 and 7.9 194
Table 7.10 Calculated shrinkage depending on the heating rate of calcination 200
Table 7.11 Calculated shrinkage depending on the air flow during calcination 200
Table 8.1 Summary of the linear, or Pockels, coefficient for PZT of different compositions 212
Table 8.2 Summary of the position of λ_{max} as the voltage was increased in the range 0-180 V for test 1 223
Table 8.3 Summary of the position of λ_{max} as the voltage was increased in the range 0-200 V for test 2 224
Table 8.4 Summary of the position of λ_{max} as the voltage was increased in the range 0-300 V for test 3 225

List of figures

Figure 1.1 Calculated band structure of a silicon inverse opal. The complete PBG is shown by the cross-hatched region (9).....23
Figure 1.2 Illustration for the first Brillouin zone for the fcc lattice and the conventional symbols for the important symmetry points (10).....25
Figure 1.3 Schematic illustration of PCs with (a) 1-D, (b) 2-D and (c) 3-D structures (1).....26
Figure 1.4 (a) a sample of gem opal demonstrating beautiful iridescence (29) and (b) SEM image showing the close packing of the silica spheres in opal (30).....28
Figure 1.5 Schematic illustration of the possible arrangements of stacked hard spheres.....30
Figure 1.6 Illustration of the fcc unit cell composed of a close packed arrangement of spheres.....31
Figure 1.7 General perovskite structure with formula ABO_3, the A, B and O ions are labelled.....34
Figure 1.8 Environment of the BO_6 octahedron.....35
Figure 1.9 Ferroelectric hysteresis loop for a PZT 45/55 film.....35
Figure 1.10 Derivation of the combined Bragg/Snell law.....37
Figure 1.11 (a) illustration of the fcc unit cell and (b) spheres in contact along the face diagonal (40).....39
Figure 1.12 Angle resolved reflectance measurements for 408 nm polystyrene spheres. The angles quoted are with reference to the sample normal.....41
Figure 1.13 Manipulated reflectance spectra can be used to calculate the interplanar spacing and n_{eff}.....42
Figure 2.1 Schematic diagram of lens system and optical path in an optical microscope.....45
Figure 2.2 A typical SEM image of the surface of a self-assembled thin film showing close packing of the polymer spheres.....47
Figure 2.3 Illustration of the main electron/specimen interactions and signals emitted in the SEM.....47
Figure 2.4 Schematic illustration of the electron column of a typical SEM.....48
Figure 2.5 Schematic illustration of the TEM column and the major components of the instrument.....52
Figure 2.6 Schematic illustration of the optical bench set-up.....55
Figure 2.7 Typical background/reference spectrum.....56
Figure 2.8 (a) Reflection and (b) transmission spectra for a thin film composed of 250 nm spheres. The angles quoted are relative to the sample normal...57
Figure 2.9 Schematic representation of the positions on the substrate the spectra were investigated.....58
Figure 2.10 Plot of λ^2 versus $\sin^2\theta$ for the standard and fitted lines.....60
Figure 3.1 Creation of the free-radical from a persulfate initiator.....62
Figure 3.2 Possible modes of addition of a free-radical to a molecule of styrene...63
Figure 3.3 Mode of head-to-tail addition of styrene monomer to the growing polystyrene chain.....63
Figure 3.4 Mode of termination of the growing polystyrene chain by combination 64
Figure 3.5 Labelled photograph of the polymerisation set-up.....69
Figure 3.6 Microscope calibration for TEM JEOL 2000FX.....71
Figure 3.7 Typical TEM micrograph of polystyrene spheres with a narrow size distribution.....71
Figure 3.8 Effect of styrene concentration on sphere size.....72

Figure 3.9 Size information for colloids synthesised with styrene concentration in the range 0.0436-0.436 molL^{-1} 73
Figure 3.10 Effect of styrene concentration in the range 0.087-0.524 molL^{-1} on sphere diameter 74
Figure 3.11 Schematic diagram of the electrical double layer (91). The surface charge on the particle is assumed to be positive. 75
Figure 4.1 Schematic diagram of the electrical double layer for a particle with negative surface charge 79
Figure 4.2 Schematic illustration of the experimental set-up of the HPPS (92) 80
Figure 4.3 Comparison of the correlation function for a sample containing small and large particles (92) 81
Figure 4.4 Plot showing a typical cumulants analysis and how the particle size can be calculated (92) 81
Figure 4.5 Extract from a typical output data file from the HPPS software 82
Figure 4.6 Plot of TEM derived size versus the Z_{av} value obtained from the HPPS for the more colloids row in table 4.1 83
Figure 4.7 Schematic illustration of the experimental set up of the Mastersizer 87
Figure 5.1 Schematic illustration of the vertical deposition method 94
Figure 5.2 Profile of the temperature and R.H. during a typical growth cycle 99
Figure 5.3 Positioning of the vials in the growth incubator 100
Figure 5.4 Optical microscope images from a film composed of (a) 408 nm and (b) 200 nm spheres 101
Figure 5.5 Reflectance (R) and transmission (T) spectra for a film composed of 254 nm spheres 102
Figure 5.6 Normalised reflectance spectra obtained from a film composed of 327 nm polystyrene spheres 103
Figure 5.7 Linear plots obtained by analysis of the position of the reflectance peaks. The plots are reference according to the TEM measured diameter 104
Figure 5.8 Variation in refractive index of polystyrene in the wavelength region 400-1100 nm 105
Figure 5.9 Normalised reflectance spectra collected with different spot sizes. The angles of incidence used were 10° and 40° 106
Figure 5.10 SEM micrographs showing (a) surface cracking and (b) crack propagating through the film thickness 107
Figure 5.11 High magnification SEM micrograph showing close packing of the polystyrene spheres 108
Figure 5.12 SEM images of films which have been cleaved to permit viewing of the internal order of the close packed planes 109
Figure 5.13 (a) SEM image of a film surface, (b) corresponding calculated FFT and (c) schematic illustration of the indexed diffraction pattern 109
Figure 5.14 SEM micrographs showing (a) cross abraded on film surface and (b) measured film thickness using the SEM 110
Figure 5.15 Schematic illustration of the origin of the main reflection peak and Fabry-Perot fringes where n_1 is air, n_2 is polystyrene and n_3 is glass. .. 112
Figure 5.16 Reflectance spectrum collected at 20° showing Fabry-Perot fringes for a film grown at 0.036 vol% 113
Figure 5.17 Straight line plotted to determine the film thickness from Fabry-Perot fringes 115
Figure 5.18 Typical output file from the ZYGO showing (a) interference profile (b) 3-D oblique plot and (c) surface profile plot 116
Figure 5.19 Comparison of thicknesses obtained from three different methods for films grown with 200 nm spheres 117

Figure 5.20 Comparison of film coverage on (a) ITO and (b) glass for films grown with the same spheres size 118
Figure 5.21 SEM micrograph showing the lack of film coverage for a concentration Tween 0.1%..... 119
Figure 5.22 Images showing (a) the surface of a film on ITO with addition of Tween and (b) SEM micrograph of the ordering in this film 119
Figure 5.23 Normalised reflectance spectra for a film grown with the addition of Tween showing pronounced Fabry-Perot fringes 120
Figure 5.24 Contact angle measurements for (a) original Delta Technologies ITO and (b) new source ITO 121
Figure 6.1 Simple schematic illustration of thin film formation 123
Figure 6.2 Incubator set-up for monitored thin film growth 124
Figure 6.3 Film growth versus time for growth at the seven temperatures investigated 126
Figure 6.4 Relative humidity profile for no salt solution and for LiCl and $MgCl_2$ saturated solutions at 60˚C 128
Figure 6.5 Relative humidity profile for $MgCl_2$ at room temperature 129
Figure 6.6 R.H. profile during high R.H. growth at 65˚C 130
Figure 6.7 Film growth versus time for growth at the three R.H. investigated..... 130
Figure 6.8 Growth versus time for growth at the three colloidal concentrations investigated 131
Figure 6.9 Dependence of the rate of thin film growth on the growth temperature..... 132
Figure 6.10 Dependence of the rate of thin film growth on the relative humidity... 132
Figure 6.11 Dependence of the rate of thin film growth on the colloidal concentration 133
Figure 6.12 Determination of the activation energy of thin film growth 134
Figure 6.13 Reflection spectra for the thin film grown at low R.H. at angles of incidence 10-50˚ 135
Figure 6.14 SEM image of the surface of the film grown at 50˚C showing close packing and the corresponding FFT. The red box indicates the region the FFT was calculated from..... 136
Figure 6.15 SEM images showing the domain widths for films grown at (a) 40 and (b) 70˚C 137
Figure 6.16 Schematic illustration of the individual and averaged methods used to measure the domain widths..... 137
Figure 6.17 Variation of domain width with increasing growth temperature 139
Figure 6.18 Illustration of hypothesised rates involved in thin film growth (a) growth rate (b) evaporation/drying rates 143
Figure 6.19 Illustration of the build up of strain between particles..... 145
Figure 6.20 Collapse of crack spacing with hydrodynamic scaling 148
Figure 6.21 Crack spacing as a function of the film thickness..... 149
Figure 7.1 Schematic illustration of the formation of a 3-DOM material from a synthetic opal template..... 153
Figure 7.2 Phase diagram for the solid solution $PbZrO_3$-$PbTiO_3$ (40)..... 162
Figure 7.3 Schematic illustration of the optimum infiltration method 165
Figure 7.4 TGA and DTA curves for the PZT sol..... 166
Figure 7.5 Indexed XRD patterns for PZT calcined at 490˚C and 530˚C 167
Figure 7.6 XRD pattern for a silicon standard showing the FWHM of the (111) diffraction peak 168

Figure 7.7 Variation in the lattice parameters a and c with the composition (where x is the percentage of Zr) (168). The red line indicates the composition PZT(30/70).....169
Figure 7.8 Schematic illustration of the process of characteristic X-rays.....171
Figure 7.9 EDX spectrum collected from region 2 of the calcined PZT sample ...171
Figure 7.10 The coordination geometry of the perovskite structure of PZT (167) ..173
Figure 7.11 Raman spectrum collected for PZT calcined at 530°C 174
Figure 7.12 TGA and DTA data collected for polystyrene colloid (reference 09/08/04) 175
Figure 7.13 Heating rate during TGA/DTA analysis showing a discontinuity around 400°C.....176
Figure 7.14 Difference in reflectance spectra for a template film before (continuous line) and after heating at 80°C for 30 minutes (dashed line).....177
Figure 7.15 SEM images of the template film after heating for 30 minutes at (a) and (b) 80°C and (c) and (d) 100°C 177
Figure 7.16 SEM micrographs showing the template film after infiltration with PZT but before sphere removal.....180
Figure 7.17 SEM micrographs of 3-DOM PZT films showing (a) the periodicity has been maintained and (b) the air spheres of the underlying layer can be observed 181
Figure 7.18 XRD pattern for a 3-DOM PZT film supported on glass. The XRD pattern for the substrate is also shown for comparison.....182
Figure 7.19 Schematic illustration of the penetration depth of the X-ray beam into a sample 183
Figure 7.20 Indexed XRD pattern collected from delaminated flakes of 3-DOM PZT compared to bulk PZT.....185
Figure 7.21 SEM micrographs showing (a) flakes and (b) structure of the flakes of 3-DOM PZT 185
Figure 7.22 Indexed XRD pattern from a 3-DOM PZT film supported on an ITO substrate.....186
Figure 7.23 Reflectance spectra collected during the infiltration process showing the Bragg peak at various times after infiltration (a) after first infiltration and (b) after second infiltration.....188
Figure 7.24 Normalised reflection peaks from a template and corresponding 3-DOM PZT film.....189
Figure 7.25 SEM micrograpahs showing the domains present in 3-DOM PZT films. the separation between domanis has increased compared to the template film. 192
Figure 7.26 SEM micrograph showing small triangular voids at the intersection of the PZT walls 195
Figure 7.27 SEM micrographs showing the surface of 3-DOM PZT films where delamination has occurred (a) regions where there is no film coverage and (b) re-adhered delaminated domains 197
Figure 7.28 SEM micrographs showing (a) crusted inverse domain surrounded by an ordered monolayer and (b) ordered 2-DOM PZT 197
Figure 7.29 SEM micrographs showing (a) large domains with a PZT crust on the top surface, (b) below the crust a 3-DOM PZT structure exists, (c) domains with partial crust formation and (d) voids surrounded by a thick PZT wall.....198
Figure 7.30 High resolution SEM images reveal differences in the microstructure and allow the grain size to be measured (a) typical wall morphology and (b) walls composed of many grains 199

Figure 7.31 SEM micrographs showing the detrimental effect on the 3-DOM material caused by (a) high heating rate and (b) fast air flow during calcination 201
Figure 7.32 High resolution SEM micrographs showing the surface of a 3-DOM PZT film formed at the optimum conditions.....201
Figure 8.1 Schematic illustration of the separation of light waves by a birefringent calcite crystal (185).....205
Figure 8.2 Illustration of the wavefront propagation in anisotropic crystals for the (a) ordinary wave, (b) extraordinary wave and (c) refractive index ellipsoid (185).....206
Figure 8.3 Illustration of the index ellipsoid showing the relationship between the ordinary and extraordinary waves.....206
Figure 8.4 Schematic illustration of the effect of an electric field on the index ellipsoid.....207
Figure 8.5 The orientation of the 5d-orbitals with respect to the ligands of an octahedral complex (a) the t_{2g} triplet, (b) the e_g pair and (c) the relative energies of the d-orbitals in an octahedral crystal field (41).....210
Figure 8.6 Schematic illustration of the effect of poling on the domains of a ferroelectric film.....211
Figure 8.7 Schematic illustration of the method used to electrically test 3-DOM PLZT (51).....213
Figure 8.8 The calculated change in refractive index for PZT with different Pockels coefficients for applied voltages in the range 0-700 V 214
Figure 8.9 Schematic illustration of the simplest method for forming a contact on the 3-DOM film 215
Figure 8.10 Normalised reflection spectra for a 3-DOM PZT film (continuous line) and a gold coated 3-DOM film (dashed line).....216
Figure 8.11 Schematic illustration of the sandwich method used for electrically testing the 3-DOM films 217
Figure 8.12 Difference in reflectance spectra for 3-DOM PZT film without (continuous line) and with (dotted line) a top ITO substrate 217
Figure 8.13 Sandwich structure after a voltage of 30 V had been applied. A black region (labelled) shows where the film started to spark 218
Figure 8.14 The optical bench set-up for the electrical measurements 220
Figure 8.15 Normalised reflection spectra for 3-DOM PZT film used for test 3.....220
Figure 8.16 Graphical illustration of the two different methods used to calculate λ_{max}. 222
Figure 8.17 Fitted parabolas for smoothed data points for test 3 (a) 0-280 V in 40 V steps and (b) 20-300 V in 40V steps 226
Figure 8.18 SEM images of FIB deposited platinum pads of diferent dimensions..229
Figure 8.19 High magnification FIB image showing a well defined platinum pad .229
Figure 8.20 Optical microscope images of copper wire (a) before etching and (b) after 1 minute etching in H_3PO_4.....230
Figure 8.21 Schematic illustration of the set-up of the 3-DOM film before being placed into the FIB 230
Figure 8.22 FIB image of the copper wire attached to the 3-DOM film surface with 3 trapezoids of platinum.....231
Figure 8.23 Picture of the set-up for attempting to attach the copper wire on the open bench using the optical microscope 232
Figure 8.24 Optical microscope images showing (a) copper wire just past deposited platinum pad, (b) blob of epoxy on the end of the glass capillary and (c) blob of epoxy on the 3-DOM film surface.....232

Figure 8.25 Labelled schematic diagram of the second method proposed to form an electrical contact to the 3-DOM films.....233
Figure 8.26 FIB images of the process used to isolate a 3-DOM domain and attach to a large pad of platinum. Each image is described in the text.....234
Figure 8.27 Schematic illustration of the most suitable proposed method for contacting the isolated 3-DOM domain.....234

Acknowledgements

Firstly I would like to thank my supervisor Dr David McComb for the support, enthusiasm and encouragement he has given me during the course of my PhD. It has been a privilege to work with him and learn from him.

I would like to thank the Department of Materials at Imperial College which has allowed me to freely use their equipment. In particular I would like to thank Mahmoud Ardakani for training and help with the electron microscopes, Richard Chater for help with the ZYGO and FIB and Richard Sweeny for his patience and expertise with XRD.

Outwith College I would like to thank the following individuals. Dr Qi Zhang (Cranfield University) and Professor R. Whatmore (Tyndall Institute) for the provision of the PZT sol and useful discussions on ferroelectric materials. Dr Caroline Kirk at the Natural History Museum for her expertise in collecting XRD data from thin films. Dr John Walker, SciVenture Maidenhead, for his ideas on electrically contacting the 3-DOM films and his FIB work presented in Chapter 8. Finally I would like to thank the EPSRC Instrument Loan Pool for the loan of the Malvern HPPS and Mastersizer and to Stuart Macauley at Malvern for his help and advice with these machines.

I would also like to thank all members of the 'McComb' group, past and present, for their friendship, support and encouragement over the last three years especially Niall Thomson and Catriona McGilvery. A special thank you is due to Martyn McLachlan for his help getting started in the early days, his continued help (especially with the FIB), advice and discussions.

I would also like to thank my fiancé Imran. For his help with TEM and Raman and general guidance with all aspects of my PhD studies. In addition I would also like to thank him on a personal level for his continued support and encouragement and for always being there for me.

Finally I would like to thank my family for their love and support at all stages of my life. Thank you to my sister Louise for her continuous emails while I was writing up. They were very much appreciated! To my mum and dad thank you for encouraging me to make my own choices in life and always being there for me to offer support – both

emotionally and financially. I am deeply grateful for everything you have done for me and continue to do for me.

Definitions/Abbreviations

1-D	One-dimensional
2-D	Two-dimensional
3-D	Three-dimensional
3-DOM	Three-dimensionally ordered macroporous
DLS	Dynamic Light Scattering
DTA	Differential thermal analysis
DVLO theory	Derjaguin, Landau, Verwey and Overbeek theory
EDX	Energy dispersive X-ray analysis
EM	Electromagnetic
eV	Electron volt
fcc	Face centred cubic
FFT	Fast Fourier transform
hcp	Hexagonal close packed
HPPS	High Performance Particle Sizer
IR	Infra-red
ITO	Indium tin oxide
kV	Kilo volts
λ_{max}	reflection peak maximum
LALLS	Low angle laser light scattering
LiCl	Lithium chloride
$MgCl_2$	Magnesium chloride
NaCl	Sodium chloride
NIBS	Non-invasive back-scatter
PBG	Photonic band gap
PC	Photonic crystal
PDI	Polydispersity index
PLZT	Lead lanthanum zirconate titanate
PMMA	Poly(methyl methacrylate)
PZT	Lead zirconate titanate ($PbZr_xTi_{1-x}O_3$)
PZT(30/70)	$PbZr_{0.3}Ti_{0.7}O_3$
R.H.	Relative humidity
RIC	Refractive index contrast
SEM	Scanning Electron Microscope
SNR	Signal to noise ratio
TEM	Transmission Electron Microscope
TGA	Thermogravimetric analysis
TiO_2	Titania
Tween	polyoxyethylene sorbiton monolaurate
vol%	Volume fraction
XRD	X-ray diffraction
Z_{av}	Z average diameter

1 Introduction

1.1 Initial concept

Many of the breakthroughs in technology result from a better understanding of the properties of materials. In the last decades of the twentieth century there were many advances in the control of the electrical properties of materials and developments in the semiconductor industry have initiated the transistor revolution in electronics (1). It is clear that these advances in technology have had immeasurable impact on today's society.

As we enter the twenty first century a new challenge has emerged – how to control the optical properties of materials. In 1987 two researchers, Eli Yablonovitch and Sajeev John, independently proposed a new type of functional material which offered the possibility of moulding the flow of light (2,3). These functional materials were termed photonic crystals (PCs).

A crystal is a periodic array of atoms and therefore presents a periodic potential to electrons propagating through it. Due to wave-particle duality electrons can behave as waves and can scatter from the regular rows of atoms in the crystal. If the wavelength of the electron wave is similar to the spacing of the successive rows of atoms in the crystal all the backscattered waves can add coherently (4). Thus gaps in the energy band structure of the crystal are introduced which forbid electrons with certain energies from propagating in certain directions of the crystal (1). If the lattice potential is strong enough these band gaps can exist in all crystallographic directions and result in a complete, or full, band gap (5). An example of a complete band gap in an electronic material would be the gap between the valence and conduction bands in a semiconductor.

The PC is the optical analogy of the electronic crystal and as such PCs have been hailed as '*semiconductors of light*' (4). A PC consists of a low absorption material within a spatially periodic dielectric lattice. If the difference in the dielectric constants of the component materials is great enough and the light absorption is minimal, then scattering at the interfaces can produce many of the phenomena for photons as the atomic potential

does for electrons (1). Thus a photonic band gap (PBG) can exist where light of particular wavelengths propagating in certain directions can be prohibited from flowing through the crystal.

Theory predicts that for a material to have a full PBG certain criteria regarding the symmetry of the crystal and its dielectric properties must be fulfilled (1). A complete PBG exists when the propagation of light of particular wavelengths is forbidden for every direction of propagation within the crystal. When the criteria required for a complete PBG in all crystallographic directions are not fulfilled a photonic stop-band may be created which is a range of frequencies which are forbidden from propagating only in certain directions within the crystal (6).

1.2 Propagation of light

The interaction of a material with incident electromagnetic (EM) radiation is described by its dielectric permittivity, ε, and its magnetic susceptibility, μ (7). The dielectric permittivity is a complex quantity $\varepsilon = \varepsilon` + i\varepsilon``$. The real part, ε`, describes the refractive properties of the material and is often represented by the refractive index, n ($n = \sqrt{\varepsilon'}$). The imaginary part, ε`` describes the dissipative damping of the propagating waves caused by absorption (7). The materials used for the construction of PCs are generally transparent, *i.e.* display no absorption over the wavelength range of the PBG. If this is the case ε`` can be ignored and $\varepsilon = \varepsilon`$. In addition, the frequency dependence of ε` is assumed to be negligible within a broad frequency range and therefore ε(ω) is approximated by the low frequency dielectric constant, ε (or refractive index, n) (7).

In order to understand the propagation of light within a PC it is necessary to examine the equations which govern the propagation of EM radiation – the macroscopic Maxwell's equations (outlined in equations 1.1-4),

$$\nabla \cdot \mathbf{B} = 0 \qquad \textbf{Equation 1.1}$$

$$\nabla \mathrm{x} \mathbf{E} = -\frac{\partial \mathbf{B}}{\partial t} \qquad \textbf{Equation 1.2}$$

$$\nabla \cdot \mathbf{D} = \rho \qquad \textbf{Equation 1.3}$$

$$\nabla \mathrm{x} \mathbf{H} = \frac{\partial \mathbf{D}}{\partial t} + \mathbf{J} \qquad \textbf{Equation 1.4}$$

, where **E** and **H** are the macroscopic electric and magnetic fields respectively. **D** and **B** are the displacement and magnetic induction fields respectively and ρ and **J** are the free charges and currents respectively.

In addition **D** and **B** can be related to **E** and **H**, as shown in equations 1.5-6,

$$\mathbf{D} = \varepsilon_0 \varepsilon \mathbf{E} \qquad \textbf{Equation 1.5}$$

$$\mathbf{B} = \mu_0 \mu \mathbf{H} \qquad \textbf{Equation 1.6}$$

, where ε_0 and μ_0 are the permittivity and permeability of free space respectively.

A PC can be considered as a mixed dielectric medium in which there is no free charge or current, hence ρ=**J**=0 (1). When considering the interaction of light with a PC four assumptions can be made:

1) all field strengths are small;
2) the material is macroscopic and isotropic;
3) the frequency dependence of the dielectric constant is ignored;
4) only low-loss dielectrics are used (can ignore ε``).

The materials used to construct PCs can be considered as non-magnetic and consequently μ can be set to unity (7). In this case **B** and **H** are equal (equation 1.6). Therefore, when all the assumptions are accounted for, the four Maxwell equations (equations 1.1.-4) can be re-written as:

$$\nabla \cdot \mathbf{B} = \nabla \cdot \mathbf{H} = 0 \qquad \textbf{Equation 1.7}$$

$$\nabla \mathrm{x} \mathbf{E} = -\mu_0 \frac{\partial \mathbf{H}}{\partial t} \qquad \textbf{Equation 1.8}$$

$$\nabla \cdot \mathbf{D} = 0 \qquad \textbf{Equation 1.9}$$

$$\nabla \mathrm{x} \mathbf{H} = -\varepsilon_0 \varepsilon \frac{\partial \mathbf{E}}{\partial t} \qquad \textbf{Equation 1.10}$$

In general **E** and **H** are complicated functions of time and space. Since the Maxwell equations are linear the time dependence can be separated out by expanding the fields into a set of harmonic modes (1). It is the restrictions imposed by the Maxwell equations on a field which vary harmonically with time which are considered. A harmonic mode can be written as a certain field pattern multiplied by a complex exponential, thus (where ω is the frequency):

$$\mathbf{E} = \mathrm{E}_0 \exp(-i\omega t) \qquad \textbf{Equation 1.11}$$

$$\mathbf{H} = \mathrm{H}_0 \exp(-i\omega t) \qquad \textbf{Equation 1.12}$$

By substituting the harmonic modes in equations 1.8 and 1.10 the Maxwell equations can be written as:

$$\nabla \mathrm{x}\mathbf{E} = \mu_0 \mathrm{i}\omega \mathrm{H}_0 \exp(-i\omega t) \qquad \textbf{Equation 1.13}$$

$$\nabla \mathrm{x}\mathbf{H} = \varepsilon_0 \varepsilon \mathrm{i}\omega \mathrm{E}_0 \exp(-i\omega t) \qquad \textbf{Equation 1.14}$$

By further simplification and substitution the '*master equation*' for harmonic modes can be obtained (equation 1.15).

$$\nabla \mathrm{x} \frac{1}{\varepsilon_0} (\nabla \mathrm{x}\mathbf{H}) = \left(\frac{\omega}{c}\right)^2 \mathbf{H} \qquad \textbf{Equation 1.15}$$

Equation 1.15 describes the propagation of EM radiation in a PC. The solutions to Maxwell's equations are most suited to computer band structure calculations which can predict the properties of PCs, avoiding costly experimentation with new technologies (8). In such computer calculations the aim is to solve the '*master equation*' for the magnetic modes of the PC determining the allowed mode frequencies and their associated wave vectors, **k**, (1) *i.e.* the band structure of the crystal can be calculated. An example of a calculated band structure diagram is shown in figure 1.1.

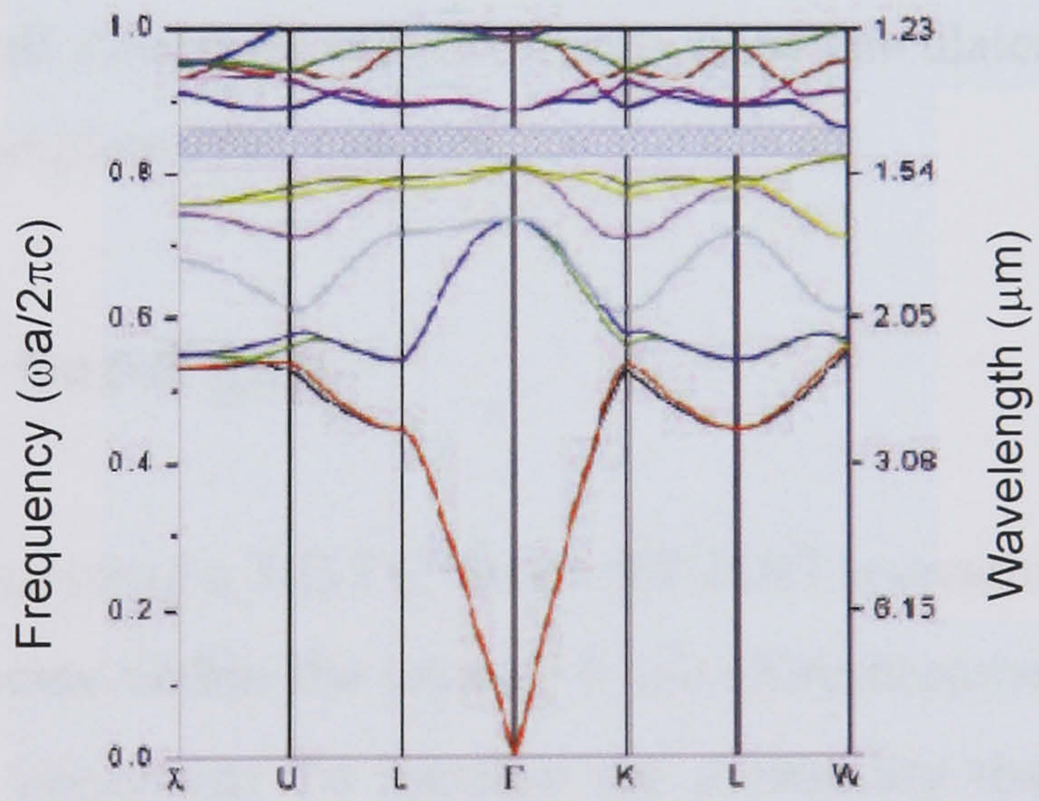


Figure 1.1 **Calculated band structure of a silicon inverse opal. The complete PBG is shown by the cross-hatched region (9)**

Light travelling through a PC experiences a periodic variation in the refractive index similar to the periodic potential experienced by electrons in an atomic crystal. It is the periodicities in an atomic crystal which cause the Bragg reflection of electrons with the correct wavelength (10). To describe the scattering of waves from a periodic array of

atoms it is necessary to use reciprocal space, since a diffraction pattern of a crystal is a map of reciprocal space (11). In reciprocal space the wave vector **k** is referred to rather than the wavelength and has dimensions of reciprocal space, ($|k|=2\pi/\lambda$). The primitive unit cell is called the Wigner-Seitz cell and is formed by the planes bisecting the lines connecting a particular lattice point with its neighbours. When considering the propagation of waves in a periodic structure it is more common to call the Wigner-Seitz cell the first Brillouin zone which exhibits all the **k** values which can be Bragg reflected from the crystal.

Since light travelling through a PC interacts with the periodic variation in the refractive index, the strength of which is determined by the refractive index contrast (RIC), the scattering of the light can be expressed as photonic band structures in a Brillouin zone (12). The RIC is defined as the difference in refractive indices between the two materials within the PC. The interaction of the incident light causes the splitting of degenerate bands and the appearance of frequency gaps for wave vectors at the edges of the Brillouin zone (12). These forbidden ranges are known as stop-bands and waves within these ranges are Bragg reflected and forbidden to propagate. The stop-bands are associated with every propagation direction and their width increases with an increase in the RIC (13). If the interaction is very strong, the stop-bands in all directions can overlap to form a complete PBG, *i.e.* a frequency band for which the propagation of light is forbidden in all directions (12,13). It has been calculated that a RIC of 2.8 is required to create a complete PBG (14-17).

1.3 A complete band gap

The key challenge in creating a 3-D PC with a full PBG is creating complete overlap of the forbidden frequencies within the crystal. It therefore becomes clear that the lattice type of a 3-D PC is important. To increase the probability that the frequencies will overlap in all directions the Brillouin zone should closely resemble a sphere (18). In all fourteen Bravais lattices for 3-D unit cells the Brillouin zone of the face centred cubic (fcc) lattice has the least percentage deviation from a sphere thus driving the fabrication of 3-D photonic structures with this lattice (18). It was the fcc lattice which was proposed by Yablonovitch and John in their initial proposals as being most likely to produce a material with a PBG (2.3). An illustration of the first Brillouin zone for an fcc lattice is shown in figure 1.2 and has the shape of a truncated octahedron.

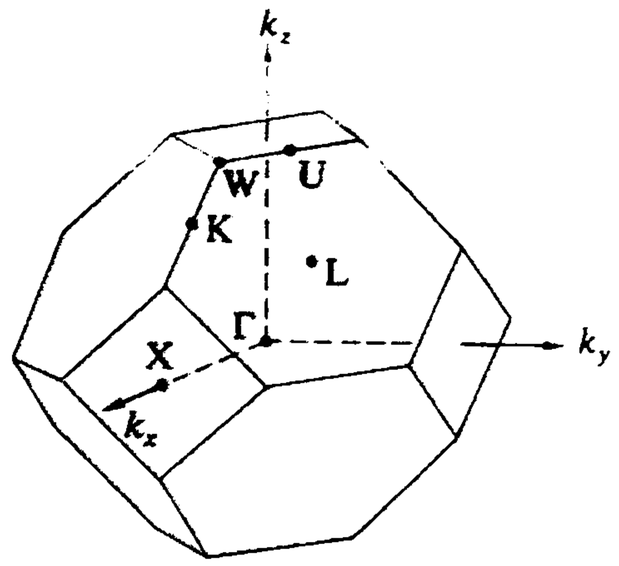


Figure 1.2 **Illustration for the first Brillouin zone for the fcc lattice and the conventional symbols for the important symmetry points (10)**

Several points on the surface of the Brillouin zone are marked, for example the Γ point which is the origin of reciprocal space (12). The L point is closest to the centre and orientated towards the body diagonal of the unit cell. The W point is furthest from the Γ point and the cubic directions, the X points, are shown. A plane wave travelling in the X direction will sense the periodicity in the cubic direction, forming a standing wave and opening up a forbidden gap. If the wave is travelling in the L direction the periodicity will be along the body diagonal and a gap will form in that direction. Crystallographically the Γ-L direction corresponds to the <111> in an fcc crystal (12). The wave vector to the L point is 14% smaller than the corresponding wave vector to the X point and therefore is likely to be centred at a frequency 14% smaller than the gap at X (18). The problem is that if the two gaps are not wide enough they will be not overlap in frequency and a full PBG will not be formed.

A sphere-like Brillouin zone improves the probability of a forbidden energy gap opening in all directions but it was unclear what the shape of the 'atoms' in the fcc array should be. Early theoretical calculations, see for example (19), focussed on dielectric spheres and spherical voids in an fcc lattice. These calculations showed that, due to symmetry induced degeneracy at the W point of the Brillouin zone, the fcc lattice did not exhibit a complete PBG. In fact only a pseudo-gap, a forbidden 'band' having zero width (*i.e.* just one wavelength of light is forbidden), existed (4).

In an attempt to change the induced degeneracy of the symmetry the lattice needs to be changed. However there was apprehension in moving away from the sphere-like fcc Brillouin zone and thus the next structure which was investigated was the diamond lattice (19). Ho, Chan and Soukoulis were the first theorists to predict that a 3-D PC would have a full PBG if it was constructed of a diamond lattice of dielectric spheres or

air spheres in a dielectric medium, as long as the appropriate sphere diameter was chosen (1). Most of the structure, 81%, was air and to maximise the size of the band gap the sphere radius was chosen to be 0.352a (where a is the lattice constant).

However, in 1992 the theorist Haus showed through band structure calculations, that an fcc lattice of ellipsoidal atoms possess a complete PBG (20). In addition it has been shown experimentally that a silicon PC can be fabricated with a PBG at 1.5 μm (9). This inverse silicon structure satisfies the two essential criteria for complete band gap formation – a high refractive index (n_{Si}=3.45 at 1.5 μm) and the optical absorption edge of silicon occurs at a wavelength well below the PBG.

1.4 Structures

The most important similarity between PCs and solid state crystals is their translational symmetry (7). One of the techniques available for the synthesis of 3-D PCs is outlined in chapter 4. The properties of one dimensional (1-D), 2 dimensional (2-D) and 3-D PCs are discussed in the following sections.

As mentioned previously for a material to exhibit a full PBG it must be periodic in all three dimensions. However, photonic stop-bands can exist in 1-D and 2-D and 3-D structures. Figure 1.3 schematically illustrates PCs with 1-D, 2-D and 3-D structures.

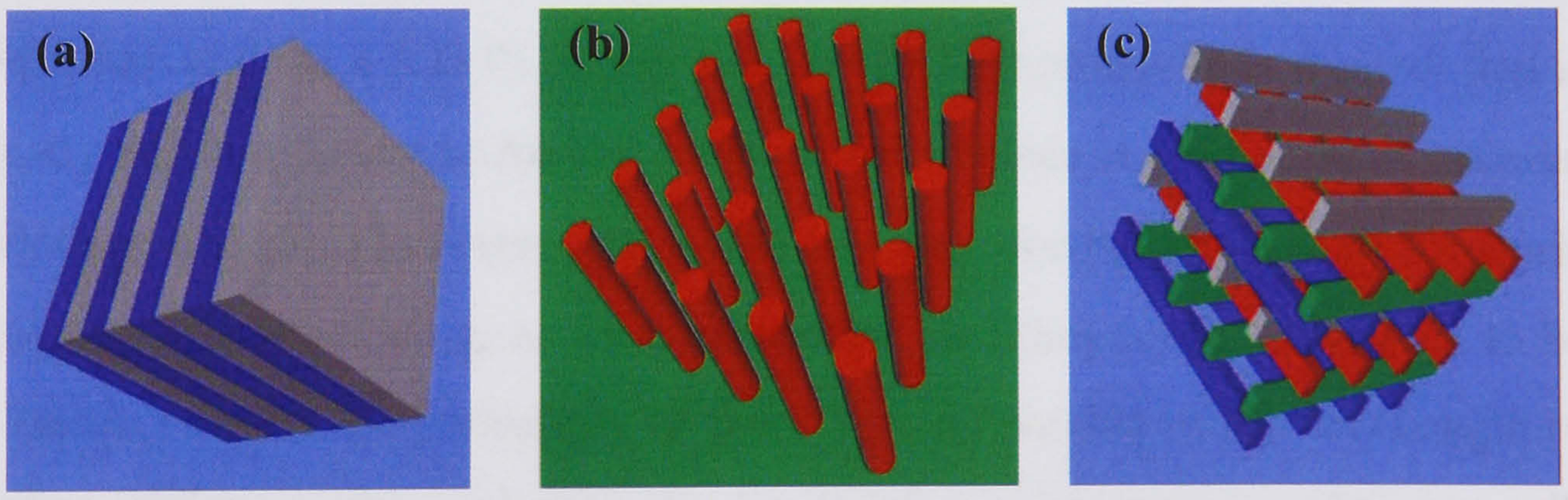


Figure 1.3 Schematic illustration of PCs with (a) 1-D, (b) 2-D and (c) 3-D structures (1)

The simplest possible PCs, as illustrated in figure 1.3(a), are typically multilayer films consisting of alternating layers of material with different dielectric constants. The material is periodic in only one direction, the stack axis (z), and homogeneous in the x-y plane. Such PC materials can act as a perfect mirror, reflecting radiation with a well defined wavelength (1). A wide variety of current techniques are used in the formation

of 1-D PCs, for example molecular beam epitaxy (MBE) and chemical vapour deposition (CVD) (7).

If the periodicity of the PC is extended into a second dimension a 2-D PC can be created. Examples of 2-D PCs are arrays of holes in a dielectric medium and arrays of dielectric rods. The photonic fibre is currently the most exploited 2-D structure where an array of capillaries is arranged in a 2-D symmetry and the array is then heated and drawn (4). The alternative 2-D structure is formed by etching a pattern of air holes in a high refractive index material (7). Existing fabrication methods are based on lithographic patterning of planar substrates (4,7).

In the case of 3-D PCs the periodicity along all three dimensions is not sufficient to ensure that a full PBG is opened. In addition the material must possess a minimum RIC (21). Theoretical calculations have shown that the RIC should be greater than 2.8 to open a full PBG (14-17).

The first 3-D PC to be produced experimentally with a complete PBG was a dielectric slab with a series of 6 mm holes drilled into it (1). This machined material is named Yablonovite, after its inventor Eli Yablonovitch, and has a complete PBG in the microwave region. If the refractive index of the dielectric slab exceeds 3.6 the material is termed a photonic insulator, as is the case for Yablonovite (8).

The simplest way to form a 3-D PC is the way in which Yablonovite is formed, that is to periodically remove dielectric material with ε_1 and replace it with another material with ε_2 (where $\varepsilon_1 \neq \varepsilon_2$) (7). However, all the methods used for the removal of dielectric material require micromachining, as for Yablonovite, or lithographic techniques to be used. The length scale of the periodicity of the PC is comparable to the wavelength of the interacting radiation (22) and thus the limits of the fabrication techniques will ultimately limit the feature size of the PCs.

However, it has been suggested that it will be for visible and near infra-red (IR) frequencies that PBG materials will have their most important impact (23). Although PBG materials have been formed which operate in the microwave region, the greatest obstacle to forming PCs operating in the visible and near IR region is the lack of a reliable means of microfabricating materials on the nanometre length scale. Using

typical top-down technologies, for example electron beam lithography and photolithography, to produce a structure which is periodic in all three dimensions with a length scale comparable to visible light has proven to be a technological challenge. This is mainly due to the feature sizes, on the nanoscale, being outwith the fabrication limits of conventional technologies and being costly (24,25).

One exception is the use of holography to pattern 3-D PCs (26,27). Using 3-D holographic lithography a sub-micron periodic structure can be generated when four non-coplanar laser beams produce an interference pattern in a film of photo resist. This technique can form structures which have photonic stop-bands in the visible spectral region (26).

1.5 Natural photonic crystals

When creating new materials scientists sometimes look towards nature for inspiration. It can be argued that nature created the first 3-D PC in the form of the gemstone opal (4,8). Natural opal is composed of a cubic close packed arrangement of sub-micron diameter hydrated silica spheres (28). Opal is common in most parts of the world but opal showing brilliant spectral colours (gem opal) is rare, although gem and common opal are chemically and physically similar (28). Spectrographic analysis showed that there was also no compositional difference between the two types of opal and it was not until the invention of the electron microscope that the two structures could be identified (8). Electron microscopy showed that both opal structures were porous but the arrays of pores in gem opal were regular compared to the random pores in common opal (28). Figure 1.4 shows an image of gem opal demonstrating beautiful iridescence and an electron micrograph showing the packing of the silica spheres.

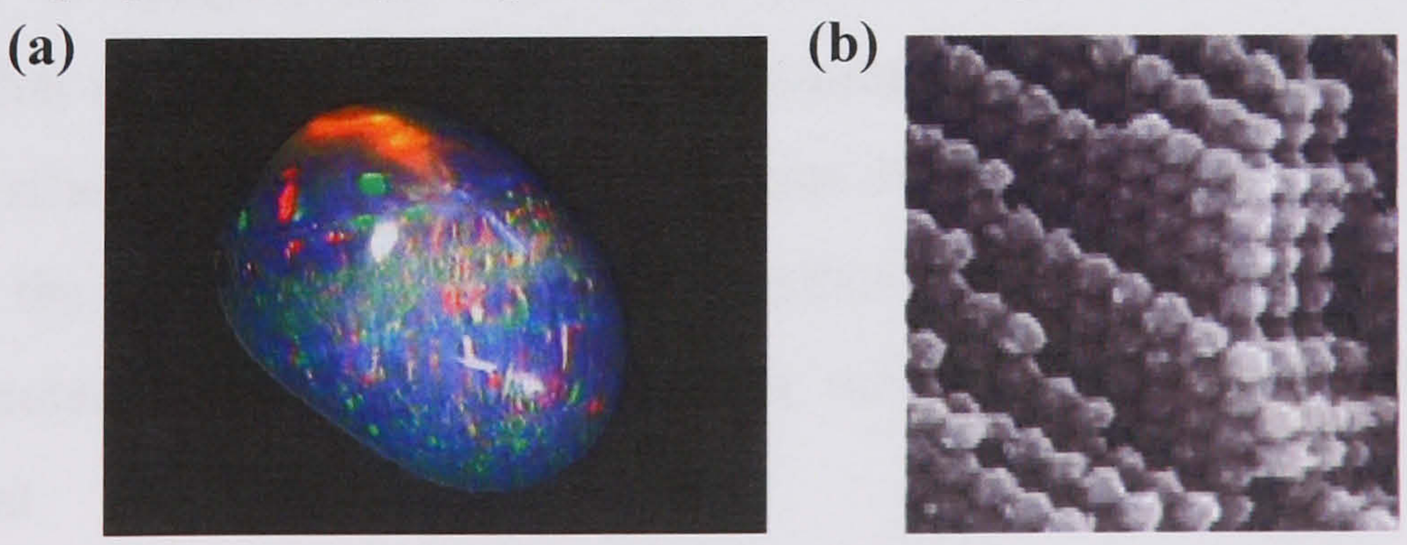


Figure 1.4 **(a) a sample of gem opal demonstrating beautiful iridescence (29) and (b) SEM image showing the close packing of the silica spheres in opal (30)**

Opal acts as an optical diffraction grating for visible light since the lattice spacings are comparable to the wavelength of visible light. Consequently the gemstone is brilliantly

coloured, as shown in figure 1.4(a). The main reason for the appearance of many colours is due to impurities (31). The impurities restrict the RIC that can be obtained and natural opal is an example of an incomplete PBG PC.

There are other examples in nature which are capable of producing 3-D PCs on a faster timescale than natural opal. There are several species of butterfly, for example the Morpho butterfly, which show beautiful iridescent colours due to sub-micron scales on their wings (32,33). Similar to natural opal these structures do not possess a full PBG.

Although the formation of a complete PBG has been eluded by nature, the structure and properties of natural opal provided a starting point for the investigation of the growth of 3-D PCs by artificial methods. It is possible to form a material, known as synthetic opal, which has a structure analogous to natural opal, *i.e.* a close packed array of dielectric spheres (as illustrated in figure 1.4(b)). The formation of synthetic opal in clean, controlled laboratory conditions can help eliminate the faults and impurities present in natural opal.

1.6 Evidence of the fcc structure

As previously discussed a spherical Brillouin zone gives the highest probability that there will be an overlap of the PBG frequencies in all directions of space and thus an fcc structure is favourable (18).

It is known that silica spheres in aqueous solution behave as hard spheres but with surfaces which are electrically charged (34). It has been reported that colloidal particles, *e.g.* silica or polystyrene, will self-assemble into ordered arrays under slow sedimentation (35-37). During the sedimentation process as water evaporates from the system the silica spheres suffer Stokes viscous drag that can outweigh Brownian motion and lodge the spheres in a particular position (35). However, due to solvent flow spheres located at unfavourable sites can move to re-organise into a more stable arrangement.

The close packed layers of spheres can stack to form a 3-D solid known as synthetic opal. Three different stacking arrangements can be considered. Once two layers are stacked (AB) the next layer can be stacked on either an A or C site. If the third layer lies

in the C site (*i.e.* ABCABC) an fcc structure is obtained. However, if the third layer lies above the first layer, *i.e.* an A site (ABABAB) a hexagonal close packed (hcp) structure is obtained. Lastly the layers can be randomly stacked (ABABCABA), a structure which is known as random hexagonally close packed (rhcp) (35). The formation of an fcc and hcp lattice is illustrated schematically in figure 1.5.

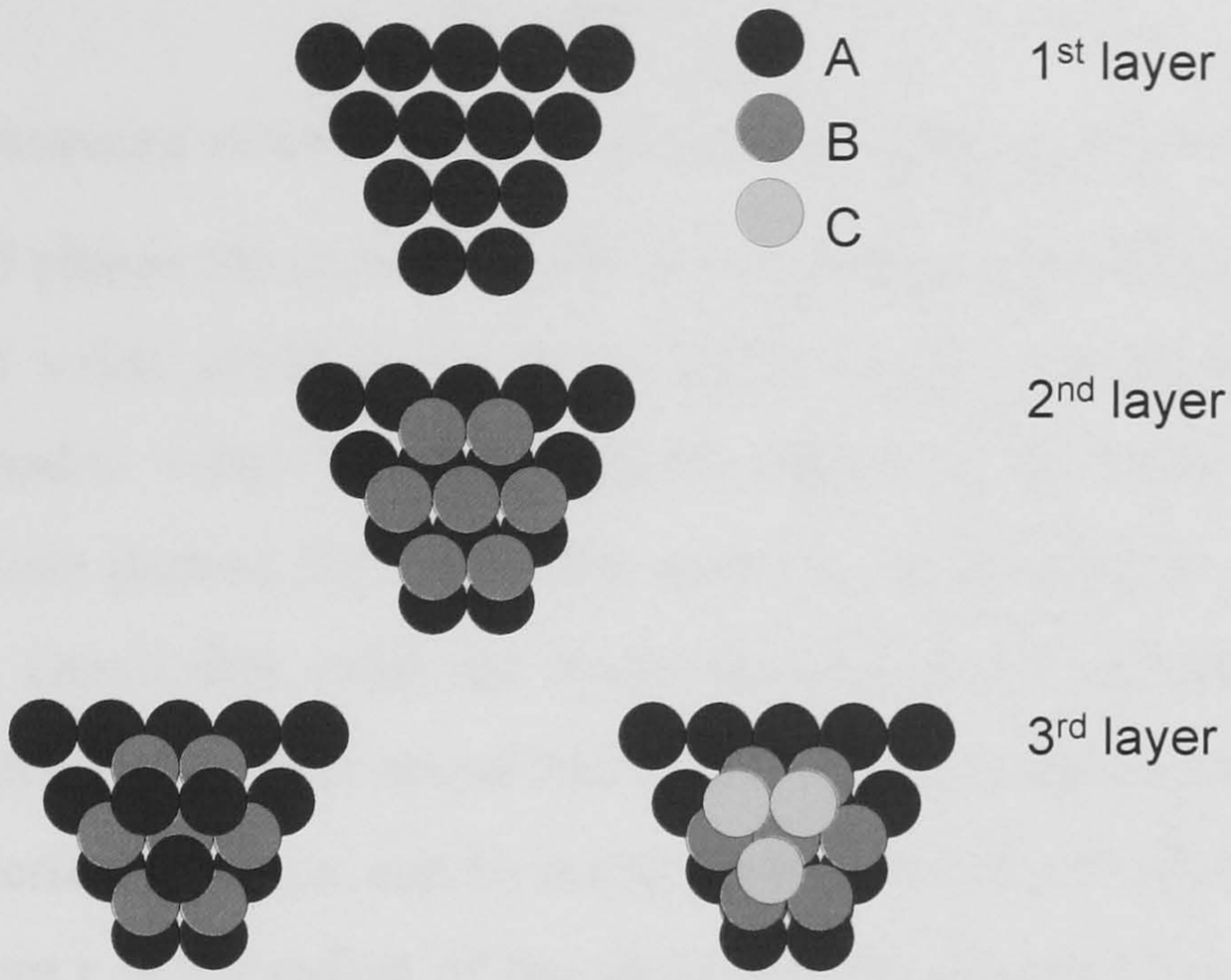


Figure 1.5 Schematic illustration of the possible arrangements of stacked hard spheres

Theoretical calculations by Woodcock (38) showed that for the stacking of hard spheres the fcc structure is more thermodynamically stable compared to the hcp phase by a Gibbs free energy of 0.005RT per mole. In addition more recent calculations have shown that the Gibbs free energy is actually twice as small, thus the C sites are favoured compared to the A sites (39). The Gibbs free energy difference between the fcc and hcp phase is much smaller than the typical thermal energy of a particle (0.5RT per mole). However, due to solvent evaporation, the spheres become closer together and can then suffer Stokes viscous drag which can outweigh Brownian motion and therefore the spheres can arrange into an fcc or hcp arrangement (35).

For both the fcc and hcp structures each sphere touches its twelve nearest neighbours – six closest neighbours in the same layer, three in the layer above and three in the layer below. An illustration of the fcc unit cell is shown in figure 1.6.

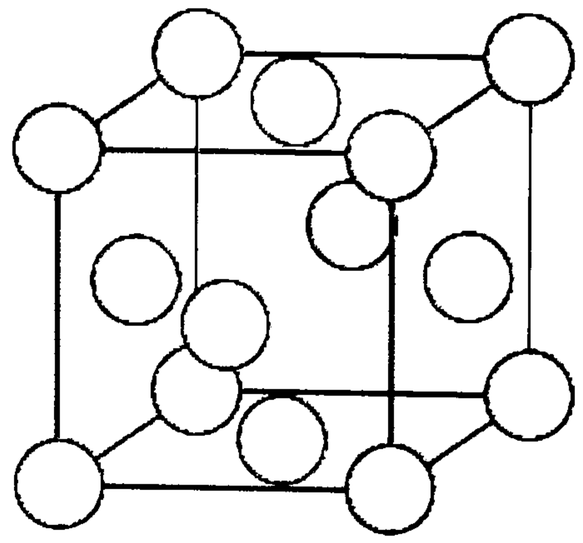


Figure 1.6 Illustration of the fcc unit cell composed of a close packed arrangement of spheres

The close packed planes are parallel to the {111} planes of the fcc unit cell (40). There are two types of voids which occur in an fcc structure – octahedral and tetrahedral voids. For tetrahedral voids the three spheres that form the base of the tetrahedron belong to one close packed layer with the apex of the tetrahedron either in the layer above or below. Octahedral voids are found between four coplanar spheres with one sphere at each apex in the layer above and below. The octahedral and tetrahedral voids, although not spherical in shape, can be occupied by a sphere of radius 0.414r and 0.225r respectively where r is the radius of the close packed spheres (41). In an fcc unit cell there are four spheres, one octahedral and two tetrahedral voids (40). Both the spheres and the voids are arranged with fcc symmetry and therefore there is the possibility of forming a normal or inverse replica while still maintaining the favourable fcc Brillouin zone.

The first experimental evidence of the fcc phase in sedimented silica spheres was reported by Miguez *et al* (42). In order to discriminate between the fcc and hcp phase SEM characterisation of the lateral facets obtained by cleavage of the synthetic opal sample were investigated. Several kinds of arrangements were observed all of which were compatible only with the fcc phase. For example a square array was observed which can only correspond to a {100} type face of an fcc structure. Similarly an internal {111} type facet was imaged which is morphologically equivalent to the growth surface but orientated in a direction which forms an angle of 70.5° with the former. Finally a {110} type surface was imaged where the arrangement is a rectangular lattice where the spheres are $\sqrt{2}$ sphere diameter apart in one direction and a sphere diameter apart in the other direction (42). Although a similar sort of lattice would be expected in hcp packing, the ratio between the sides of the rectangle would be different. These three mentioned arrangements observed in sedimented synthetic opal would indicate that the spheres arrange in the fcc phase.

Further experimental evidence of the fcc structure was reported by Cheng *et al* (43). Similar to the aforementioned method, characterisation by SEM was used to probe the packing in sedimented silica spheres. At least three planes are required to define a lattice point in 3-D space. Therefore it is necessary to find a sphere which can be located simultaneously in three different crystal planes (43). The possible cleaved facets for an fcc structure are the boundary planes of a truncated octahedron. Hence superimposing a truncated octahedron on SEM images of cleaved synthetic opal samples, which is the method used by Cheng *et al* (43), is the most direct evidence to confirm the fcc structure. Cheng *et al* (43) also used the optical properties of the crystal and the relationship of the position of the reflection peak, which will be discussed in section 1.11, to prove the packing was fcc.

1.7 Synthetic opal

Initially natural sedimentation of colloidal spheres was used to obtain samples of synthetic opal but this method offers little control over the morphology of the top surface, the number of layers formed and the process takes a significant amount of time (36). In addition the samples formed are polycrystalline which decreases their attractiveness for use as PC materials (35). The approach used routinely today for the growth of synthetic opal is the simple method first reported by Colvin and co-workers (24) referred to as the self-assembly technique. In this technique monodisperse, sub-micron colloidal spheres, typically silica or polymer, assemble into close packed arrays either free-standing or as thin films (*i.e.* supported on a substrate) see for example (6,24,44,45). A more in depth discussion of the formation of synthetic opal thin films will be given in chapter 4.

Although, as discussed in section 1.2, the frequency dependence of the refractive index is assumed to be negligible within a broad frequency range, certain materials used in the formation of synthetic opal do have a frequency dependent refractive index. For example the refractive index of polystyrene, which was the material of choice in this project, is known to be dependent of wavelength. Using the method proposed by Ma *et al* (46), based on the Cauchy dispersion relation, the refractive index of polystyrene can be calculated in the wavelength range 370-1610 nm using equation 1.16.

$$n(\lambda) = A + \frac{B}{\lambda^2} + \frac{C}{\lambda^4} \qquad \textbf{Equation 1.16}$$

where λ is the wavelength (in μm) and the constants A,B and C are 1.5725, 0.0031080 and 0.00034779 respectively (46).

For the visible region (λ=400-750 nm) the refractive index of polystyrene ranges from 1.606 to 1.579. Therefore an average refractive index over the visible region of 1.59 can be calculated and this value was used as the refractive index for polystyrene in all calculations. This value agrees well with the value for bulk polystyrene as reported in the literature (47).

1.8 Inverse opal

To achieve a complete PBG the refractive index of the dielectric must be greater than 2.8 for an fcc lattice of air spheres in a dielectric matrix (15). The refractive index of polystyrene (1.59) is not large enough to create a full PBG. However, synthetic opal structures can be used as a template where the voids between the spheres are filled with a material of high refractive index and then the opal template is removed. The resulting structure is three dimensionally ordered and macroporous and is commonly referred to as inverse opal. A more detailed discussion of the formation of the inverse opal structure will be given in chapter 7.

1.9 Multifunctional photonic crystals

While the initial concept of a full PBG material by forming inverse opal was straight forward the reality of forming such structures has proven more difficult. Success has been achieved for silicon and germanium inverse opals with PBGs around 1.5 μm and 2 μm respectively (17). Silicon is the most suitable material to infill the opal template because it has a high refractive index (n=3.5). Recently Rugge *et al* (48) proposed a method which could be suitable for the development of tantalum(V) nitride inverse opal with a complete PBG in the visible region.

In the realisation that the formation of a full PBG inverse structure is difficult there is now growing interest in forming multifunctional, or tunable, PCs. Arguably the first

tunable PC was proposed by John and Busch whereby an electrically tunable liquid crystal-PC switch was proposed (49). Since then other methods have been proposed for forming functional 3-D PCs – for example ferroelectrics tuned by an electric field (50-52), ferromagnetics tuned by a magnetic field (53), liquid crystal materials (49,54) and electrochromic materials tuned by an electric field (55). A recent example of a tunable PC was the formation of inverse structured ferroelectric lead lanthanum zirconate titanate (51,56).

1.10 Basics of Ferroelectricity

A ferroelectric can be defined as a material with a spontaneous polarisation which can be re-orientated with an electric field and varies with temperature (40). Ferroelectric materials can be divided into three categories – inorganic ferroelectrics, ferroelectric polymers and ferroelectric liquid crystals (57). The most studied category is the inorganic ferroelectrics and the most important group of materials within this category are oxides that have distorted oxygen octahedra as the primary structural building unit. This group includes the perovskites with generalised formula ABO_3, such as $BaTiO_3$, $Pb(Zr,Ti)O_3$ and $KNbO_3$. Figure 1.7 illustrates the general perovskite structure where A is usually a large positive ion situated at the corner of the lattice, B is a small positive ion located at the body centre and the oxygen ions are situated at the face centres. For electrical neutrality the sum of the charges on the A and B ions must be equal to six.

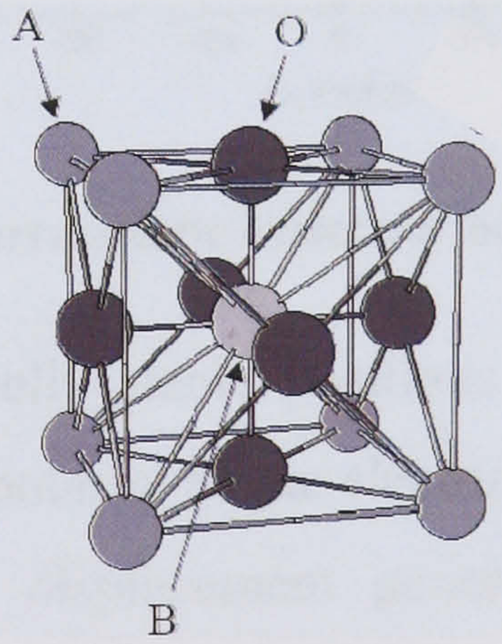


Figure 1.7 General perovskite structure with formula ABO_3, the A, B and O ions are labelled

The spontaneous polarisation found in ferroelectric materials arises from the centre of positive charge not being coincident with that of the negative charge. In the distorted ferroelectric phase, the tetragonal or rhombohedral perovskite structure which is stable at room temperature, the spontaneous polarisation of ~10 $\mu C/cm^2$ is produced primarily by the displacement up or down of the B ions with respect to the other ions (58). Figure 1.8 illustrates the BO_6 octahedra environment.

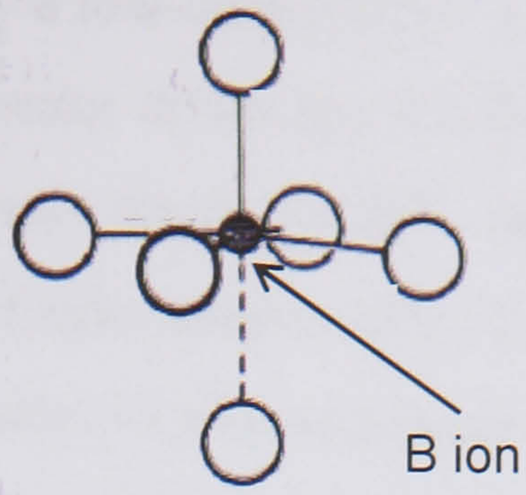


Figure 1.8 Environment of the BO_6 octahedron

Determination of the structure of the tetragonal form of $BaTiO_3$ by both neutron and X-ray diffraction has shown that the titanium atom can be displaced from the centre of its octahedron (figure 1.8), giving one short Ti-O distance of 1.86 Å (59). The individual BO_6 octahedra are polarised all of the time and applying an electric field aligns the individual dipoles with the electric field. The value of the polarisation plotted versus the applied electric field shows a specific response, as shown in figure 1.9 for PZT, called ferroelectric hysteresis.

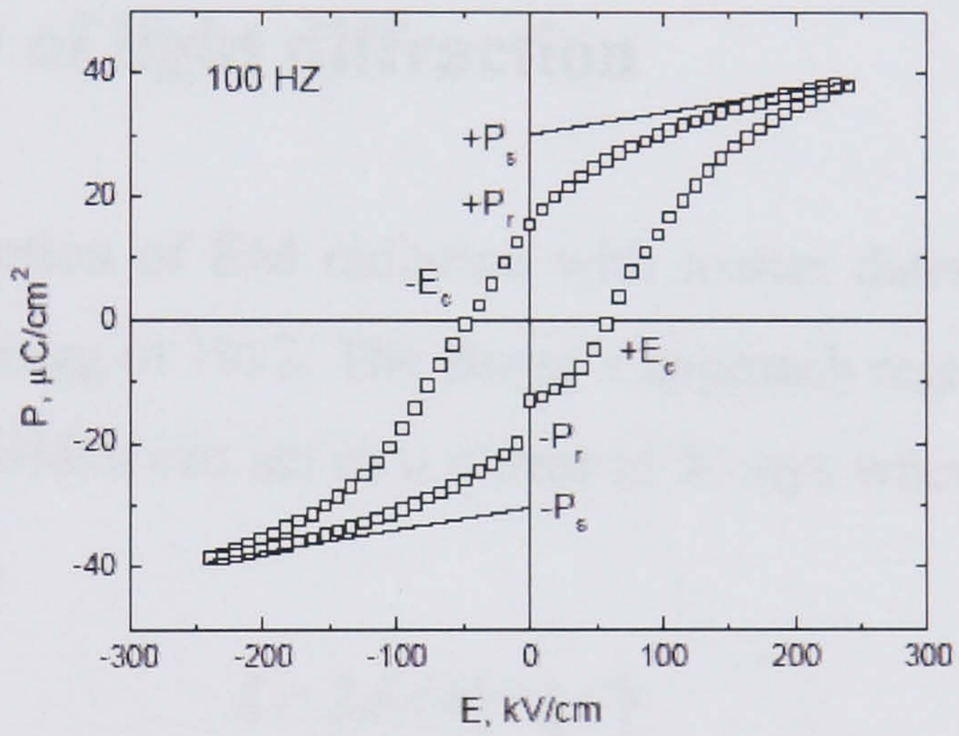


Figure 1.9 Ferroelectric hysteresis loop for a PZT 45/55 film

There are two thermodynamically stable positions of the B ions inside the oxygen octahedron. Depending on the polarity of the electric field, the B ion is either displaced upwards or downwards. This displacement generates a dipole moment inside the oxygen octahedron leading to a saturation polarisation ($\pm P_s$). When the applied electric field is removed the B ion remains in the displaced position and generates a remnant polarisation (40). A ferroelectric crystal generally consists of regions called domains within which the polarisation is in the same direction but in adjacent domains the polarisation is in different directions (11). Therefore the net polarisation depends on the average polarisation direction.

The ferroelectric state is usually a low temperature condition because increased thermal motion at high temperatures breaks down the common displacement in adjacent BO_6 octahedra and destroys the domain structure (40). The temperature at which the break down occurs is known as the Curie temperature, T_c, and above this temperature the material is paraelectric. The ferroelectric-paraelectric phase transition is an order to disorder phase transition because in the paraelectric phase the distortion or tilts of the BO_6 octahedra are randomised (11).

A number of theoretical approaches have been proposed to explain the behaviour of ferroelectric crystals, for example the Landau theory of phase transition (11). A ferroelectric with a first order phase transition between the ferroelectric and paraelectric state is distinguished by a discontinuous change of the saturation polarisation at the transition temperature. Landau theory considers the form of the expansion of the energy as a function of the polarisation and is a formal thermodynamic theory (11).

1.11 Theory of light diffraction

The theory of the interaction of EM radiation with matter dates back to the work of William and Lawrence Bragg in 1912. The Bragg's approach regards crystals as regular planes of atoms each of which can act as a mirror to X-rays when the Bragg condition, equation 1.17, is fulfilled.

$$\lambda = 2d\sin(\theta \pm \delta) \qquad \textbf{Equation 1.17}$$

Where λ is the wavelength of the radiation, d is the interplanar spacing of the crystal, θ is the incident, or Bragg, angle and δ is a range of angles (8). When λ, d and θ satisfy the Bragg condition the incident radiation is reflected and cannot propagate through the crystal. In addition the incident and diffracted beams form equal but opposite angles with the normal to the plane, even though the lattice plane is not necessarily parallel to the sample surface (60).

All crystals with their regular repeating structures should be capable of diffracting radiation that has a wavelength similar to their interatomic separations (40). Synthetic opal, which as discussed previously has a periodic crystal structure, can also diffract EM radiation and therefore Bragg's law can be applied. However, for Bragg diffraction from the surface of synthetic opal the refraction of the beam at the sample surface must

also be considered (Snell's law), as shown in figure 1.10. Although Bragg's law (equation 1.18) applies to light in periodic structures and Snell's law (equation 1.19) to light in a homogeneous medium, the two laws can be successfully combined to give the combined Bragg/Snell law (equation 1.20) to describe the position of angle resolved reflection peaks indicating that the wavelength of light is intermediate between the two extremes (22).

$$\lambda = 2d \sin\theta \qquad \textbf{Equation 1.18}$$

$$n_1 \sin\theta_1 = n_2 \sin\theta_2 \qquad \textbf{Equation 1.19}$$

$$\lambda = 2d\sqrt{n_2^2 - \sin^2\theta} \qquad \textbf{Equation 1.20}$$

1.11.1 Derivation of the Bragg/Snell law

The refractive index of a material, n, can be calculated by equation 1.21 where c is the speed of light and λ is the wavelength of the light.

$$\frac{n_2}{n_1} = \frac{c_1}{c_2} = \frac{\lambda_1}{\lambda_2} \qquad \textbf{Equation 1.21}$$

Figure 1.10 is a schematic illustration of the interactions which takes place when an incident beam of radiation is reflected from the sample surface.

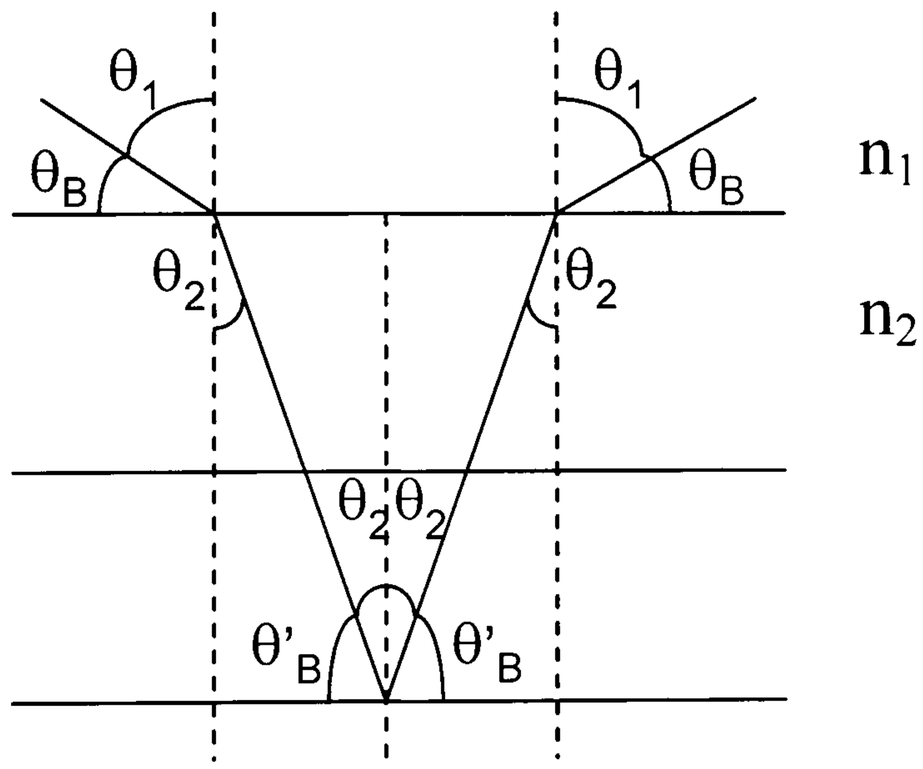


Figure 1.10 Derivation of the combined Bragg/Snell law

If we consider the reflection from one of the internal planes

$$\lambda_2 = 2d \sin\theta_B^{'}$$

But from re-arrangement of equation 1.21 $\lambda_1 = n_2\lambda_2$ and if n_1=1

$$\Rightarrow \lambda_1 = 2dn_2 \sin\theta_B^{'} \text{ but } \theta_B^{'} = 90 - \theta_2$$

$$\Rightarrow \lambda_1 = 2dn_2 \sin(90 - \theta_2)$$

$$= 2dn_2 \cos\theta_2$$

$$= 2dn_2 \sqrt{1 - \sin^2\theta_2}$$

From Snell's law (equation 1.19) $\sin\theta_2 = \frac{\sin\theta_1}{n_2}$ if n_1=1

$$\Rightarrow \lambda_1 = 2dn_2 \sqrt{1 - \frac{\sin^2\theta_1}{n_2^2}}$$

$$= 2dn_2 \sqrt{\frac{n_2^2 - \sin^2\theta_1}{n_2^2}}$$

Therefore

$$\boxed{\lambda_1 = 2d\sqrt{n_2^2 - \sin^2\theta_1}}$$

In conventional X-ray diffraction, equation 1.17, the reflection holds for a range of angles, shown as ±δ, determined by how strongly the atoms scatter the X-rays (8). When considering the interaction of light with a PC, the ±δ term in equation 1.17 can be related to the magnitude of the RIC.

In equation 1.20 the refractive index of the PC material, n_2, is a combination of the two components of the fcc lattice, *i.e.* the air and the dielectric material (61,62) and is commonly denoted n_{eff} – an effective refractive index. Thus, equation 1.20 can be re-written as

$$\lambda = 2d\sqrt{n_{eff}^2 - \sin^2\theta} \qquad \textbf{Equation 1.22}$$

The effective refractive index can be calculated by the effective medium approximation, which is outlined in equation 1.23,

$$n_{eff} = \sum n_i f_i \qquad \textbf{Equation 1.23}$$

, where n_i and f_i are the refractive index and volume fraction of the ith component respectively (63).

When considering an fcc unit cell the volume occupied by the dielectric spheres can be calculated in the following way.

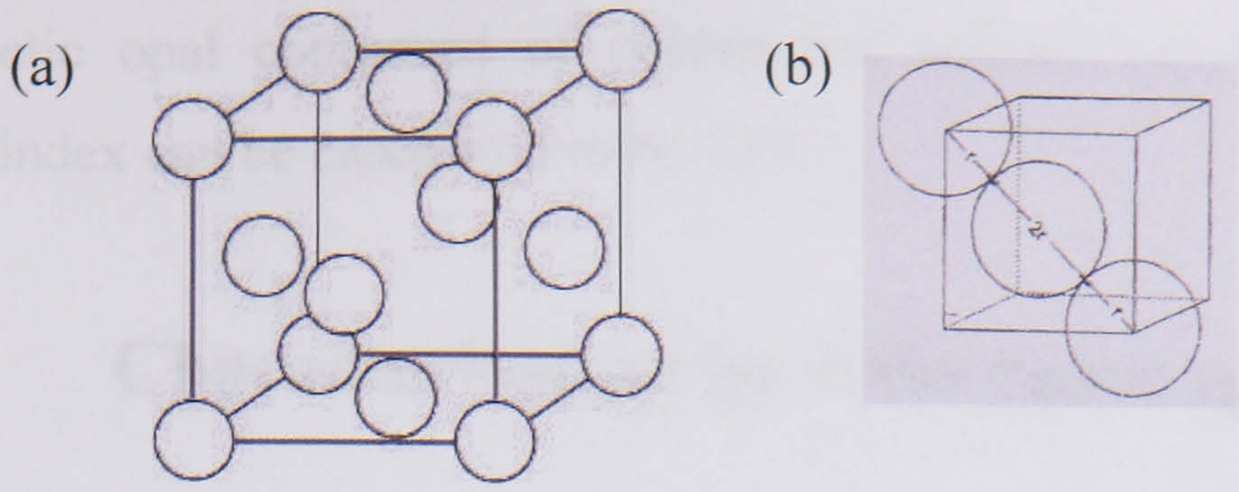


Figure 1.11 **(a) illustration of the fcc unit cell and (b) spheres in contact along the face diagonal (40)**

As shown in figure 1.11(b) the only spheres which touch each other in the fcc lattice are the three spheres across the face diagonal and thus the length of the face diagonal can be expressed as four sphere radii (4r or 2D where r and D are the sphere radius and diameter respectively). Since the unit cell is cubic, Pythagoras' theorem can be used to calculate a value for the unit cell parameter, a, since the face diagonal is the hypotenuse of a right angled triangle in which the other two sides are a.

$$a^2 + a^2 = 16r^2 \Rightarrow a = \sqrt{\frac{16}{2}}r = \sqrt{8}.r \qquad \textbf{Equation 1.24}$$

The unit cell volume can therefore be calculated as shown in equation 1.25.

$$Volume = a^3 = (\sqrt{8}.r)^3 = 8\sqrt{8}.r^3 \qquad \textbf{Equation 1.25}$$

In the fcc unit cell there are a total of four spheres since the eight spheres at the corners are shared between eight adjacent unit cells and the six spheres at the face centre positions are each shared with the neighbouring unit cell. The volume of each sphere can be calculated as:

$$\textit{Sphere volume} = \frac{4}{3}\pi r^3 \qquad \textbf{Equation 1.26}$$

Since the volume of each unit cell and the volume of a sphere are known, the percentage of the unit cell occupied by the dielectric spheres can be calculated as:

$$\frac{4x\left(4/3\,\pi r^3\right)}{8\sqrt{8}.r^3} = 0.7405 \qquad \textbf{Equation 1.27}$$

Equation 1.27 reveals that for an fcc lattice 74% of the unit cell volume is occupied by spheres and the remaining 26% is unoccupied. Therefore, the effective refractive medium approximation, equation 1.23, for an fcc unit cell becomes

$$n_{eff} = (0.74 \text{x} n_{sphere}) + (0.26 \text{x} n_{air}) \qquad \textbf{Equation 1.28}$$

For synthetic opal composed of polystyrene spheres (n_{PS}=1.59 (64)) the effective refractive index can be calculated to be 1.44.

1.12 Characterisation by reflectance spectroscopy

Characterisation of the internal order of the structure of synthetic opals can be performed in two ways – directly by electron microscopy (see chapter 2) or by observing optical or X-ray diffraction when the sample is illuminated by monochromatic radiation (60).

As previously discussed, Bragg type reflections can occur from the 3-D lattice of synthetic opal. Reflection and transmission spectroscopy are techniques which can reveal PC stop-bands as increased reflection or decreased transmission respectively over a range of wavelengths (65).

When white light is used to measure reflectivity from a PC a stop-band will manifest itself as a peak in the reflectance spectrum containing the frequencies which cannot propagate through the crystal. These measurements will show a cross section of the electromagnetic dispersion relations of the crystal for a certain direction of propagation (65). However, if reflectivity is measured with monochromatic radiation as a function of incident angle, information will be obtained about dispersion surfaces. Bragg reflection at 0° incidence probes the stop-band in the Γ-L direction in the Brillouin zone, see figure 1.2.

The apparatus used to obtain angle resolved reflectance or transmission measurements is described in chapter 2. The diffraction from the atomic planes within synthetic opal is a test for crystalline quality and order (43,44). Reflectance spectroscopy probes the close packed planes within the sample and, since there is no appreciable absorption of polystyrene in the wavelength range 370-1400 nm (46), is equivalent to transmission spectroscopy. However, as the angle of incidence increases away from the normal the Bragg dip in transmission rapidly disappears but the peak in reflection can still be clearly resolved (13). Consequently reflection spectroscopy was routinely used during this project. An example of typical angle resolved reflectance measurements for a synthetic opal sample composed of 408 nm polystyrene spheres is shown in figure 1.12.

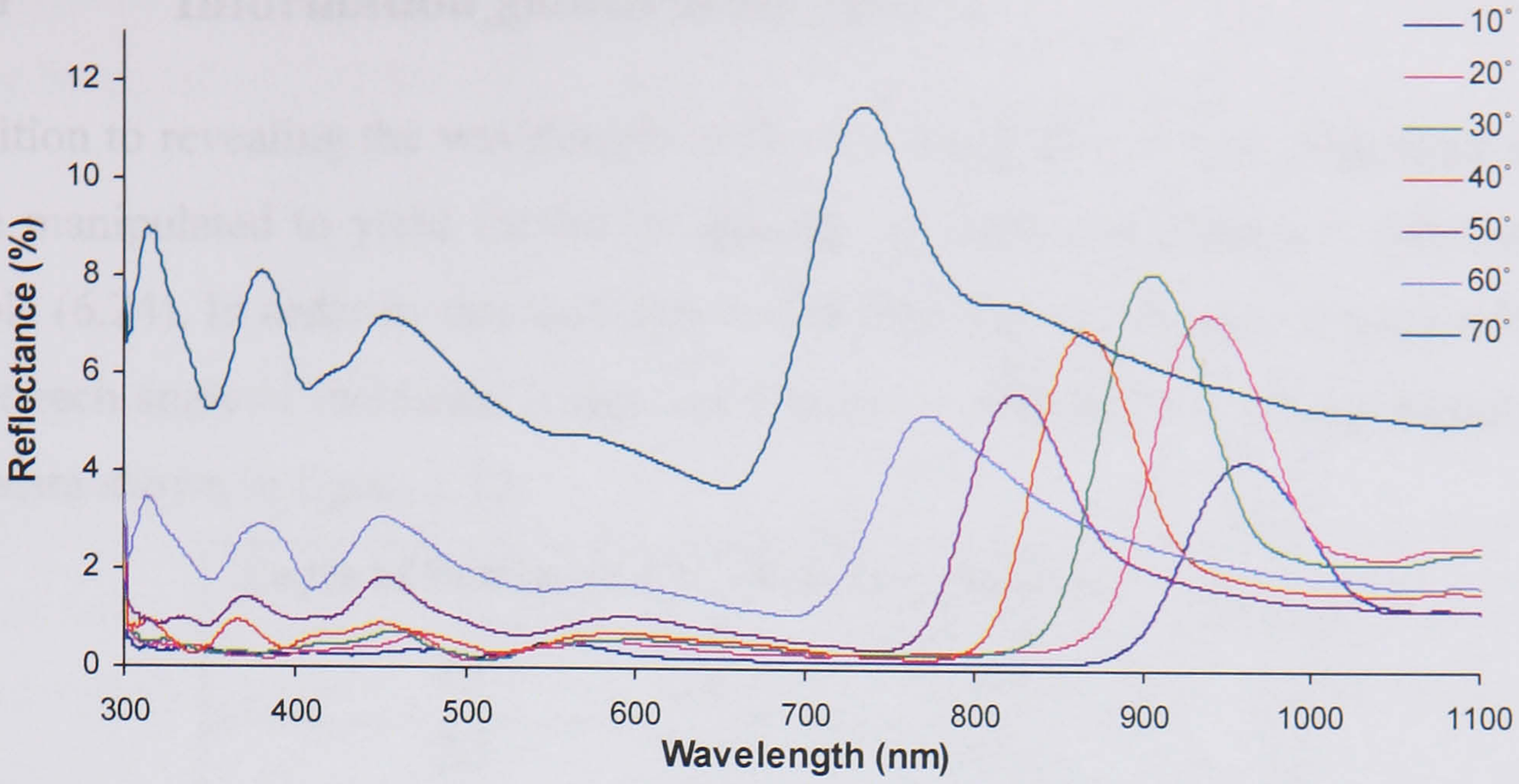


Figure 1.12 Angle resolved reflectance measurements for 408 nm polystyrene spheres. The angles quoted are with reference to the sample normal.

As the angle of incidence increases, the position of the reflectance peak shifts to shorter wavelength, higher energy, confirming that the reflection peaks result from Bragg diffraction (12). The angular dependence of the peak positions demonstrates the lack of a complete PBG in the sample but there is overlap of the reflection peaks as the angle of incidence increases indicating a strong interaction between the incident radiation and the sample (12).

The intense reflection peaks are a result of constructive interference of the reflected waves of consecutive (111) planes. An increase in incidence angle corresponds to moving away from the <111> direction and, as shown in figure 1.12, the reflection peaks shift in position and become less intense (66). The increased intensity of the spectrum obtained at 70° could be attributed to reflection from another set of (111) planes, for example the angle between (111) and (-111) is 70.5° (42). At shorter wavelength (λ~300-500 nm) a series of reflection peaks can be observed which can be attributed to reflections from other planes, *e.g.* (220) (67).

The maximum reflectance is not equal to 100% for many reasons. Firstly the incident beam, when compared to the dimensions of a domain, is large and will therefore illuminate many domains. These domains may be misaligned and will reflect non-specularly (68). Secondly, grain boundaries, point defects and unstructured material will also decrease the reflected intensity (65,69). The width of the reflectance peak depends on the quality and dimensionality of the crystal. As the sample thickness increases the peak width decreases (24). This observed narrowing of the reflectance peak is similar to the Debye-Scherrer effect in small crystallites (62).

1.12.1 Information gained from spectra

In addition to revealing the wavelength of the stop-band of a PC the reflectance spectra can be manipulated to yield the lattice spacing and effective refractive index, see for example (6,24). In order to calculate this information the wavelength of each reflection peak at each angle of incidence is required. Table 1.1 summarises the peak positions for the spectra shown in figure 1.12.

Angle of incidence (°)	Wavelength of peak (nm)
10	961
20	936
30	905
40	865
50	824
60	771
70	734

Table 1.1 Position of reflection peaks for the spectra shown in figure 1.12

Since the main reflection peaks are attributed to reflection from consecutive (111) planes, equation 1.22 becomes

$$\lambda = 2d_{111}\sqrt{n_{eff}^2 - \sin^2\theta} \qquad \textbf{Equation 1.29}$$

Thus a plot of λ^2 versus $\sin^2\theta$ will be a straight line, as shown in figure 1.13 for the data in table 1.1. Further explanation of plotting a best fit straight line using Excel is given in Appendix 1.

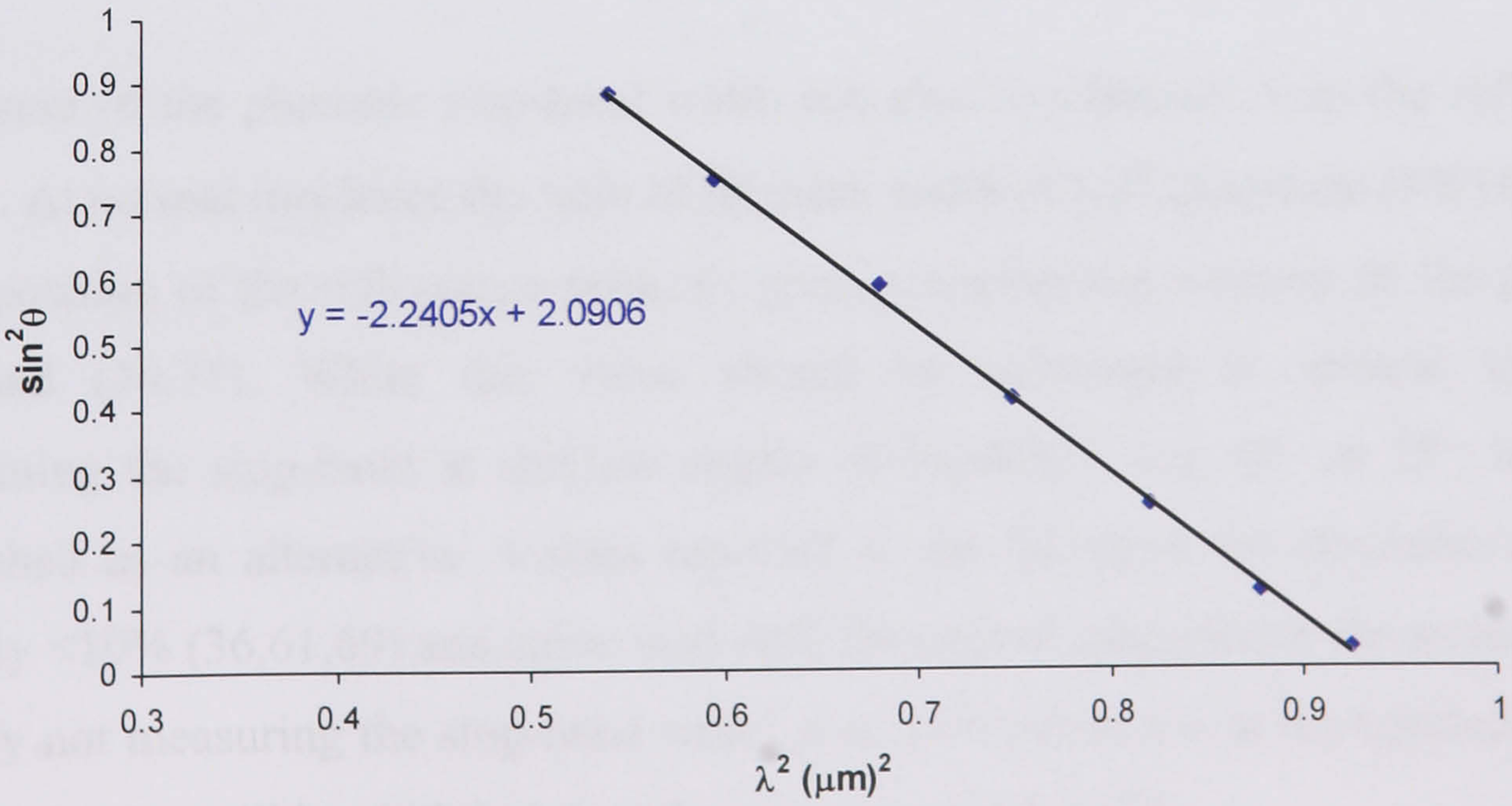


Figure 1.13 Manipulated reflectance spectra can be used to calculate the interplanar spacing and n_{eff}

By manipulation of equation 1.29 the gradient of the line, m, is related to the interplanar spacing by equation 1.30 and the y-intercept related to n_{eff} by equation 1.31.

$$m = \frac{-1}{4d_{111}^2} \qquad \textbf{Equation 1.30}$$

$$y - \text{int} = n_{eff}^2 \qquad \textbf{Equation 1.31}$$

By applying equations 1.30 and 1.31 to the data extracted from figure 1.13, the d_{111} spacing is calculated to be 334 nm and n_{eff} to be 1.45. The interplanar spacing of a cubic unit cell can be expressed in terms of the unit cell parameter, a, and the Miller indices (hkl) by equation 1.32.

$$d_{hkl} = \frac{a}{\sqrt{\left(h^2 + k^2 + l^{2)}\right)}} \qquad \textbf{Equation 1.32}$$

As previously shown in equation 1.24 the lattice parameter a is equal to $\sqrt{2}$ multiplied by the diameter of the spheres, D. Thus, the diameter of the spheres can be calculated from the (111) interplanar spacing by equation 1.33.

$$D = \frac{\sqrt{3}}{\sqrt{2}} d_{111} \qquad \textbf{Equation 1.33}$$

Therefore the magnitude of the d_{111} spacing, and the photonic stop-band, can be tailored by simply altering the diameter of the spheres used in the formation of the synthetic opal sample. It can be calculated that for stop-bands in the visible wavelength region (400-750 nm) the diameters of the polystyrene spheres should be in the range 200-400 nm.

A measure of the photonic stop-band width can also be obtained from the reflectance spectra. At normal incidence the ratio of the peak width at half maximum (FWHM), ΔE, to the position of the reflectance peak, E, gives a normalised measure of the photonic stop-band (70,71). While this value should be calculated at normal incidence determining the stop-band at shallow angles of incidence, *e.g.* 10° or 15°, has been established as an alternative. Values reported in the literature for synthetic opal are typically <10% (36,61,69) and agree well with theoretical calculations for an fcc crystal (72). By not measuring the stop-band width at normal incidence, it is expected that the calculated value will be slightly larger than the actual value (73).

1.13 Structure of thesis

The self-assembly of sub-micron polystyrene spheres is one route used in the formation of 3-D PCs. In order to characterise the PCs synthesised during this project a variety of complementary techniques were used. The techniques and instrumentation used are introduced in chapter 2.

Chapter 3 describes the polymerisation technique used to form the polystyrene colloids required for the growth of synthetic opal thin films. Since the diameter of the polystyrene spheres determines the position of the PC stop-band it is important to be able to accurately measure the size of the spheres. The results presented in chapter 4 compare three different techniques used to measure the diameter of the synthesised colloids.

The results associated with the formation and characterisation of thin film PCs are reported and discussed in chapter 5. Since it is clear from the literature that the thin film growth procedure is not well understood chapter 6 presents work that was carried out in order to find the optimum conditions for film growth and also a hypothesised model for film growth is introduced and discussed.

In chapter 7 the formation of inverse opal, or three-dimensionally ordered macroporous (3-DOM), films is discussed. The PC thin films are used as a template to form 3-D ordered macroporous lead zirconate titanate (PZT) films. Chapter 8 presents the initial results of electrically testing the 3-DOM PZT films in the hope of forming a truly multifunctional PC.

Although each chapter contains discussion of the presented results and conclusions, chapter 9 contains the overall conclusions of the project and possibilities for further work.

2 Instrumentation

2.1 Optical Microscopy

The concept of the modern optical microscope dates from around 1590 but the development in optical microscopy was slow until the wavelike character of light was properly understood by the 1800's (74).

An optical microscope is capable of magnifications up to the order of 1000x without the use of an oil-immersion objective (74). The magnification in an optical microscope is a product of the magnifications of the objective and eye-piece lenses (74). Generally, the eye-piece remains fixed and the objective lens is changed to control the magnification. A schematic illustration of a conventional optical microscope and its lenses is shown in figure 2.1.

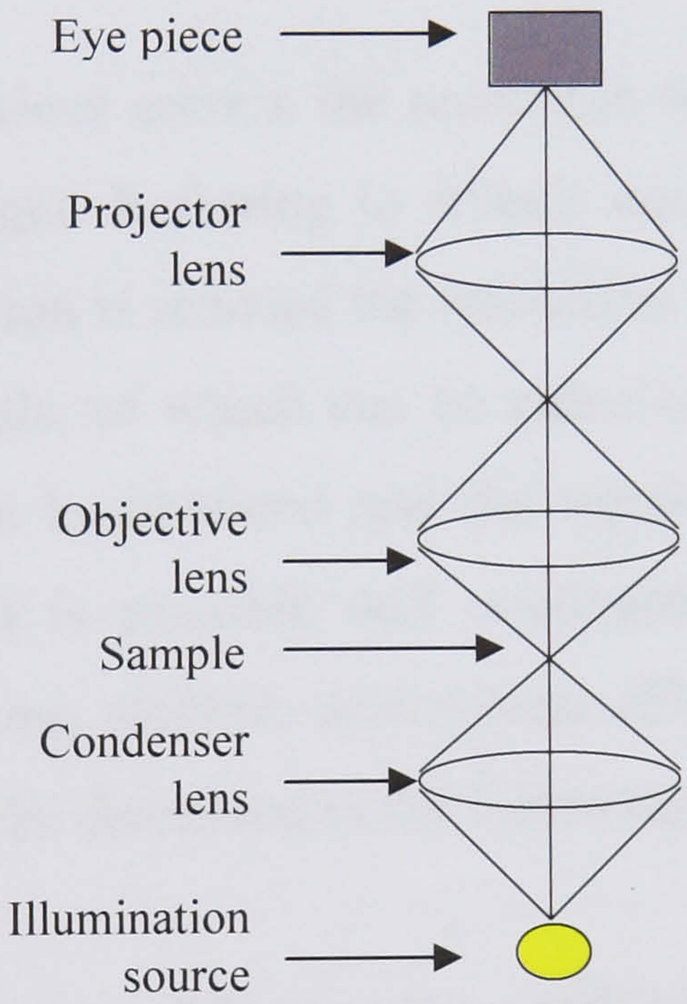


Figure 2.1 Schematic diagram of lens system and optical path in an optical microscope

The resolution of the optical microscope, or the smallest distance that can be resolved, is governed by Abbe's relationship (equation 2.1),

$$\delta = \frac{0.61\lambda}{n\sin\alpha} \qquad \textbf{Equation 2.1}$$

, where δ is the minimum resolvable distance, λ is the wavelength of radiation, n is the refractive index of the viewing medium and α is the half-angle subtended by the objective at the object (75). Since α can never exceed 90°, for an objective in air (n=1) a

distance smaller than 0.61λ cannot be resolved. If the wavelength of white light is taken as 550 nm it can be calculated that a resolution better than 0.3 μm cannot be achieved. This resolution has been attainable since the 19th century and cannot be improved on using modern, conventional optics (74). Nevertheless, the resolution of the optical microscope is much better than the resolution that can be obtained using the un-aided eye. The smallest distance the human eye can resolve is 0.1-0.2 mm at a distance of 25 cm (76).

The optical microscope was routinely used to acquire low magnification, well resolved images of the photonic crystal thin films. Although the optical microscope cannot resolve individual spheres, optical images can give information on the length and width of domains.

2.2 Electron Microscopy

As discussed in the previous section the resolution of the optical microscope is limited by the wavelength of light. Referring to Abbe's equation 2.1 it is apparent that if the wavelength of the radiation is reduced the resolution could be improved. Thus, by using electrons, the wavelengths of which can be calculated by the de Broglie relationship, shorter wavelengths can be obtained and the resolution improved (74). Theoretically atomic scale resolution is possible and obtainable using state of the art electron microscopy. The scanning electron microscope (SEM) and the transmission electron microscope (TEM) will be described in the following sections.

2.2.1 Scanning Electron Microscopy (SEM)

The SEM was used to characterise the thin films giving detailed information on periodicity, long range order, domain shape and film thickness. SEM imaging was carried out using either a JEOL JSM-5610LV or a LEO 1525 FEG. The images formed are easily interpreted and show close packing of the films, as shown in figure 2.2. The SEM allows large areas of the specimens to be analysed and requires minimum sample preparation.

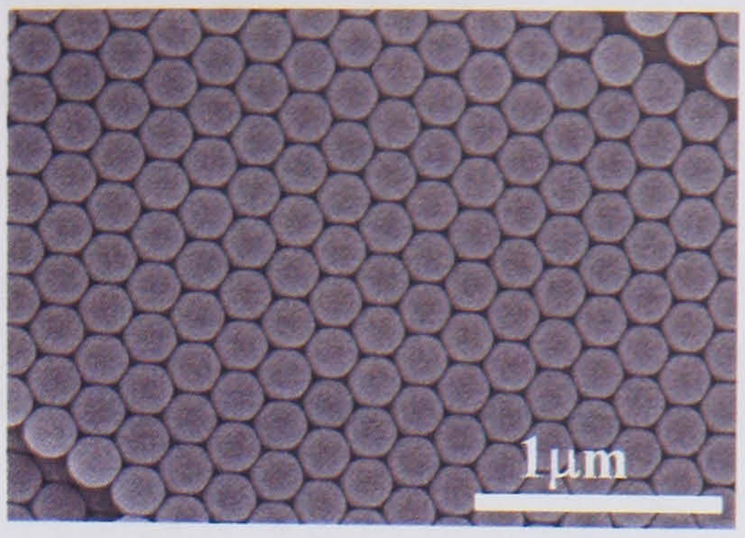


Figure 2.2 **A typical SEM image of the surface of a self-assembled thin film showing close packing of the polymer spheres**

In the SEM electrons are focussed into a small probe which is scanned across the sample surface. As the beam interacts with the sample, a number of signals are emitted from the point of contact of the beam (figure 2.3) (75).

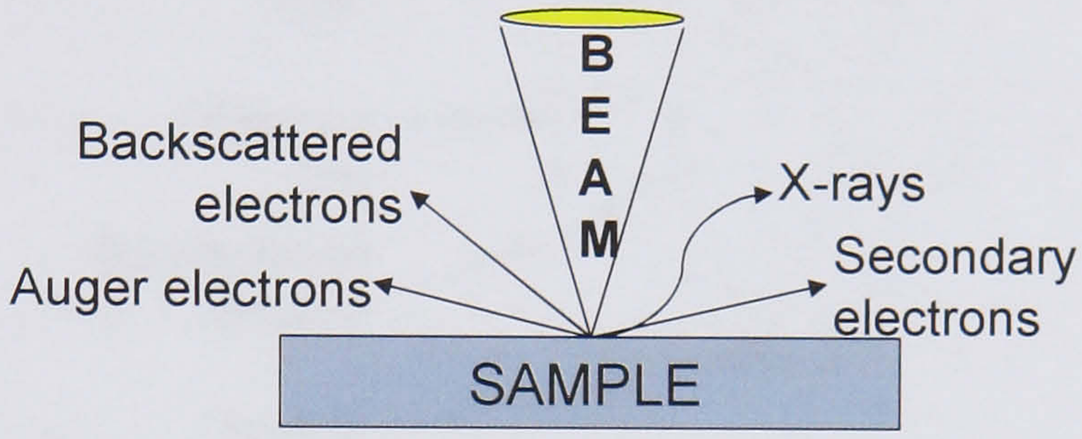


Figure 2.3 **Illustration of the main electron/specimen interactions and signals emitted in the SEM**

Generally for the purpose of imaging secondary electrons are collected. When the electron beam contacts the sample inelastic collisions can occur between the energetic beam electrons and the weakly bound conduction electrons of the sample. The sample absorbs these high energy electrons and acquires a net negative charge. To resume ground potential the sample releases secondary electrons, which are of lower energy (≤50 eV) than the primary electron beam (77). The probability of the secondary electrons escaping from the sample is outlined in equation 2.2,

$$p \propto \exp\left(\frac{-z}{\lambda}\right) \qquad \textbf{Equation 2.2}$$

, where p is the probability of escape, z is the depth below the surface where generation takes place and λ is the mean free path of the secondary electrons (78). To escape the sample, and therefore be detected as a signal, the secondary electrons must overcome the work function of the sample material and, from equation 2.2, the probability of escape decreases as the beam electron moves deeper into the sample. Thus secondary

electrons are emitted from shallow depths within the sample, typically around 5λ where λ can be up to 10 nm for insulators (78).

Figure 2.4 shows a schematic illustration of the basic components of the SEM and the role of some of the key elements will be discussed in the following sections.

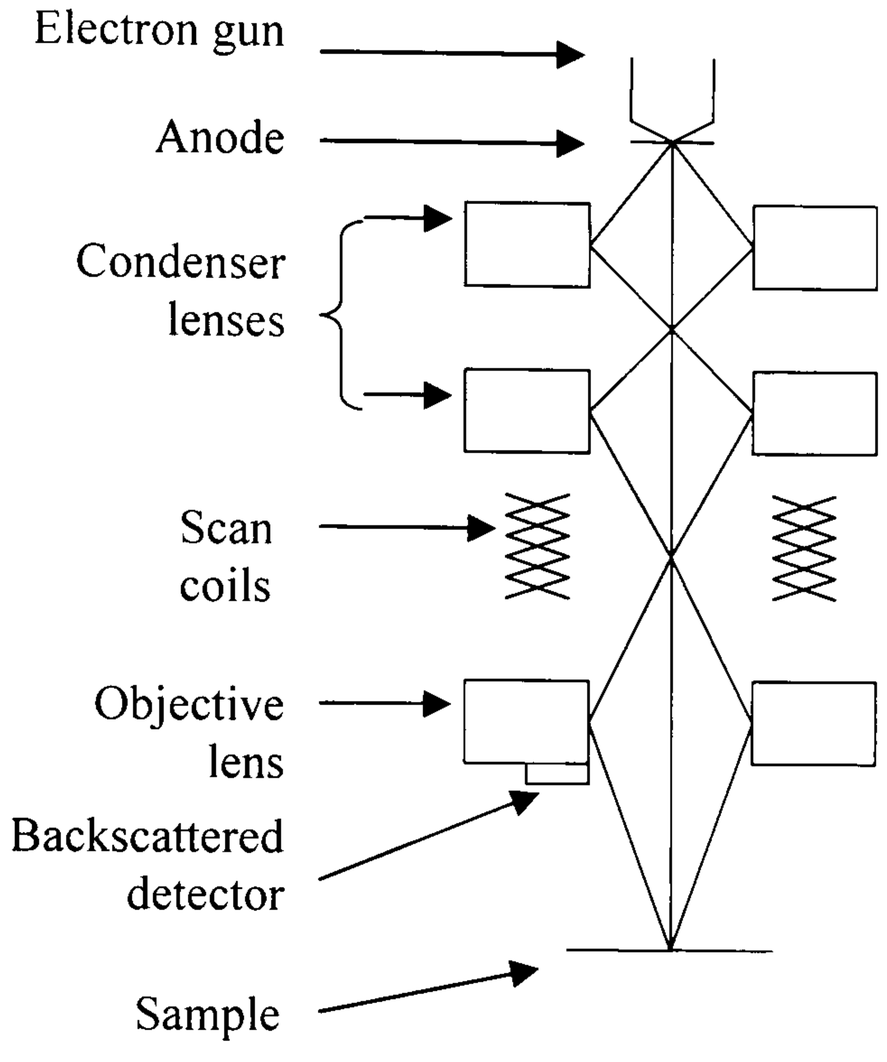


Figure 2.4 Schematic illustration of the electron column of a typical SEM

2.2.1.1 Electron Gun

The electron gun is the source of electrons in an electron microscope. A typical gun is composed of an electron source (usually a filament), an aperture shield at a slightly positive potential and an anode at very high positive potential (77). The filament is surrounded by a shield, commonly referred to as a Wehnelt cylinder, which is slightly biased and collimates the electrons from the filament and directs them towards the anode (77). The electrons which pass through the shield aperture are accelerated towards the anode by the large potential difference between the cathode and the anode. This potential difference is known as the accelerating voltage and in modern SEMs is typically in the range 1-30 kV (78).

The brightness of the electron gun sets the limit of the performance of the SEM (75) and the size of the probe determines the resolution (78). Hence, it is desirable to form the narrowest beam possible with the highest current density.

The current density depends on the type of electron source used and how the electrons are produced. In the course of this study two different types of electron sources were used – thermionic emission and field emission.

2.2.1.1.1 Thermionic Emission

Thermionic emission occurs when a material is held at a sufficiently high temperature that a certain percentage of the electrons can overcome the work function of the material and escape the source (78). The most common filament used is the tungsten hairpin filament. During normal operation the filament is heated to ~2700 K, which is high enough for some electrons to have sufficient thermal energy to overcome the work function of tungsten (4.5 eV), and be drawn from the tip (78). Tungsten filaments are most commonly used since they are relatively inexpensive, their properties are well understood, they can operate under relatively high vacuum (~0.001 Pa) and long lifetimes can be achieved.

An alternative thermionic source is lanthanum hexaboride (LaB_6) which offers superior brightness and lifetime to the tungsten filament. LaB_6 has a lower work function than tungsten and can therefore operate at lower temperatures. However, LaB_6 is chemically reactive and requires a good vacuum, typically <100 μPa *i.e.* an order of magnitude higher than the tungsten filament.

2.2.1.1.2 Field Emission

There is another method of generating electrons without the input of heat known as field emission. In this method the cathode is held at very high negative potential relative to the anode and, since the tip of the filament is extremely sharp (~100 nm compared to ~100 μm for tungsten and LaB_6 (78)), a large electric field is generated. Due to the large electric field the potential barrier of the cathode material becomes narrow and electrons can 'tunnel' directly through the barrier and leave the cathode without requiring thermal energy (78).

The cathode is typically made from tungsten but, unlike the hairpin filament, an orientated single crystal of tungsten is used since the work function depends on crystal orientation (78). The work function also depends on the cleanliness of the tungsten surface and hence it is critical to have a good vacuum (~10 nPa) (78). Under these

conditions brightness hundreds of times greater than a thermionic source at the same accelerating voltage can be achieved.

2.2.1.2 Electron Lenses

In the 1920's it was realised that an electrostatic or magnetic field could be used to focus electrons. The electromagnetic lens is now virtually universal in all electron microscopes. A magnetic lens consists of a central bore, through which the electrons travel, surrounded by a 'pole-piece' (74). The pole-piece is a cylindrically symmetric core of a soft magnetic material, typically iron, with a hole drilled through it. The pole-piece is held within a casing that includes many turns of current carrying wire. The lens operates by varying the current applied to the coils, which alters the strength of the magnetic field which in turn varies the interaction with the electron beam.

The schematic of the SEM (figure 2.4) shows that there are two principal lens systems in the SEM – the condenser and the objective lens system. The condenser lens system condenses the electron beam, narrowing the diameter of the electron beam so it becomes an effective imaging probe, and causes it to pass through a focal point. The condenser lens system also determines the current of the beam which interacts with the specimen. The objective lens brings the electron beam to focus on the sample surface and determines the final spot size of the beam, which ultimately determines the resolution.

2.2.1.3 Specimen Platform

The specimen is mounted on a platform that can be moved in the x, y and z directions and can also be tilted and rotated. Typically the specimen can be titled by around 70° which enables the imaging of the internal planes of cleaved opal samples. By tilting cleaved samples the internal ordering of the films can be assessed and the thickness of the films can be determined, see chapter 5 for further explanation.

2.2.1.4 Electron Detectors

When the electron beam contacts the sample surface each of the signals produced can be collected and amplified as long as the correct detector is used. The conventional secondary electron detector is based on the Everhart and Thonley model (78). In this detector, secondary electrons are attracted to a Faraday cage, held at ~300 V (78). The

Faraday cage has a mesh to permit the entrance of electrons and once the electrons enter they are accelerated at ~10 keV towards a scintillator (79). The energetic electrons strike the scintillator, producing photons which are converted to an electrical signal before amplification (78).

2.2.1.5 Imaging

There are several considerations to take into account for optimal imaging in the SEM. The scan speed, or the rate the beam passes over the specimen, can be varied. Slower scan rates improve the clarity of the image since electrons have sufficient time to interact with the specimen, thus releasing more signals.

Imaging in the SEM requires the electron beam to be focussed at a point on the specimen surface and below this point the beam will broaden due to the angular divergence of the focussed beam above and below the point of optimum focus (78). When the lens conditions focus the beam it is still possible to observe areas that lie outwith the focal plane but still remain in focus. The range over which these areas remain in focus is known as the depth of field. The depth of field can be increased by making two changes to the operating conditions of the SEM. Firstly the working distance, the distance between the second condenser lens and the highest point on the specimen, can be increased. Effectively this is the same as reducing the final aperture angle and consequently the current at the specimen is reduced (80). The second way in which the depth of field can be increased is to reduce the diameter of the final lens aperture. Again this reduces the angular divergence of the beam yielding a smaller beam current at the specimen surface.

A suitable working distance also needs to be selected before imaging in the SEM. The working distance is changed by moving the sample upwards or downwards. In addition to decreasing the depth of field a short working distance raises the lower limit of magnification. However, a compromise has to be made in selecting the optimum working distance since at very short or long distances the clarity of the image is affected.

Finally the accelerating voltage needs to be selected. When the electron beam interacts with the specimen surface the distance it penetrates is dependent on the beam energy

and inversely proportional to the atomic number (75). As the accelerating voltage is increased the penetration into the sample is increased because the beam electrons have greater energy. Thus additional signals are created which limits the detail of the surface that can be imaged. Hence, an optimum accelerating voltage needs to be chosen. In this project an accelerating voltage of 5-10 kV was chosen.

2.2.2 Transmission Electron Microscopy (TEM)

The TEM is used to analyse materials which are thin enough to transmit electrons, with the transmitted electrons used to either form an image of the specimen or a diffraction pattern (76). A JEOL 2000FX TEM was used during the course of this study to measure the diameter of the colloidal spheres synthesised, further information on the sizing protocol is given in chapter 3. Figure 2.5 illustrates the main components of a typical TEM and a ray diagram for the instrument.

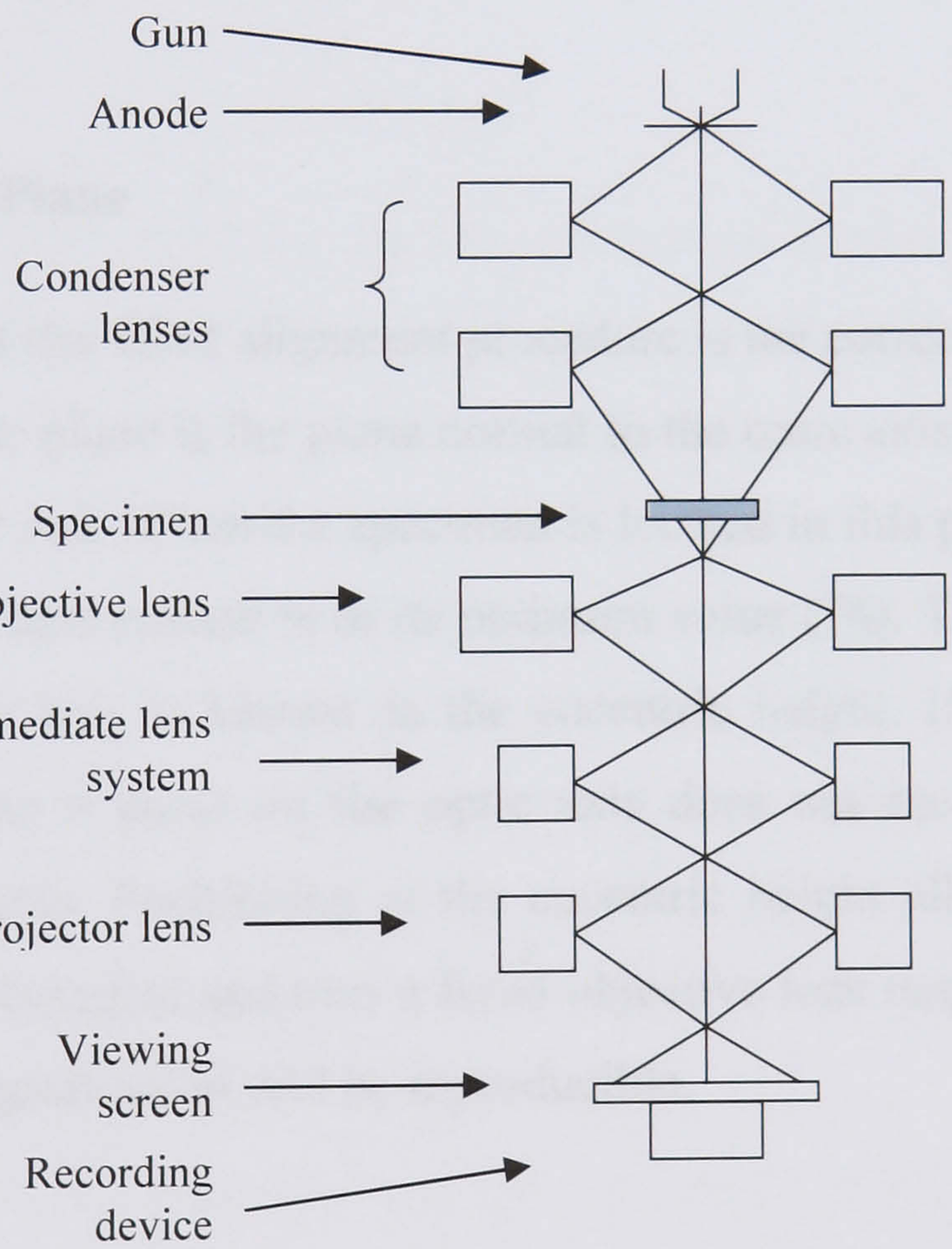


Figure 2.5 Schematic illustration of the TEM column and the major components of the instrument

2.2.2.1 Electron Source

The electron source was a tungsten hairpin filament and the electrons are produced by thermionic emission, as explained in section 2.2.1.1.1. The accelerating voltage used was 200 kV.

2.2.2.2 Electron Lenses

The condenser lenses are used to illuminate the sample with a parallel beam of electrons a few microns in diameter. The first condenser lens, often labelled spot size, forms a demagnified image of the gun crossover. The second condenser lens controls the convergence angle of the beam leaving the condenser system which ultimately controls the diameter of the focussed beam on the sample.

The objective lens is the most important lens in the TEM column since it forms both images and diffraction patterns. The objective lens images the electrons scattered when the electron beam interacts with the sample.

Magnification occurs after the beam has interacted with the specimen, the objective lens forming the first image which is then further magnified by the intermediate and projector lenses.

2.2.2.3 Eucentric Plane

An important part of the TEM alignment procedure is the correct setting of the eucentric height. The eucentric plane is the plane normal to the optic axis and contains the axis of the specimen holder rod. When the specimen is located in this plane and the image is in focus, the objective lens current is at its optimum value (76). The position of this plane within the objective lens is known as the eucentric height. If the specimen is at the eucentric height then a point on the optic axis does not move laterally when tilted around the holder axis. Positioning at the eucentric height allows the same objective lens current to be worked at and thus a fixed objective lens magnification. This ensures that the selected magnification will be reproducible.

2.2.2.4 Resolution

Referring to equation 2.1 the maximum theoretical resolution of the TEM can be calculated. If it is assumed that $n\sin\alpha$ is set to unity and the TEM is operating at 200 kV ($\lambda = 2.73 \times 10^{-12}$ m) then the maximum attainable resolution is of the order of 1.7×10^{-12} m. It would therefore seem feasible that the TEM would be able to resolve detail at the sub-atomic level. However, due to lens aberrations, this is not possible in standard instruments. There are three main types of aberrations which limit the achievable

resolution in the TEM. State of the art TEMs can achieve atomic scale resolution via the correction of these lens aberrations.

The first lens aberration is spherical aberration. Spherical aberration arises due to the magnetic field at the periphery of the lens being much stronger than in the centre (77). Thus, electrons travelling within the centre of the lens are not as influenced by the magnetic field as those travelling at the perimeter of the beam. Although apertures can intercept these electrons and eliminate spherical aberration, theoretical resolution is reduced by their presence (77).

The second aberration is chromatic aberration. The assumption is that the electrons which make up the electron beam are monochromatic but there is a slight variation in energy, typically smaller than one part in a million (77). Images become blurred because the lens brings radiation of different wavelength (energy) to focus at different points.

The final reason for the TEM not reaching theoretical resolution is astigmatism which arises from a non-uniform magnetic field within the lenses, although this is corrected for in most microscopes. This lack of uniformity arises because the pole-pieces cannot be manufactured perfectly cylindrical and the iron core may have inhomogenieties. Both of these factors lead to variations in the magnetic field strength (76). Astigmatism is corrected by stigmators which are small octopoles that induce a compensating magnetic field and are found in both the condenser and objective lenses.

2.3 Optical Spectroscopy

In order to measure the photonic stop-band position, as described in chapter 1, the sample needs to be illuminated with light. When the Bragg condition is satisfied, the incident radiation is unable to propagate through the sample and this radiation can be detected as either a peak in the reflectance spectrum or a dip in the transmission spectrum.

2.3.1 Instrumentation

The optical characterisation of all thin films produced throughout the course of this study was carried out using a specifically assembled optical bench, a Bentham 2000 Series Spectrophotometer, controlled by BenWin+ software. A schematic of this optical set-up is illustrated in figure 2.6.

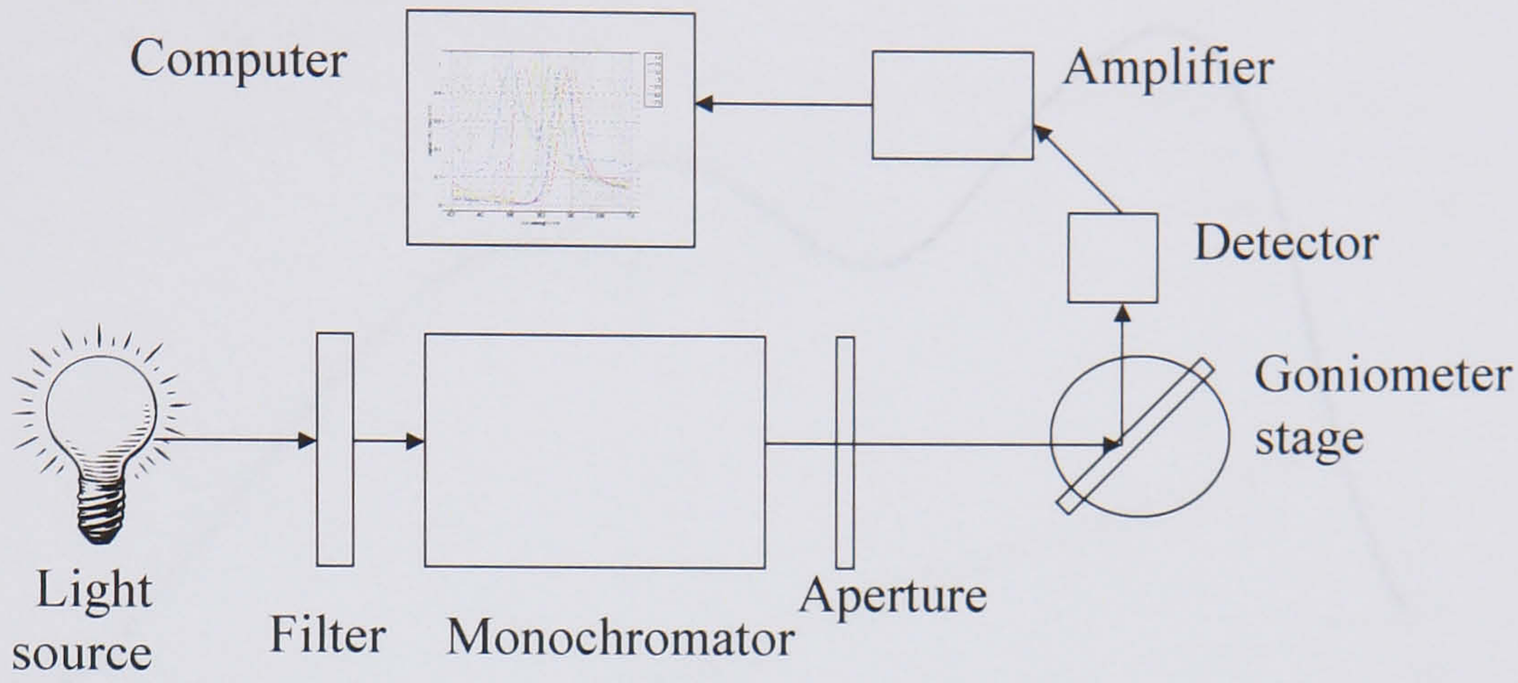


Figure 2.6 **Schematic illustration of the optical bench set-up**

The white light source is a 100 W quartz halogen lamp which is passed through a filter. The filter removes the second harmonic of the light generated due to the broad spectral emission of the lamp. The filtered light is then passed through a triple grating monochromator (TM300V) which allows wavelengths in the range 300-1100 nm to be selected. The wavelengths are selected according to the first order grating equation, shown in equation 2.3,

$$\lambda = 2d \sin\theta \cos\beta \qquad \textbf{Equation 2.3}$$

, where λ is the wavelength, d is the groove spacing of the diffraction grating, θ is the grating angle in degrees and β is a fixed angle (for the TM300V β=13°) (81). The monochromated beam is then passed through an aperture which controls the diameter of the incident beam which can be varied from 0.7 mm to over 1 cm.

The sample is mounted on a goniometer stage which allows the angle of the incident radiation to be varied from 0-75°. The goniometer is placed on a 12.5x12.5 mm x-y stage allowing the sample to be moved with millimetre precision. A silicon semiconductor detector (DH-Si) with an angular range of 0-180° is used which can detect radiation with wavelengths in the region 200-1100 nm. The signal from the detector is amplified and converted by the BenWin+ software to a graphical trace, as illustrated in figure 2.6. The optical system offers a spectral resolution of 1 nm and an angular resolution of 1°.

The optical set-up offers the benefit that both reflectance and transmission measurements can be made. However, due to the experimental set-up specular reflectance measurements at an incident angle of 0° cannot be collected since the detector blocks the incident beam. The detector response is non-linear across the wavelength region and therefore a background/reference reading is taken, shown in figure 2.7, which is subsequently removed from any obtained spectra.

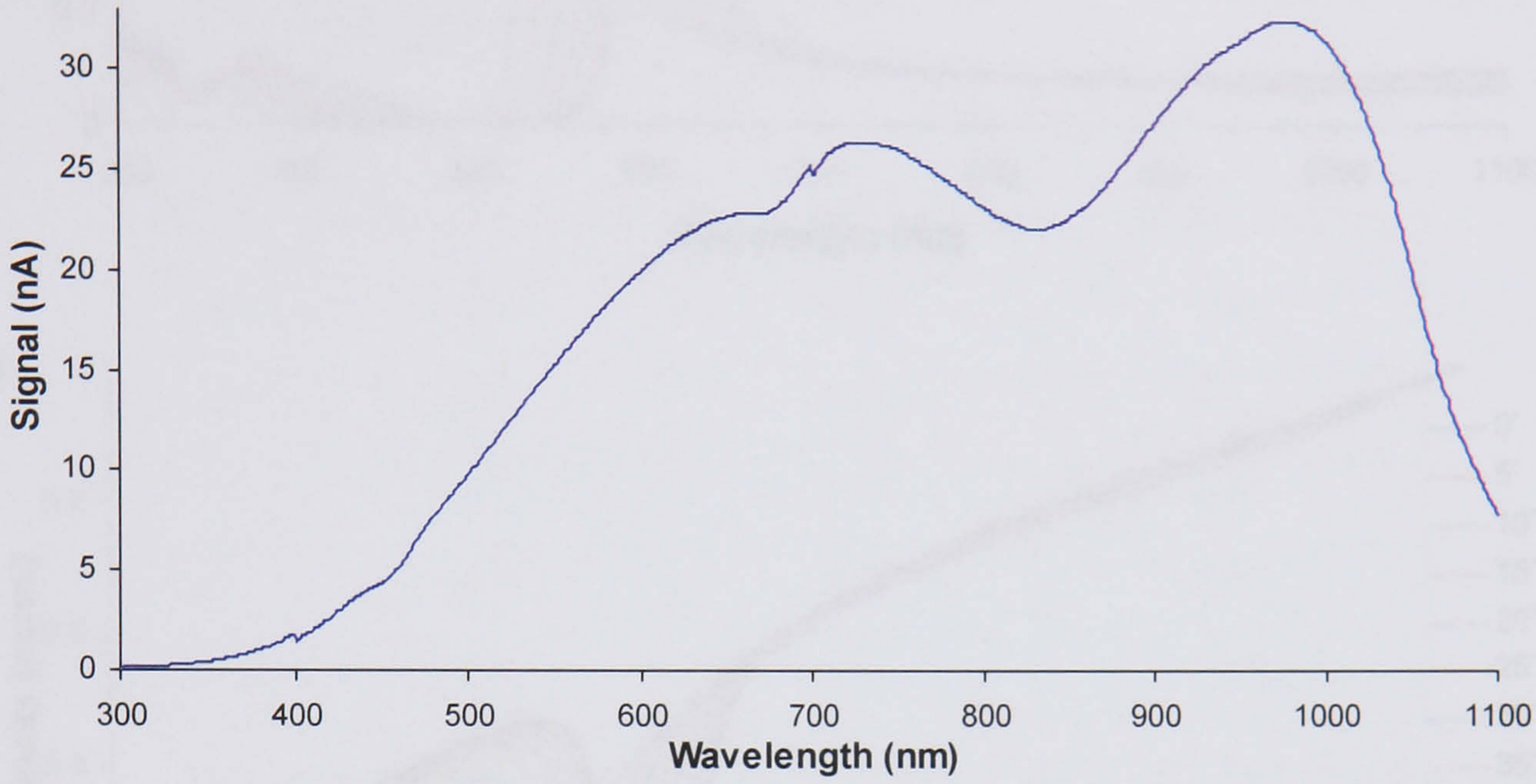


Figure 2.7 Typical background/reference spectrum

The signals recorded during a measurement are in nanoAmps (nA), as shown in figure 2.7, but calibrating against the background/reference spectrum allows the input signal to be converted to percentage reflection or transmission. The software can be set up to measure the radiant intensity as a function of wavelength and angle so that angle resolved measurements can be undertaken. A typical series of reflection and transmission spectra for a film composed of 250 nm spheres is shown in figure 2.8.

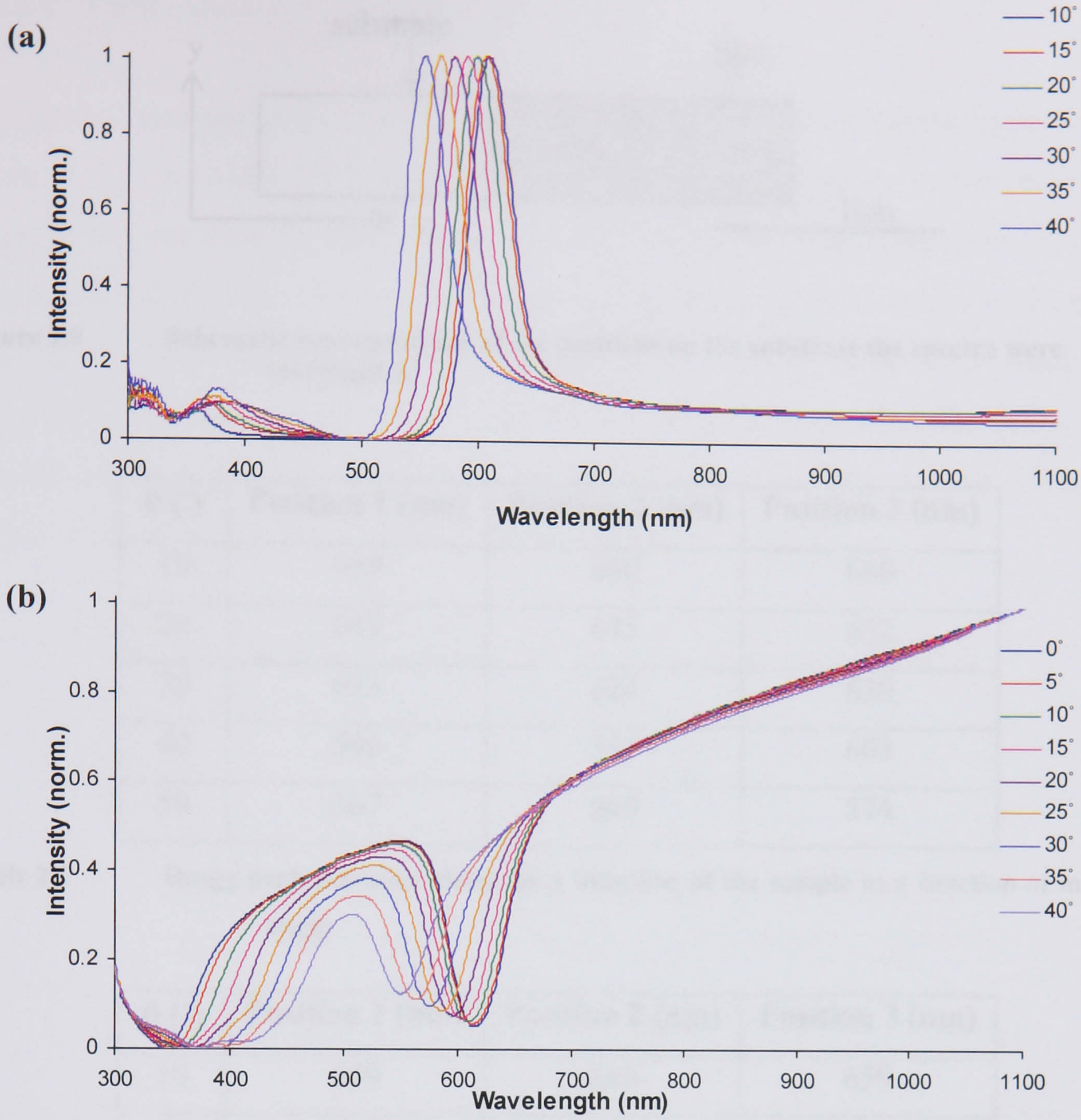


Figure 2.8 **(a) Reflection and (b) transmission spectra for a thin film composed of 250 nm spheres. The angles quoted are relative to the sample normal**

2.3.2 Experiments

Since the optical bench set-up was purchased at the start of this project a series of experiments were conducted to ensure that the optical data obtained was comparable to data previously collected (64).

2.3.2.1 Position of the incident beam

The first series of experiments were conducted to investigate the position of the incident beam on the sample surface. As such, the variation in the position of the Bragg peak was investigated at three different positions along a thin film in both the x and y directions, shown schematically in figure 2.9. Tables 2.1 and 2.2 summarise the positions of the reflectance peaks at the different positions along the film surface.

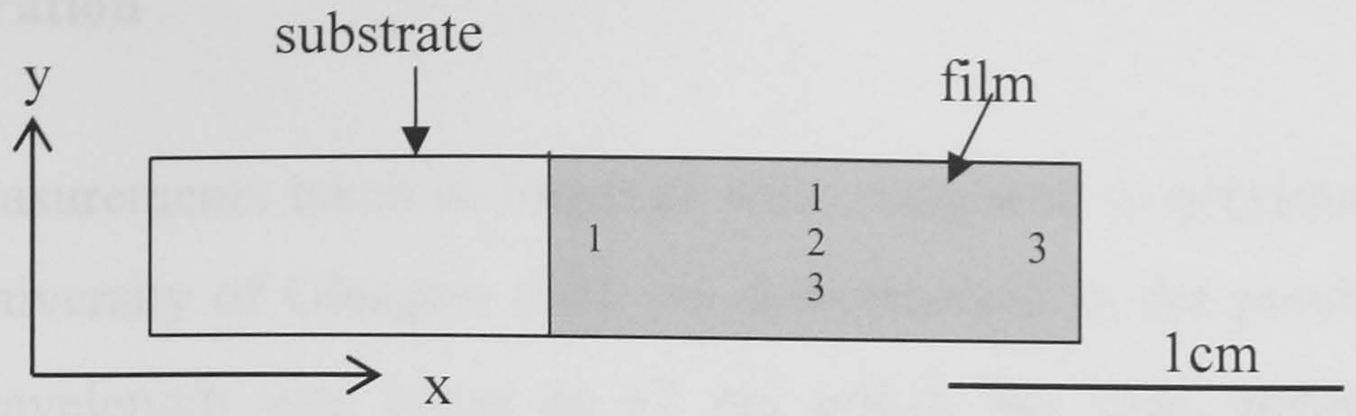


Figure 2.9 **Schematic representation of the positions on the substrate the spectra were investigated**

θ (°)	Position 1 (nm)	Position 2 (nm)	Position 3 (nm)
10	659	660	666
20	645	645	652
30	623	624	630
40	596	597	603
50	567	569	574

Table 2.1 **Bragg peak positions along the x direction of the sample as a function of incident angle**

θ (°)	Position 1 (nm)	Position 2 (nm)	Position 3 (nm)
10	659	660	659
20	644	645	644
30	623	624	623
40	597	598	597
50	567	569	568

Table 2.2 **Bragg peak positions along the y direction of the sample as a function of incident angle**

The data presented in tables 2.1 and 2.2 shows that the maximum difference between the positions of the reflection peaks is 7 nm in the x direction and 2 nm in the y direction. The difference in the peak position along the two directions could be due to the shorter distance travelled along the y direction compared to the x direction, see figure 2.9. It had previously been hypothesised that cracking in the <110> directions may cause a change in the Bragg peak but since the change in the peak position is small it can be concluded that the change is due to another factor. It is thought that surface roughness could cause this magnitude of peak position change.

2.3.2.2 Calibration

The optical measurements taken at Imperial were compared to previous measurements taken at the University of Glasgow (64). As demonstrated in the previous section, the error in the wavelength was taken as ±7 nm which has been attributed to surface roughness and therefore means that the sample can be investigated at any position. The error in θ (y-coordinates) was taken as negligible because any error in this would arise from the goniometer motor drive and would therefore be systematic. The analysis was carried out for a thin film composed of 230 nm spheres and the error of ±7 nm was added to the reflection peak position, as demonstrated in table2.3.

θ(°)	Reflection peak (nm)	+ error (nm)	- error (nm)
15	565	572	558
30	539	546	532
45	505	512	498
60	477	484	470
75	444	451	437

Table 2.3 Bragg peak positions and errors at different angles of incidence

As shown in chapter 1, a plot of the stop-band position against the incidence angle produces a straight line, the gradient of which can be used to calculate the sphere diameter. This standard line was plotted for the peak positions shown in table 2.3 and the following lines were also plotted:

Fit 1 – error + through error –

Fit 2 – error – through error +.

These three lines are shown in figure 2.10.

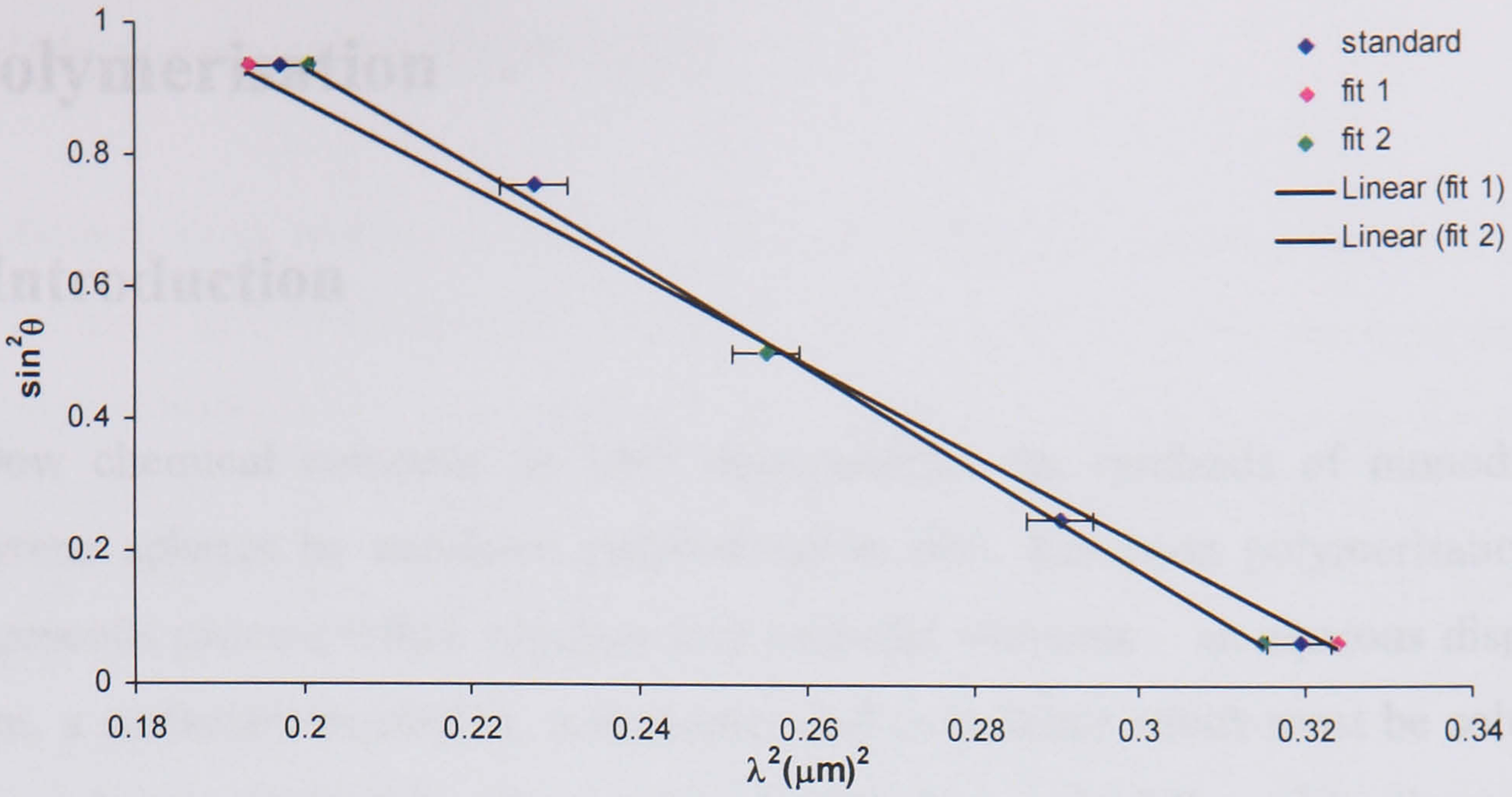


Figure 2.10 Plot of λ^2 versus $\sin^2\theta$ for the standard and fitted lines

Following the manipulations outlined in section 1.12.1, the three lines gave the following results for sphere diameter:

standard = 227 nm

fit 1 = 243 nm

fit 2 = 216 nm.

It is most probable that the film would have been measured at different positions in Imperial and Glasgow and therefore the ±7 nm error needs to be taken into account. When the results for the three fitted lines are compared to the diameter calculated in Glasgow (240 nm) it can be seen that the results are consistent.

3 Polymerisation

3.1 Introduction

The Dow chemical company in 1947 demonstrated the synthesis of monodisperse polystyrene spheres by emulsion polymerisation (82). Emulsion polymerisation is a heterogeneous process which requires four essential elements – an aqueous dispersion medium, a surfactant/emulsifier, a monomer and an initiator which must be soluble in the dispersion medium (83). The product formed is a colloidally stable dispersion of polymer in water, known as a latex. The diameter range of polymers synthesised by emulsion polymerisation is typically 0.05-1 μm compared to, for example, colloids formed via suspension polymerisation which are approximately 0.1-0.2 mm (84).

For the growth of three-dimensional photonic crystal (3-D PC) films the presence of a surfactant is not desirable. The surfactant may affect the properties of the latex since the surfactant ions can arrange in different ways on the particle surface leading to an apparent increase in the diameter of the polymer spheres or affecting the surface charge (85). Since the removal of the surfactant from the synthesised spheres is difficult Matsumoto and Ochi demonstrated that polystyrene, and other latexes, could be synthesised without the addition of an emulsifier/surfactant (85). This polymerisation technique is known as emulsifier-free, or soap-free, emulsion polymerisation and the latexes synthesised are stabilised by chemically bound surface groups supplied by the initiator.

Whilst work on emulsifier-free emulsion polymerisation was carried out in the 1960s a detailed study of the mechanism of the polymerisation technique was not completed until the 1970s by Goodall and co-workers (85-87). The latexes formed by emulsifier-free emulsion polymerisation can form a wide range of monodisperse (σ<5%) particles in the size range 0.1-1 μm (86).

3.2 Polymerisation Technique

The polymerisation technique used to synthesis submicron polymer spheres is free-radical addition polymerisation. Free-radical polymerisation is one of the most common chain polymerisation techniques in which each polymer molecule grows by the addition of a monomer unit to a terminal free-radical reactive, known as an 'active centre' (84). This polymerisation method is used predominantly for the synthesis of polymers from monomers of the general structure CH_2=CHX. In a similar manner to other methods of chain polymerisation the reaction can be divided into three distinct stages:

1. Initiation
2. Propagation
3. Termination

3.2.1 Initiation

The initiation stage is associated with the creation of a free-radical active centre and usually takes place in two stages. The first stage is the formation of the free-radical from the initiator as shown in figure 3.1 for the free-radical initiator potassium persulfate, and the second stage is the addition of one of these free-radicals to a molecule of monomer.

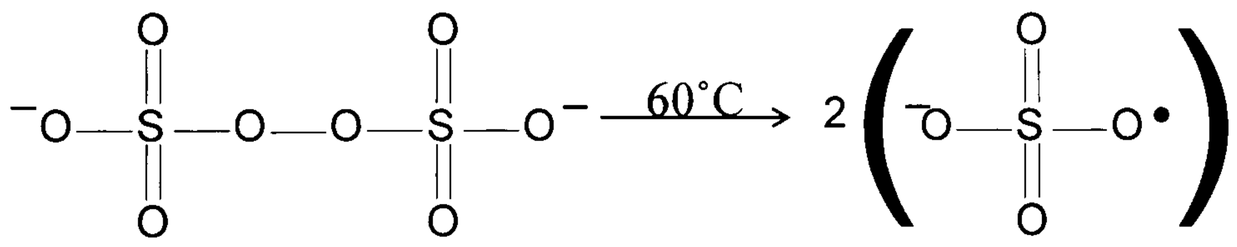


Figure 3.1 Creation of the free-radical from a persulfate initiator

There are two principle ways in which the free-radical can be formed – homolysis of a single bond or single electron transfer from an ion or molecule (*e.g.* redox). Homolysis can be affected by temperature and compounds containing peroxide (O-O) linkages undergo thermolysis in the temperature range 50-100°C (84).

An active centre is then created when a free-radical generated from the initiator (In·) attacks the π-bond of a molecule of monomer, which in the case of styrene has two possible addition modes, as outlined in figure 3.2.

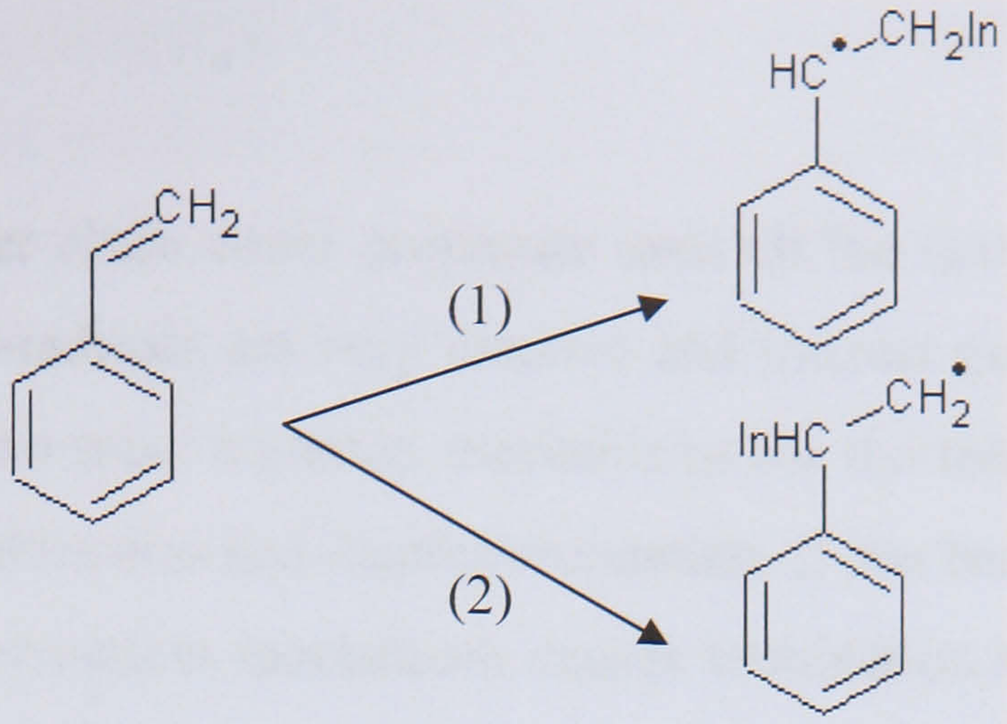


Figure 3.2 Possible modes of addition of a free-radical to a molecule of styrene

The first addition mode, (1), predominates because attack at the methylene carbon is less sterically hindered. In addition there is a greater possibility of resonance stability by the interaction of the aromatic ring and the unpaired electron on the adjacent α-carbon (84).

3.2.2 Propagation

The propagation stage involves the growth of the polymer chain by addition of monomer units to the active centre. As with initiation there are two possible modes of propagation, either head-to-head addition or head-to-tail addition. Experimental evidence supports the dominance of head-to-tail addition for polystyrene (88) and the general mode is outlined in figure 3.3.

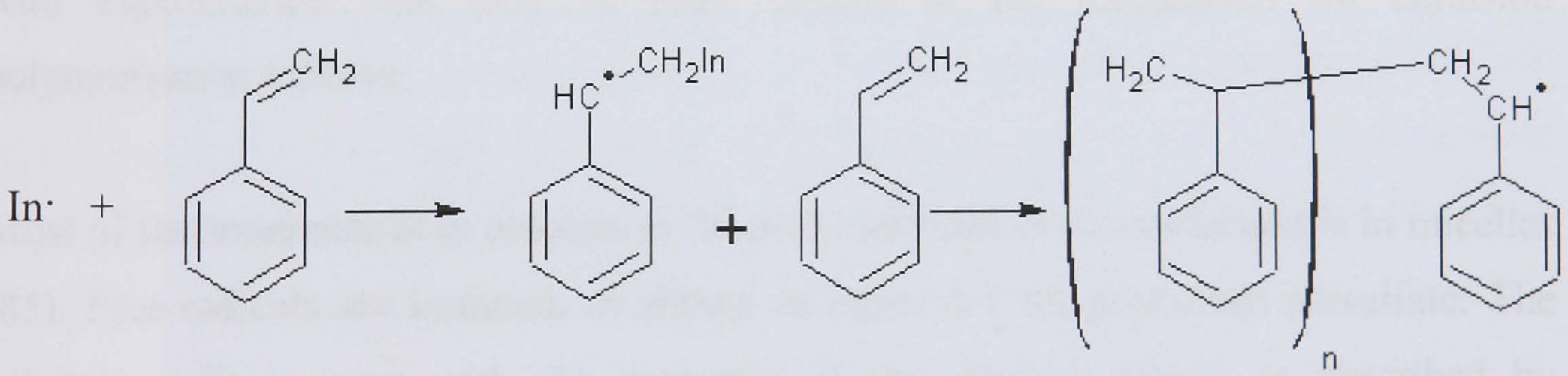


Figure 3.3 Mode of head-to-tail addition of styrene monomer to the growing polystyrene chain

The head-to-tail mode is favoured for polystyrene due to less steric hindrance than head-to-head addition, although head-to-head linkage may occur occasionally (88). The time for addition of one monomer unit is typically of the order of a millisecond (84).

3.2.3 Termination

Theoretically a polymer chain could propagate until all the monomer units have been consumed but the free-radicals are very reactive and interact quickly to form inactive covalent bonds. The two most common mechanisms for the termination of a growing polymer chain are combination and disproportionation. It has been reported for styrene at 330-370 K, the combination mechanism causes termination (88). The combination mechanism is outlined in figure 3.4.

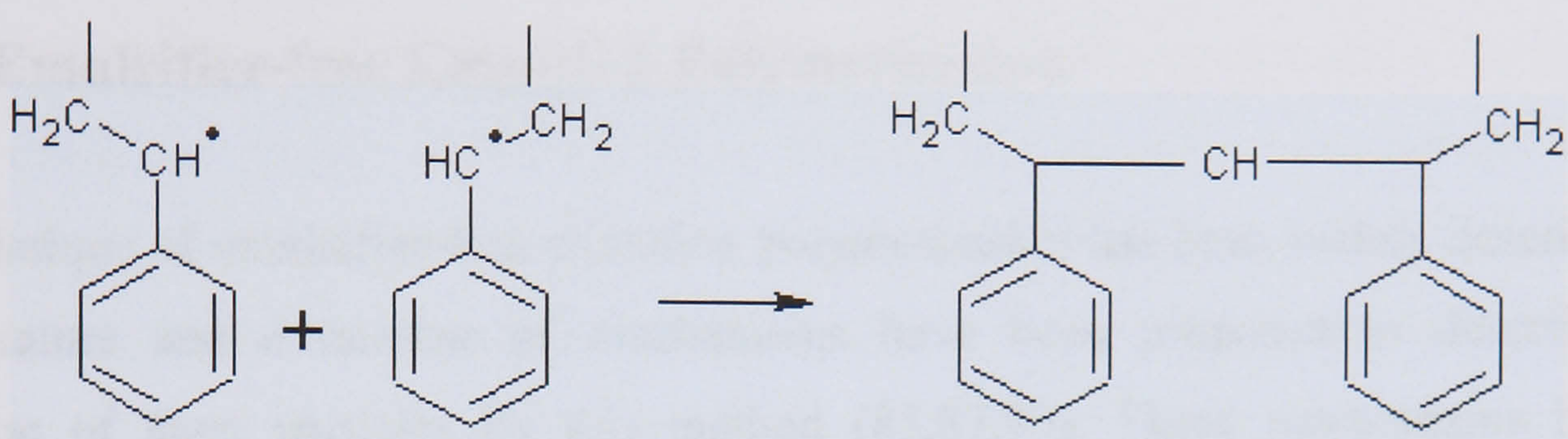


Figure 3.4 **Mode of termination of the growing polystyrene chain by combination**

3.3 Polymerisation Mechanism

3.3.1 Emulsion polymerisation

The mechanism proposed by Harkins (89) for the polymerisation of styrene type monomers by emulsion polymerisation has been accepted and agrees reasonably well with experimental data (90). A basic outline of the mechanism for emulsion polymerisation follows.

Most of the monomer is in droplets (1-10 μm) and most of the surfactant is in micelles (85). Free-radicals are initiated, as shown in figure 3.1 for potassium persulfate. The sulphate radicals react with the monomer in the aqueous phase, as described by equations 3.1-3.

$$SO_4^{-\bullet} + M \rightarrow SO_4^- M^\bullet \qquad \textbf{Equation 3.1}$$

$$SO_4^- M^\bullet + M \rightarrow SO_4^- MM^\bullet \qquad \textbf{Equation 3.2}$$

$$SO_4^- MM^\bullet + M \rightarrow SO_4^- MMM^\bullet \qquad \textbf{Equation 3.3}$$

As the reaction proceeds, the number of monomer units incorporated into the oligomeric ion radical increases until the hydrophobic chain length becomes long enough to give surface active properties (85). An oligomer is a low molecular mass polymer formed from two or more monomer units linked together (47). These surface active free-radical oligomers can enter the swollen micelles, and once within the micelle can continue to grow until another radical enters and causes termination. Thus, the monomer-swollen micelle transforms to a monomer-swollen polymer particle of greater size (85).

3.3.2 Emulsifier-free Emulsion Polymerisation

The technique of emulsifier-free emulsion polymerisation has been widely described in the literature and a number of mechanisms have been proposed to describe the formation of latex particles by this method (85,87,90). These mechanisms include homogeneous nucleation, oligomeric micellisation and coagulation (87). The nucleation mechanism and colloidal stability are key features in understanding the emulsifier-free emulsion polymerisation mechanism.

Goodall *et al* (85) have studied the nucleation mechanism of emulsifier-free emulsion polymerisation in the styrene/potassium persulfate/water system. This study suggested that the formation mechanism was micellar nucleation due to the large number of styrene oligomers (MW *ca* 1000) present in the nucleation period, as observed by gel-permeation chromatography (GPC). The oligomers with ionic chain ends aggregate to form micelles in the aqueous phase and the primary free-radicals generated from the decomposition of the initiator (figure 3.1) diffuse into these micelles to initiate polymerisation (90). Once the stable latex particles are formed particle growth resembles that of emulsion polymerisation since the polymerisation mainly takes place within the latex particles swollen by the monomer, as opposed to continued growth in the aqueous phase.

As the polymerisation proceeds, there is an increase in surface area which results in a decrease in surface charge density and the primary particles undergo coagulation to regain colloidal stability (85). The surface charge density is low since the latex particles are stabilised by ionic fragments of initiator and therefore the solid content is low (90).

3.3.3 Surface Chemistry

In emulsifier-free emulsion polymerisation the groups attached to the surface of the colloidal particles give colloidal stability. By varying the amount and decomposition rate of the initiator, the surface groups on the latex can be controlled (83).

Characterisation of the surface of polymer spheres synthesised by emulsifier-free emulsion polymerisation reveals the presence of sulphate (SO_4^-) and weak acid (COO^-) groups, although not all samples displayed the weak acid groups (85). In addition surface hydroxyl groups have also been identified (85). The SO_4^- groups clearly originate from the free-radical persulfate initiator and it is supposed that the hydroxyl groups arise from the hydrolysis of SO_4^- and from side reactions the persulfate undergoes with water to produce $OH^{\cdot}$ free-radicals. The presence of the weak acid groups is most likely from the oxidation of some of the hydroxyl groups during the polymerisation reaction. Titrations carried out on old (< 2 years) polystyrene samples revealed little or no acid groups, probably due to hydrolysis, yet the samples were still colloidally stable.

3.4 Size control

It has been discussed in chapter 1, that for the formation of good quality 3-D PCs the monodispersity of the spheres is one of the most important factors (24) and there is agreement in the literature, see for example (43,68), that the polydispersity typically needs to be less than 5%. Films grown with spheres with a particle size distribution greater than 5% show dislocations, stacking faults and poor long range order (24).

The important characteristics of a latex are particle size, particle size distribution and surface charge. These characteristics depend on the raw materials and the synthesis technique and conditions. There are many parameters which can be altered to affect the diameter and polydispersity of a polymer latex for example synthesis temperature, monomer concentration, initiator concentration and agitation rate. When considered individually each variable associated with size control can be explained and the individual effect understood.

However, the emulsifier-free emulsion polymerisation reaction has proven to be a complex procedure, complicated by the interaction of the variables associated with controlling the reaction (64). The interaction of many of these factors in addition to the necessity for rigorous control of each has highlighted the complexity of this area of polymer chemistry.

Only the effect of varying the monomer concentration is investigated in the course of this project but for completeness an explanation of each individual parameter is discussed in the subsequent sections.

3.4.1 Synthesis Temperature

When the free-radical initiator potassium persulfate is used the synthesis temperature should be greater than 60°C due to the slow decomposition rate of the initiator below this temperature (64). It has been shown that as the temperature of the polymerisation reaction increases the diameter of the synthesised spheres decreases (83,86). This relationship can be explained simply. As the reaction temperature increases, the rate of free-radical production increases and therefore a large number of nuclei are produced. Goodall *et al* (86) have proposed that the total number of particles present at the end of the reaction may be proportional to the rate of formation of free-radicals. In addition the monomer solubility also increases with increased temperature and thus more monomer can dissolve in the solvent resulting in more particles. The more particles there are, the smaller the particle size.

3.4.2 Monomer concentration

Madaeni and Ghanbarian (83) have shown that as the monomer concentration increases the particle size also increases. A large monomer concentration allows the formation of large size nuclei which result in large diameter spheres. In addition increasing the monomer concentration increases the time during which the viscosity of the latex particles allows coalescence, thus producing larger spheres.

3.4.3 Initiator concentration

It has been reported that increasing the initiator concentration results in a decrease in particle size (83,86). If the initiator concentration is increased the number of free-radicals increases and consequently the polymerisation rate is increased. As discussed previously in section 3.2.1, the free-radical initiator potassium persulfate dissociates into two sulphate radical anions. Wang *et al* (90) have proposed that in emulsifier-free emulsion polymerisation the styrene oligomers aggregate to form micelles and the primary free-radicals diffuse into these micelles to initiate polymerisation. An increase in the number of free-radicals results in a large number of particles which consequently have small diameters.

3.4.4 Agitation

The agitation or stirring rate during the course of polymerisation can have an effect on the diameter of the spheres synthesised and their size distribution. The syntheses described in this study were stirred with a twin-paddled overhead stirrer placed approximately 2 cm from the bottom of the reaction flask. An increase in the stirring rate leads to an increase in the number of polymer nuclei formed resulting in a decrease in the particle diameter. Madaeni and Ghanbarian (83) have also reported that the degree of monodispersity of the synthesised latex increases with agitation speed.

3.5 Styrene Polymerisation

The polystyrene spheres in this study were synthesised by emulsifier-free emulsion polymerisation using the free-radical initiator potassium persulfate ($K_2S_2O_8$, 99% Aldrich) and the monomer styrene (99%, Aldrich). Styrene (bp 145-146˚C) was distilled at reduced vacuum to remove traces of the inhibitor 4-tert-butylcatechol (bp 285-286˚C). An inhibitor reacts with free-radical active centres producing species which are incapable of re-initiating polymerisation and is added by the manufacturer to prevent thermal self-initiation during transit and storage. Distillation at low pressure further reduced the risk of thermal initiation and the distillation apparatus was wrapped in tin foil to prevent light-initiated polymerisation. After distillation, the styrene was stored in amber bottles in the refrigerator, under a nitrogen atmosphere until required. The polymerisation experimental set-up is illustrated in figure 3.5.

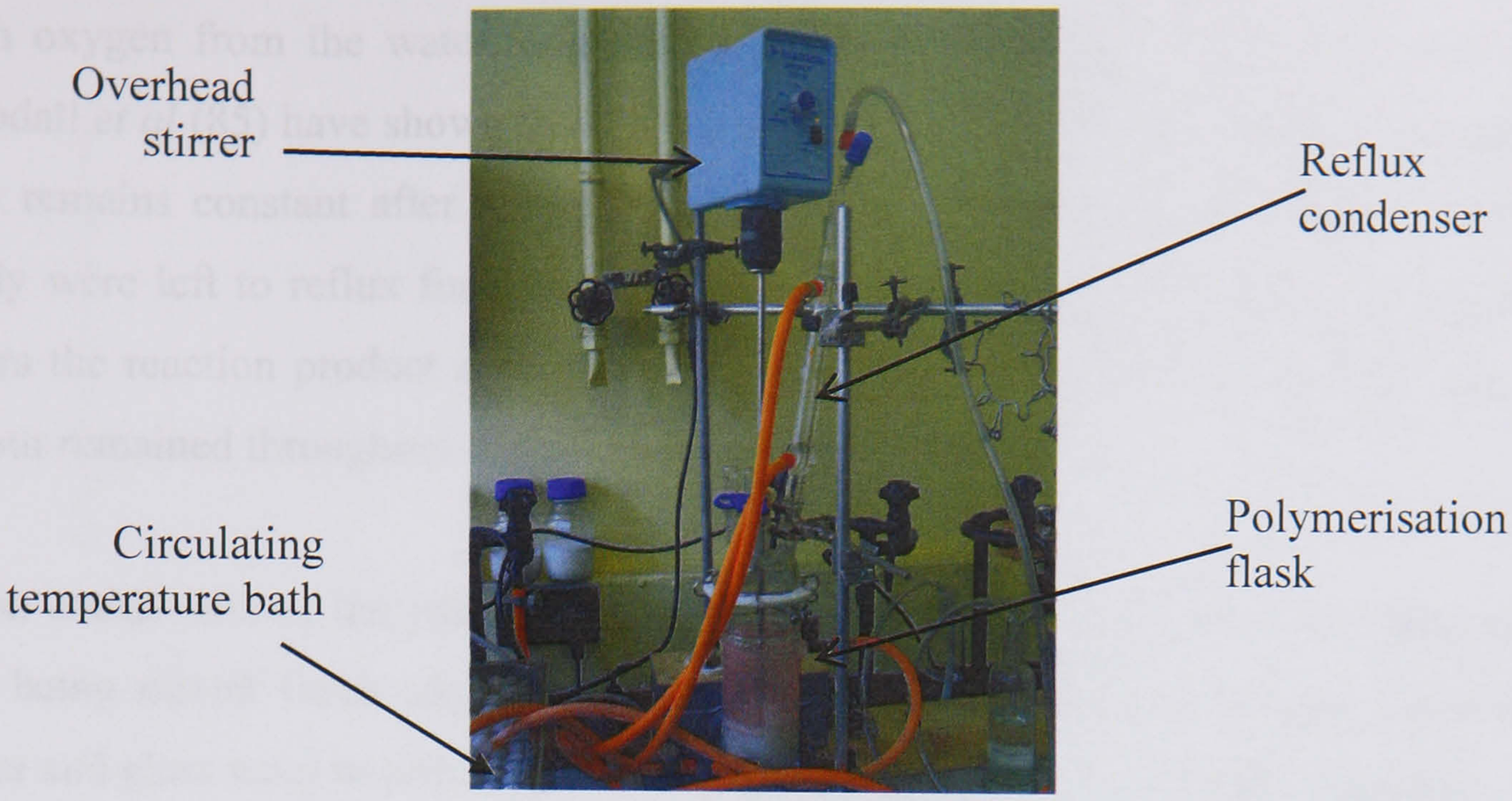


Figure 3.5 Labelled photograph of the polymerisation set-up

The polymerisation reaction was carried out in a jacketed reaction flask, which contained a twin-paddled overhead stirrer, a reflux condenser and a nitrogen/reagent inlet. Previous work (64) indicated that the overhead stirrer suffered from a 'lag' period during which time there was variation in stir speed. This lag period was approximately one hour after switching on and as such the stirrer was started a couple of hours before the polymerisation reaction commenced and a hand-held tachometer was used to calibrate the stirrer. The stirrer was set to 450 rpm and the reaction flask was charged with 200 ml of de-ionised water which was de-oxygenated by bubbling with nitrogen. After thorough de-oxygenation, around 15 minutes, the nitrogen flow was stopped and the temperature was increased to ~75°C, by connecting the water from the bath, and allowed to stabilise. Throughout the polymerisation reaction the temperature was maintained at ~75°C through the jacket of the reaction flask with the use of the circulating temperature bath. After 30 minutes of heating, the styrene monomer was added, via a syringe, to the de-ionised water. The monomer was stirred for 15 minutes before the free-radical initiator was added.

Since in this study the only parameter varied was the concentration of monomer used, the same concentration of potassium persulfate was used for all the polymerisation reactions. 2.0015 g of potassium persulfate was dissolved in 250 ml de-ionised water and sonicated to ensure complete dissolution. Similar to the distilled styrene, the potassium persulfate solution was stored in the refrigerator until needed. 10 ml of this initiator solution, equal to a concentration of 1.185×10^{-3} $molL^{-1}$, was added to the reaction flask. As soon as the initiator had been added the polymerisation reaction solution was de-oxygenated to ensure that the free-radicals formed did not re-combine

with oxygen from the water, and the stir speed was reduced to 350 rpm. Although Goodall *et al* (85) have shown that for the polymerisation of styrene at 70°C the particle size remains constant after approximately ten hours of stirring, the reactions in this study were left to reflux for around 24 hours, maintained at ~75°C. After a couple of hours the reaction product appeared milky white, due to Rayleigh scattering, and this colour remained throughout the reaction.

Upon completion of the reaction, the colloidal suspension was allowed to cool, while still being stirred. Once completely cool, the solution was filtered through fluted filter paper and glass wool to remove any unreacted monomer and any formed coagulum.

The volume fraction of the colloidal suspension was calculated by allowing the water from the suspension to evaporate at room temperature and measuring the mass of the dried sample (83).

3.6 Sizing Method

Electron microscopy was used for the first time in 1949 by Backus and Williams to determine the particle diameter and size distribution of polystyrene latexes (83). The TEM was used to size all the colloids produced in this study as it is the only method which can give accurate and precise results, although other techniques have been investigated (see chapter 4). The diameter of the colloidal spheres synthesised was determined using a TEM JEOL 2000FX operating at 200 kV. Since accurate measurements are required it is necessary to calibrate the TEM because the imaging system does not give reproducible lens strengths. Lens strengths vary depending on external temperature, efficiency of the lens cooling system and lens hysteresis (76). Standard specimens are used to calibrate the magnification, typically a patterned carbon grid with 2160 lines per mm (giving a line spacing of 0.463 μm). The TEM is set to standard imaging conditions with the calibration grid at the eucentric plane, see chapter 2, and the image in focus. This calibration grid is measured at a range of nominal magnification values and then a graph of nominal versus actual magnification for the TEM is plotted, as shown in figure 3.6.

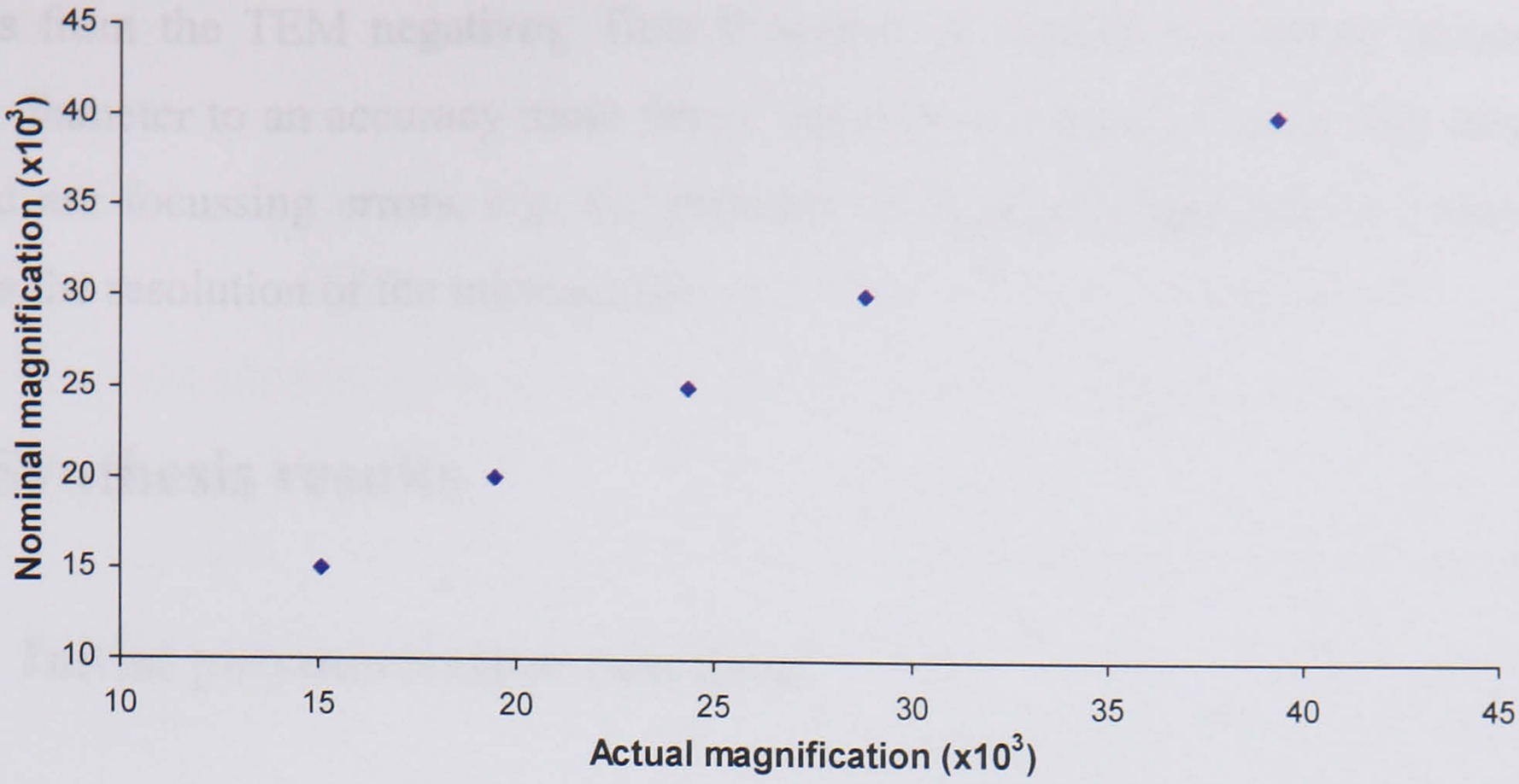


Figure 3.6 Microscope calibration for TEM JEOL 2000FX

The latex suspension was sonicated for 30 minutes to ensure any aggregates were broken up. The latex suspension was then further diluted, until the white colour was just observable and then a droplet of the diluted suspension was placed on a holey carbon film coated copper grid and allowed to evaporate. Images of each colloid produced were then recorded by TEM (figure 3.7).

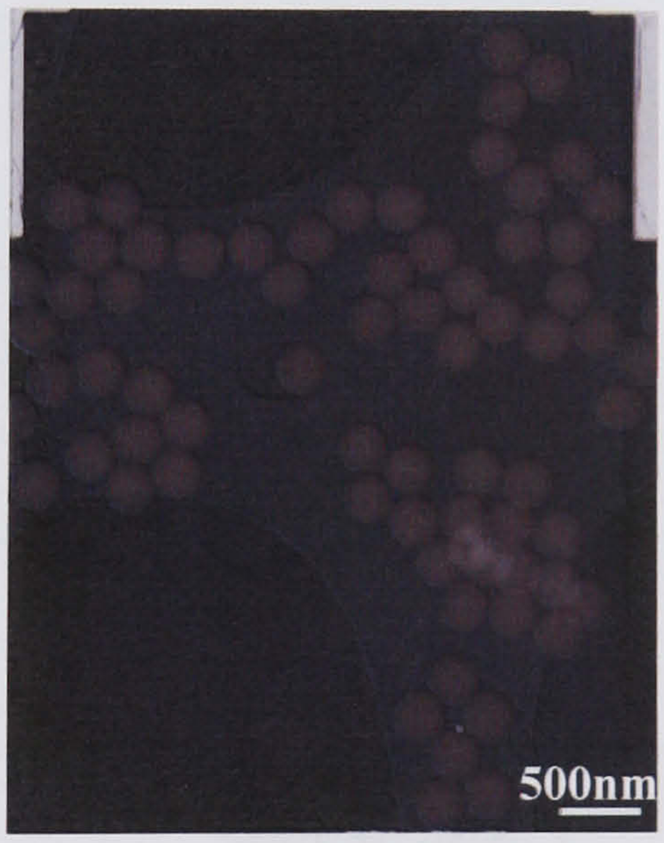


Figure 3.7 Typical TEM micrograph of polystyrene spheres with a narrow size distribution

At least 200 spheres were measured manually using a calibrated eye-piece and their absolute diameters and size distribution were determined by reference to the calibration plot (figure 3.6). The sizing data for all synthesised colloids, referenced by the date the synthesis was commenced, is contained within Appendix 2.

To reduce possible sources of error in this sizing method the eucentric height should be set correctly and the magnification of the TEM should be calibrated properly. The main source of error is introduced by the eye-piece when measuring the diameter of the

spheres from the TEM negatives. Thus it cannot be thought reasonable to quote the sphere diameter to an accuracy more than 1 nm. Other sources of error with this sizing method are focussing errors, *e.g.* the presence of Fresnel fringes, and for very small spheres the resolution of the microscope.

3.7 Synthesis results

3.7.1 Initial polymerisation reactions

In the preliminary experiments a number of polystyrene syntheses were conducted to investigate the effect of varying the styrene concentration on the diameter of the polystyrene spheres formed. Two different reaction flasks were used in the syntheses, flask A and flask B. The size information for the colloids synthesised are summarised in figure 3.8. The error bars on the diameter axis are obtained from the standard deviation of particle size for each specimen.

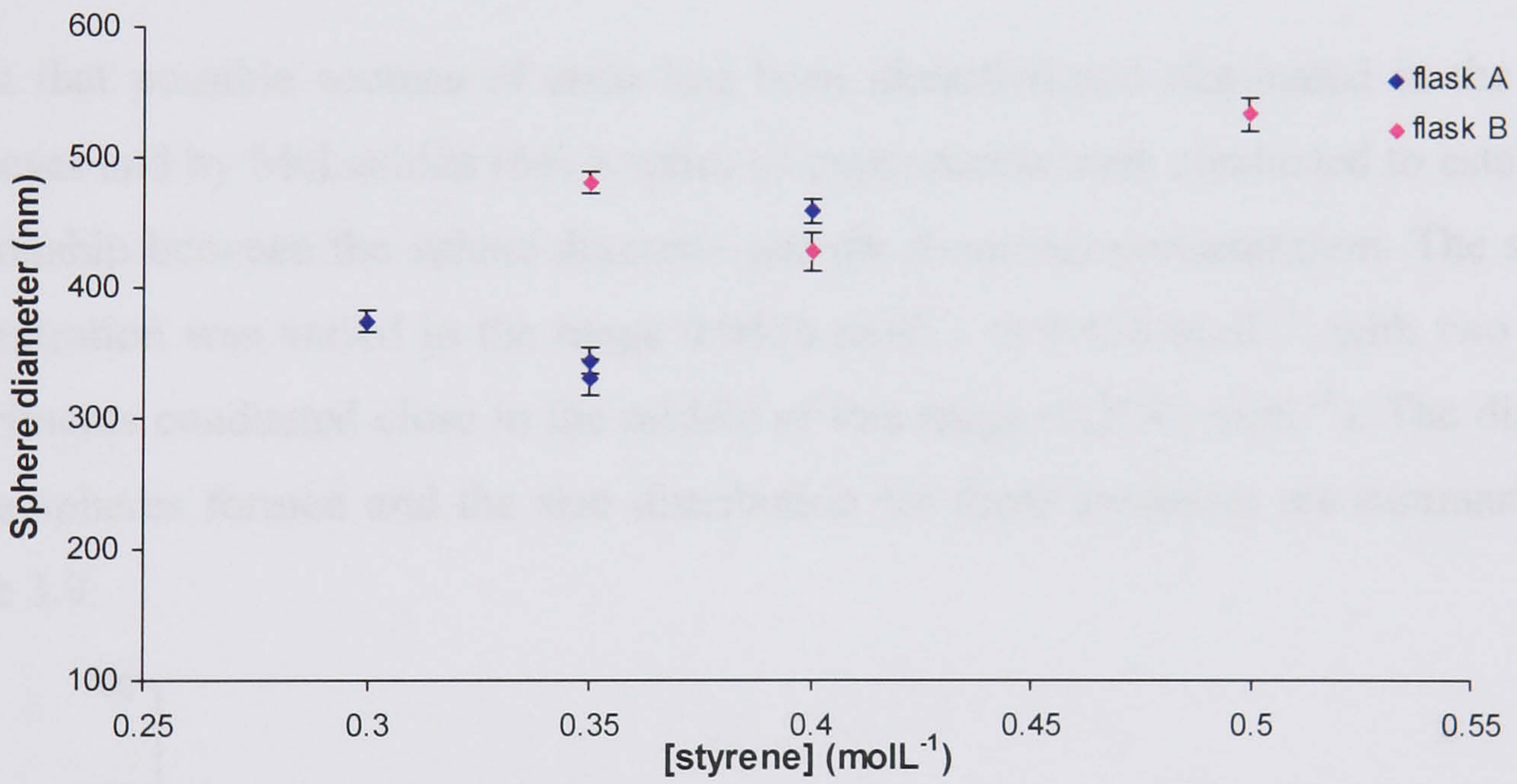


Figure 3.8 Effect of styrene concentration on sphere size

The results presented in figure 3.8 show a general increase in sphere size with increasing styrene concentration although a few anomalous points occurred. However significant variation in the results from the two reaction flasks used for polymerisation were observed. These reaction flasks, although of similar shape, had slightly different internal volumes which may explain the observed variation in results. Since the dimensions and set-up of the reaction flask are important the same reaction flask was used for all subsequent polymer syntheses.

In addition the styrene monomer had been opened for around six months prior to use. The half life of the inhibitor 4-tert-butylcatechol is 6-10 weeks (47) and since the seal of the monomer bottle had been broken self-polymerisation of the monomer could have occurred. Consequently for each subsequent batch of colloids a fresh bottle of styrene was opened and, once opened, was not kept longer than two months.

Furthermore if there was still some inhibitor in the distilled styrene this would also affect the size of the formed colloid. The presence of inhibitor in the styrene would cause an induction period in the polymer growth during which time the inhibitor is consumed by mopping up the free-radicals. It has been reported that the inhibitor used in styrene can cause a yellowing of the monomer (47) and therefore, for all future polymer syntheses, care was taken to that no yellow colour was present in the freshly distilled styrene.

3.7.2 Subsequent syntheses

Given that possible sources of error had been identified and eliminated in the initial syntheses and by McLachlan (64) a series of experiments were conducted to establish a relationship between the sphere diameter and the monomer concentration. The styrene concentration was varied in the range 0.0436 $molL^{-1}$ to 0.436 $molL^{-1}$, with two repeat experiments conducted close to the middle of this range (0.2180 $molL^{-1}$). The diameter of the spheres formed and the size distribution for these syntheses are summarised in figure 3.9.

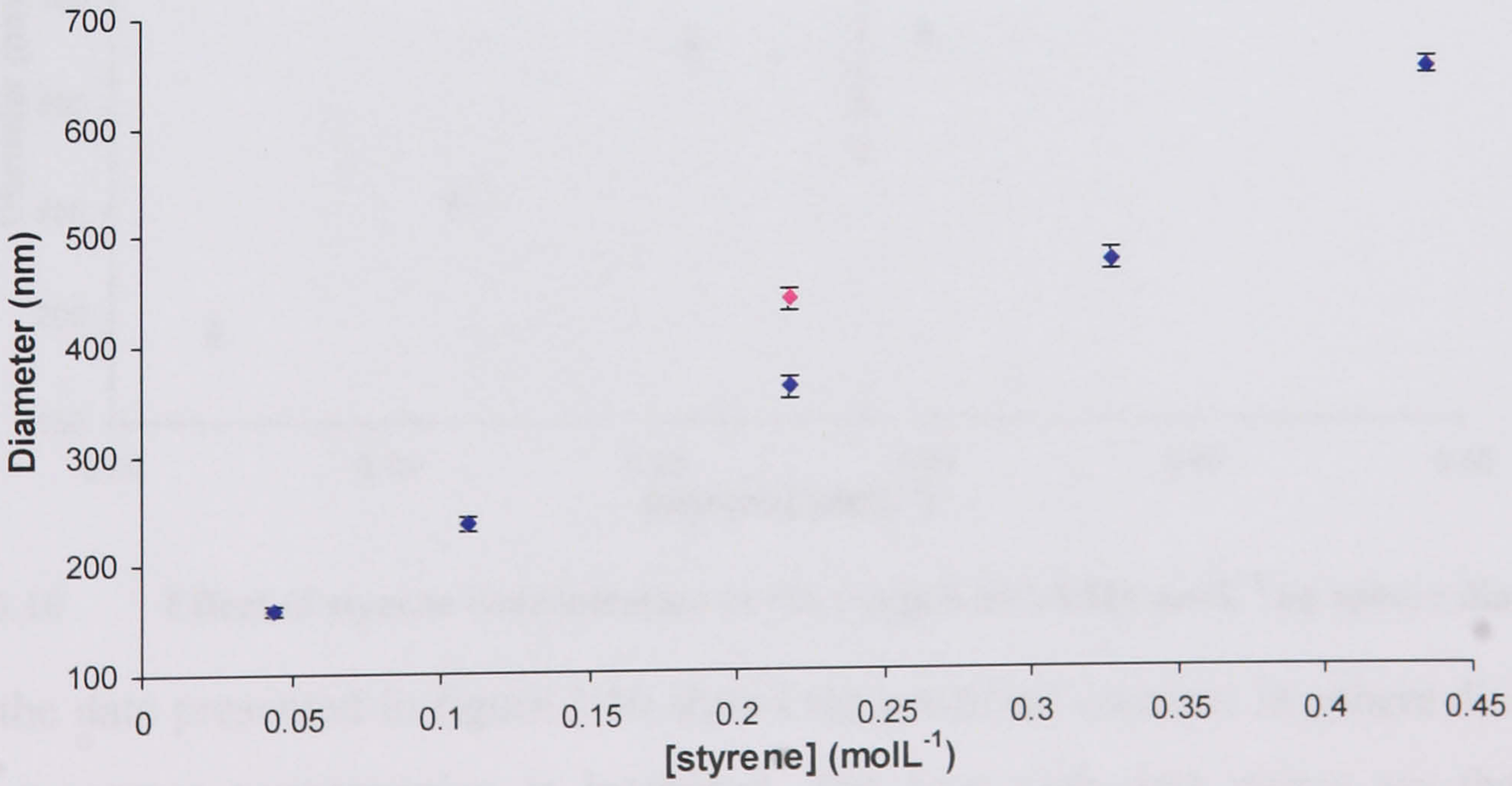


Figure 3.9 **Size information for colloids synthesised with styrene concentration in the range 0.0436-0.436 $molL^{-1}$**

The data presented in figure 3.9 shows the predicted increase in sphere diameter as the concentration of styrene increases and all of the spheres have a small standard deviation (<3%). However, the two syntheses conducted at a styrene concentration of 0.2180 $molL^{-1}$ do not show reproducibility. During the course of the polymerisation reaction shown by the pink marker in figure 3.9 evaporation of water took place due to poor sealing of the reaction flask. This would have resulted in a higher monomer concentration than calculated, and as mentioned previously, a higher monomer concentration results in spheres of bigger diameter.

One objective in this project was to form thin film PCs with a stop-band in the visible and near infra-red spectral regions. As previously discussed in chapter 1, the diameter required for polystyrene spheres to behave in this region is 200-400 nm. The data in figure 3.9 shows that spheres can be made in this diameter range with the styrene concentrations chosen and thus a similar monomer range was used in the following syntheses to provide a continuous supply of materials.

In the final series of experiments the monomer concentration was varied in the range 0.087 $molL^{-1}$ to 0.524 $molL^{-1}$ and four experiments were carried out with a styrene concentration of 0.326 $molL^{-1}$. The size information for these experiments is detailed in figure 3.10.

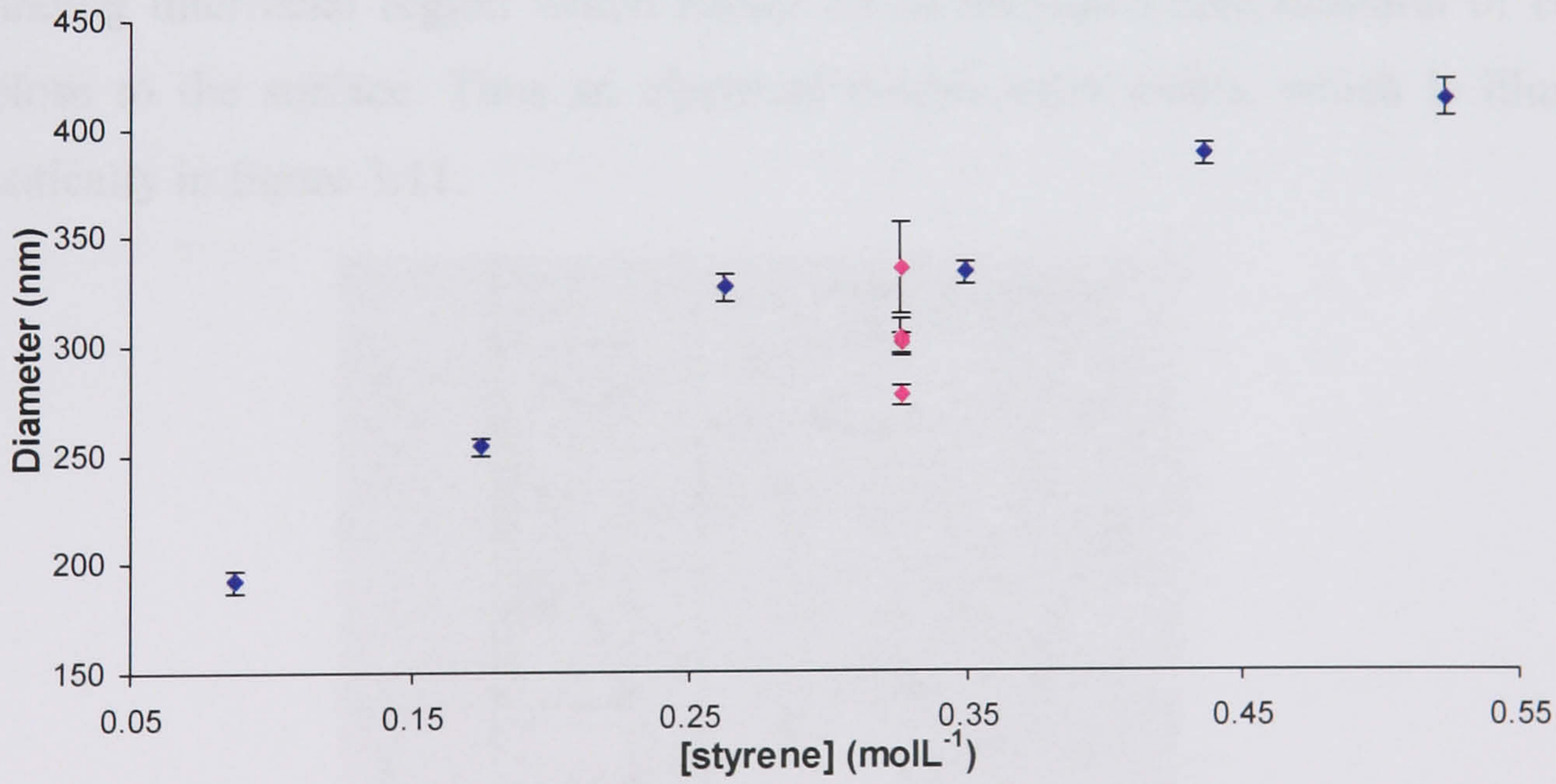


Figure 3.10 Effect of styrene concentration in the range 0.087-0.524 $molL^{-1}$ on sphere diameter

Again the data presented in figure 3.10 shows the predicted increase in sphere diameter as the monomer concentration is increased. The four pink data points are the four experiments carried out with the same styrene concentration. At a styrene concentration of 0.326 $molL^{-1}$ the size difference between the replicate samples was measured to be

57 nm. However, the synthesis with the largest error bars in figure 3.10 was problematic and during the course of the reaction the overhead stirrer fell out of place. This could explain why the size results for this synthesis do not fit with the other colloids formed at the same styrene concentration. When the other three syntheses are compared the size difference is only 35 nm which confirms that the polymerisation process is reasonably reproducible.

The results presented in figures 3.9 and 3.10 show that polystyrene spheres can be routinely synthesised with diameters in the range 150-650 nm. The results from the two batches of colloids produced confirm that with care the polymerisation process is reproducible and that a sphere diameter can be targeted prior to synthesis with a certain degree of error.

3.8 Zeta potential

The Derjaguin, Landau, Verwey and Overbeek theory, abbreviated as DVLO theory, explains the stability of colloids by electrostatic repulsion (91). The net force between particles in a suspension is assumed to be the sum of the attractive van der Waals forces and the electrostatic repulsion created by charges adsorbed on the particle surface. The development of this net force at the particle surface affects the distribution of ions in the surrounding interfacial region which results in an increased concentration of counter ions close to the surface. Thus an electrical double layer exists, which is illustrated schematically in figure 3.11.

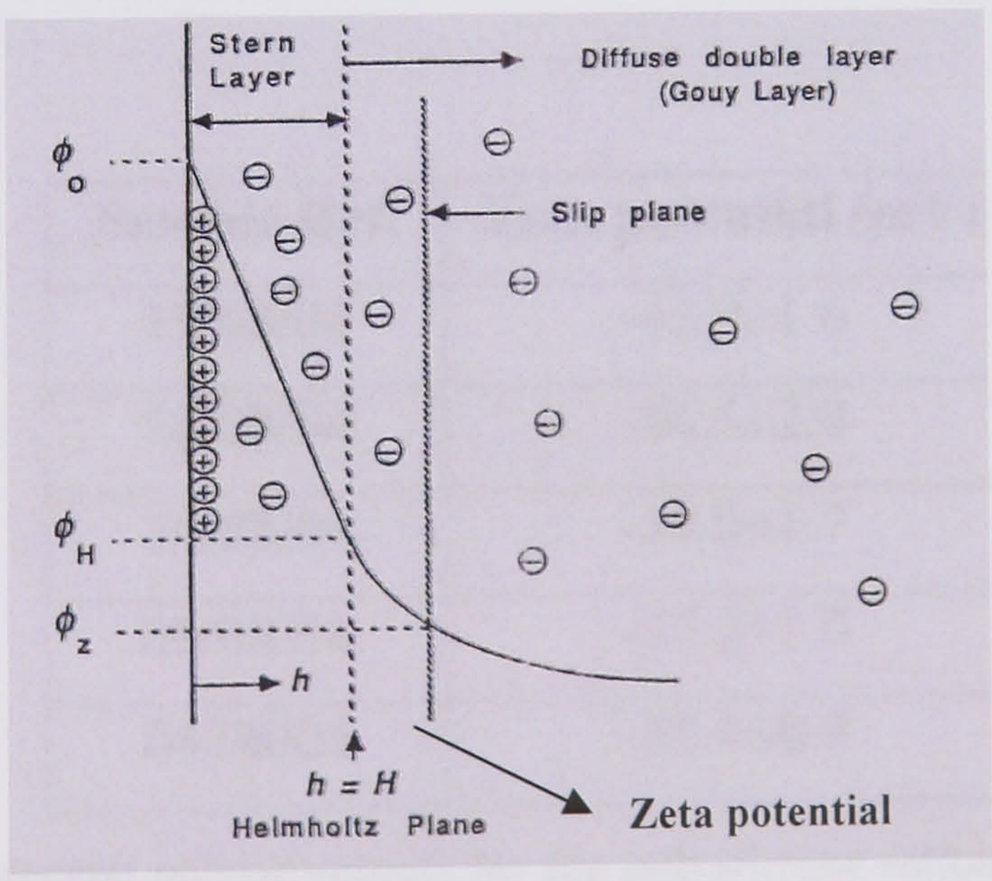


Figure 3.11 **Schematic diagram of the electrical double layer (91). The surface charge on the particle is assumed to be positive.**

The electrical double layer consists of two parts, an inner region where the ions are strongly bound (Stern layer) and an outer diffuse region (Gouy layer) where the ions are less closely bound (91). Within this diffuse layer is a notional boundary within which the particle behaves as a single entity and the potential at this boundary is termed the zeta potential, ξ (91).

3.8.1 Zeta potential measurement

The zeta potential measurements for the polystyrene colloids detailed in figure 3.9 were carried out on a Malvern Zetasizer at the University of Strathclyde by Dr. R. Littleford. The Zetasizer uses the principle of electrophoresis, the movement of a charged particle suspended in a liquid under the influence of an applied electric field, to measure the zeta potential. The electrophoresis system consists of a capillary cell, into which the colloid is added, with electrodes at either end to which the electric field is applied. Under the electric field the charged particles move towards the electrode of opposite charge. When the particle moves it carries with it the absorbed layer and part of the cloud of counter ions, while the more distant part of the diffuse layer is drawn towards the opposite electrode. The slip plane separates the region of fluid that moves with the particle from the region that flows freely (91). The particles move with a characteristic velocity which is dependent on the electric field, the dielectric constant, the viscosity of the medium and the zeta potential. The electric field, dielectric constant and viscosity of the medium are known, the velocity of the particles is measured and thus the zeta potential can be calculated. Table 3.1 summarises the zeta potentials (ξ) calculated for some of the synthesised colloids.

Sample Ref.	Zeta potential (mV)
19/08/04	-42.9±1.6
16/08/04	-44.5±2.0
10/08/04	-39.0±1.7
09/08/04	-37.2+1.0
04/08/04	-33.4±0.9

Table 3.1 Zeta potential measurements for the polystyrene colloids detailed in figure 3.9

The magnitude of the zeta potential gives an indication of colloidal stability. Particles with a zeta potential more positive than +30 mV or more negative than -30 mV are

normally considered stable (91). The data presented in table 3.1 shows the colloids formed in this study were all more negative than -30 mV and would therefore be considered as stable colloidal dispersions.

In addition, all the zeta potential values calculated were negative indicating that the synthesised polystyrene spheres have a negative surface charge. This supports the statement that the spheres would be terminated by the negatively charged sulphate group arising from the potassium persulfate initiator and agrees with reports in the literature (83,85).

3.9 Conclusions

The polystyrene spheres in this project were synthesised by emulsifier-free emulsion polymerisation. The polymerisation technique has been shown to be reproducible and, provided the reaction conditions are carefully controlled, it is possible to target a specific sphere diameter prior to synthesis within a certain degree of error. All spheres synthesised had a small size distribution, ideal for the formation of 3-D PC thin films.

4 Sizing Methods

4.1 Introduction

Electron microscopy, especially transmission electron microscopy (TEM). is an excellent technique used to measure the size of particles since not only can the size and dispersity of the sample can be measured but the shape of the particles can also be investigated. However, one disadvantage of microscopy is that relatively few particles are examined, in this study only around 200 spheres are sized for each sample (see chapter 3), and thus the method may be unrepresentative of the complete sample. Manual sizing, see chapter 3 using a graticule is also tedious and slow. Another problem is that the particles may be damaged by the electron beam, as occurs with poly(methyl methacrylate) spheres (64,76), or the particles may deform upon immobilisation onto the TEM grid.

For the reasons mentioned, especially the time consuming nature of manual sizing, it was thought beneficial to investigate alternative methods for measuring the diameter of the polystyrene colloids synthesised during the course of this study. This chapter summarises the theory and the results obtained using two alternative sizing methods both of which use the principle of light scattering to measure the diameter of particles. The two instruments are the High Performance Particle Sizer (HPPS) and the Mastersizer S both manufactured by Malvern Instruments Ltd. A batch of fourteen colloids spanning a wide diameter range, the diameter of which had already been measured by TEM (see chapter 3 and Appendix 2), were investigated using the two different techniques.

4.2 Dynamic Light Scattering

4.2.1 Theory

In this section the diameter of the polystyrene spheres was measured using a Malvern High Performance Particle Sizer (HPPS) instrument fitted with a 3 mW He-Ne laser operating at a wavelength of 633 nm. All analysis was carried out using Malvern software HPPS version 4.20.

The HPPS uses the principle of dynamic light scattering (DLS) which measures the Brownian motion of particles and relates this to their size. The Brownian motion of a particle is related to its size by the Stokes-Einstein equation, equation 4.1 (92),

$$d(H) = \frac{kT}{3\pi\eta D}$$ **Equation 4.1**

, where d(H) is the hydrodynamic diameter, k is the Boltzmann constant, T is the temperature, η is the viscosity and D is the diffusion coefficient.

In an aqueous medium most colloidal systems carry an electric charge due to the accumulation of charge on their surface. This development of net charge affects the distribution of ions in the surrounding region leading to an increase of counter ions close to the surface of the particle. Thus an electrical double layer exists, as shown in figure 4.1, and the thickness of this layer is equal to the Debye length (1/K).

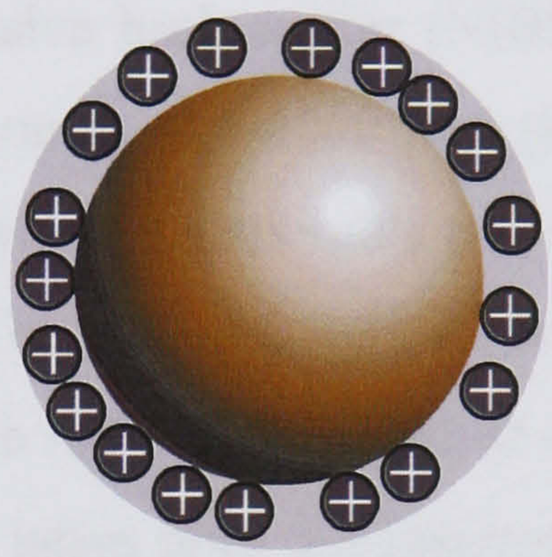


Figure 4.1 Schematic diagram of the electrical double layer for a particle with negative surface charge

The size of the electrical double layer, or Debye length, depends on the ionic strength of the aqueous medium as shown by equation 4.2 (93),

$$\frac{1}{K} = \sqrt{\frac{\varepsilon_0 \varepsilon_r kT}{2N_A e^2 I}}$$ **Equation 4.2**

, where 1/K is the Debye length, ε_0 is the permittivity of vacuum, ε_r is the relative permittivity of the suspending fluid, k is the Boltzmann constant, T is the temperature, N_A is the Avogadro number, e is the elementary charge and I is the ionic strength. The size of the electric double layer is therefore inversely proportional to the ionic strength (equation 4.2). As such, a high ionic strength medium is usually used for sizing measurements, typically a 10 mM NaCl solution (94), to decrease the electrical double layer and bring the hydrodynamic diameter closer to the actual particle diameter.

A basic schematic illustration of the set-up of the HPPS is shown in figure 4.2.

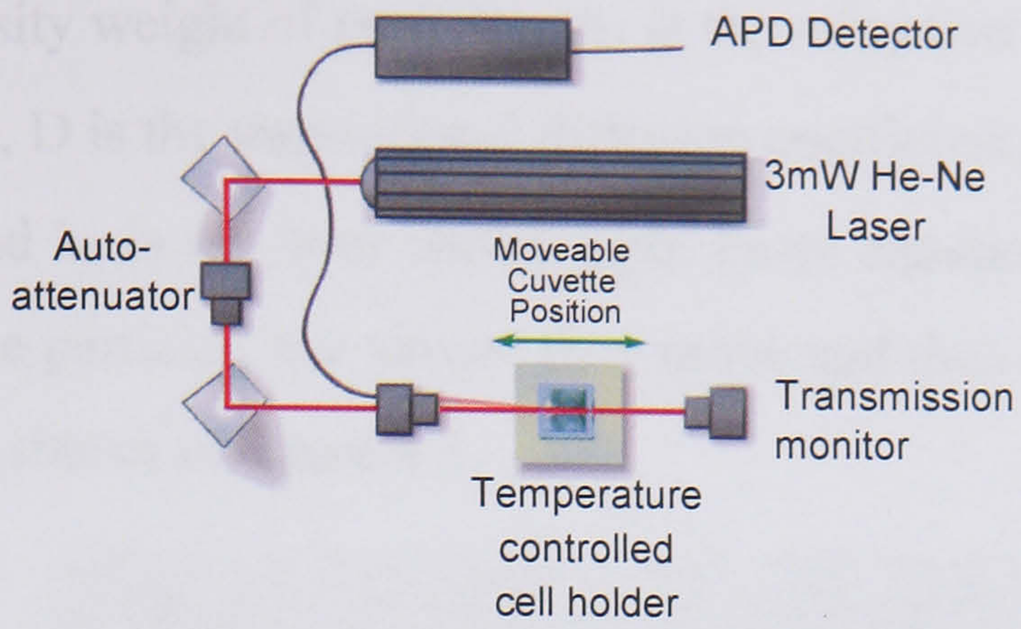


Figure 4.2 Schematic illustration of the experimental set-up of the HPPS (92)

The cell temperature is controlled at 25°C and the cell is automatically positioned for optimum settings, allowing an extended range of concentrations to be investigated. The HPPS uses the patented non-invasive back-scatter (NIBS) optics technology enabling high sensitivity over a wide size range (0.6-6000 nm) (95). The measurement is non-invasive since the sample is held within a disposable cuvette which allows the sample to be measured in its original state. The scattered light is measured using a back scattering detector, at an angle of 173°, which reduces the effect of dust. Another advantage of the NIBS technology is that the laser beam does not penetrate the entire sample, reducing multiple scattering effects and therefore allowing more concentrated samples to be used.

Due to the large number of particles which are measured using HPPS technology, there are many scattered beams which interfere with each other leading to a very complex overall scattering intensity pattern. Since the particles are continuously undergoing Brownian motion the intensity pattern constantly fluctuates, the rate of which depends on the particle size. The intensity of the signal at time, t, is compared to the intensity of the signal at time ($t+\delta t$) by a correlator (92). The period of time δt is chosen to be small, <1 μsecond, since the intensity pattern is fluctuating rapidly (92). The correlation of the signal intensity decreases with time until eventually there is no correlation. For monodisperse particles the correlation function, [G], can be calculated by equation 4.3 (96)

$$[G](\tau) = \sum_{i=1}^{n} c_i \exp\left(\frac{-4\pi m_1 \sin(\theta/2) D\tau}{\lambda_0}\right) \qquad \textbf{Equation 4.3}$$

, where c_i is the intensity weight of particles, m_1 is the refractive index of the solution, θ is the scattering angle, D is the translational diffusion coefficient, τ is the correlator time delay (equal to δt) and λ_0 is the laser wavelength. From equation 4.1 and 4.3 it can be seen that the larger the particles, the slower they move and thus the correlation function persists for longer, as shown in figure 4.3.

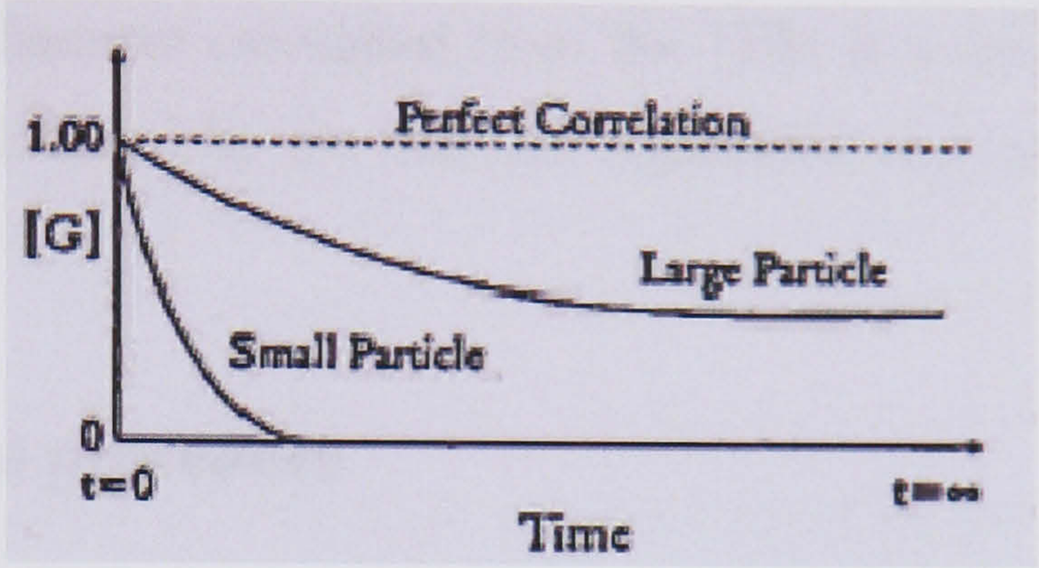


Figure 4.3 **Comparison of the correlation function for a sample containing small and large particles (92)**

The particle size can be obtained from the correlation function using the cumulants analysis, that is by plotting a graph of log [G] versus time (96) (figure 4.4).

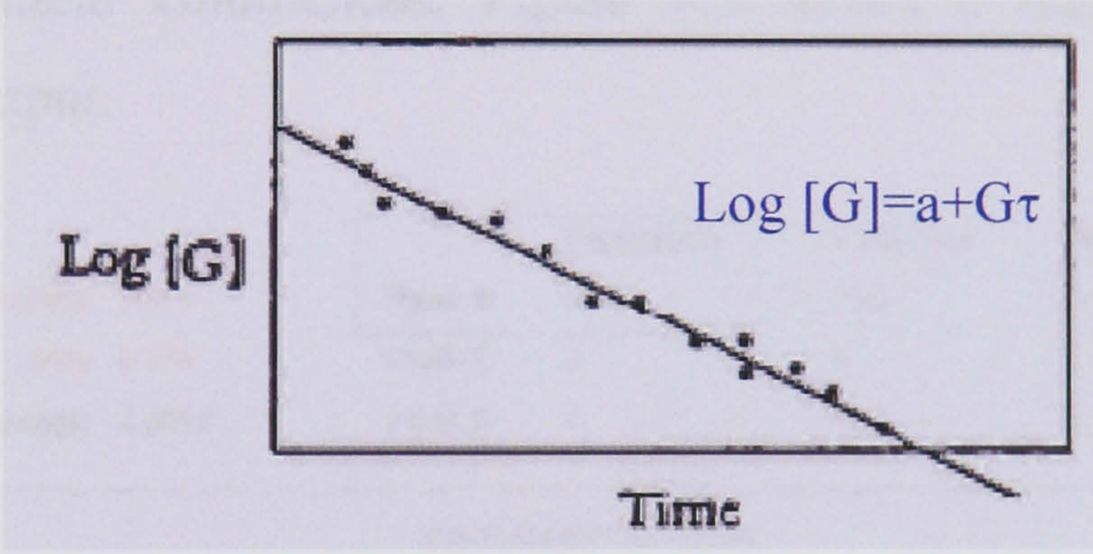


Figure 4.4 **Plot showing a typical cumulants analysis and how the particle size can be calculated (92)**

The gradient of the line illustrated in figure 4.4 is related to the Z average (Z_{av}) diameter. If the sample is polydisperse the plot of log [G] versus time will not be a straight line, as shown in figure 4.4, but will be a curve. The best fit of the curve can be obtained by fitting a power series and generally a quadratic fit is used, *i.e.* $\log[G]=a+bt+ct^2$, and the polydispersity, is defined as $2c/b^2$ (96).

Since Z_{av} is calculated from the signal intensity it is an intensity mean diameter – not a volume, mass or number mean diameter. To obtain a volume or mass mean, which can be compared to other techniques used to measure the diameter of the polystyrene colloids, Mie theory needs to be employed (97). When the size of the particles becomes

approximately equal to the laser wavelength (λ=633 nm) the scattering pattern becomes a complex function with respect to angle (95). Mie theory is the only theory which can correctly explain the observed maxima and minima in the plot of intensity versus angle by solving the Maxwell equations relating the interaction of light with matter (92). However, for Mie theory the refractive indices of the particle and suspending medium and a term for the absorption of light by the particle needs to be known. The derived intensity mean can be converted to different means, such as mass or number, by the Hatch-Choate transformation (96), which is done by the Malvern software using algorithms. Since the diameter calculated from the TEM is a number distribution, the number distribution calculated by the Malvern algorithms was investigated as well as the Z_{av} value.

4.2.2 Experimental procedure

The experimental procedure for the HPPS is extremely straightforward. The colloidal suspension is added to a clean cuvette and placed in the cuvette holder. The cuvette position is automatically adjusted to optimise the settings for the particular sample before the measurement commences. Figure 4.5 shows a typical example of the experimental data output.

		Diam. (nm)	% Number	Width (nm)
Z-Average (nm):	508.9	Peak 1:	487.3	100	68.07
PDI:	0.269	Peak 2:	0	0	0
Intercept:	0.9058	Peak 3:	0	0	0

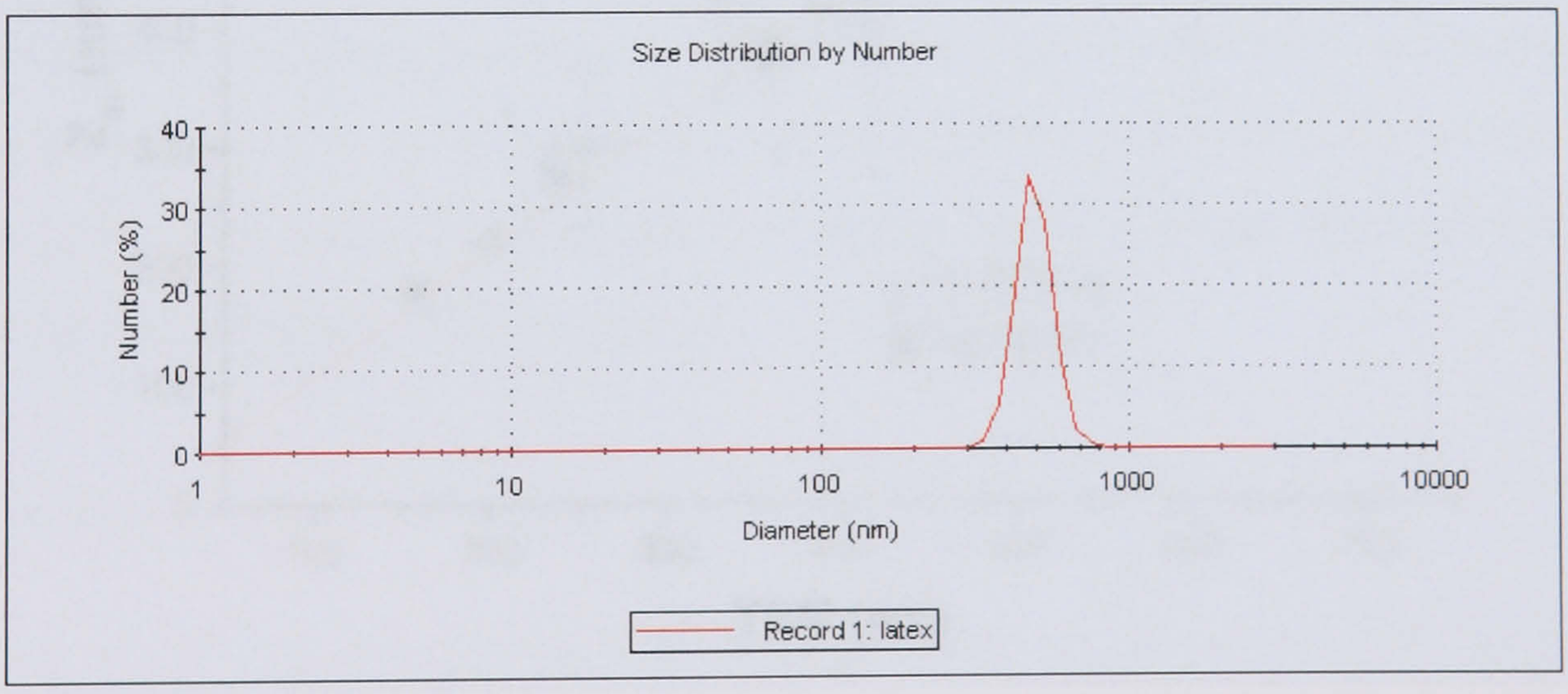


Figure 4.5 Extract from a typical output data file from the HPPS software

The required size information is obtained from the data output as shown in figure 4.5 – the Z_{av} and polydispersity index (PDI) are highlighted in red and the number diameter is

shown by the blue box. Since the size distribution is Gaussian in nature, the error on the measurement was taken to be the width of the peak, indicated by the pink box.

4.2.3 Results

The diameters obtained from the HPPS were plotted against the corresponding diameter calculated from the TEM in an attempt to compare the results. Using Origin a straight line was fitted to the data points the y-intercept set to zero and the equation of the line and the fit (R value) were noted. Figure 4.6 shows an example of the graphs which were plotted in order to compare the values from the TEM and HPPS technique. The number averages and the Z_{av}-10% results for each sample preparation method have been summarised in table 4.1. Ten percent has been removed from the Z_{av} value to help take into account the electrical double layer (92). If the diameter measured by HPPS matches the TEM data exactly, although the same values are not expected, a straight line with gradient equal to one, *i.e.* y=x, would be obtained with R=1 (see Appendix 1 for further explanation).

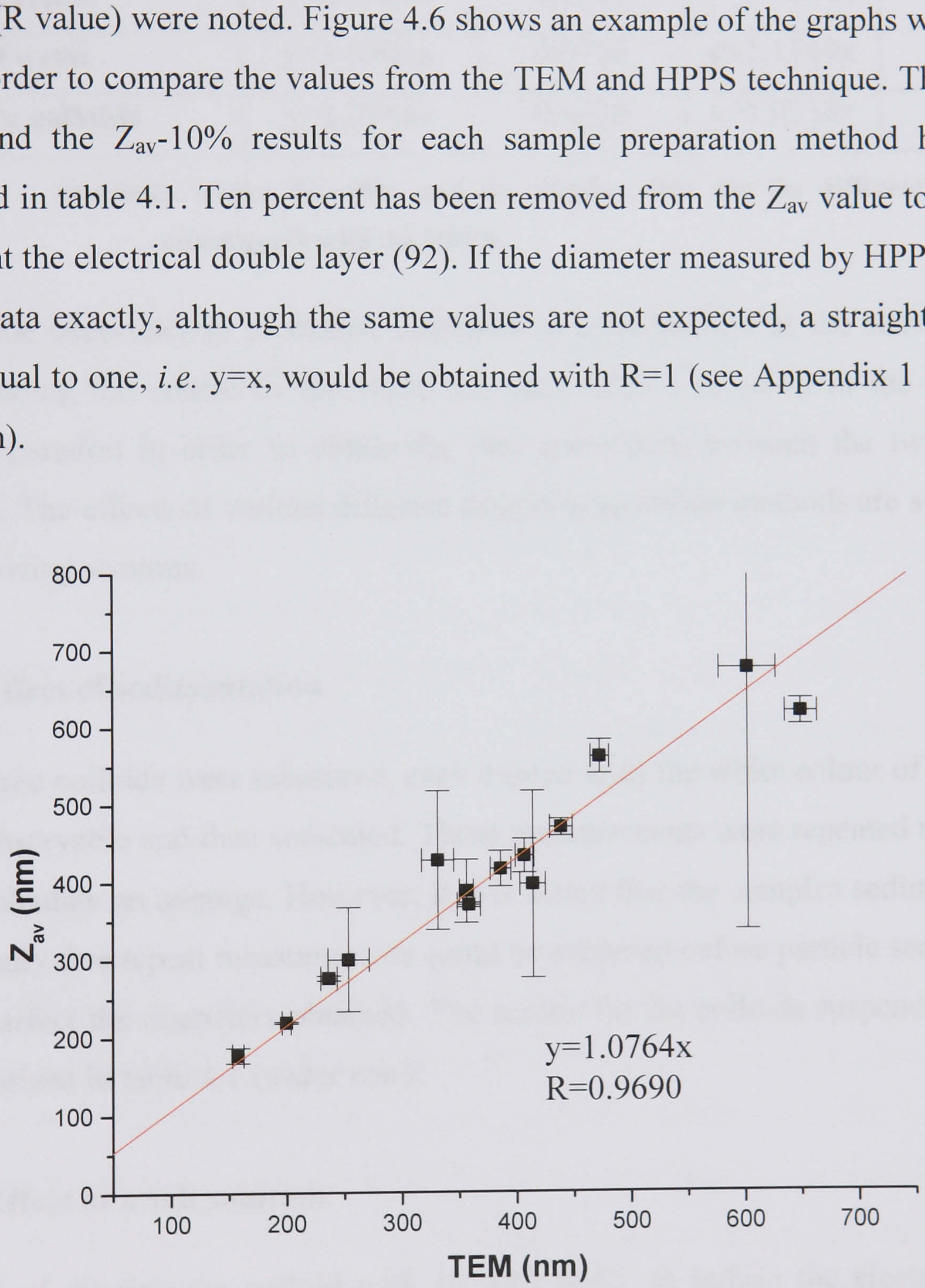


Figure 4.6 **Plot of TEM derived size versus the Z_{av} value obtained from the HPPS for the more colloids row in table 4.1**

Method	Z_{av}-10%		Number	
	Eqn. line	R value	Eqn. line	R value
Water	y=1.3321x	0.9952	y=1.2423x	0.9861
Sonicated/NaCl	y=0.9355x	0.9763	y=0.9686x	0.9145
$5x10^{-4}$ vol%	y=1.2361x	0.8202	y=0.9969x	0.8302
$5x10^{-5}$ vol% & 0.6 μm filter	y=1.2443x	0.9847	y=1.1062x	0.9249
Teepol	y=0.9736x	0.8945	y=0.6154x	0.9818
Tween	y=1.0505x	0.9758	y=1.1149x	0.9820
More colloids	y=1.0764x	0.9690	y=1.0734x	0.9404

Table 4.1 Summary of the Zav-10% and the number data for the different techniques investigated with the HPPS

Although the experimental procedure appeared straight forward at the start it became apparent during the course of the study that care had to be taken in the method of sample preparation in order to obtain the best correlation between the two different techniques. The effects of various different sample preparation methods are summarised in the following sections.

4.2.3.1 Effect of sedimentation

Initially three colloids were measured, each diluted until the white colour of the colloid was just observable and then sonicated. These measurements were repeated ten times in order to calculate an average. However, it was found that the samples sedimented over time and only five repeat measurements could be achieved before particle sedimentation started to affect the diameters obtained. The results for the colloids suspended in water are summarised in table 4.1 (*water row*).

4.2.3.2 Effect of a salt solution

The effect of diluting the colloid with 10 mM NaCl, to reduce the electrical double layer, rather than using de-ionised water, was also investigated. These results are summarised in table 4.1 (*Sonicated/NaCl* row) and from the data it can be seen that the equation of the line becomes closer to y=x than the results discussed in the previous section. This would indicate that the diameters calculated from the colloids dispersed in the NaCl solution are closer to those calculated from TEM analysis than those dispersed

in water and consequently all the colloids investigated were diluted with 10 mM NaCl solution.

4.2.3.3 Effect of particle concentration

The use of the NIBS detection system means that the laser beam does not have to travel through the entire sample thus reducing multiple scattering effects which arise from the presence of many particles. This should therefore enable measurements to be made at high concentrations. However, at high concentrations the particles which are being measured will be closer together and there will be more particle-particle interactions which could influence the measured particle diameter. Therefore the effect of further dilution of the colloids was investigated.

It was estimated that the initial colloids discussed in the previous two sections, were diluted to $5x10^{-3}$ vol% to obtain the slight milky white colour. In order to investigate the effect of concentration the colloid samples were first diluted to $5x10^{-4}$ vol% and then further diluted to $5x10^{-5}$ vol% and also passed through a 0.6 μm filter in order to remove any large aggregates. These results are summarised in table 4.1 (*$5x10^{-4}$ vol%* and *$5x10^{-5}$ vol% & 0.6 μm filter* row respectively). The first dilution to $5x10^{-4}$ vol% worsened the fit of the line but the combination of further dilution to $5x10^{-5}$ vol% and filtration improved the fit. This is probably due to any large aggregates being removed in the filtration step.

4.2.3.4 Effect of surfactant

Colloidal suspensions should be stable if the zeta potential is -30-50 mV (91). Zeta potential measurements on the polystyrene colloids synthesised in this project have been measured to be below –30 mV (table 3.1) and should therefore be stable. However, in an attempt to stabilise the colloids further the surfactant, Teepol (0.5 ml Teepol in 250 ml 10 mM NaCl solution), was added to the diluted colloidal suspension before the size measurement was commenced. The results for the samples with added Teepol are shown in table 4.1 (*Teepol* row). The results for these samples gave multimodal peaks, unlike the results shown in figure 4.5, meaning that one exact value for the size of the colloid could not be obtained. It was later discovered that Teepol was not a good surfactant to use because of the large agglomerates in it which would affect the scattering profile and thus confuse the size measurement.

An alternative surfactant, polyoxyethylene sorbiton monlaurate (Tween 20). was investigated. Around 0.5 ml of as received Tween was added to 250 ml of 10 mM NaCl solution. The addition of Tween appears to have stabilised the colloids and gave the best correlation with the TEM data, as shown in table 4.1 (*Tween* row).

Since the addition of Tween gave best correlation with the diameters measured by TEM another eight colloids were investigated using the same sample preparation method covering a wide range of sphere diameters. These results are summarised in the *more colloids* row in table 4.1.

4.2.4 Conclusions

The results presented in table 4.1 show that the best correlation between the diameters measured by the TEM and those obtained using the HPPS was when a low concentration of colloid and the surfactant Tween was used. This method achieved almost perfect correlation, with the equation of the best fit line giving a gradient almost equal to one and a R^2 value indicating a good fit. This indicates that the HPPS could be used to give a quick estimate of the size of the synthesised polystyrene colloids.

4.3 Low Angle Laser Light Scattering

4.3.1 Theory

The sizing in this section was performed using a Malvern Mastersizer S fitted with a 633 nm He-Ne laser. All data analysis was carried out using Malvern software v2.18.

The Mastersizer system uses the principle of low angle laser light scattering (LALLS) and has an applicable size range from 0.1-3000 μm (98). The LALLS technique relies on the fact that particles passing through a laser beam scatter light at an angle inversely proportional to their size (99). A schematic illustration of the experimental set-up is shown below in figure 4.7 (99).

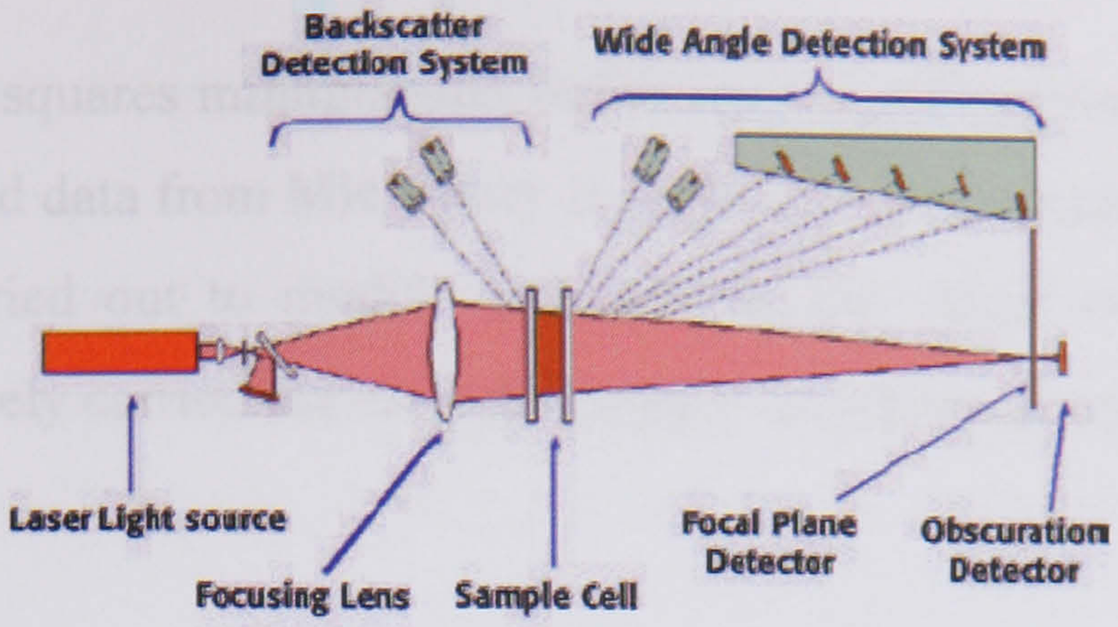


Figure 4.7 Schematic illustration of the experimental set up of the Mastersizer

A 2 mW He-Ne laser is used for stability and as an intense source of light ensuring that there is as much scattered light as possible. The detector is composed of 42 composite solid state detectors in a circular array and one centre detector. The array of different detectors aids the observation of scattering which changes as a function of angle. The detectors increase in size as the scatter angle increases, in order to optimise the weak signals scattered from small particles, and the distance between detectors also increases. The centre, or obscuration detector, acts as a method for calculating the concentration of particles passing through the laser beam.

Due to the size of the colloids investigated in this study, less than 600 nm in diameter, the 300RF (Reverse Fourier) lens was used which allows particles as small as 50 nm to be measured (99). The reverse Fourier lens is placed before the sample area and rather than collimating the laser beam it expands the beam and focuses it to a point in the plane of the detector. This allows measurement of scattering at high angles *i.e.* from smaller particles.

In a typical experiment the light scattering pattern continuously changes due to particles flowing through the laser beam. The detector takes a snapshot of the scattering pattern and builds up a pattern from around 2000 snapshots. Therefore the light scattering characteristic that is built up encompasses millions of particles. This collected light scattering data is then transferred to a computer and analysed by Malvern software. This software uses Mie theory which predicts the scattering intensities for all particles, wavelengths and scattering angles and also predicts the secondary scattering, caused by light refraction within the particle (99). Secondary scattering becomes important for small particles (99). Mie theory is used to calculate a particle size distribution for which the actual scattering data is compared to.

A constrained least squares minimisation technique is used to give the size distribution result. The computed data from Mie theory is compared to the actual scattering data and corrections are carried out to modify and improve the initial computed result. This procedure is iteratively carried out until the computed and actual scattering data agree to an acceptable level.

The analysis described above calculates a volume distribution, D[4,3] or the De Broucker mean. Using the Hatch-Choate transformation (100) this volume distribution can be converted to different means *e.g.* the number length mean D[1,0], which is the value comparable with the size obtained from TEM.

4.3.2 Experimental procedure

The experimental procedure is extremely straightforward. Before an actual measurement was commenced it was ensured that the small volume sample unit (QS) was clean. The sample unit was then filled with de-ionised water and stirred at 800 rpm for data collection. A background reading was taken with only water circulating through the system which removes any electrical noise or light scattered from impurities. This background reading is then removed from all subsequent measurement readings. The colloid is then added into the sample unit until an obscuration rate of around 30% has been achieved, which ensures that there is an adequate concentration of particles circulating through the laser beam. The sizing measurement can then be commenced.

The data output from the Mastersizer gives the percentage of spheres lying within a certain range, the smallest range being 0.05-0.06 μm. The data output also gives a list of the American Society for Testing and Materials (ASTM) derived diameters *e.g.* D[4,3] and D[1,0].

4.3.3 Results

The statistics from the data output were processed using an Excel spreadsheet to calculate an average particle size and corresponding polydispersity, shown in the *Av. size* column in table 4.2. The D[1,0], or the number length mean, was also investigated since it is the diameter which is comparable to the diameter obtained by TEM.

In a similar manner to the results presented for the HPPS the diameters obtained from the Mastersizer were plotted against the corresponding diameter calculated from the TEM. A straight line was fitted to the data points, the y-intercept set to zero and the equation of the line and the fit (R value) were noted. The average size and the D[1,0] results for each sample preparation method are summarised in table 4.2.

Method	**D[1,0]**		**Av. Size**	
	Eqn. line	**R value**	**Eqn. line**	**R value**
1st attempt	y=0.3683x	0.9584	y=0.7604x	0.9402
Filter	y=0.3867x	0.6344	y=0.8143x	0.9830
Teepol	y=0.3943x	0.6623	y=0.7499x	0.9906
Filter & Teepol	y=0.4111x	0.3827	y=0.7419x	0.6154

Table 4.2 Summary of the D[1,0] and Av. size for the different techniques investigated with the Mastersizer

4.3.3.1 Stabilisation

At the start of the investigation it became clear that the colloids needed time to stabilise before the measurement was commenced and thus for subsequent measurements the colloids were allowed 5-10 minutes circulating time before the measurements were started. These results are shown in the *1st attempt* row in table 4.2 and show that there is little correlation between the diameters obtained from the Mastersizer and the TEM.

4.3.3.2 Filter

In a similar manner to the experimental procedure for the HPPS, the colloids were filtered through a 0.6 μm filter to remove any large aggregates, results shown in the *filter* row of table 4.2. There appears to be little improvement in correlation between TEM and the Mastersizer upon filtering the colloid before use.

4.3.3.3 Surfactant

A little surfactant was added to the small dispersion unit before the colloid was added to ensure the particles would not agglomerate. Unlike the HPPS, Teepol can be used as the surfactant since a background reading is taken which accounts for any large particles and means that they are not included in the actual measurement. These results are summarised in the *Teepol* row in table 4.2. The results presented in table 4.2 indicate

that the addition of surfactant has improved the correlation between the TEM and Mastersizer since the equation of the line is closer to y=x.

4.3.3.4 Filter and Surfactant

Finally the effect of filtering the colloid prior to use and also adding a surfactant was investigated summarised in the *Filter & Teepol* row in table 4.2. The equation of the line for the D[1,0] values and the average size is the closest to the TEM sizes that the results get, however, the R values indicate that the fit of the lines are not very good.

4.3.4 Conclusions

The values obtained from the Mastersizer are not accurate or reproducible indicating that no correlation can be found between the values obtained from TEM sizing and the Mastersizer. Differences encountered between the two methods may be attributed to the inaccuracy of the estimated light absorption characteristics, which are used in Mie theory to calculate the size distribution.

4.4 Overall Conclusions

In this chapter two alternative methods to the TEM method for measuring the diameter of the synthesised polystyrene colloids have been investigated. Both of these methods use the technique of light scattering and offer fast, non-destructive and, once the experimental procedure has been optimised, simple analysis of a large population of particles. This makes these techniques attractive when compared to the time consuming TEM method which tends to sample only a small number of particles. However, using the TEM method the shape of the particles can be investigated and the microscope can be calibrated to known size standards, as described in chapter 3, which inspires confidence in the method. The main problem with light scattering techniques is that the optical properties of the sample need to be known. If these parameters are estimated incorrectly, errors in the calculations, which determine the size information from the scattering patterns, can occur leading to an incorrect size distribution. The results in tables 4.1 and 4.2 indicate that of the two methods investigated, the HPPS gives the best correlation with the diameters obtained by TEM and could therefore be used as a quick method for initial measurement of the colloids but the TEM should always be used for confident accurate results.

5 Thin Film Growth

5.1 Colloidal Crystallisation Methods

Several strategies have been exploited for the creation of three-dimensional (3-D) photonic band gap (PBG) structures. Currently 3-D photonic crystals (PCs) are fabricated by three main methods – microfabrication techniques (101,102), holographic patterning (26,27) and colloidal self-assembly (6,24,64,103,104).

Recently a microfabrication method has been used to form 3-D PCs with omni-directional PBGs at ~1.5 μm. The PC has a woodpile architecture and structural defects are micromachined into a high refractive index III-V semiconductor (GaAs or InP) (105). The woodpile structure is formed by stacking alternating layers at right angles to each other. However forming 3-D PCs by microfabrication methods operating in the visible spectral region has proven to be a technological challenge mainly due to the feature sizes being outwith the fabrication limits of conventional microfabrication technologies.

Holographic patterning has been shown to be capable of forming periodic structures with sub-micron periodicity (26). A periodic structure is formed in a thick (~30 μm) layer of photoresist by the interference of four non-coplanar laser beams. Highly exposed photoresist is insoluble and a 3-D periodic structure of crosslinked polymer with air voids is formed by dissolving unexposed regions of photoresist.

Although microfabrication and holographic patterning have proven successful methods for forming periodic structures with photonic stop-bands in the near infra-red and visible spectral regions respectively, both processes involve expensive, complex and multi-step processing. Conversely the fabrication of 3-D PCs by colloidal self-assembly (24,37,45,106) is particularly attractive partly because it is the only technique which could potentially realise a complete PBG in the visible spectral region and, in addition, the method is generally inexpensive, fast and requires little specialist equipment.

While the self-assembly technique may be the most common approach to fabricating synthetic opal the methods used for self-assembly vary considerably. The most common

methods are sedimentation, Langmuir-Blodgett type growth and vertical deposition. each of which will be discussed in the following sections.

5.1.1 Sedimentation

Since the formation of natural opal occurs from the sedimentation of silica spheres the process of gravitational, or natural, sedimentation was the first method considered for the synthesis of free-standing opals (107). In this method a colloidal suspension of spheres is allowed to settle under gravity and self-assemble to form a cubic close packed structure. Natural sedimentation should be carried out in the absence of vibration and thermal gradients, the spheres should be monodisperse (108) and if the growth is onto a substrate, the substrate should be smooth, clean and chemically homogeneous (109).

However the process of natural sedimentation is not as simple as it would first appear since problems occur if the spheres are too small or large (110). When the spheres are small, <300 nm, the time taken to form synthetic opal samples can take several weeks or not occur at all because thermal agitation compensates for the small gravitational forces felt by the spheres. On the other hand if the spheres are greater than 550 nm the formation of an ordered array is difficult because the gravitational energy is much greater than the thermal energy and the spheres sediment before there is time for ordering to occur.

Electrophoresis offers a solution whereby the sedimentation rate can be increased or decreased (110). In electrophoresis a cell is created and a controlled current is passed across a volume of colloidal spheres. Both silica and polystyrene spheres carry a slight negative charge and are therefore attracted to the anode of the cell. The use of electrophoresis has been reported to improve the quality of the synthetic opal when the sedimentation rate is decreased but when the rate is increased the opal sample showed poor ordering (110). More recently it has been reported by Rogach *et al* (111) that the use of a polar but non-electroactive dispersion medium, which prevents gas evolution at the electrodes, can reduce the structural defects reported by Holgado and co-workers (110).

Alternatively the rate of natural sedimentation can be increased by using centrifugation which can typically reduce the opal growth period to a few hours (22,34,70,71,112).

Care has to be taken as to the angular velocity chosen for centrifugation, for example if the centrifugal force is too strong a randomly ordered structure is produced. Johnson *et al* (22) have reported that for silica spheres in the diameter range 375-480 nm an angular velocity of ~4000 rpm gave samples with the best ordering.

Although sedimentation offers a convenient and simple route to the formation of 3-D PCs and was the natural progression from the formation of natural opal the process has many disadvantages. The samples formed typically contain polycrystalline domains and there is little control over the morphology of the top surface and the number of layers formed (36). Although using methods such as electrophoresis or centrifugation can control the sedimentation process these techniques add extra complications and in some cases do not improve the quality of the opal sample.

5.1.2 Langmuir-Blodgett

In the Langmuir-Blodgett technique a monolayer of particles is assembled on the surface of a suspension and then deposited onto a substrate as the substrate is removed from the suspension (113-115). Bardosova *et al* (113) have recently reported the formation of a well ordered thirty layer structure of silica spheres using the Langmuir-Blodgett technique. The spheres in this publication were made hydrophilic first and then centrifuged to remove any large particles. It was hoped that, since the ordered layers of spheres are added sequentially in the Langmuir-Blodgett technique, the number of layers, or thickness, of the crystal can be controlled precisely which cannot be done using the sedimentation technique.

5.1.3 Vertical Deposition

Of all the self-assembly techniques proposed for the formation of 3-D PCs the process of vertical deposition has shown the greatest promise and has therefore attracted the majority of research interest (see for example (6,24,36,44,45)). The vertical deposition technique is based on the work of Nagayama and co-workers where capillary forces are used to drive the assembly of polystyrene colloids onto a substrate (116-118). Conceptually similar to the Langmuir-Blodgett technique, Dimitrov and Nagayama (117) were able to create well ordered monolayers on nearly any vertical substrate. More recently Colvin and co-workers (24) extended the method to grow well ordered

multilayer colloidal crystals with controllable thicknesses. The vertical deposition technique, illustrated schematically in figure 5.1, relies on the balance between sphere sedimentation and evaporation of the colloidal suspension (119).

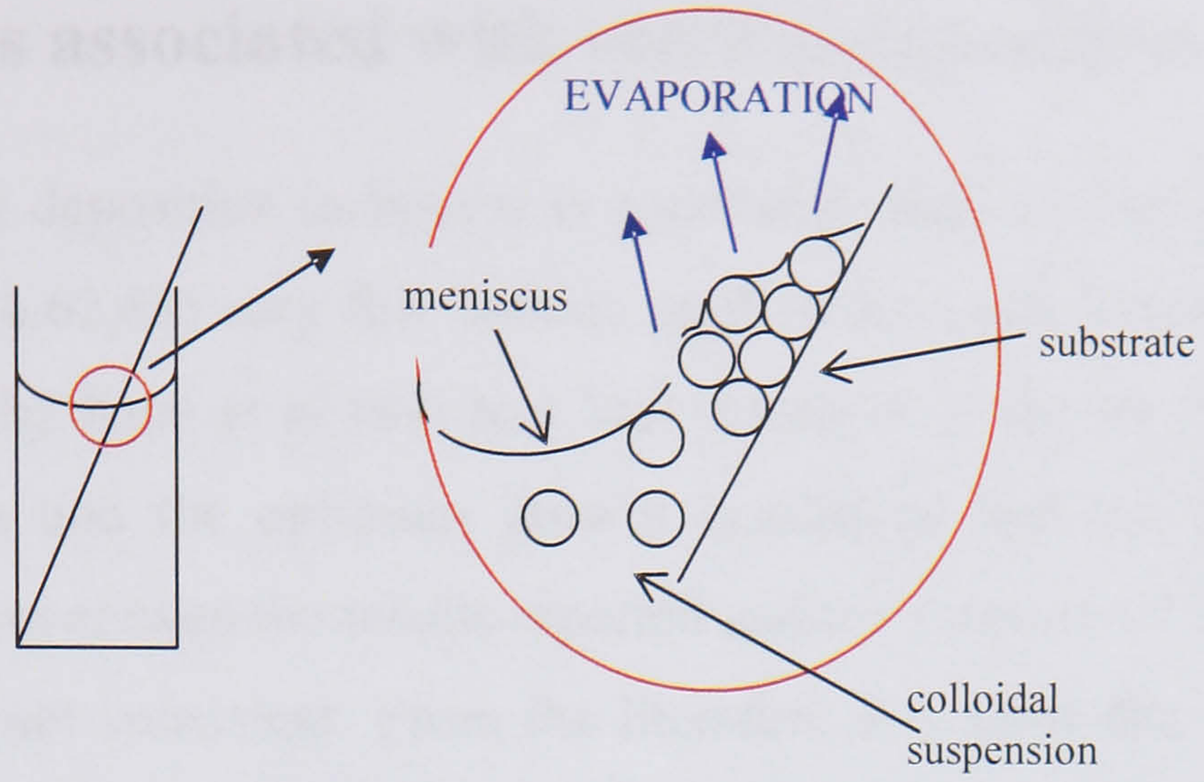


Figure 5.1 Schematic illustration of the vertical deposition method

The general consensus is that evaporation of solvent from the meniscus region draws colloidal spheres into the area of film formation and inter-particle capillary forces assemble the spheres into close packed arrays. Alternatively the substrate can be mechanically withdrawn from the colloidal suspension instead of relying on the solvent evaporation rate and this method has been reported to control the film thickness (36).

It is clear from the literature that the growth procedure of the vertical deposition technique is not well understood although Dimitrov *et al* (117,118) have gone some way to describe the process. It has been proposed that the formation of ordered arrays of spheres can be split into two main stages. Firstly, when the thickness of the solvent layer approaches the diameter of the spheres, a nucleus is formed. When the tops of the spheres protrude from the solvent, capillary forces act to pull the spheres together. Theoretical calculations have shown that these lateral capillary forces can exceed the thermal energy of the spheres by many orders of magnitude (120). Secondly evaporation from the small menisci formed between the spheres causes a flux of water which pulls the spheres towards the nucleated area where the growth of a close packed array occurs.

The vertical deposition technique offers many advantages compared to the other self-assembly techniques available. The technique is relatively cheap, simple and does not require sophisticated apparatus. In addition high quality films can be formed and the film thickness can be controlled. However, the realisation of a perfect colloidal crystal using the self-assembly technique is still an immense challenge since the films formed

exhibit a high number of structural defects *e.g.* stacking faults, dislocations and vacancies (45).

5.2 Variables associated with vertical deposition

While the vertical deposition technique is commonly used for the growth of synthetic opal thin films (36,62,68) very few authors publish the exact experimental conditions. Until the studies by Kuai *et al* (44) and McLachlan *et al* (6) the factors affecting the growth procedure and the optimum growth conditions had not been systematically investigated. However even the results reported and the measure of film quality between these studies are not consistent. From the literature it is clear that the most important variables associated with the vertical deposition technique are growth temperature and relative humidity (R.H.), sphere diameter and colloidal concentration. In this chapter the growth conditions have been kept constant at the reported optimum conditions, except for colloidal concentration, but the following chapter will discuss the effect of varying some of the growth parameters.

The quality of the films depends on the wettability, cleanliness and smoothness of the substrates used for growth. Both the type of substrate used and the cleaning protocol vary considerably between different publications. Common substrates include glass (6,45,121-123), silicon (106,124) and conducting glass (68,109). The cleaning procedure also varies from simple solvent cleaning to piranha solution (ammonia, hydrogen peroxide and water) (106) and acid cleaning (24). The following four sections give a brief overview of the effect each individual variable has on the quality of the resulting synthetic opal samples.

5.2.1 Temperature

The temperature at which vertical deposition occurs is an important parameter as it influences the solvent evaporation rate and R.H. and also affects the kinetic energy of the spheres.

Initially the temperature used for vertical deposition was in the range 18-22°C, *i.e.* close to room temperature (24,106). Ethanol was chosen as a suitable solvent because the rate of evaporation is faster than water and would therefore compete with the sedimentation of the spheres. Water can be used as a solvent but the temperature needs to be increased

to overcome sedimentation of the spheres. Growth temperatures of 55-65˚C have been reported to result in thin films of good quality (6,44,45,122). Goldenburg *et al* (123) have grown at temperatures of 60˚C for spheres <1 μm and increased the temperature to 95˚C for spheres up to 2.5 μm. Macroscopically the films were not uniform and consisted of horizontal lines ~1 mm wide. Such lines are indicative of either poorly dispersed colloid or temperature instability.

Both the growth temperature and the temperature stability are important. For the initial vertical deposition experiments it was considered acceptable to control the temperature to ±1˚C (24,121). The drift in temperature has been shown to give poorly ordered samples and horizontal striping visible to the naked eye (64). More recently the growth temperature has been controlled to ±0.2˚C (6). While it is normal for growth to occur in a closed environment, *e.g.* an oven or incubator, Norris and co-workers have discussed experiments which have been conducted on the open bench (125). In these experiments a temperature gradient, 80˚C at the base to 65˚C near the top, is introduced by the use of a sand-bath. This experimental set-up has helped to eliminate sedimentation because the evaporation of solvent is faster towards the bottom of the growth vial.

The general consensus in the literature is that as the growth temperature is increased to above 60˚C the growth rate becomes too fast and the films demonstrate more cracking (44). However, at elevated growth temperatures the number of defects will be reduced since the spheres have more kinetic energy to explore possible lattice sites (45). These topics will be discussed further in chapter 6.

5.2.2 Relative Humidity

The R.H. during film growth is an important factor because it will also affect the solvent evaporation rate (44). However, there is a lack of experimental evidence in the literature for the effect of R.H. during growth and the few results reported are often contradictory. In one case a temperature of 21˚C and R.H. of 90-95% is quoted to be optimum for growth (106) whereas Kuai *et al* (44) have suggested that an R.H. of ~70% gives best crystalline quality. Reports in the literature generally do not describe how the R.H. has been measured/defined except for the work reported by McLachlan *et al* (6) who suggest an optimum value of 10-20% for the best film quality.

However it can be hypothesised that higher R.H. conditions will allow favourable high temperature conditions to be utilised while achieving a slower growth rate. Consequently since cracking is a result of the shrinkage of spheres during the drying process (36,122) or to drying induced tension (6,126), the amount of cracking should be reduced.

5.2.3 Colloidal Concentration

In the literature the terms colloidal concentration and volume fraction are often interchanged and this approximation can be made since the density of polystyrene (ρ=1.008 g/cm^3) is close to that of water (ρ=1 g/cm^3). Colloidal concentration is one of the easiest growth parameters to control and, since a numerical value is assigned, comparisons can be made with published data.

As the colloidal concentration increases the film thickness increases (24,36,44,122). Based on the film formation conditions used by Dimitrov and Nagayama (117) for the growth of monolayer films Colvin and co-workers (24) derived a theoretical relationship between film thickness and colloidal concentration (equation 5.1):

$$k = \frac{\beta L \phi}{0.605 d (1 - \phi)} \qquad \textbf{Equation 5.1}$$

, where k is the number of layers (or thickness), β is the ratio between the velocity of a particle in solution and the fluid velocity (taken to be 1), L is the meniscus height, ϕ is the volume fraction in solution and d is the particle diameter.

Equation 5.1 predicts a linear relationship between film thickness and colloidal concentration. This relationship is found experimentally for colloid concentrations in the range 0.1-3% (24,62). At concentrations above 4% the film quality is degraded and it has been reported that at concentrations >5% the adhesion of the film to the substrate decreases and the film delaminates from the substrate surface (6). For the formation of thicker films successive dip coatings are required (24) but it has been suggested that multiple re-immersions of the film causes damage to the film surface (6).

It can be argued that during the growth period there is a concentration gradient present. During the growth solvent evaporates from the system, the meniscus moves down and spheres are deposited onto the substrate. Therefore the concentration of spheres will

change during evaporation, becoming more concentrated as the growth proceeds, which may have an effect on the film thickness. In order to overcome this problem Gu *et al* (36) have developed a technique whereby the substrate is mechanically lifted out of the suspension at constant speed instead of relying on solvent evaporation. Films in the range 1-30 layers have been reported by varying the lifting speed in the range 0.1 μm/s to 1.56 μm/s (thickness is inversely proportional to the lifting speed). However the films grown by conventional vertical deposition have been reported to have uniform thickness (6,44).

5.2.4 Sphere Diameter

The diameter of the spheres used for self-assembly is important as is the deviation in the diameter. Sphere size affects the film thickness in a systematic way – for the same volume fraction a solution of smaller spheres produces a film of more layers than a solution of larger spheres (24), see equation 5.1. In this study one objective is the growth of self-assembled films with a stop-band in the visible spectral region and hence the sphere diameters investigated were in the range 200-700 nm. The diameter of the spheres also influences the stability of the colloidal suspension because as the spheres increase in diameter the onset of sedimentation occurs.

With regard to the deviation in sphere size, the results are well understood and documented – a small sphere size deviation is desirable for any system where close packing is required not just vertical deposition. From early publications a standard deviation <8% (24) was suggested to be acceptable for well ordered film formation but more recently this figure has been lowered to <4% (45,60,68,121,122).

5.3 Experimental procedure

A temperature stable incubator (±0.2˚C) was used for the growth of all films during the course of this project and the incubator was always allowed at least twenty-four hours to stabilise prior to the film growth. The incubator was placed out of the way of draughts and sits on a vibration-free table.

The experiments discussed in this chapter were carried out in the temperature range 55-65˚C with the R.H. between 10-30% regardless of temperature. The R.H. is defined as the amount of water vapour present in the air divided by the maximum amount of water vapour the air can hold at a given temperature (6). In order to monitor the conditions within the incubator during growth the temperature and R.H. values were recorded using a data logger (Dicksonware TM125) situated inside the incubator. A typical graph of the variation in temperature and R.H. for a growth cycle is illustrated in figure 5.2.

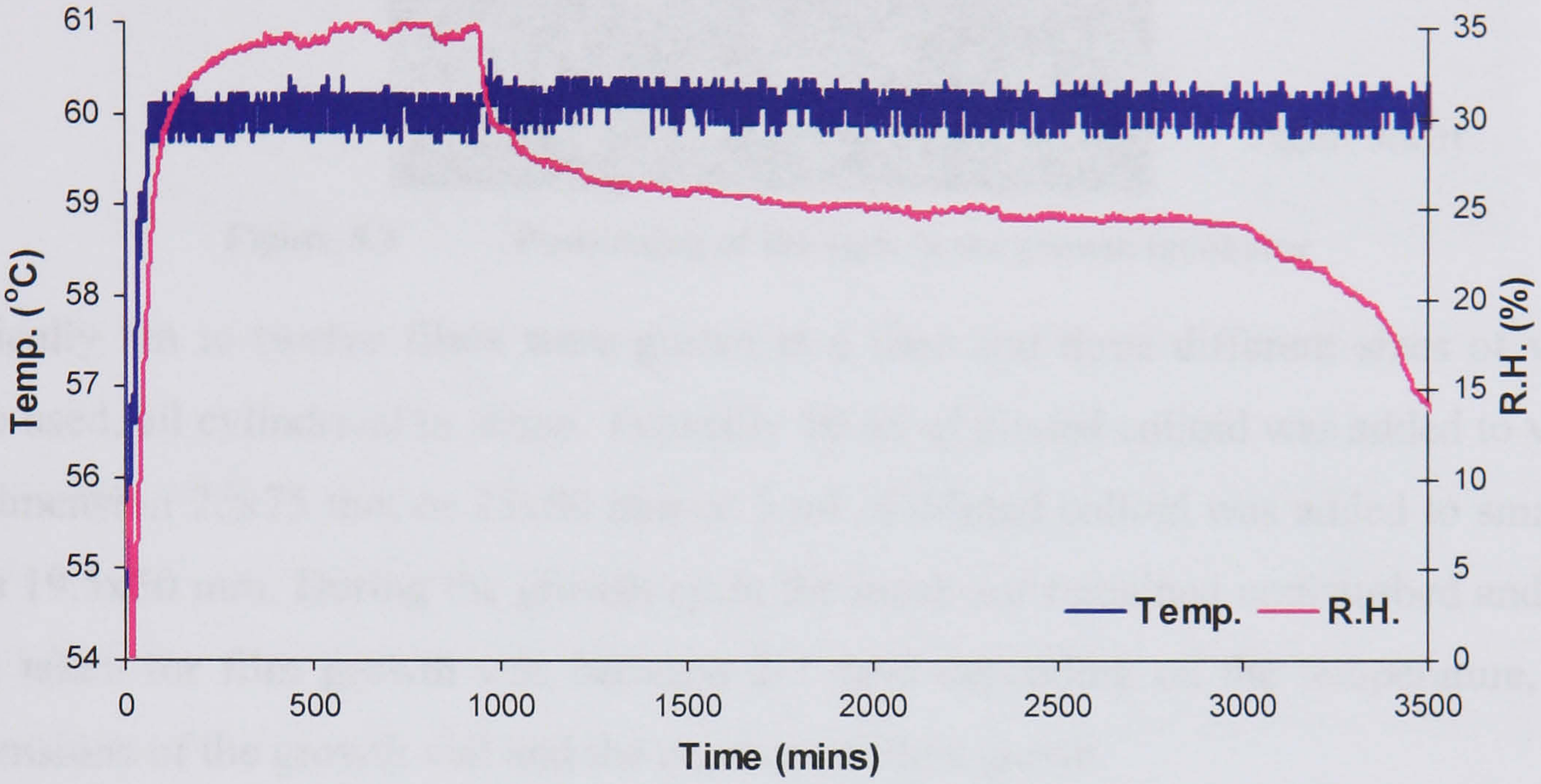


Figure 5.2 Profile of the temperature and R.H. during a typical growth cycle

When the samples are introduced into the incubator there is a fall in temperature of approximately 6˚C. During the first 90 minutes of the growth process the temperature stabilises to the preset value. The R.H. also rises due to the evaporation of water from the growth vials. During the growth period the R.H. gradually falls due to the solvent loss from the enclosed system.

Growth on both glass and indium tin oxide (ITO) substrates was investigated. The substrates were cut to approximately 10x50 mm. The substrates were cleaned with sequential washing (ten minutes each under sonication) in Opticlear™, acetone, methanol and de-ionised water. The substrates were then blow-dried in a stream of nitrogen before use.

The colloidal suspensions were placed in an ultrasonic bath for 10-15 minutes to disperse any aggregates. For the results presented in this chapter only the colloidal concentration was varied and once the colloid had been diluted with de-ionised water to the required concentration it was sonicated for a further 10-15 minutes. Immediately

after this the diluted colloidal suspension was added to the growth vials, the clean substrates were inserted and the vials were placed into the incubator on a metal sheet to ensure a constant temperature gradient (figure 5.3).

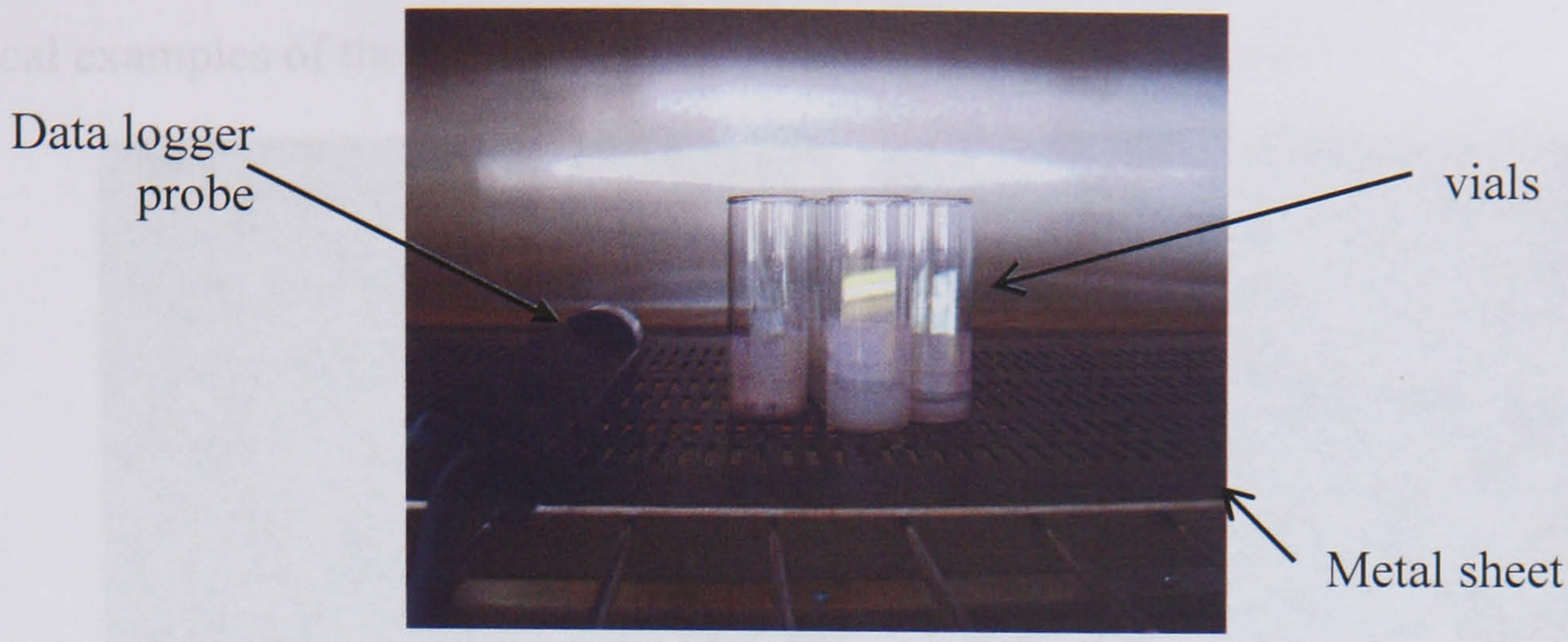


Figure 5.3 Positioning of the vials in the growth incubator

Typically ten to twelve films were grown at a time and three different sizes of vials were used, all cylindrical in shape. Typically 10 ml of diluted colloid was added to vials of dimension 25x75 mm or 25x50 mm or 5 ml of diluted colloid was added to smaller vials 19.5x50 mm. During the growth cycle the incubator remained undisturbed and the time taken for film growth was between 2-3 days depending on the temperature, the dimensions of the growth vial and the number of films grown.

5.4 Analysis

Once grown, the films were analysed using a range of complementary techniques in order to characterise their microscopic and macroscopic structure and properties. The methods employed were optical microscopy, reflectance spectroscopy and scanning electron microscopy (SEM).

The growth rates for the films with different growth parameters are discussed in detail in the following chapter. However it was found that for the three different growth vials the average evaporation rates changed depending on the dimensions of the growth vial with the fastest evaporation from the 25x50 mm vial and the slowest from the 19.5x50 mm vial.

5.4.1 Optical Microscopy

The films were observed using an optical microscope equipped with a CCD camera. Typical examples of the optical images obtained are shown in figure 5.4.

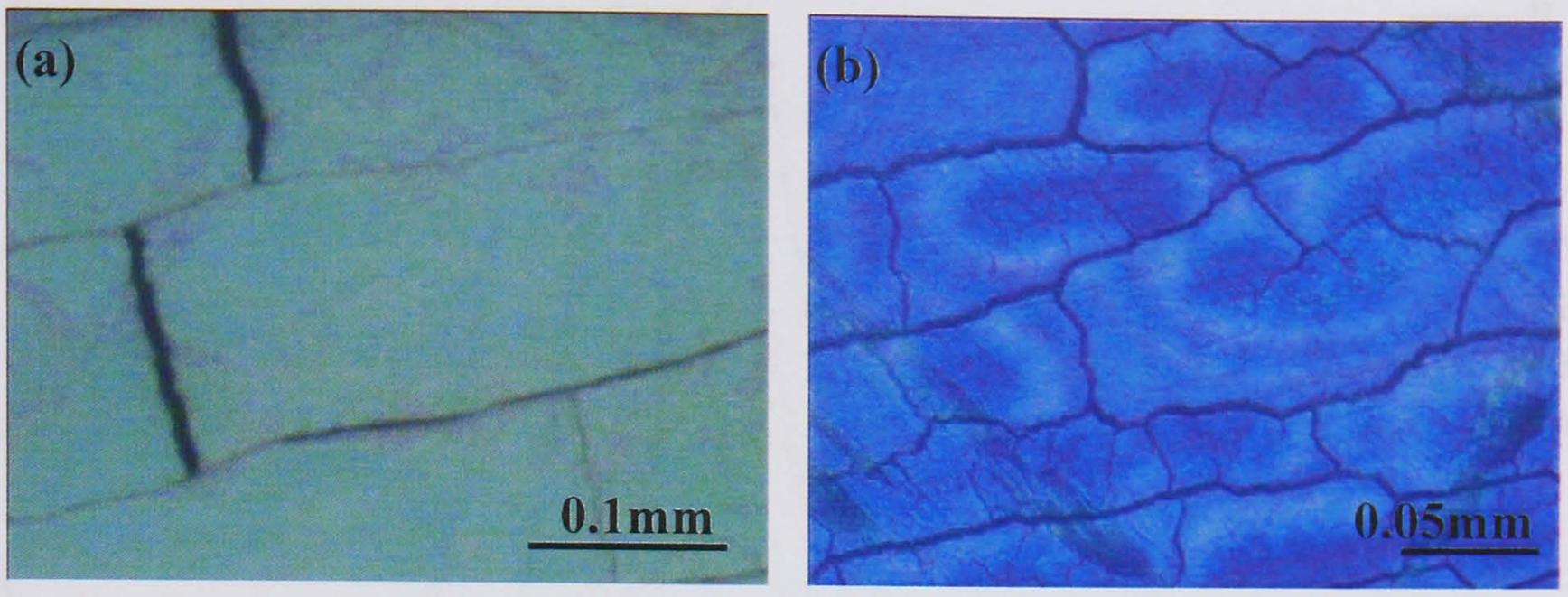


Figure 5.4 **Optical microscope images from a film composed of (a) 408 nm and (b) 200 nm spheres**

The colour change of the reflected light is a result of the different sphere sizes and is direct evidence of the films acting as a photonic crystal. It is apparent that there are a large number of cracks on the surface of each film and that the number of cracks is different in the samples. Although it was previously suggested that the cracks formed were due to exposure of the films to the high vacuum of the SEM (24) the use of optical microscopy allows the evaluation of cracking immediately after solvent evaporation and without any sample preparation. Thus the cracking found in thin film PCs must be due to a combination of the shrinkage of the polystyrene spheres during the drying process (36,122) and drying induced tension (6,126).

5.4.2 Reflectance Spectroscopy

The optical properties of the films were characterised using both transmission and reflectance spectroscopy, which are equivalent in the wavelength range 370-1400 nm since there are no appreciable absorptions for polystyrene (46). However at wavelengths beyond the stop-band the transmission is strongly reduced due to diffuse scattering (12) which can alter the position and width of the stop-band. In addition as the angle of incidence increases away from the normal the Bragg dip in transmission rapidly disappears but the peak in reflection can still be clearly resolved (13). However the use of transmission spectroscopy allows normal angle incidence measurements to be carried out. Consequently the two techniques should be considered complementary and both should be used to gain maximum information from the thin film PCs. However, in

practice reflectance spectroscopy was used routinely. The angle resolved spectra shown in figure 5.5 show results for a thin film characterised by both reflection and transmission spectroscopy.

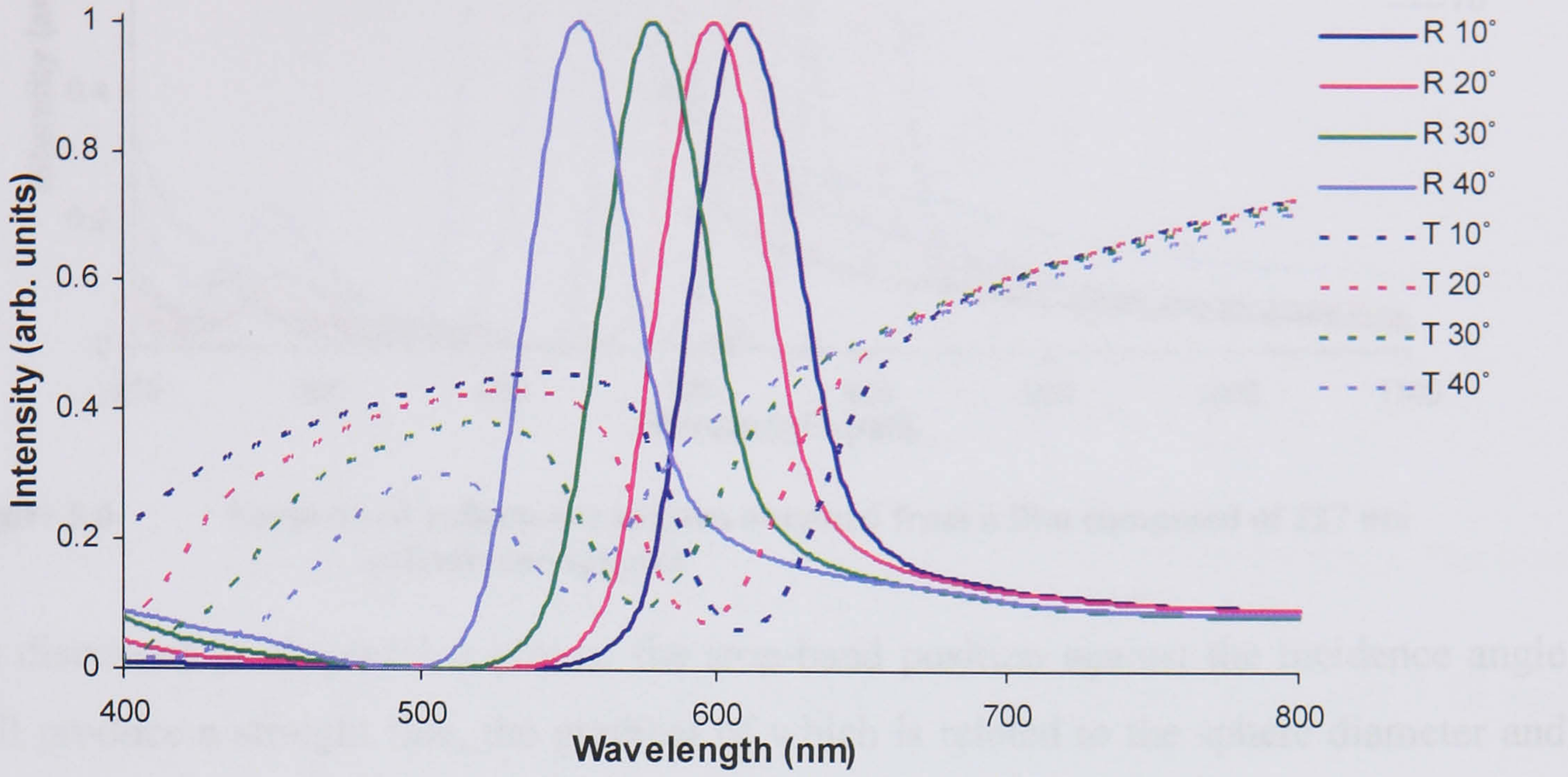


Figure 5.5 **Reflectance (R) and transmission (T) spectra for a film composed of 254 nm spheres**

The wavelength positions of the peak/troughs for the reflectance and transmission spectra illustrated in figure 5.5 are summarised in table 5.1.

Angle of incidence (°)	Reflectance peak (nm)	Transmission dip (nm)
10	609	609
20	599	595
30	579	575
40	554	549

Table 5.1 **Wavelengths of Bragg reflection peaks for reflectance and transmission spectra for a film composed of 254 nm spheres**

The data presented in table 5.1 illustrates the complementarity of reflectance and transmission spectroscopy since the difference in peak/dip position between the two methods is within the experimental error of ±7 nm (see chapter 2 for explanation).

The plot shown in figure 5.6 shows an example of typical angle resolved reflectance measurements for a synthetic opal sample composed of 327 nm polystyrene spheres.

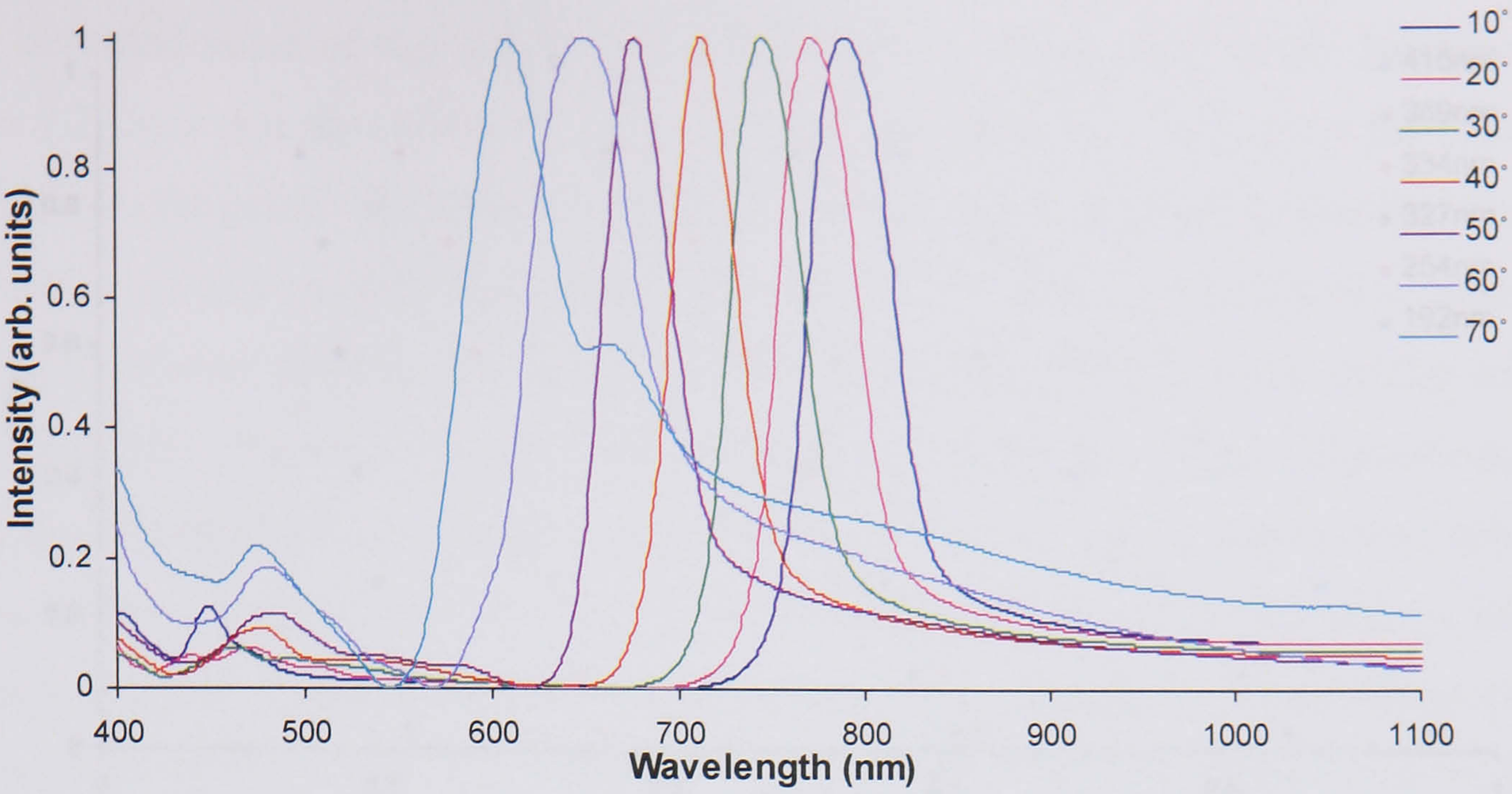


Figure 5.6 Normalised reflectance spectra obtained from a film composed of 327 nm polystyrene spheres

As discussed in chapter 1 a plot of the stop-band position against the incidence angle will produce a straight line, the gradient of which is related to the sphere diameter and the y-intercept related to the effective refractive index (n_{eff}). This assumes that the reflection peaks are a result of constructive interference of the reflected waves from consecutive (111) planes.

In order to compare the sphere diameter calculated from reflectance spectroscopy with the TEM measured diameter the following study was conducted. A series of thin films were grown from the batch of colloids illustrated in figure 3.9. For each colloid three films were grown at the same growth conditions and volume fraction. Angle resolved reflectance measurements were carried out for each film and the average stop-band positions were calculated for each colloid at each angle of incidence. A plot of the average stop-band position against the angle of incidence for each colloid is shown in figure 5.7.

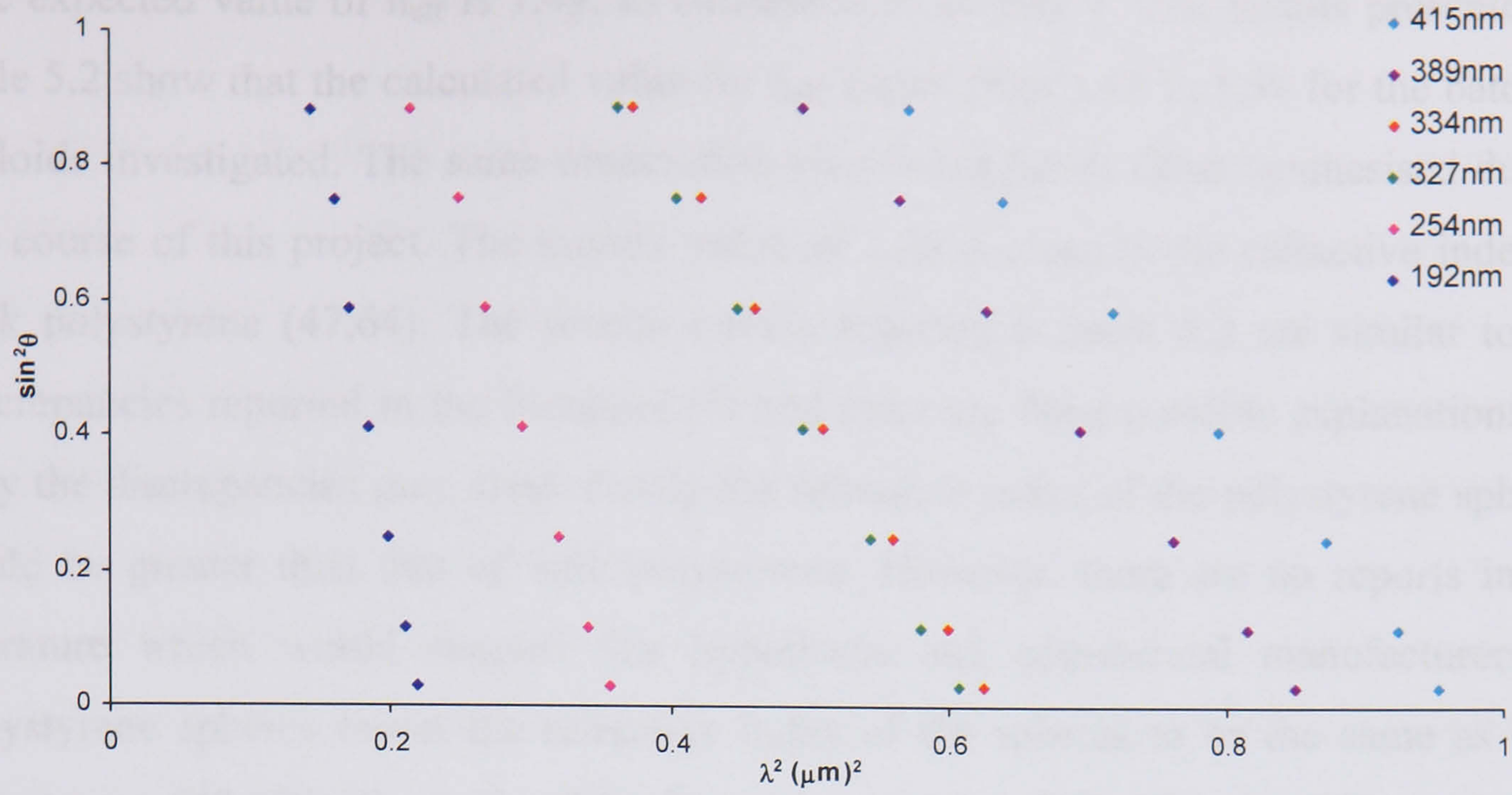


Figure 5.7 **Linear plots obtained by analysis of the position of the reflectance peaks. The plots are reference according to the TEM measured diameter**

The data presented for each colloid was manipulated as described in chapter 1.12 and the results for the sphere diameter and n_{eff} are summarised in table 5.2.

TEM	REFLECTANCE SPECTROSCOPY		
Diameter (nm)	**d_{111} (nm)**	**Diameter (nm)**	**n_{eff}**
192±5	148±6	181±8	1.59±0.05
254±4	200±14	245±13	1.50±0.09
327±6	266±3	326±4	1.47±0.01
334±5	269±5	330±4	1.48±0.02
389±5	320±3	392±3	1.45±0.01
415±9	336±4	412±6	1.47±0.02

Table 5.2 **Data calculated from the modified Bragg law for thin films of varying diameter**

Table 5.2 demonstrates that there is good correlation between the diameter of the spheres calculated from reflectance spectroscopy and TEM. The diameter calculated optically is generally smaller than the size from TEM which is consistent with the argument that the colloidal spheres shrink slightly during the process of film formation. The TEM technique used to measure the diameter of the colloidal spheres is a representative measurement of the sample since only ~200 spheres are investigated whereas the optical data is collected from a large (~0.28 mm^2) area and is therefore an average over many thousands of spheres. The fact that the sphere diameter calculated from reflectance spectroscopy is close to that measured by TEM is important for the results which will be discussed in chapter 7.

The expected value of n_{eff} is 1.44, as calculated in chapter 1. The results presented in table 5.2 show that the calculated value for n_{eff} varies from 1.45 to 1.59 for the batch of colloids investigated. The same observation was found for all films synthesised during the course of this project. The highest value of 1.59 is close to the refractive index of bulk polystyrene (47,64). The results for n_{eff} reported in table 5.2 are similar to the discrepancies reported in the literature (6) and there are three possible explanations for why the discrepancies may arise. Firstly the refractive index of the polystyrene spheres could be greater than that of bulk polystyrene. However, there are no reports in the literature which would support this hypothesis and commercial manufacturers of polystyrene spheres report the refractive index of the spheres to be the same as bulk polystyrene (47,127). Secondly if the films have a higher filling fraction of polystyrene, *i.e.* >74% of the unit cell occupied by spheres, the value of n_{eff} would be different. This would be possible if the spheres could touch more than a point contact, for example by deformation due to high drying temperatures (34). However, the films are grown at temperatures well below the glass transition temperature of polystyrene (T_g~120°C) and therefore this hypothesis is probably not correct. The final explanation involves the variation in refractive index with wavelength, as discussed in chapter 1. Figure 5.8 shows a plot of how the refractive index of polystyrene varies over the wavelength region 400-1100 nm, as calculated by the parameters described by Ma *et al* (46).

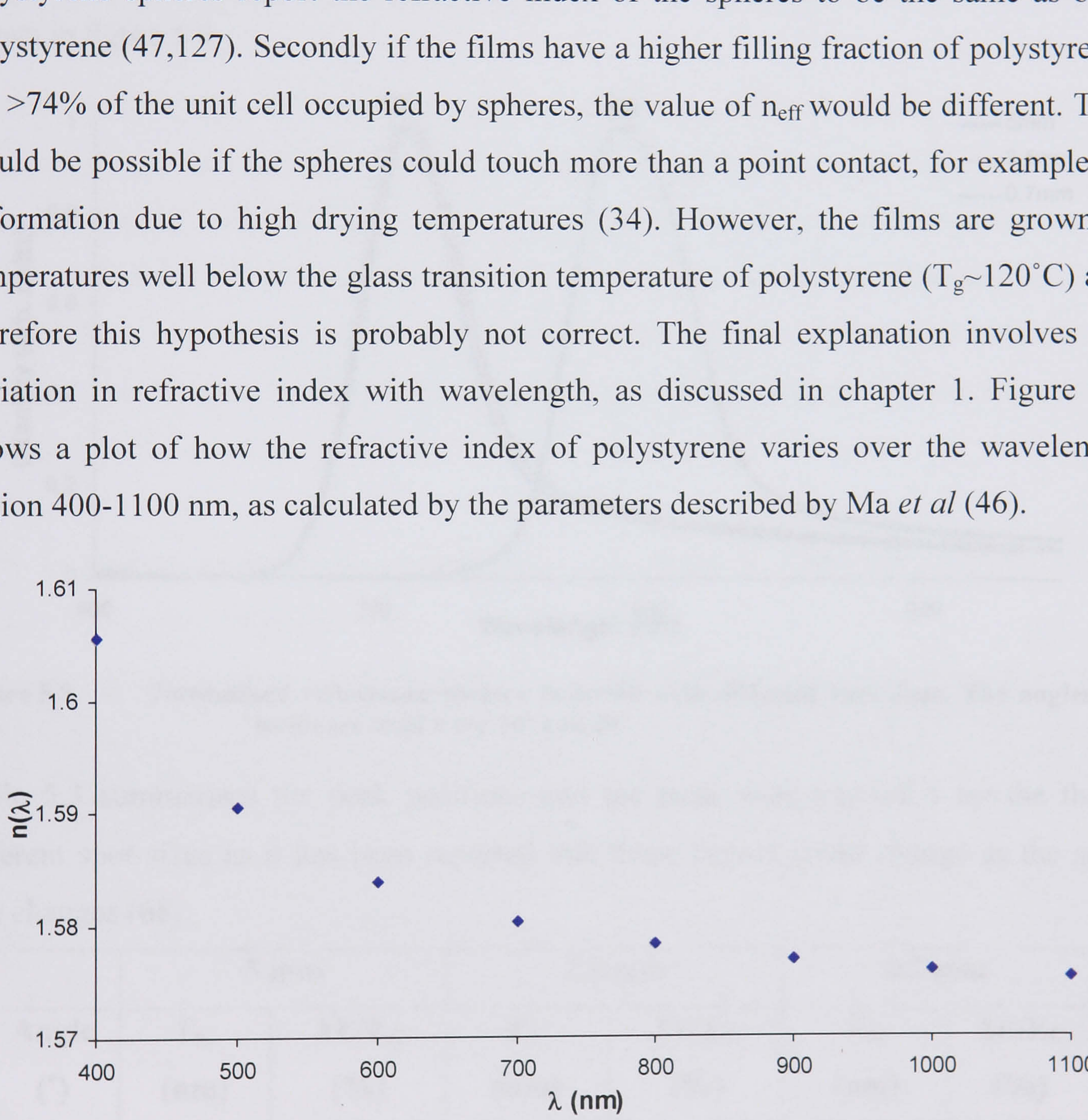


Figure 5.8 Variation in refractive index of polystyrene in the wavelength region 400-1100 nm

This factor may account for variation between theoretical and experimental observations and the general trend shown in table 5.2 is supported since as the stop-band position shifts to longer wavelength the calculated n_{eff} decreases.

5.4.2.1 Spot size variation

The size of the illumination spot used to obtain optical spectra has been reported to be important. When the spot size is increased and the sample demonstrates short range order it is reported that there will be a broadening of the stop-band accompanied by a loss in intensity (68). A smaller spot size probes a smaller sample region and, if decreased enough, will eventually reach an area where a regular, well defined region of spheres can be measured. Thus a more pronounced stop band is expected. Experimentally the spot size was varied between a big spot (~5 mm), a medium spot (~2.5 mm) and a small spot (~0.7 mm) and the corresponding reflectance spectra are shown in figure 5.9.

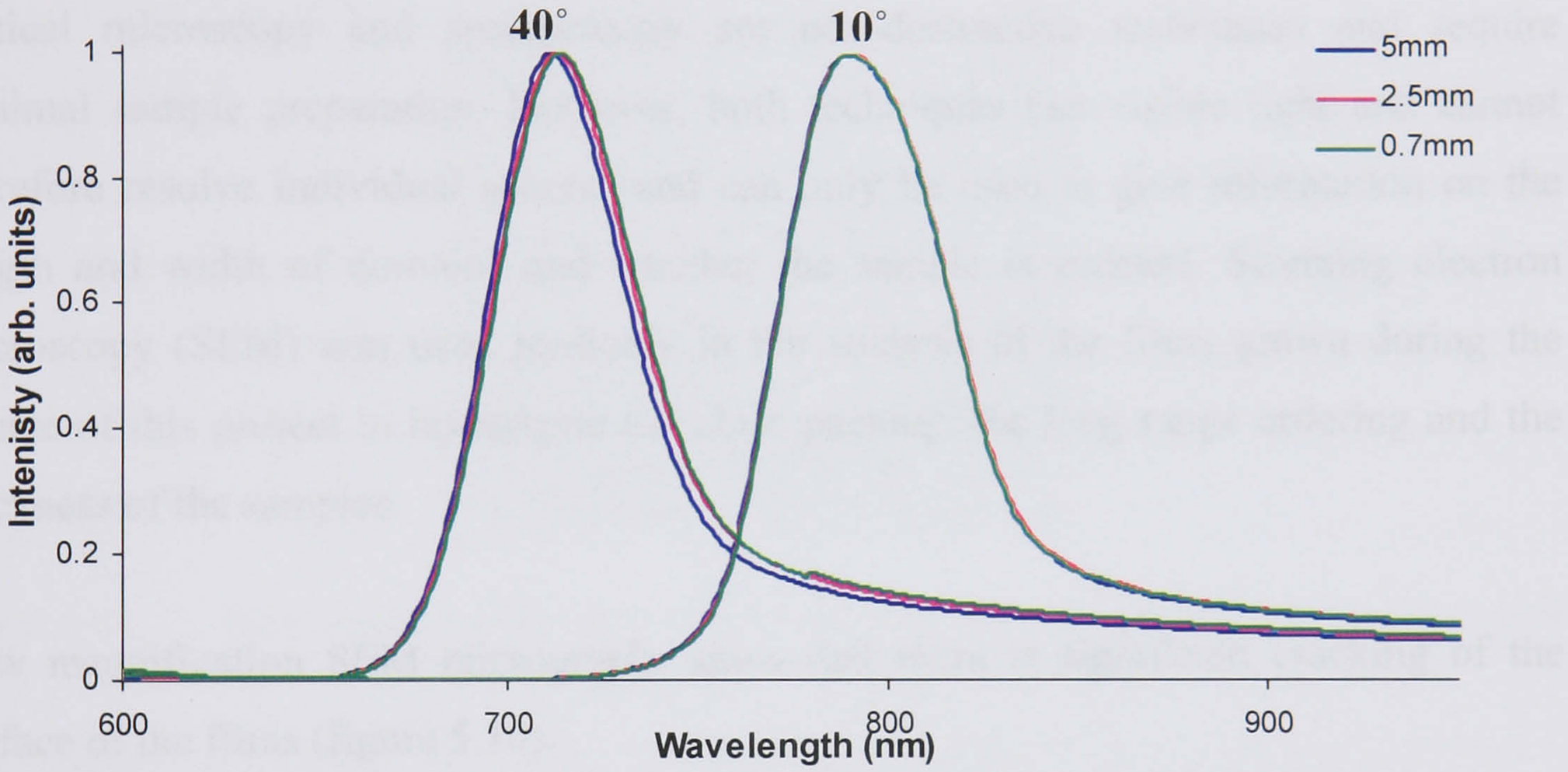


Figure 5.9 **Normalised reflectance spectra collected with different spot sizes. The angles of incidence used were 10° and 40°**

Table 5.3 summarises the peak positions and the peak widths ($\Delta E/E_c$) for the three different spot sizes as it has been reported that these factors could change as the spot size changes (68).

	5 mm		2.5 mm		0.7 mm	
Angle (°)	E_C (nm)	$\Delta E/E_C$ (%)	E_C (nm)	$\Delta E/E_C$ (%)	E_C (nm)	$\Delta E/E_C$ (%)
10	789	6.8	790	6.7	790	6.6
20	771	6.5	773	6.6	773	6.6
30	745	6.3	747	6.6	748	6.6
40	711	6.2	713	6.3	714	6.4

Table 5.3 **Comparison of the wavelength position and $\Delta E/E_c$ for spectra gathered with different spot sizes**

The results presented in figure 5.9 and table 5.3 show that changing the spot size has no appreciable effect on the position or width of the reflection peaks which similar to the observations made by Goldenburg *et al* (123). The smallest spot size investigated (~0.7 mm) far exceeds the average domain width of the films and therefore the long range ordering present in the film samples prevents any shift in the reflected wavelength. The size of the ordered array is thought to be determined by the cracks formed during the drying process and plays a significant role in the optical properties of the films. Hence the reduction in cracking is of great importance.

5.4.3 Scanning Electron Microscopy

Optical microscopy and spectroscopy are non-destructive techniques and require minimal sample preparation. However, both techniques use visible light and cannot therefore resolve individual spheres and can only be used to give information on the length and width of domains and whether the sample is ordered. Scanning electron microscopy (SEM) was used routinely in the analysis of the films grown during the course of this project to investigate the close packing, the long range ordering and the thickness of the samples.

Low magnification SEM micrographs show that there is significant cracking of the surface of the films (figure 5.10).

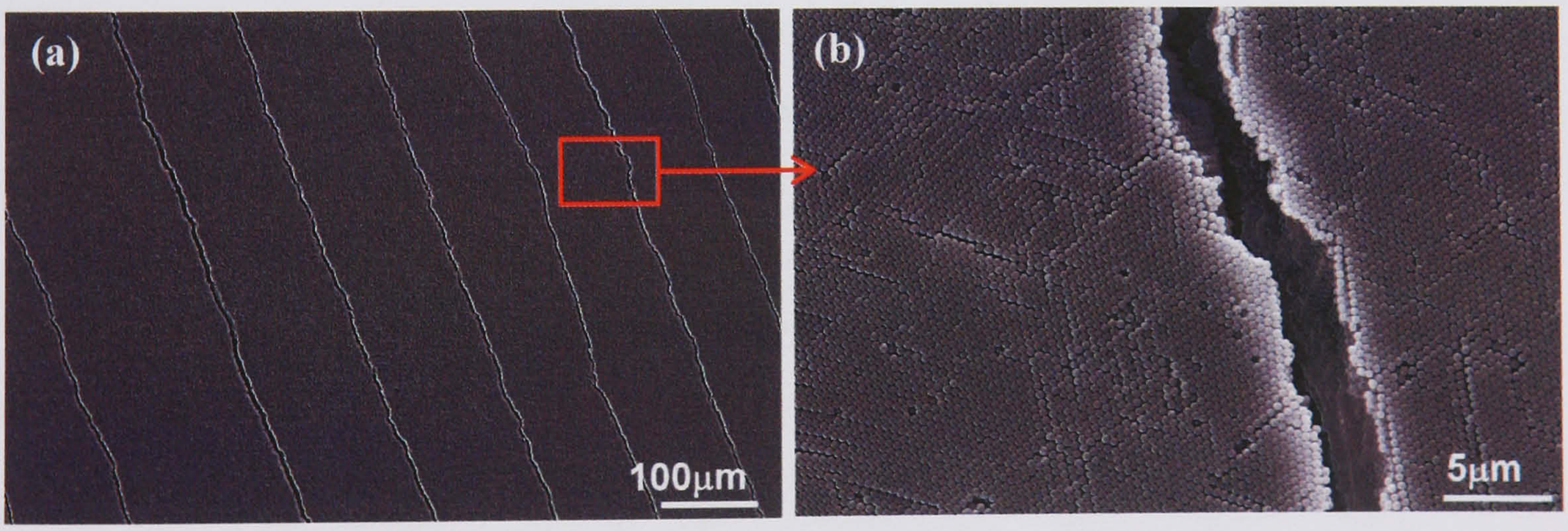


Figure 5.10 SEM micrographs showing (a) surface cracking and (b) crack propagating through the film thickness

It has been hypothesised that the observed cracks occur due to drying induced tension (6,126) or the shrinkage of the polystyrene spheres during the drying process (36,122). The distance between cracks, or the domain width, for the films grown in this chapter was typically 70-100 μm with the crack itself approximately 2 μm wide. Results in the following chapter will investigate the effect of changing the experimental growth

conditions on the domain width. The cracks which are visible in the micrographs presented in figure 5.10 are parallel to the growth direction of the film, *i.e.* perpendicular to the meniscus, and occur along the close packed <110> directions (6). The registry of the hexagonal packing is preserved across the crack (figure 5.10(b)), similar to the observations reported by Colvin and co-workers (24). It can also be argued that the presence of any large spheres may facilitate cracking. This would correlate with increased strain in the crystal structure during drying and therefore, by minimising the surface energy of the system, the surface becomes more cracked.

Higher magnification SEM micrographs of the film surface establish that the films are well ordered, as shown in figure 5.11.

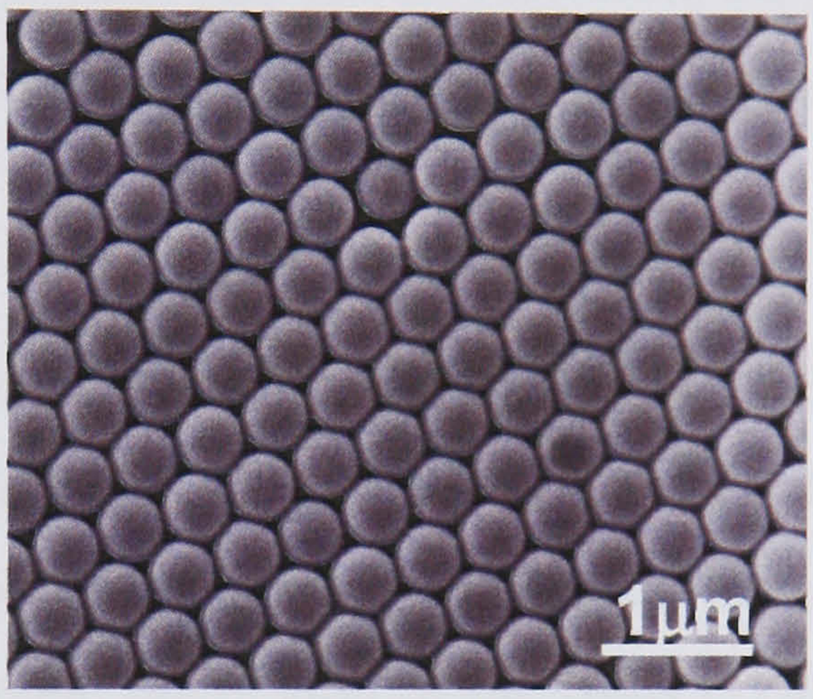


Figure 5.11 High magnification SEM micrograph showing close packing of the polystyrene spheres

The surface of the films show that the spheres are arranged in a close-packed array – either face centred cubic (fcc) or hexagonal close packed (hcp) – with each sphere touching six others in the same layer. SEM images of the top surface of the films cannot be used to distinguish whether fcc or hcp structures exists due to the difficulty in determining the angle of the cross-sectional view (24). A fluorescence microscopy technique has been used to determine the crystal structure and indicated that the layers stack in the ABC form, *i.e.* the fcc structure (36) which is consistent with the theoretical calculations conducted by Woodcock (38).

The thin film samples can be abraded or cleaved to permit viewing of the internal order of the close packed planes and to evaluate the film thickness (figure 5.12).

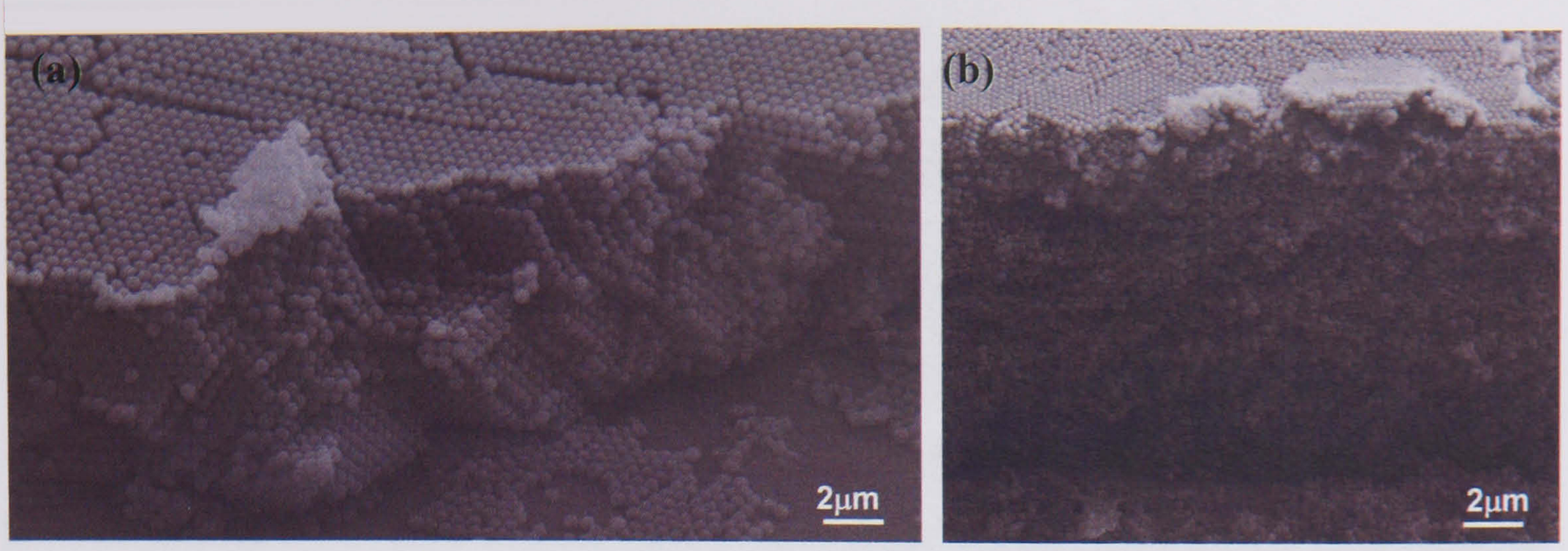


Figure 5.12 SEM images of films which have been cleaved to permit viewing of the internal order of the close packed planes

Analysis of the cross-sectional SEM images confirm that a <111> direction is perpendicular to the sample normal and the close packing extends through all the layers of the film. The majority of films were not cleaved since the process damages the fragile film and, as shown in figure 5.12(b), difficulties were encountered in cleaving along a close packed direction.

Two-dimensional Fast Fourier Transforms (FFTs) were used to evaluate the long range ordering of the thin films (6,24,36,123). FFTs are 2-D spatial frequency diagrams which can be considered to represent a surface diffraction pattern and can be indexed to determine the crystallographic orientation of the films (128). If a sample demonstrates short range order, weak spots and ring patterns are observed in the FFT compared to the higher order spots calculated for well ordered samples. Figure 5.13 shows a SEM image and the corresponding calculated FFT for a film surface.

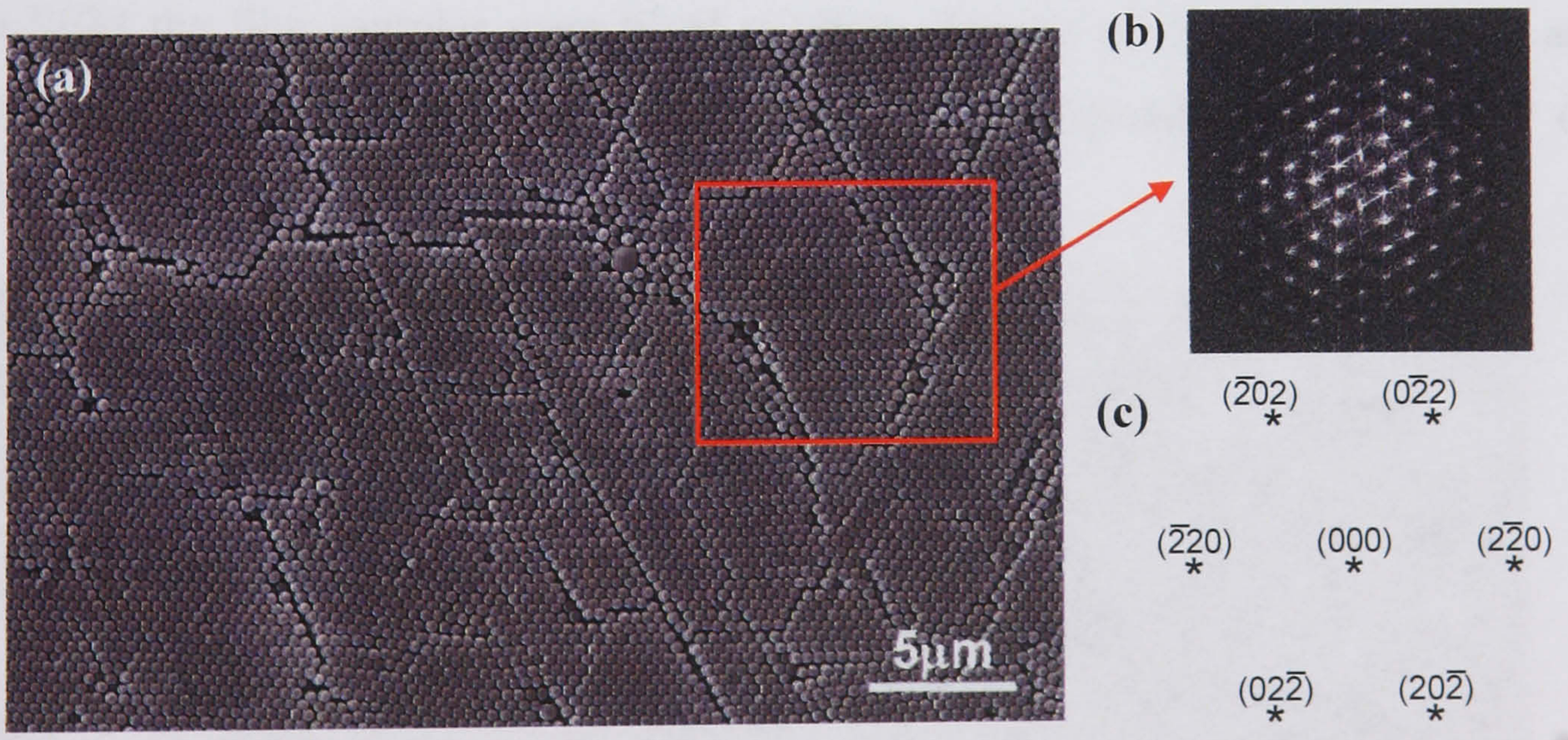


Figure 5.13 (a) SEM image of a film surface, (b) corresponding calculated FFT and (c) schematic illustration of the indexed diffraction pattern

The calculated FFTs show bright spots indicative of long range ordering. The angle between the centre point and the diffracted spots is equal to 60° indicating that the <111> direction is parallel to the sample normal. It has been reported that the long range ordering in the samples can be confirmed by investigating the rotation of the FFTs calculated from a sequence of SEM images (6,24). It has been published that over the entire length of a sample (~40 mm) the rotation of the <220> spots relative to the surface normal is ~5% (6) confirming that the crystallographic orientation of the film is preserved regardless of the presence of the drying cracks (121). This suggests that cracking occurs after the self-assembly procedure and during the drying process, in agreement with the work reported by Koh and Wong (129).

5.4.4 Thickness

Three complementary techniques were used to evaluate the thickness of the thin film PCs – SEM, reflectance spectroscopy and white light interferometry.

5.4.4.1 SEM

As mentioned previously in this chapter the thin films were cleaved to facilitate viewing of the internal planes and the thickness of the films. A clean scalpel blade was used to scrape a cross shape onto the films for SEM observation (figure 5.14(a)). Care was taken to ensure that all the layers of spheres had been removed down to the substrate. In the SEM the film samples were tilted to allow viewing of the internal planes and the thickness measurements were made from the corresponding micrographs (figure 5.14(b)).

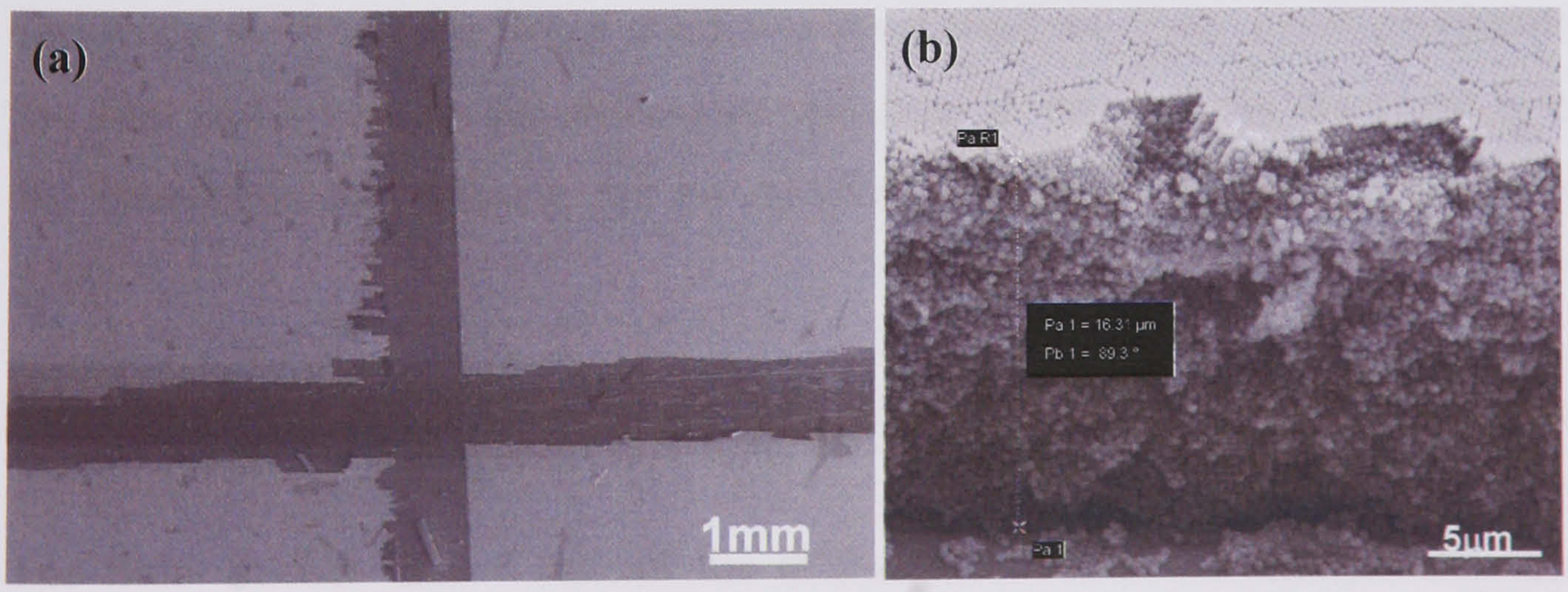


Figure 5.14 **SEM micrographs showing (a) cross abraded on film surface and (b) measured film thickness using the SEM**

For the thinnest films the thickness could be calculated by counting the number of layers of spheres (*e.g.* figure 5.12(a)) but this technique proved difficult when the films become thicker. In these cases the microscope magnification was calibrated and the measurement tool in the SEM was used to measure the thickness (figure 5.14(b)). Images presented in the literature used to measure film thickness or to show the ordering of the internal planes (6,24,36,37) show that the films have been cleaved along a close packed direction. However difficulties were encountered in this project cleaving the films along a close packed direction resulting in the images shown in figures 5.12(b) and 5.14(b).

5.4.4.2 Reflectance Spectroscopy

An alternative and non-destructive method for measuring thin film thickness is an optical technique which uses Fabry-Perot fringe positions to analyse the film thickness (24). The Fabry-Perot fringes are located on either side of the main refection peak and confirm that the films are of high crystal quality (24,61,123). The disadvantage of using the position of the Fabry-Perot fringes to calculate film thickness is that only thicknesses <8 μm can be measured.

The Fabry-Perot fringes result from interference between reflections from the top surface of the film and the underlying substrate. With reference to Bragg's law (equation 5.2) the presence of the fringes can be explained.

$$n\lambda = 2d_{111}\sqrt{n_{eff}^2 - \sin^2\theta} \qquad \textbf{Equation 5.2}$$

In a typical reflectance measurement the wavelength, λ, is scanned at each angle of incidence, θ. When the Bragg condition is satisfied the light cannot propagate through the film and a peak in the reflectance spectrum is obtained. As discussed in chapter 1 the interplanar d_{111} spacing can be calculated provided λ and θ are known (equation 5.3).

$$d_{111} = \frac{n\lambda}{2\sin\theta} \qquad \textbf{Equation 5.3}$$

For films thicker than 8 μm all the diffraction is from the consecutive d_{111} planes. However, if the film thickness is below 8 μm the incident beam will penetrate the entire sample and also be reflected from the substrate. Thus, there are two components to the reflectance spectrum. The first component arises from reflection from the d_{111} planes of

the film, similar to the case for thicker films, and has only one solution for λ, the main reflection peak. The second component manifests itself as a series of Fabry-Perot fringes on either side of the main reflection peak arising from reflections between the substrate and the specimen surface. The distance between the film surface and the substrate, *i.e.* the thickness of the film, T, must be an integer number of interplanar spacings. The thickness of the film is sufficiently large that multiple solutions for equation 5.2 can exist, which is observed in the reflectance spectrum as a series of fringes on either side of the main reflection peak. A schematic illustration of the origin of Fabry-Perot fringes is shown in figure 5.15.

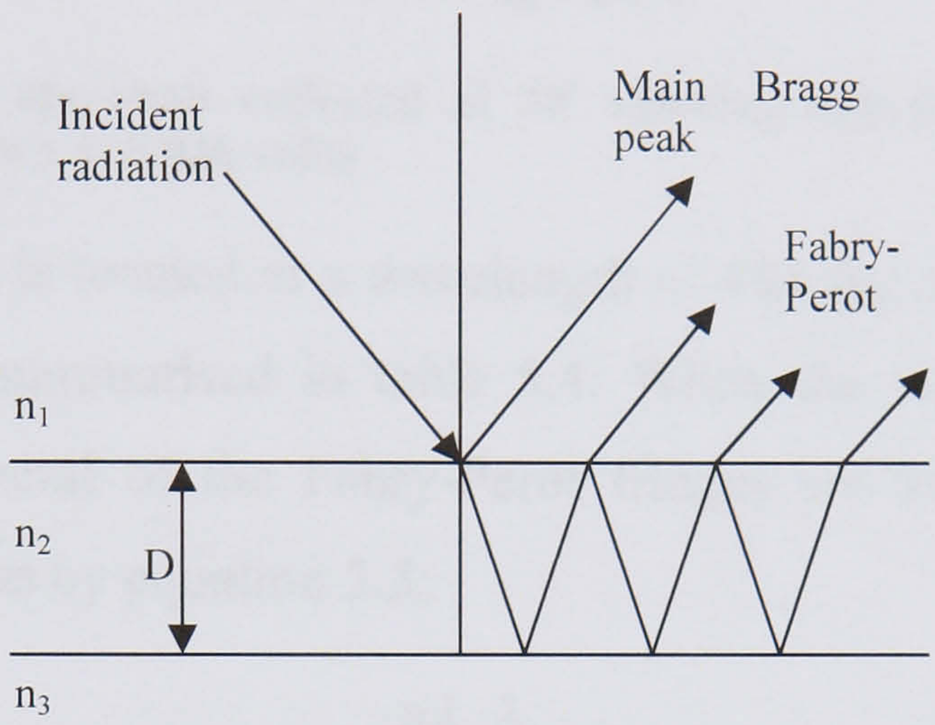


Figure 5.15 Schematic illustration of the origin of the main reflection peak and Fabry-Perot fringes where n_1 is air, n_2 is polystyrene and n_3 is glass.

Therefore, by replacing d_{111} in equation 5.3 with an integer number of d_{111} the thickness of the sample can be calculated.

$$D = \frac{\lambda}{2\sin\theta} \qquad \textbf{Equation 5.4}$$

The reflectance spectra obtained for films grown with a low colloidal concentration demonstrate a well defined maximum reflection peak followed by a series of Fabry-Perot peaks, as shown in figure 5.16.

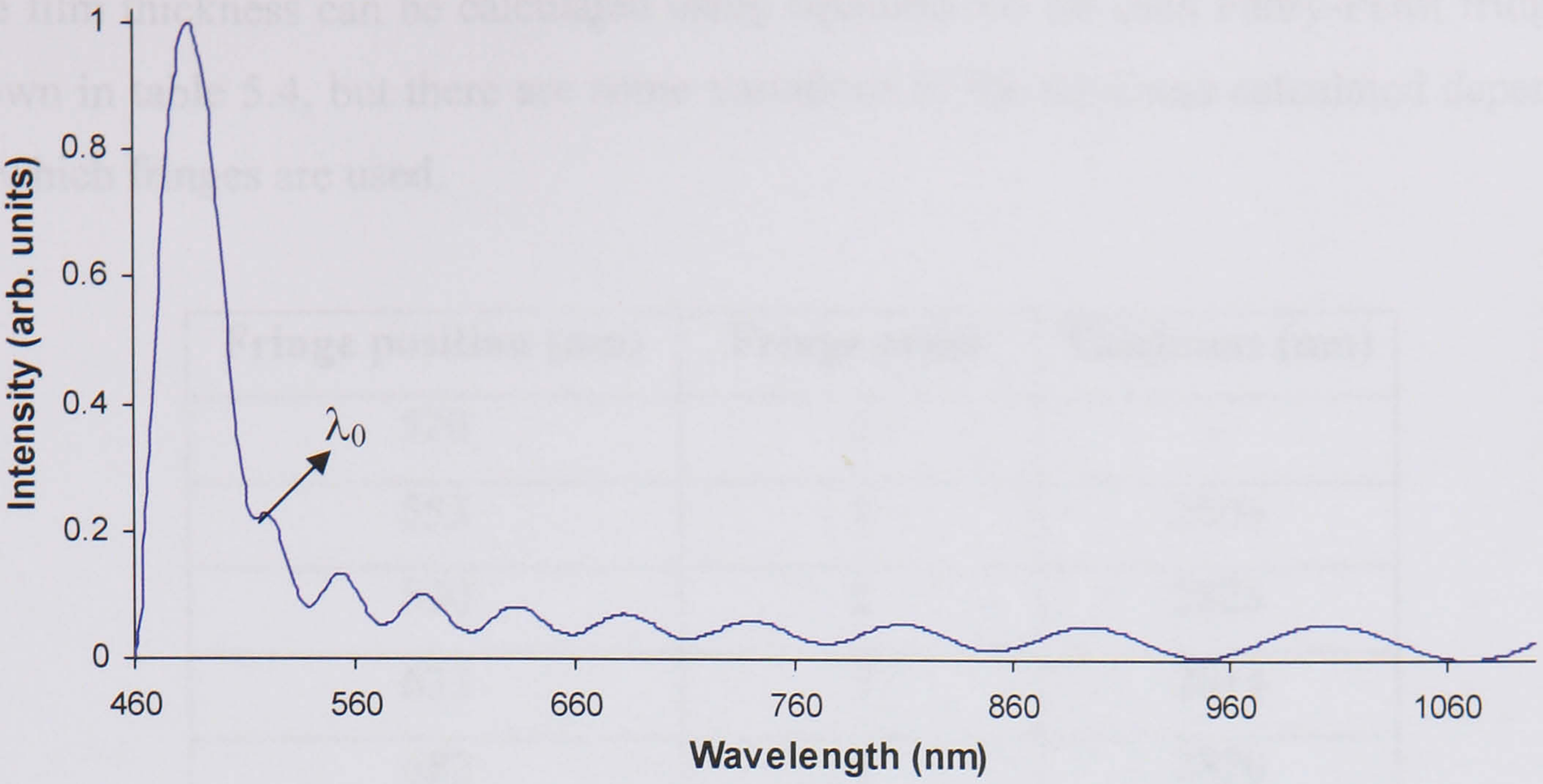


Figure 5.16 Reflectance spectrum collected at 20° showing Fabry-Perot fringes for a film grown at 0.036 vol%

The main reflection peak is located at a wavelength of 484 nm and the positions of the Fabry-Perot fringes are summarised in table 5.4. When the wavelength of the main reflectance peak and several of the Fabry-Perot fringes are known it is possible to calculate the film thickness by equation 5.5;

$$T = \frac{p\lambda_p\lambda_0}{2n_{eff}(\lambda_0 - \lambda_p)} \qquad \textbf{Equation 5.5}$$

where T is the film thickness, p is an integer number of consecutive maxima (start numbering at zero), λ_0 is the fringe adjacent to the main reflection peak, λ_p is the pth maxima and n_{eff} is the effective refractive index.

Colvin and co-workers (24) have shown that the thicknesses calculated from the position of Fabry-Perot fringes at normal incidence are close to those obtained from SEM analysis. Equation 5.5 can be modified to take into account the angular dependence, as demonstrated by equation 5.6, allowing the position of the Fabry-Perot fringes from non-incident measurements to be used to calculate the thickness of the films formed in this project.

$$T = \frac{p\lambda_p\lambda_0}{2(\sqrt{n_{eff}^2 - \sin^2\theta})(\lambda_0 - \lambda_p)} \qquad \textbf{Equation 5.6}$$

Where all parameters have the same values as equation 5.5 and θ is the angle of incident light.

The film thickness can be calculated using equation 5.6 for each Fabry-Perot fringe. as shown in table 5.4, but there are some variations in the thickness calculated depending on which fringes are used.

Fringe position (nm)	Fringe order	Thickness (nm)
520	0	-
553	1	2806
590	2	2823
633	3	2814
682	4	2820
740	5	2816
809	6	2812
893	7	2806
1006	8	2773

Table 5.4 **Wavelength of Fabry-Perot fringes from reflectance spectra of a thin film composed grown at 0.036 vol% and calculated film thickness**

The range of thickness calculated for each fringe position is small but an average thickness can be calculated by plotting a graph of fringe order, p, versus $\frac{2\left(\sqrt{n_{eff}^2 - \sin^2\theta}\right)(\lambda_0 - \lambda_p)}{\lambda_p \lambda_0}$ (figure 5.17).

The plot is fitted to a straight line and the average thickness of the film is equal to the gradient of the line.

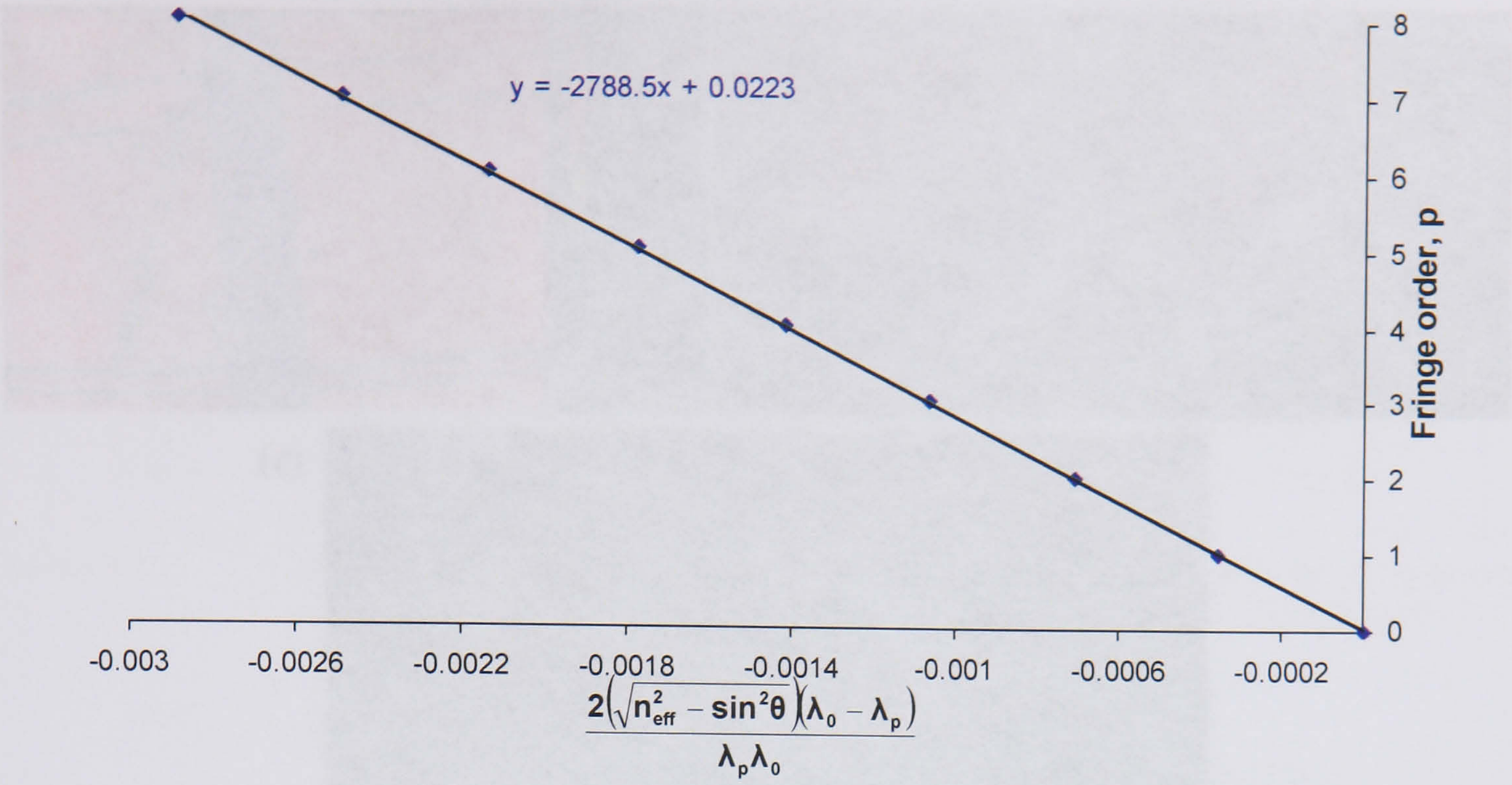


Figure 5.17 Straight line plotted to determine the film thickness from Fabry-Perot fringes

The line plotted in figure 5.17 has a negative gradient because the Fabry-Perot fringes have been measured from the right hand side of the main reflection peak. From the gradient of the line an average film thickness is found to be 2789 nm which is close to the individual calculated thicknesses outlined in table 5.4.

5.4.4.3 White light interferometry

The final method used to determine the thickness of the films formed is an interferometry based technique. A Newview Zygo white light interferometer was used which employs scanning white light to produce 3-D surface contour diagrams. This technique can be used to measure the topography of substrates, crack spacing and film thickness.

Compared to the time consuming SEM and optical methods, the interferometry technique is relatively simple. The film is prepared in the same manner as for SEM analysis, *i.e.* cleaved with a clean scalpel blade, and placed under the ZYGO microscope. The microscope is focussed until interference fringes are observed. Depending on the sample an appropriate scan length is chosen (100 μm for the thin films investigated) and the white light is scanned across the sample surface. A surface profile is built up, as shown in figure 5.18(a), due to the difference in the interference pattern between the sample surface and the reference arm of the microscope. The film thickness can be determined from the surface profile (figure 5.18(c)) by drawing a line across the surface profile (shown in figure 5.18(a)).

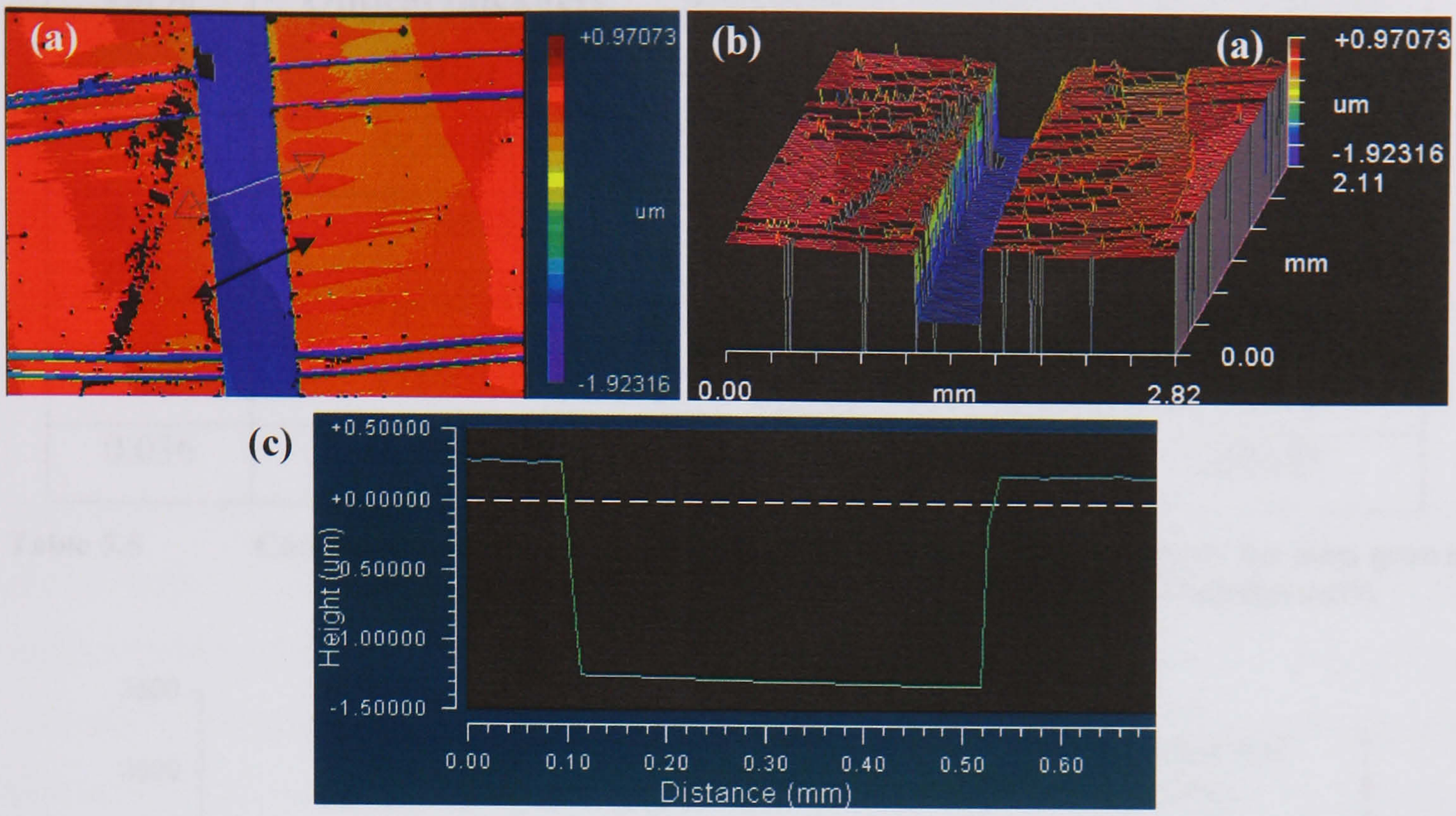


Figure 5.18 **Typical output file from the ZYGO showing (a) interference profile (b) 3-D oblique plot and (c) surface profile plot**

The main disadvantage with the ZYGO is that, because white light is used, individual spheres cannot be resolved. Since it cannot be guaranteed that cleaving the film will remove all the layers of spheres down to the substrate the accuracy of the Zygo is questionable because, unlike in the SEM, the layers of spheres cannot be counted.

5.4.4.4 Comparison

A series of thin films with volume fractions in the range 0.012-0.036 vol% were grown and their thickness was determined by SEM, Fabry-Perot fringes and white light interferometry. In the SEM method the number of layers was counted at various points of the film and an average was calculated. To obtain the actual film thickness the average number of layers was multiplied by the diameter of the colloidal spheres calculated by TEM (200 nm). Table 5.5 and figure 5.19 summarise the thicknesses of the films calculated using the three different measurement techniques.

vol%	Optical thickness (nm)	Microscopy thickness (nm)	Interferometry thickness (nm)
0.012	910±105	884±121	582±73
0.018	1286±158	1259±111	1217±84
0.024	1600±116	1756±181	1559±82
0.030	1956±167	2116±213	2024±103
0.036	2600±127	2966±268	2298±85

Table 5.5 **Comparison of the thickness calculated by three different methods for films grown with 200 nm spheres at concentrations in the range 0.012-0.036 vol%**

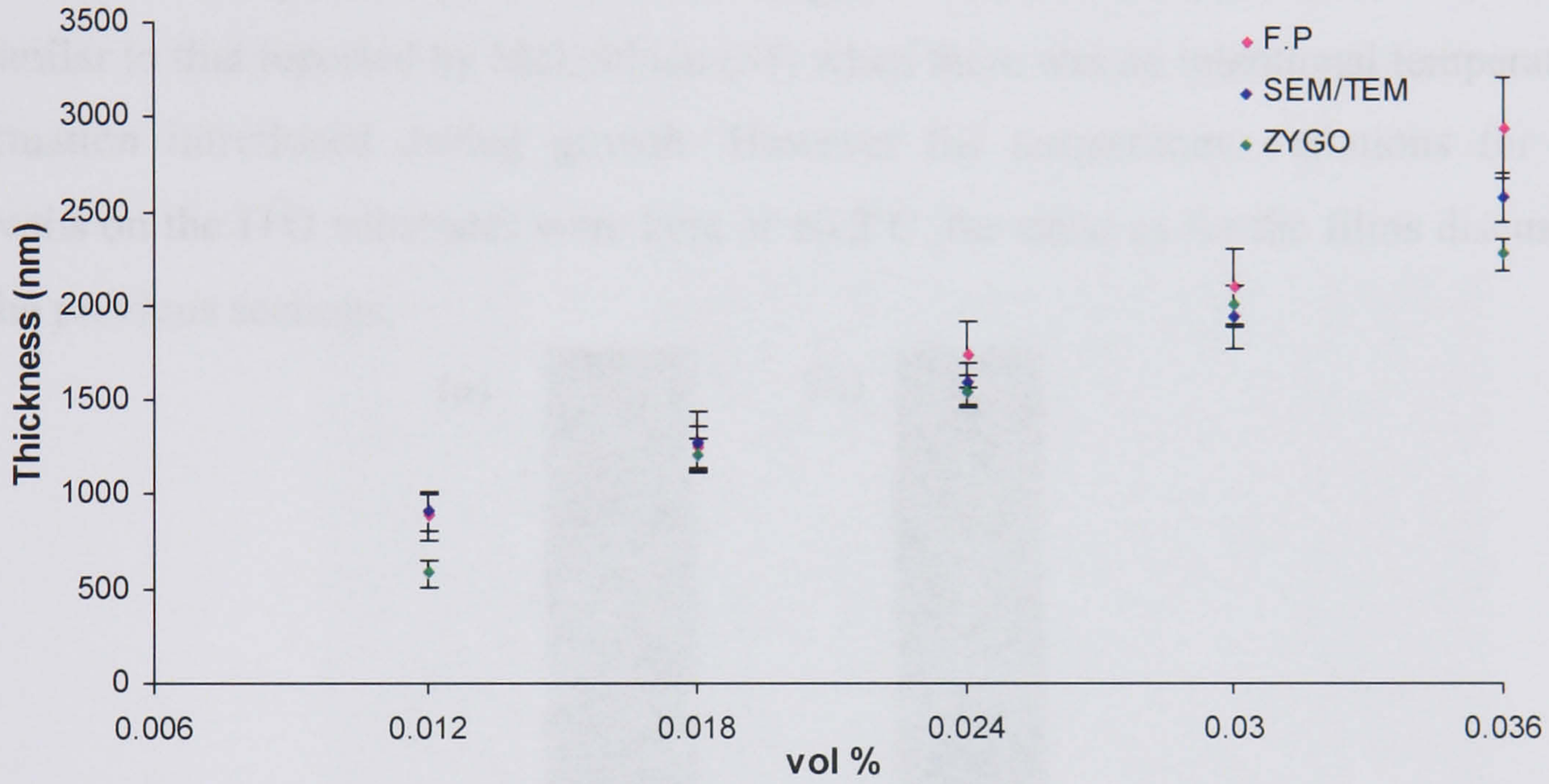


Figure 5.19 **Comparison of thicknesses obtained from three different methods for films grown with 200 nm spheres**

The thicknesses obtained from the three different methods are in good agreement especially when experimental errors are taken into account. In general it has been found that the SEM gives the most accurate thickness result since the actual number of layers of spheres can be counted. The main problem with using the Fabry-Perot fringes is that in calculating the thickness the effective refractive index calculated from the modified Bragg law is required. As discussed previously this value is not always close to the expected value of 1.44 which therefore introduces a source of error into the thickness calculation.

5.5 Growth on other substrates

So far all the results presented have been grown on cleaned glass substrates. Growth on a conductive substrate, indium tin oxide (ITO), was also investigated. The cleaning procedure for the ITO and the film growth procedure was the same as for glass substrates.

Initial growths on ITO substrates supplied by Delta Technologies USA were found to be problematic. The films demonstrated horizontal striping, with regions of high concentration of spheres and delamination (figure 5.20(a)). The appearance of the films is similar to that reported by McLachlan (64) when there was an intentional temperature fluctuation introduced during growth. However the temperature variations for the growths on the ITO substrates were kept at ±0.2˚C, the same as for the films discussed in the previous sections.

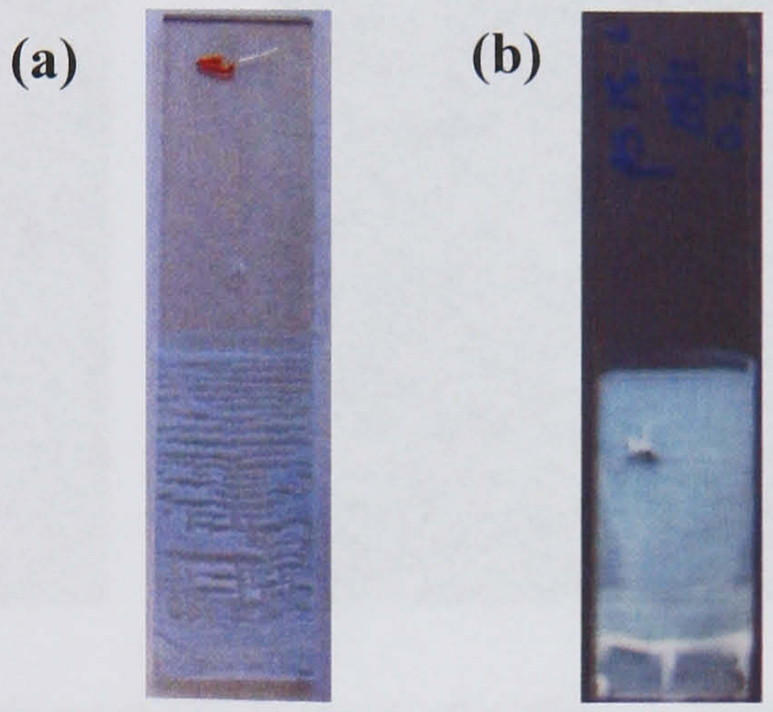


Figure 5.20 Comparison of film coverage on (a) ITO and (b) glass for films grown with the same spheres size

It was hypothesised that the problem growing on ITO was due to the properties, *e.g.* wettability or contact angle, being different to glass. It has been reported that the use of a surfactant can change the contact angle and the surface tension of a solution on a substrate (126,130,131). The use of the surfactant Tween20, polyoxyethylene sorbiton monlaurate, was investigated in an attempt to grow films of good quality on ITO.

Firstly a 0.1% solution of Tween/de-ionised water was made and used to dilute the colloid and then the growth procedure was completed as normal. Once grown these films demonstrated even film coverage but no optical properties could be detected. When the films were investigated by SEM the film surface showed sparse coverage of spheres, no ordering and a film over the top of the spheres (figure 5.21).



Figure 5.21 **SEM micrograph showing the lack of film coverage for a concentration Tween 0.1%**

The concentration of Tween was decreased to 0.025% and the growth process was repeated. Not only did these samples demonstrate good film coverage, opalescence was visible to the naked eye. SEM investigation of the films showed that the spheres were ordered in the usual close packed nature (figure 5.22(b)).

(a) (b)

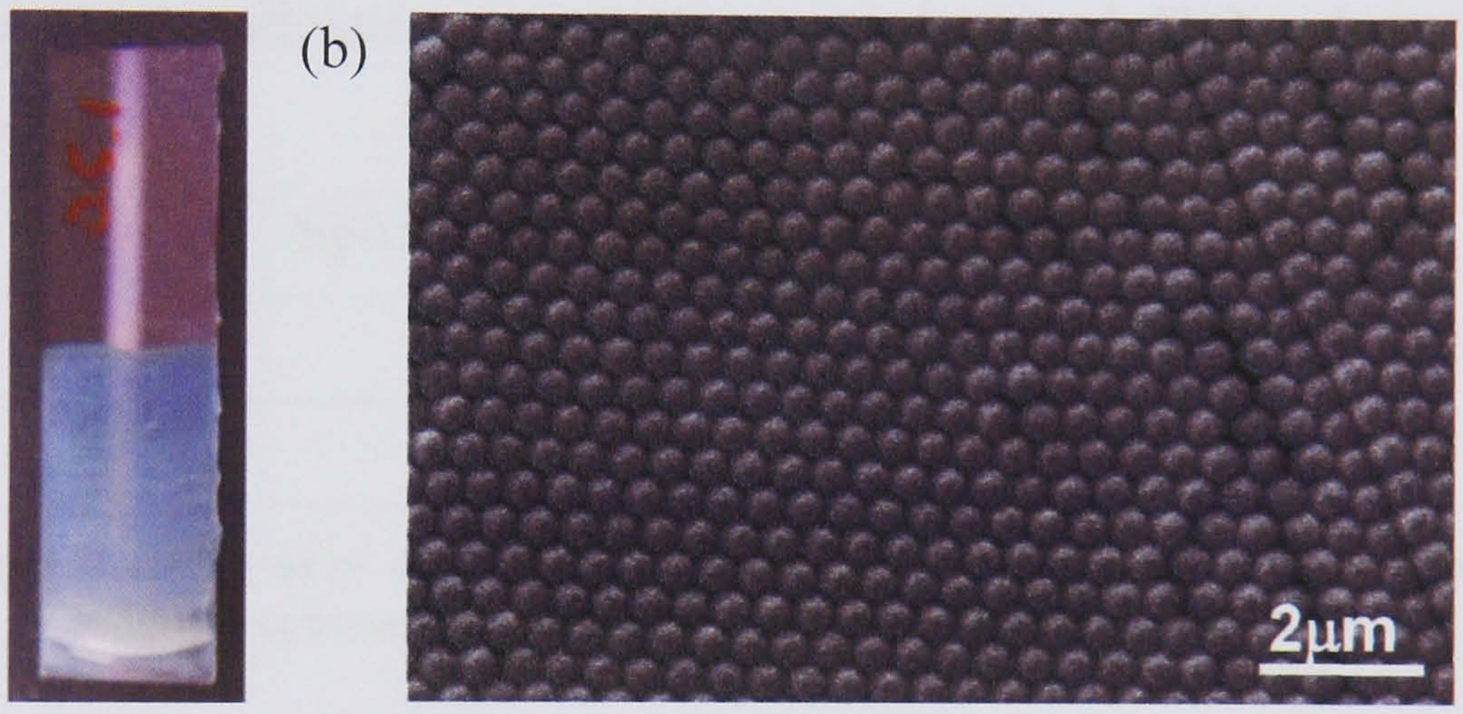


Figure 5.22 **Images showing (a) the surface of a film on ITO with addition of Tween and (b) SEM micrograph of the ordering in this film**

A similar result has shown that for the surfactant sodium dodecyl sulfate when the concentration is increased from 37.7 mM to 52.1 mM the surface morphology and periodicity of the colloidal crystals is destroyed (130).

The reflectance spectra of the films grown on ITO with Tween solution (figure 5.23) show well defined reflectance peaks followed by very intense Fabry-Perot fringes.

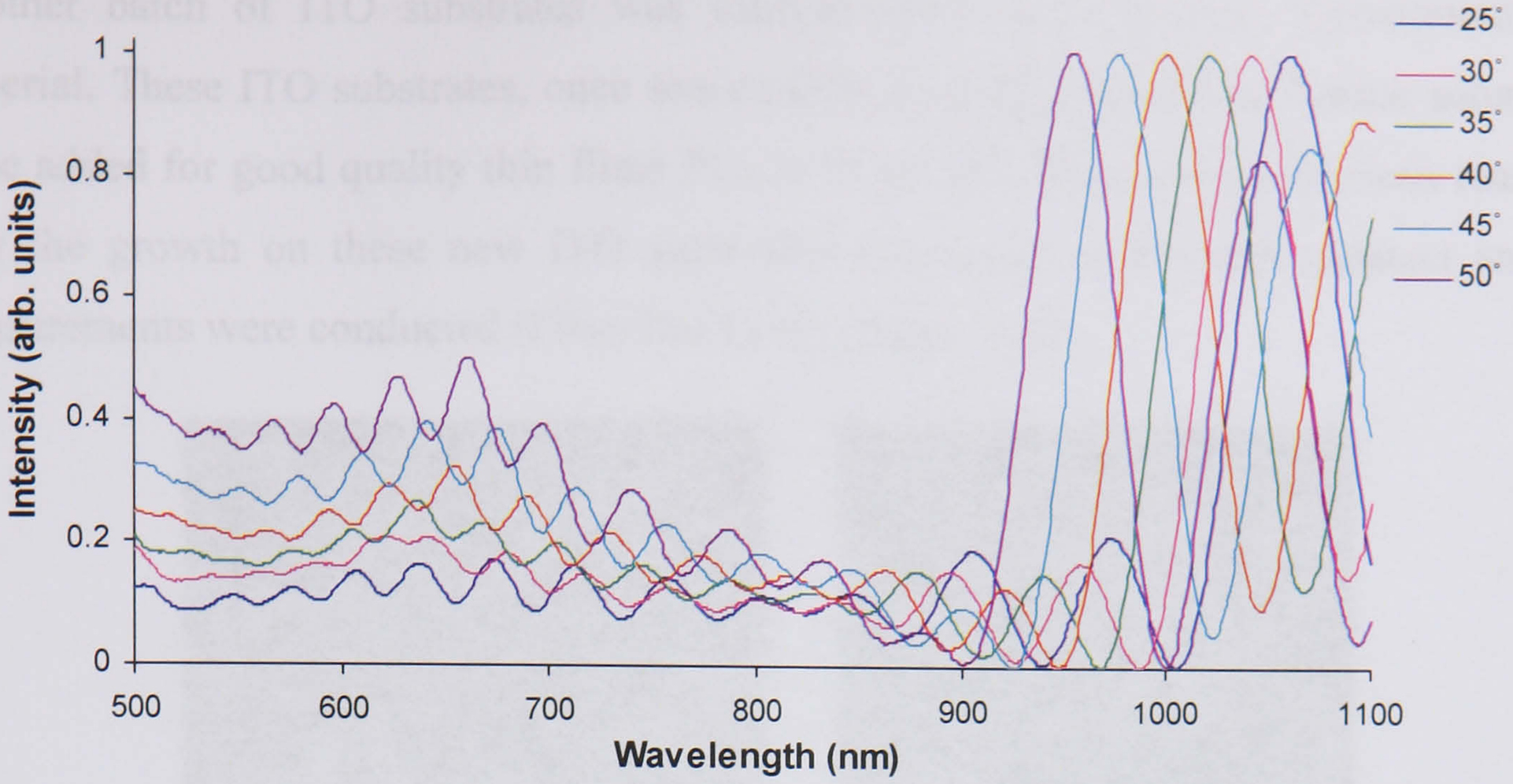


Figure 5.23 **Normalised reflectance spectra for a film grown with the addition of Tween showing pronounced Fabry-Perot fringes**

The difference in sphere diameter and n_{eff} calculated from the modified Bragg law for films grown at the same colloidal concentration on glass and ITO substrates are summarised in table 5.6.

	Sphere diameter (nm)	**n_{eff}**
Glass	426	1.430
ITO	445	1.519

Table 5.6 **Comparison of sphere diameter and n_{eff} calculated for films grown at the same colloidal concentration on glass and ITO substrates**

The sphere diameter and n_{eff} for the film grown on the ITO substrate are larger than the films on glass. This is to be expected since the refractive index is now a combination of the refractive indices of air (n=1), polystyrene (n=1.59) and Tween (n=1.468 (132)).

The films grown on ITO substrates are also thinner than those grown on glass at the same colloidal concentration. With reference to equation 5.1 for the thickness of colloidal crystal films:

$$k = \frac{\beta L \phi}{0.605 d (1 - \phi)}$$

, the parameter L, the meniscus height, is determined by the surface tension of the colloidal suspension (24,130). The use of Tween decreases the surface tension of the colloidal suspension, therefore L decreases and there is a corresponding decrease in the film thickness.

Another batch of ITO substrates was sourced from the Chemistry Department at Imperial. These ITO substrates, once sequentially cleaned, required no Tween solution to be added for good quality thin films PCs to be grown. There was no obvious reason why the growth on these new ITO substrates was easier, even when contact angle measurements were conducted (Fibro Dat 1100) (figure 5.24).

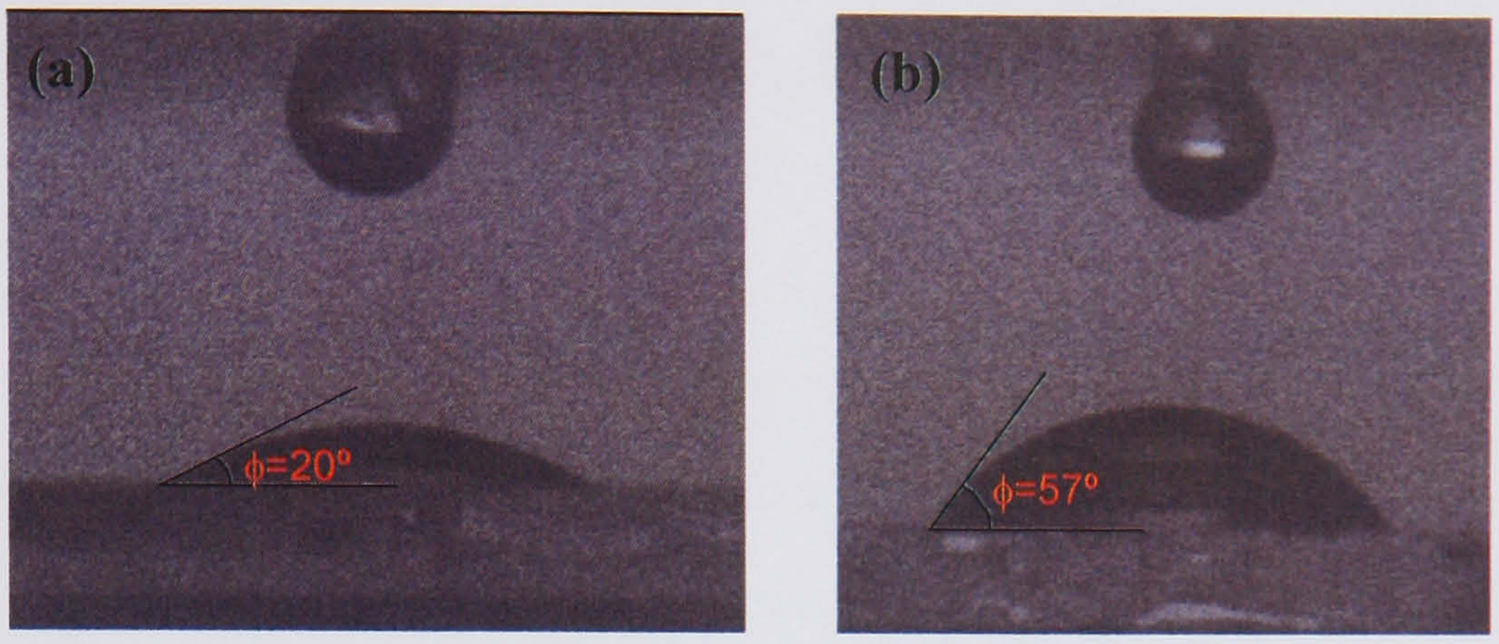


Figure 5.24 **Contact angle measurements for (a) original Delta Technologies ITO and (b) new source ITO**

The contact angle data shows that the original source ITO substrate has a smaller contact angle than the new source of ITO, *i.e.* is more hydrophilic. These measurements would indicate that the original ITO should be easier to grow on because it has a contact angle closer to that of glass, measured to be close to 0˚, but this was not the case. No obvious explanation could be found for why difficulties were encountered when trying to grow thin films on the original source of ITO but it was clear that the addition of Tween improved the film quality (see figure 5.22).

The films on ITO are grown as templates for the formation of macroporous materials (see chapter 7) and therefore it was deemed best to grow on a substrate which required no extra treatment which may complicate things and therefore the new source ITO substrates were used routinely for the growth of templates for the formation of macroporous materials.

5.6 Conclusions

Ultimately the films grown in this project were used as templates for the formation of macroporous materials but it was important to learn the appropriate growth procedure and conditions in order to grow the best templates possible. This chapter summarises the growth procedure which was used to form thin film PCs on both glass and ITO substrates. The films were analysed by optical microscopy, optical spectroscopy and

SEM and were shown to have good long range ordering. to demonstrate close packing and have controllable thickness and to therefore be suitable for the use as template films.

6 Towards a Model for Thin Film Growth

6.1 Introduction

As discussed in chapter 5, the process of controlled vertical drying, or colloidal self-assembly, produces high quality photonic crystal (PC) thin films. Although this growth process is widely used to produce thin film PCs (6,44,122) it is clear from the literature that the growth procedure is not well understood (6,35,126,129). The general consensus is that evaporation of water from the meniscus region, as shown in figure 6.1, draws colloidal spheres into the area of film formation and inter-particle capillary forces assemble the spheres into close packed arrays.

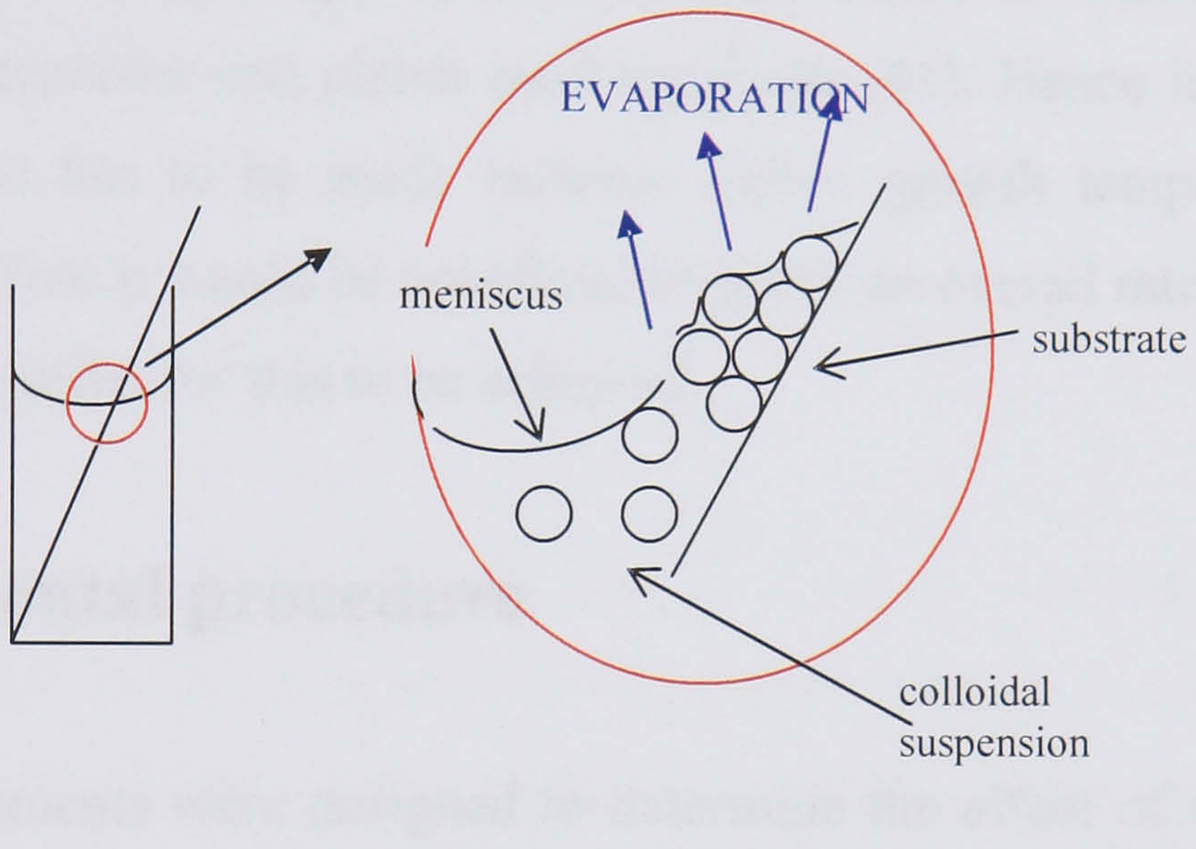


Figure 6.1 Simple schematic illustration of thin film formation

Until the systematic studies by Ye *et al* (45) and more recently McLachlan *et al* (6) and Kuai *et al* (44) the factors affecting the growth procedure and the optimum growth conditions had not been systematically investigated. These studies demonstrated that temperature, relative humidity (R.H.) and colloidal concentration (volume fraction) are the most important growth parameters. An optimum growth temperature of 55-65˚C has been suggested to give the best crystalline quality. There is some disagreement about the optimum R.H., with McLachlan *et al* (6) quoting a value below 20% and Kuai *et al* (44) reporting 80-90%. These discrepancies are probably due to the manner in which the R.H. has been defined, which is reported by McLachlan and not by Kuai. The colloidal concentration has been shown not only to affect the film thickness but also the macroscopic domain size (122).

At the moment, although it is reported that high quality PCs can be grown, all the films described in the literature show cracks between domains (6,44,45,122,126). If the

optimum conditions can be identified for the growth of thin film PCs it is hoped that the problem of cracking can be minimised. In order for self-assembled PC films to be adopted in device technologies such as sensors and photonic switches the films would need to possess as few cracks as possible *i.e.* demonstrate large domain widths (122). Hence it is apparent that the process of film growth needs to be better understood.

It has been hypothesised that the cracks found in thin film PCs can be attributed to the shrinkage of the polystyrene spheres during the self-assembly procedure (36,122), or, to drying induced tension between neighbouring spheres as the solvent evaporates (6,126). As the drying induced tension will increase with temperature it can be hypothesised that films grown at higher growth temperatures will exhibit more cracking. However, it has been demonstrated that higher growth temperatures reduce the number of defects, such as dislocations, vacancies and planar stacking faults (45). Hence it becomes apparent that a compromise has to be made between higher growth temperature and slower growth rate. Therefore it would be beneficial to derive an overall rate law for the growth of thin film PCs in order for this to be achieved.

6.2 Experimental procedure

A series of experiments were designed to determine the effect of varying the growth temperature, R.H and the colloidal concentration on the growth of good quality thin film PCs.

The experiments were conducted as follows. The growth incubator was allowed to stabilise at the required temperature for at least 24 hours before use. Figure 6.2 illustrates the experimental set-up.



Figure 6.2 Incubator set-up for monitored thin film growth

The colloidal suspensions and the growth substrates were prepared as described in chapter 5. The colloidal suspension was added to a clean vial (25x75 mm) and the glass substrate was placed vertically inside. A graticule was drawn on the side of the glass vial starting at the initial position of the meniscus, which enabled the drop of the meniscus to be measured as the growth proceeded. The growth vial was then placed inside the incubator and the growth was started. The temperature and R.H. were recorded throughout the growth period. The growth proceeded as normal with the exception that the web camera was programmed to record an image every hour during growth.

The change in height of the meniscus, measured from the hourly web camera images using Adobe Photoshop, is a measure of the growth of the film. A plot of length of film grown versus time allows the growth rate to be extracted from the gradient (see for example figure 6.3).

6.2.1 Temperature

Since it had previously been reported that the growth temperature was the most important parameter in thin film growth (64) eight experiments were conducted to investigate the effect of varying the growth temperature in the range 40-70˚C while maintaining a constant R.H. and colloidal concentration. This temperature range was chosen because experiments at temperatures below 40˚C would take too long, in excess of one week, and at temperatures above 70˚C the growth would progress too fast for accurate monitoring. The R.H. was maintained in the range 0-10% by loading the growth incubator with activated silica gel and a colloidal concentration of 0.213 vol% was used. The average evaporation rate and growth rate for each temperature is shown in figure 6.3 and table 6.1.

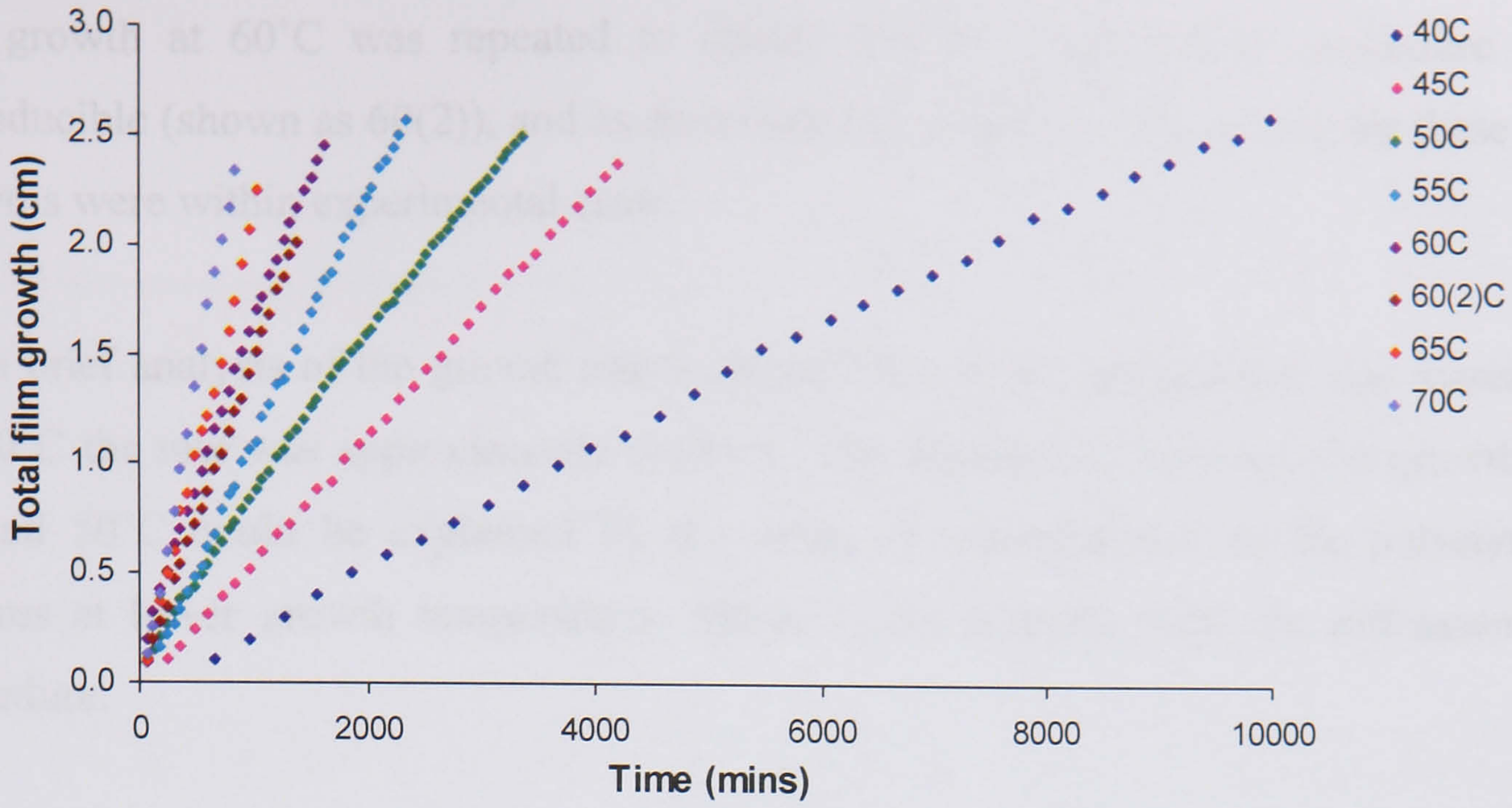


Figure 6.3 **Film growth versus time for growth at the seven temperatures investigated**

Temp. (˚C)	Av. evaporation rate (cm/hr)	Growth rate (cm/min)	Growth rate (m/s)
40	0.0160	0.00027±0.00002	$(4.50\pm0.30)\times10^{-8}$
45	0.0306	0.00058±0.00005	$(9.67\pm0.83)\times10^{-8}$
50	0.0453	0.00072±0.00004	$(1.20\pm0.06)\times10^{-7}$
55	0.0668	0.00114±0.00009	$(1.90\pm0.14)\times10^{-7}$
60	0.0868	0.00145±0.00003	$(2.42\pm0.04)\times10^{-7}$
60(2)	0.0868	0.00146±0.00015	$(2.43\pm0.24)\times10^{-7}$
65	0.1342	0.00214±0.00022	$(3.57\pm0.37)\times10^{-7}$
70	0.1704	0.00293±0.00031	$(4.88\pm0.52)\times10^{-7}$

Table 6.1 **Calculated growth rates at the seven temperatures investigated**

The evaporation rate of water is proportional to the vapour pressure, which has been shown by Rakers *et al* (133) to vary exponentially with temperature, as shown by equation 6.1.

$$p \propto \exp\left(\frac{-W}{RT}\right) \qquad \textbf{Equation 6.1}$$

Where p is the vapour pressure, W is the molar evaporation energy, R is the universal gas constant and T is the temperature. Thus, as shown in table 6.1, as the growth temperature increases, the vapour pressure increases and the solvent evaporation rate increases.

The growth at 60°C was repeated to ensure that the experimental procedure was reproducible (shown as 60(2)), and as demonstrated in table 6.1 the results for these two growths were within experimental error.

From brief analysis of the growth rate it appears that as the temperature was increased by 10°C the rate was approximately doubled. The discrepancy between the growths at 40 and 50°C could be explained by the onset of sedimentation of the polystyrene spheres at lower growth temperatures which would compete with the self-assembly procedure.

6.2.2 Relative Humidity (R.H.)

It can be hypothesised that the R.H., since it will affect the evaporation rate of the water, will have an effect on the growth rate. As mentioned previously, controlling the R.H. could be a way to achieve a slower growth rate while maintaining a high growth temperature, which has been shown to be optimum for film growth.

Three experiments were conducted to investigate the effect of increasing the R.H. while maintaining a constant growth temperature and colloidal concentration. In these experiments the R.H. was defined as the amount of water vapour in the air divided by the maximum water vapour the air can hold at a given temperature, and was measured using a datalogger, see chapter 5. Although it has been shown by McLachlan *et al* (6) that increasing the R.H. to 40-50% has a detrimental effect on the quality of the films, the experiments described below were designed to investigate if a small increase in R.H might improve film quality.

As shown in figure 5.2 the R.H. value does not remain constant throughout the growth period due to the evaporation of water from the system. In an attempt to overcome this problem saturated solutions of constant R.H salts were investigated. Saturated salts of LiCl and $MgCl_2$ have constant R.H values of around 11 and 30%, respectively. at the temperatures to be investigated (134). Figure 6.4 shows the measured R.H. profile over a twenty hour period for the LiCl and $MgCl_2$ saturated solutions at 60°C in the growth incubator.

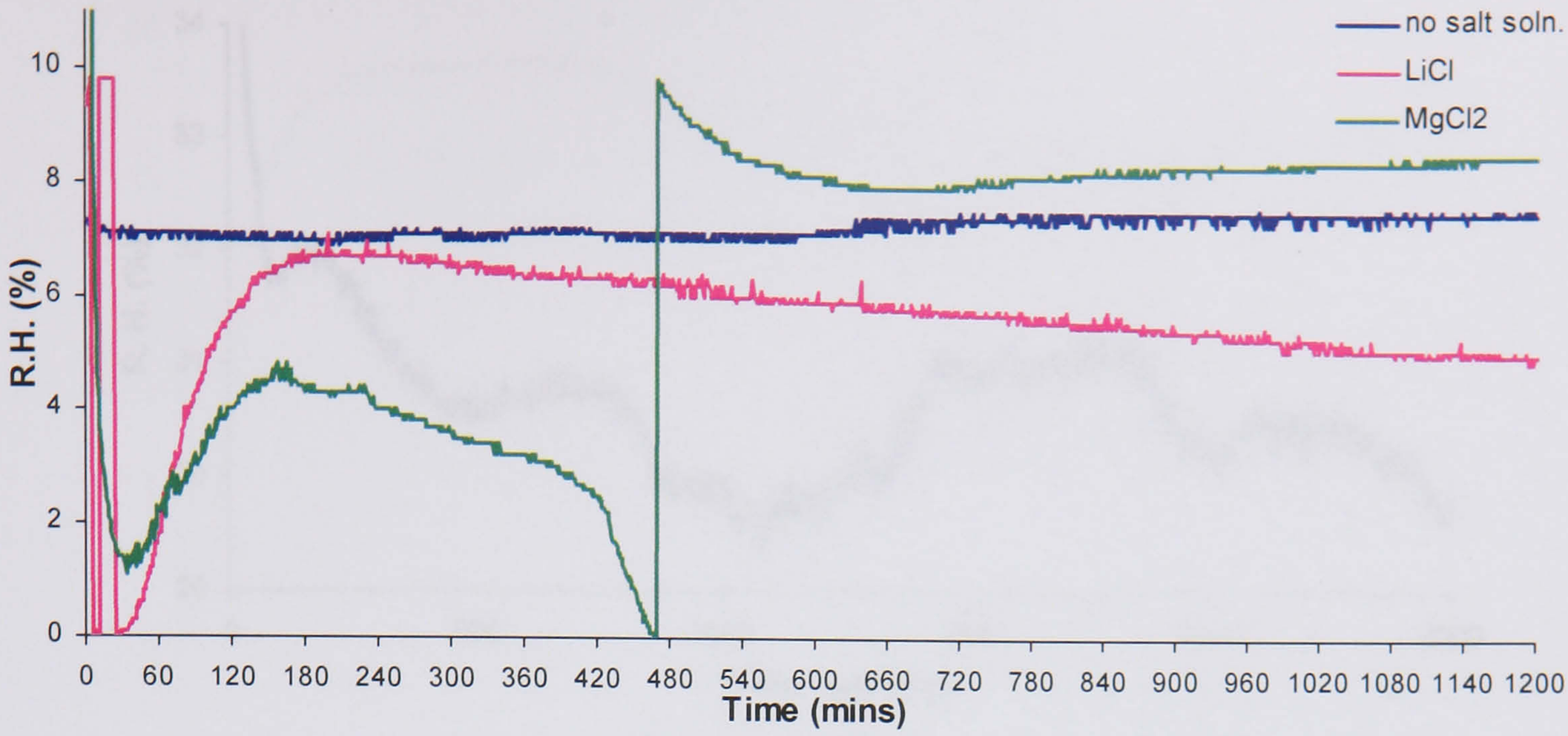


Figure 6.4 **Relative humidity profile for no salt solution and for LiCl and $MgCl_2$ saturated solutions at 60°C**

The sets of data presented in figure 6.4 for LiCl and $MgCl_2$ suggest that little control over the R.H. has been achieved. In the R.H. profile of LiCl the R.H. value fluctuates between 0 and 10% for the initial sixty minutes before rising to ~7%. A gradual decrease then occurs for the remainder of the experiment until close to the normal background R.H. reading, shown by the blue line, for the incubator was obtained. Figure 6.4 also shows that the $MgCl_2$ R.H. profile did not reach the required value of 30%. Instead the R.H. fluctuated between 3-4 % before increasing to 8 % at which point the value remained constant. In both the R.H. profiles the points at which the R.H. dropped to zero would appear to be due to a problem with the datalogger and this behaviour is occasionally observed during normal growths. From the R.H. profile of a standard film growth experiment (see figure 5.2) the R.H. value obtained is typically 5-10 % once the growth is complete. Thus the salt solutions have not influenced the R.H. obtained at 60°C. When the $MgCl_2$ solution was removed from the incubator a white crust had formed over the top of the solution. It was thought that this crust would act as a barrier to the measurement of the local R.H. from above the water.

The R.H. behaviour for the $MgCl_2$ solution was investigated at room temperature, shown in figure 6.5. This time it is clear that an R.H. value of 30% has been attained for a long period of time.

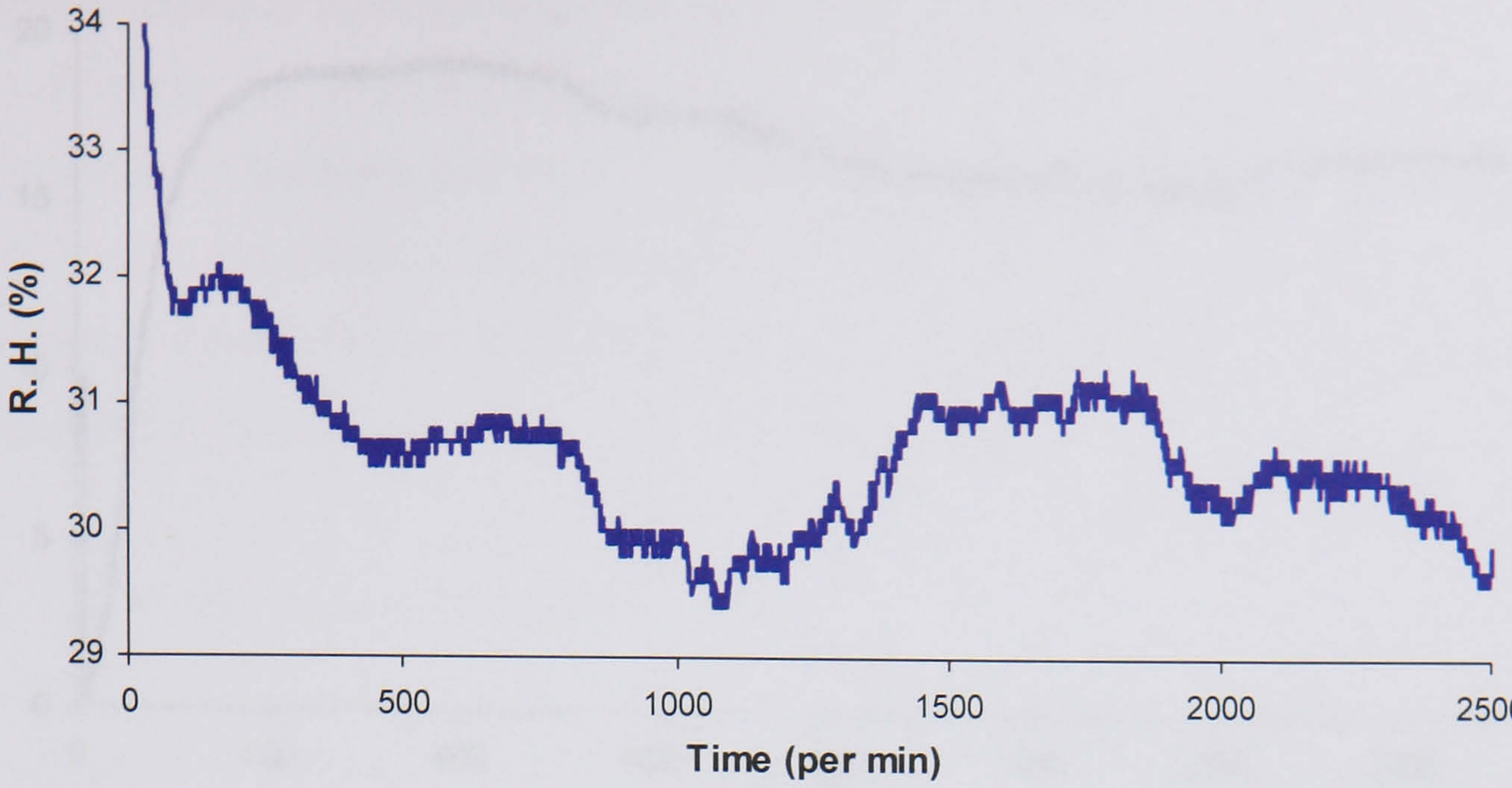


Figure 6.5 Relative humidity profile for $MgCl_2$ at room temperature

The data presented in figure 6.5 shows that the method used for preparing the saturated solutions must be correct since an R.H. value of 30% was maintained for the $MgCl_2$ at room temperature. The following two reasons were hypothesised in an attempt to explain why the saturated solutions may not have performed properly at 60˚C. In order to aid the dissolution of the salt the saturated solution was heated which could have resulted in the solution becoming supersaturated. As the temperature decreased to 60˚C some of the excess $MgCl_2$ could come out of solution and act as a nucleation site for crystallisation resulting in the formation of a crust. On the other hand, if the saturated solution was not fully saturated, water would be able to evaporate from the system leading to the re-crystallisation of the $MgCl_2$. Both of these hypothesised reasons could contribute to the difficulty of achieving the correct R.H. values.

Therefore, due to difficulty in preparing the saturated salt solutions to work at 60˚C this method of controlling the R.H. was abandoned. Instead three different R.H. conditions, low (~7%), medium (~11%) and high (~16%) were prepared. As before a low R.H. was synthesised by loading the incubator with activated silica gel. Medium and high R.H. values were obtained by adding 40 ml and 80 ml of water respectively into the incubator in addition to the growth vial. It is interesting to note that the conditions for the high R.H. growth mimic the normal growth procedure where more than one film is grown at a time, see chapter 5. Figure 6.6 illustrates the R.H. profile at the high R.H. condition.

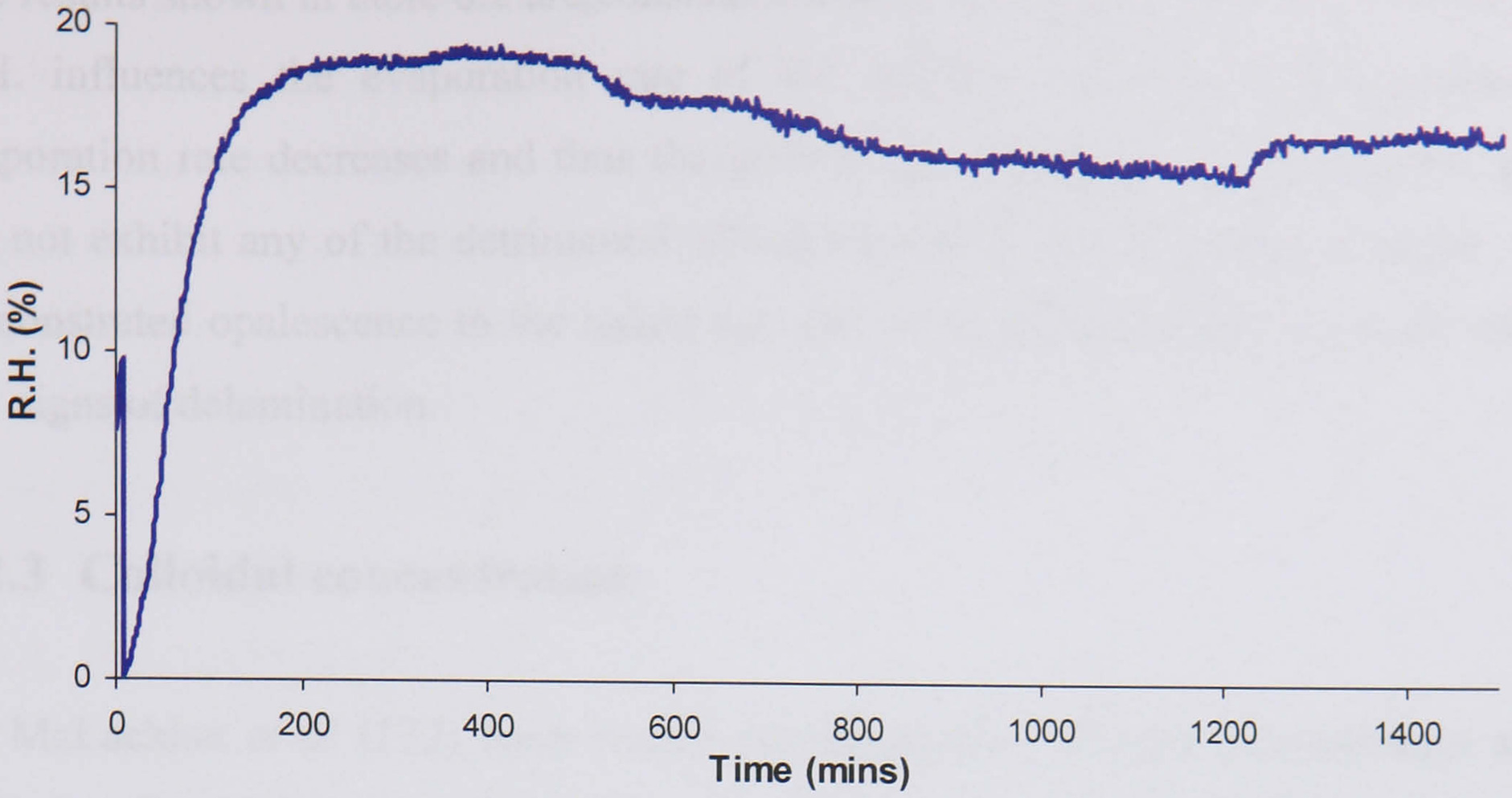


Figure 6.6 R.H. profile during high R.H. growth at 65°C

The growth temperature was set to 65°C and a colloidal concentration of 0.213 vol% was used. The average evaporation rate and growth rate for each R.H. condition is shown in figure 6.7 and table 6.2.

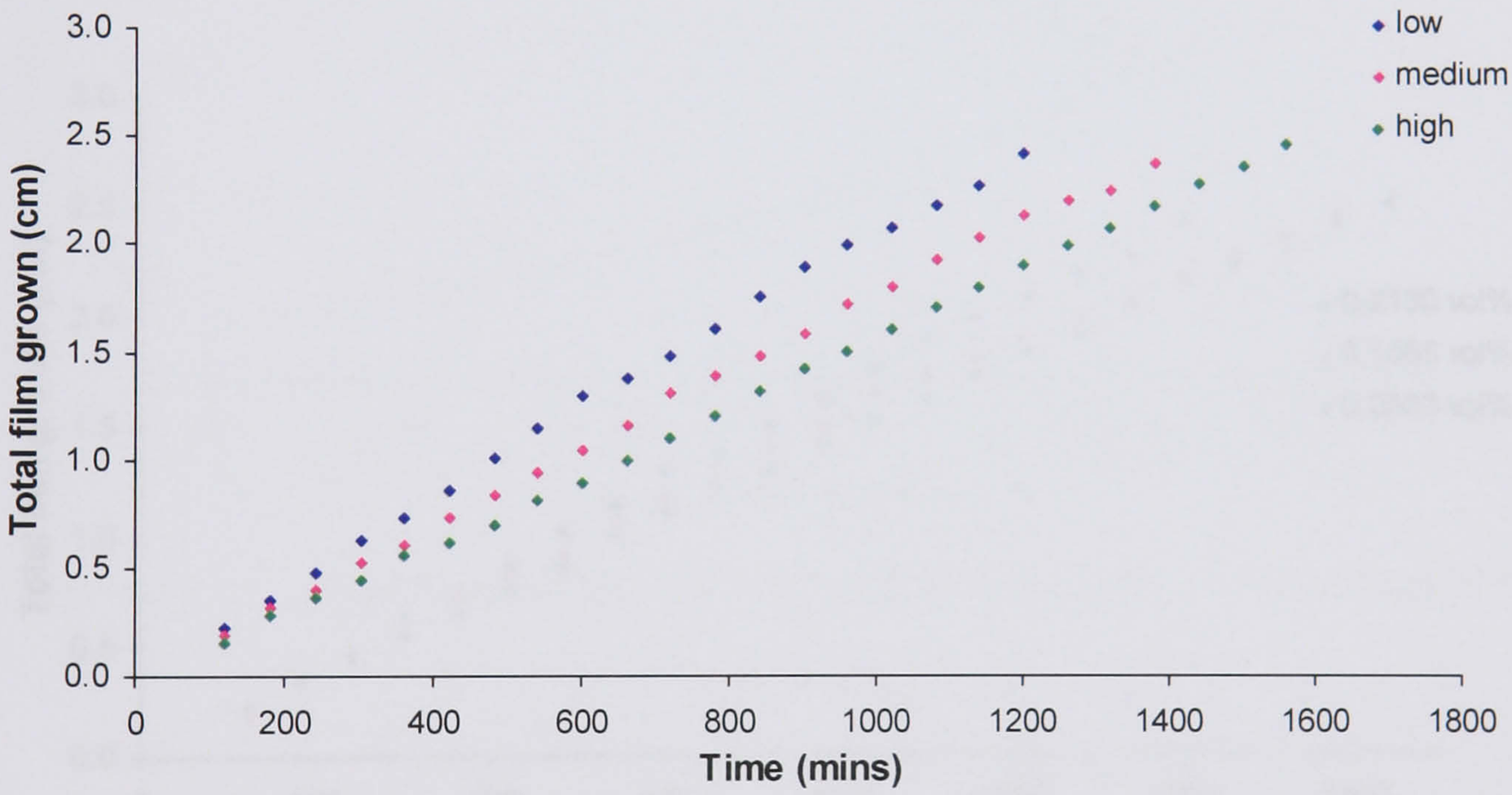


Figure 6.7 Film growth versus time for growth at the three R.H. investigated

R.H.	Av. evaporation rate (cm/hr)	Growth rate (cm/min)	Growth rate (m/s)
low	0.1232	0.00205±0.00020	$(3.42\pm0.33)\times10^{-7}$
medium	0.1048	0.00177±0.00017	$(2.95\pm0.28)\times10^{-7}$
high	0.0973	0.00162±0.00015	$(2.70\pm0.26)\times10^{-7}$

Table 6.2 Calculated growth rates at the three R.H.values investigated

The results shown in table 6.2 are consistent with those reported by Kuai *et al* (44). The R.H. influences the evaporation rate of the solvent – as the R.H. increases, the evaporation rate decreases and thus the growth rate decreases. The three films grown did not exhibit any of the detrimental effects discussed by McLachlan *et al* (6) – they demonstrated opalescence to the naked eye and were attached to the substrate without any signs of delamination.

6.2.3 Colloidal concentration

As McLachlan *et al* (122) have shown previously the colloidal concentration affects both the film thickness and the domain size. Three experiments were conducted to investigate the effect of decreasing the colloidal concentration from 0.213 vol% to 0.0533 vol% while maintaining a constant growth temperature and R.H. The temperature and R.H. were set to 65˚C and 0-10% respectively. The average evaporation rate and growth rate for each colloidal concentration is shown in figure 6.8 and table 6.3.

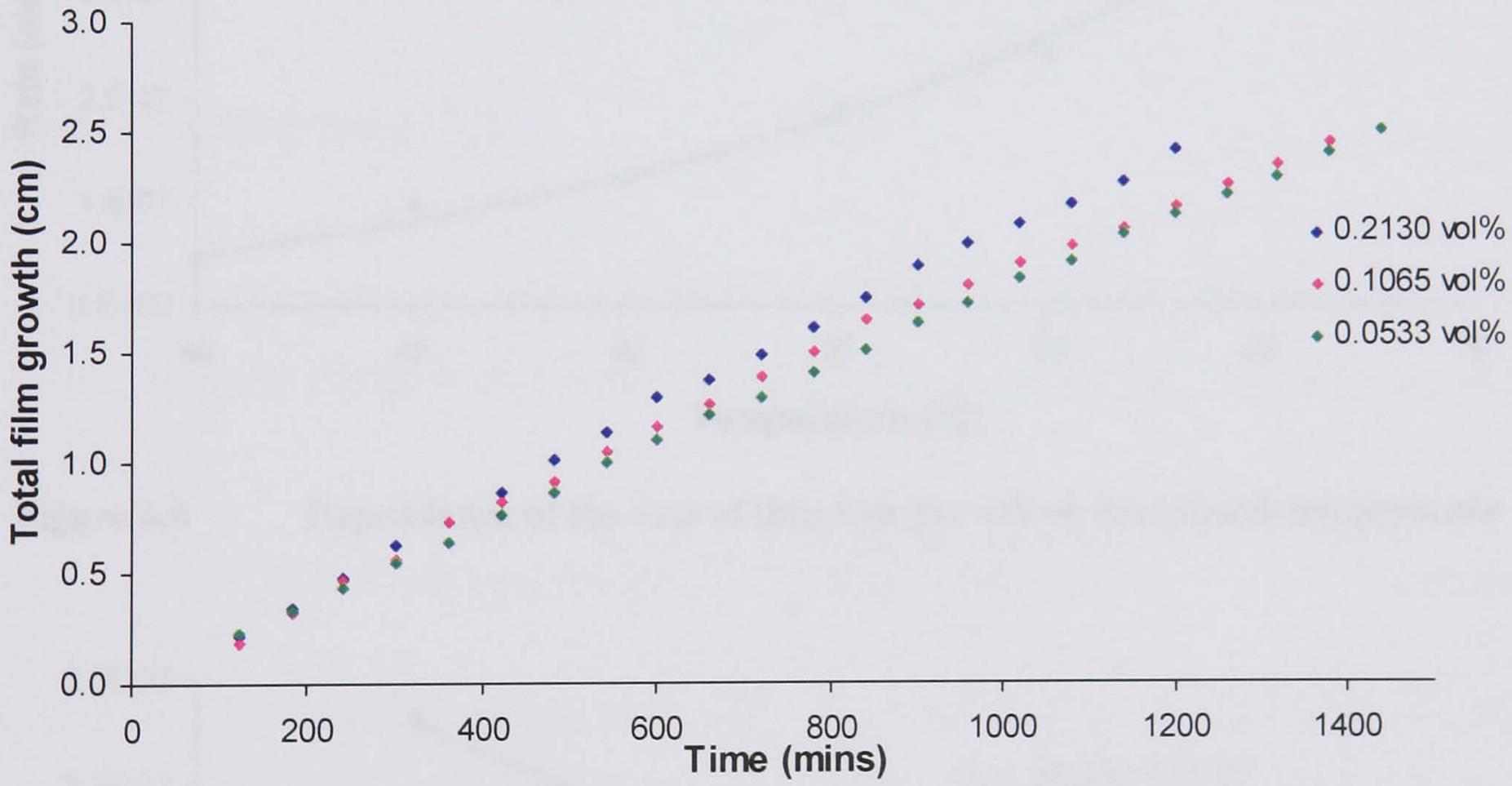


Figure 6.8 **Growth versus time for growth at the three colloidal concentrations investigated**

vol%	Av. evaporation rate	Growth rate (cm/min)	Growth rate (m/s)
0.0533	0.1046	0.00175±0.00017	$(2.92\pm0.28)\times10^{-7}$
0.1065	0.1090	0.00179±0.00018	$(2.98\pm0.29)\times10^{-7}$
0.2130	0.1232	0.00205±0.00020	$(3.42\pm0.33)\times10^{-7}$

Table 6.3 **Calculated growth rates at the three colloidal concentrations investigated**

Table 6.3 shows that as the colloidal concentration is increased the time taken for a unit length of film decreases slightly. As the colloidal concentration is increased, there becomes less water in the growth vial and thus the time required for complete solvent evaporation to occur decreases but the water evaporation rate should remain constant. However, when the data displayed in table 6.3 is examined closely and experimental errors are taken into account it can be concluded that the colloidal concentration does not have much effect on the growth rate

6.2.4 Overall growth rate

In order to determine the dependence of the rate of film growth on each of the three investigated parameters graphs were plotted of the growth parameter versus the growth rate, shown in figures 6.9-11.

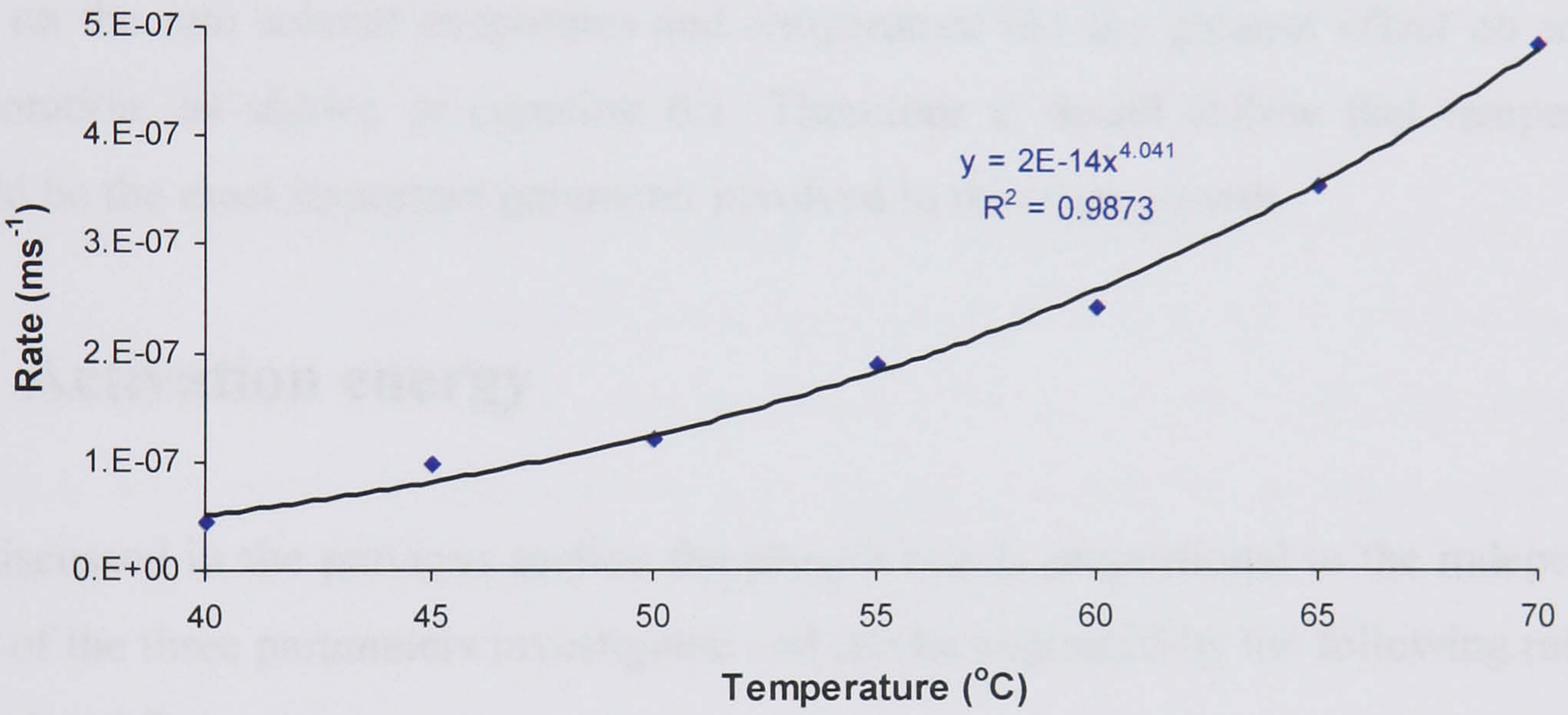


Figure 6.9 Dependence of the rate of thin film growth on the growth temperature

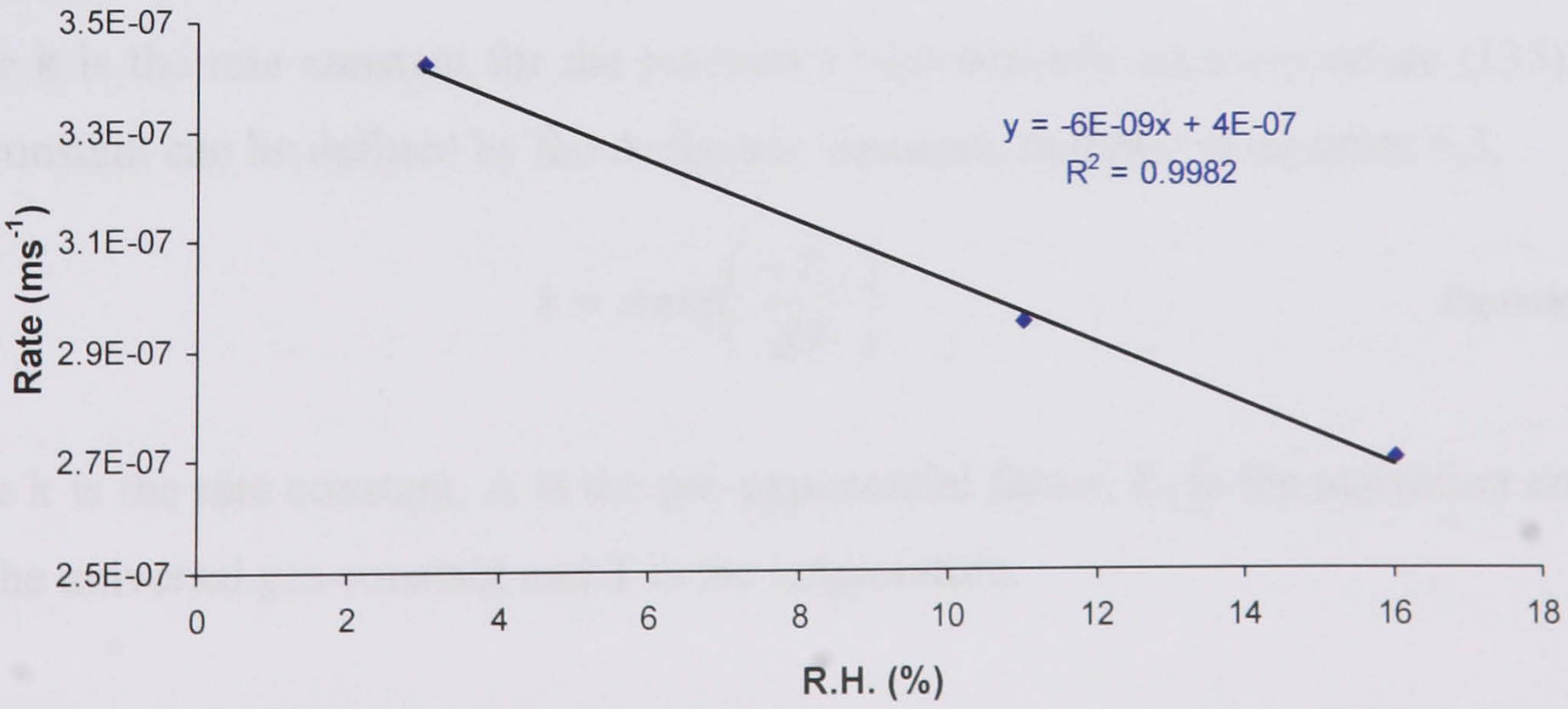


Figure 6.10 Dependence of the rate of thin film growth on the relative humidity

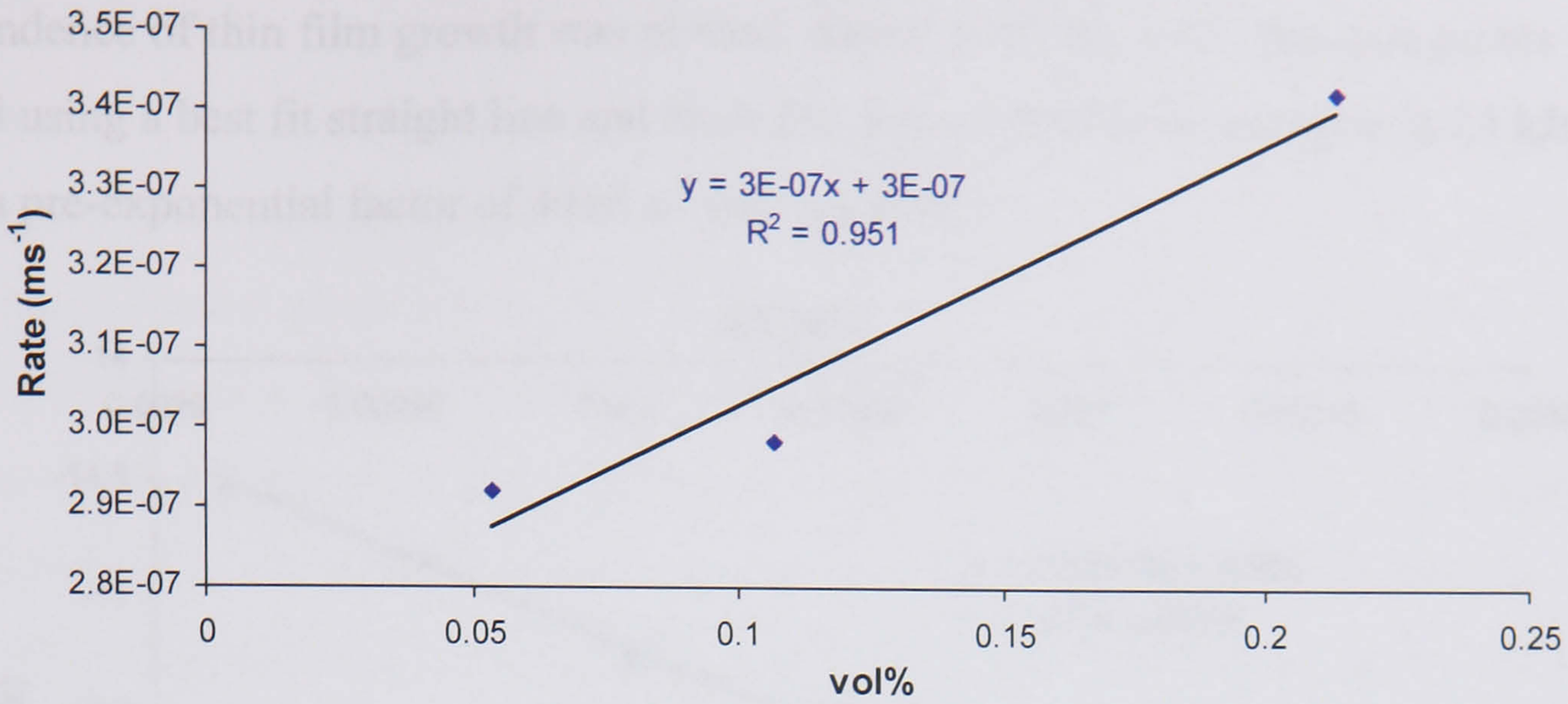


Figure 6.11 Dependence of the rate of thin film growth on the colloidal concentration

A significant change in growth rate occurs with varying the growth temperature but not for changes in R.H. or colloidal concentration. This indicates that temperature is the most important growth parameter. As shown by Kuai *et al* (44) the growth rate depends only on the rate solvent evaporates and temperature has the greatest effect on solvent evaporation, as shown in equation 6.1. Therefore it would follow that temperature would be the most important parameter involved in thin film growth.

6.3 Activation energy

As discussed in the previous section the growth rate is proportional to the independent rates of the three parameters investigated and can be explained by the following rate law (equation 6.2).

$$Rate = k[temperature]^x [R.H.]^y [colloid]^z \qquad \textbf{Equation 6.2}$$

where k is the rate constant for the reaction which depends on temperature (135). The rate constant can be defined by the Arrhenius equation, outlined in equation 6.3,

$$k = A\exp\left(\frac{-E_a}{RT}\right) \qquad \textbf{Equation 6.3}$$

where k is the rate constant, A is the pre-exponential factor, E_a is the activation energy, R is the universal gas constant and T is the temperature.

Thus, a plot of *ln(k)* versus 1/T yields a straight line with a gradient equal to $-E_a/R$ and the y-intercept equal to the pre-exponential/frequency factor. The natural logarithms of

the growth rates in table 6.1 were calculated and the Arrhenius plot for the rate dependence of thin film growth was plotted, shown in figure 6.12. The data points were fitted using a best fit straight line and from this line an activation energy of 65.5 kJmol^{-1} and a pre-exponential factor of 4416 s^{-1} was calculated.

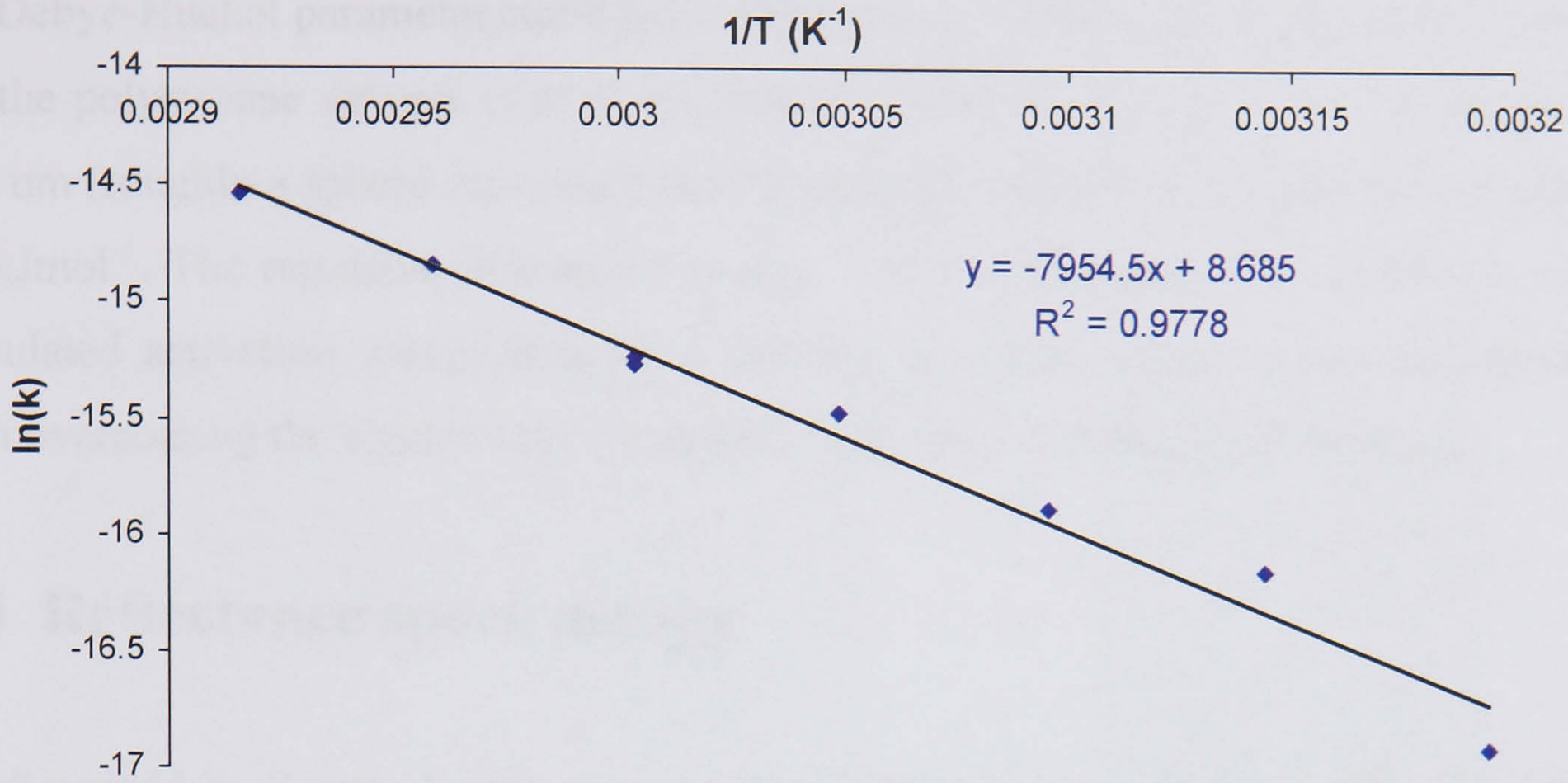


Figure 6.12 Determination of the activation energy of thin film growth

In physical chemistry the activation energy is the minimum amount of kinetic energy that reactants need to form products and the pre-exponential factor is a measure of the collision frequency (135). The calculated activation energy for thin film growth is relatively high which signifies that the rate constant is dependent on temperature which further indicates that temperature is an important factor in film growth.

Experimentally the growth rate of the thin films has been equated to the evaporation rate of the water, or the drop in the meniscus height, from the growth vial. Therefore the activation energy for thin film growth should be the same as the latent heat of evaporation of water, which has a value of ~41 kJ/mol (174). The calculated activation energy from the Arrhenius plot is higher than the latent heat of evaporation of water which may be due to the activation energy being calculated for temperatures other than 100°C. The fact that the calculated activation energy is not equal to the latent heat indicates that the activation energy for film growth may be dependent on some other factor *e.g.* overcoming the electrostatic repulsion energy of the spheres as they self-assemble. The repulsive interaction potential between two particles V_{LSA} can be expressed by the linear standard approximation (93) (equation 6.4).

$$V_{LSA} = 4\pi\varepsilon\varepsilon_0 a^2 (\xi \exp(\kappa d))^2 \frac{\exp(-\kappa s)}{2a + s} \qquad \textbf{Equation 6.4}$$

where ε is the relative permittivity of the suspending fluid, ε_0 is the permittivity of vacuum, a is the particle radius, ξ is the zeta potential of the particles in suspension, κ is the Debye-Huckel parameter and d is the thickness of the Stern layer. Initial calculations for the polystyrene spheres used in this study indicate that, at a separation distance of 400 nm (roughly a sphere diameter), the repulsive interaction potential is approximately 40 kJmol^{-1}. The repulsive interaction energy is of the same order of magnitude as the calculated activation energy indicating that the activation energy could be associated with overcoming the electrostatic repulsion of the spheres during self-assembly.

6.4 Reflectance spectroscopy

As discussed in chapter 1, the photonic stop-band properties of a thin film PC depend on the crystal quality of the film (6,44) and can be measured using reflectance spectroscopy. The presence of defects, which may occur due to different growth conditions, results in strongly localised photonic band tail states which would enhance the transmission, or decrease the reflection, in the stop-band (45).

All the films investigated in this chapter demonstrated well resolved reflectance peaks, as illustrated in figure 6.13, indicating that the quality of the films had not been affected by changing the growth parameters.

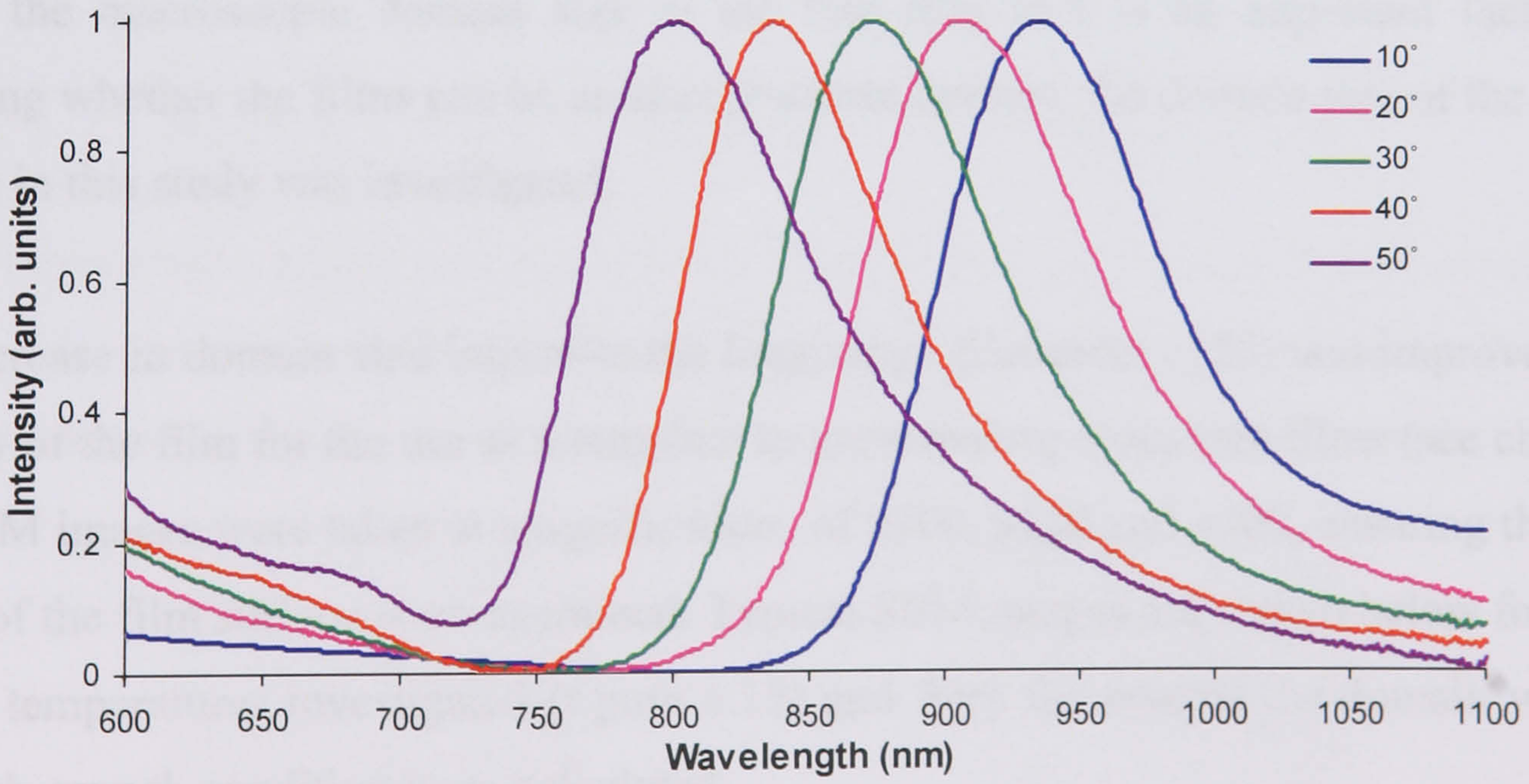


Figure 6.13 Reflection spectra for the thin film grown at low R.H. at angles of incidence 10-50°

At each angle of incidence the position of the reflection peak for all the films grown in this chapter was within the experimental error of ±7 nm (see chapter 2 for explanation).

6.5 SEM

As shown in chapter 5 the SEM was used to analyse the surface of the films to ensure that well ordered samples with few defects were formed at all growth conditions investigated. 2-D Fast Fourier Transforms (FFTs), see chapter 5, were calculated to determine the long range order in the samples. Figure 6.14 shows the SEM image and the corresponding FFT calculated for the film grown at 50˚C. All the calculated FFTs showed high order spots which are indicative of long range order.

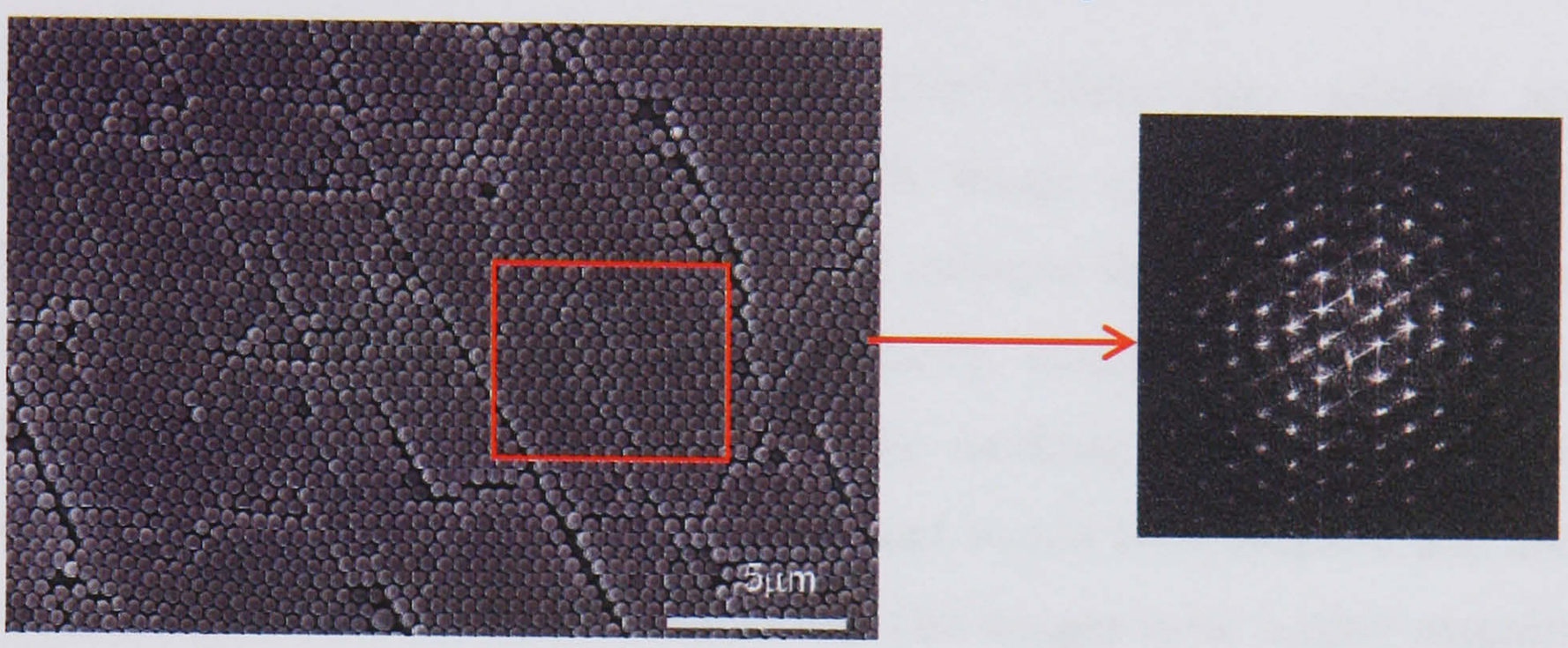


Figure 6.14 SEM image of the surface of the film grown at 50˚C showing close packing and the corresponding FFT. The red box indicates the region the FFT was calculated from.

6.5.1 Domain widths

Since the macroscopic domain size in the thin film PCs is an important factor in deciding whether the films can be used as photonic devices, the domain size of the films grown in this study was investigated.

An increase in domain size improves the long range film order (122) and improves the quality of the film for the use as a template to grow macroporous thin films (see chapter 7). SEM images were taken at magnifications of x100, x150 and x300, ensuring that all areas of the film surface were examined. Typical SEM images are shown below for two of the temperatures investigated (figure 6.15) and from the images the domain widths for each growth condition were calculated.

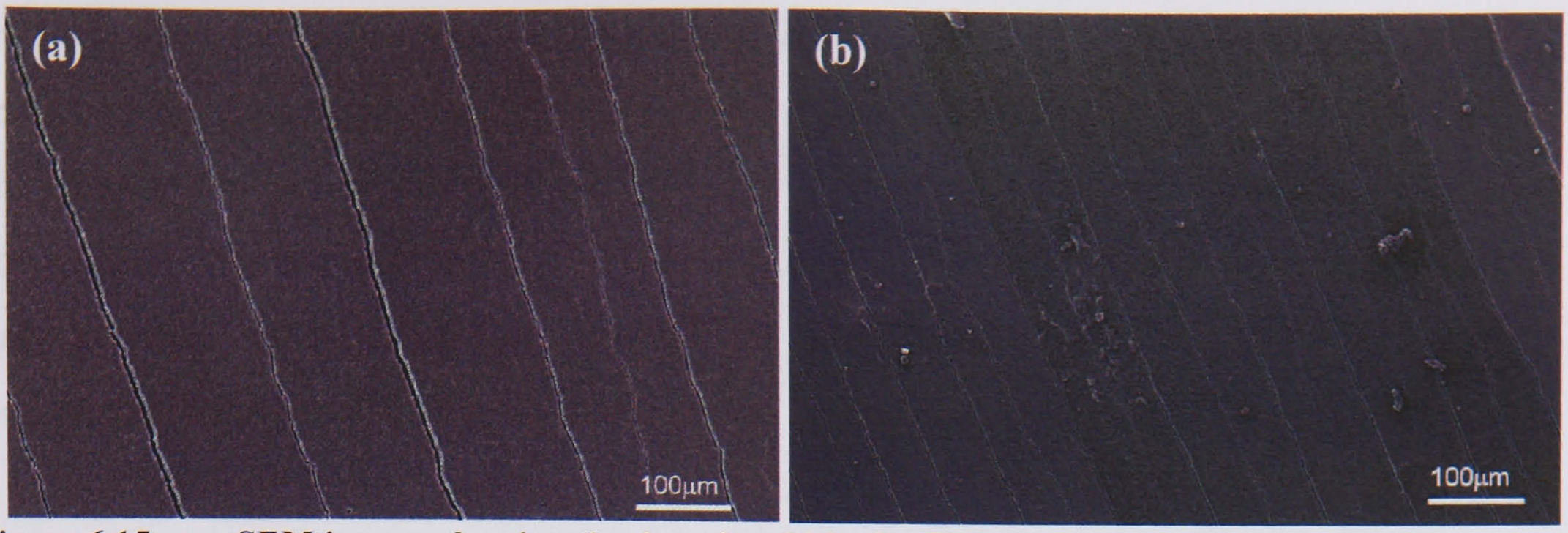


Figure 6.15 **SEM images showing the domain widths for films grown at (a) 40 and (b) 70˚C**

The domain widths were measured using DigitalMicrograph software and were calibrated to the SEM image scale bar. The SEM image scale bar is a calibrated value, which is dependent on experimental set-up, for example sample height, and thus it can be assumed that scale bar will not be completely accurate. However, all the films investigated by SEM were imaged at the same working distance, see chapter 2 for explanation, and therefore any errors encountered would be systematic and allowed at least a trend in domain width to be calculated. The images were further magnified and, when the histogram tool was used, it was the image pixels that were measured. The pixel, or smallest measurable feature, size for each of the chosen magnifications is summarised in table 6.4.

Magnification	Smallest feature size (μm)
x100	2.00
x150	1.32
x300	0.66

Table 6.4 **Smallest measurable size from DigitalMicrograph**

The domain widths were measured in two different ways, each of which is illustrated in figure 6.16, where the domains are shaded in grey and the cracks are white. In both methods at least 200 domain widths were measured and the averages calculated.

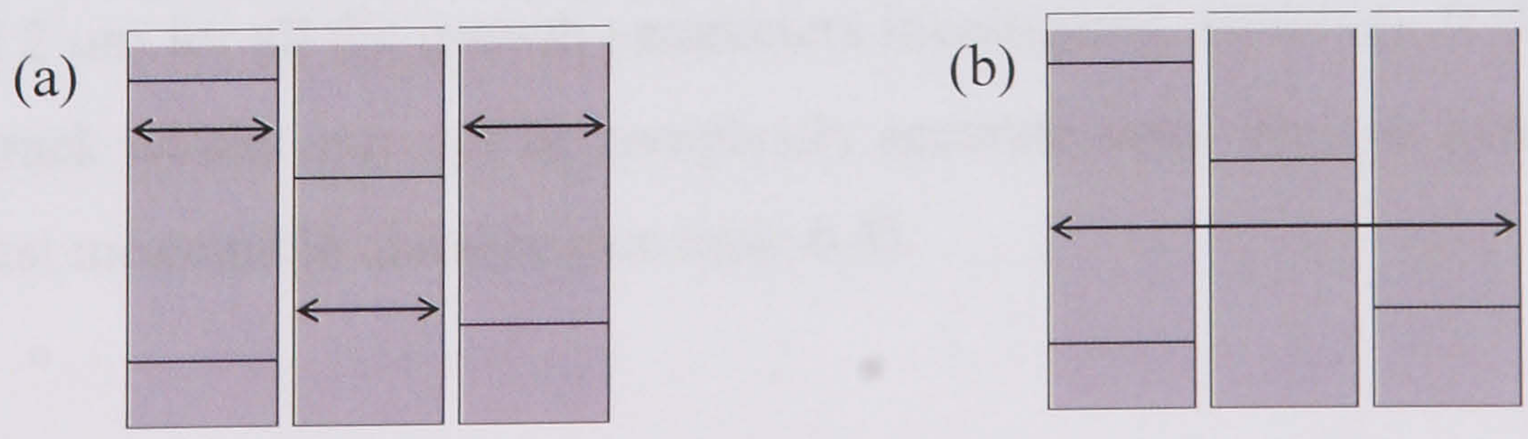


Figure 6.16 **Schematic illustration of the individual and averaged methods used to measure the domain widths**

In the first method, illustrated in figure 6.16(a) the individual widths were measured as indicated by the arrows. In the second method, as shown in figure 6.16(b) a distance, indicated by the arrow was measured across both the domains and cracks. Then in order to calculate the average domain width, the cracks widths also had to be taken into account. The measured domain widths for each method and the crack widths are summarised in table 6.5.

Parameter		**Domain width (μm)**		**Crack width (μm)**
		Individual method	**Averaged method**	
Temp. (°C)	40	89.4±48.1	95.5±45.7	1.54±0.71
	45	85.4±21.3	82.0±13.8	1.46±0.83
	50	78.1±24.1	74.2±24.0	1.32±0.51
	55	68.7±16.6	57.9±9.3	1.52±0.62
	60	101.9±24.5	99.3±17.0	2.01±0.71
	60(2)	88.0±30.0	82.6±24.0	1.50±0.67
	65	71.3±36.5	70.4±28.1	1.48±0.52
	70	64.3±18.5	52.9±16.5	1.66±0.73
R.H.	low	67.5±19.2	59.6±14.8	1.30±0.47
	medium	73.4±22.2	63.4±22.8	1.81±0.61
	high	68.4±16.9	58.4±18.8	1.39±0.55
vol%	0.0533	40.6±10.2	59.6±14.8	1.30±0.32
	0.1065	55.3±14.0	51.7±9.0	1.22±0.40
	0.2130	67.5±19.2	33.6±6.7	1.11±0.47

Table 6.5 **Average domain widths and crack widths calculated by both methods for the films investigated. Each entry represents an average of 200 measurements.**

The data presented in table 6.5 shows that the crack width remains constant at between 1 μm and 2 μm for all the growth parameters investigated. However, it should be noted that the crack widths may not be completely accurate since they are generally close to the smallest measurable distance (see table 6.4).

6.5.1.1 Temperature

The results presented in table 6.5 and illustrated graphically in figure 6.17 suggest that the general trend is that the domain width decreases as the growth temperature increases. However, the data points around 60˚C do not fit this trend.

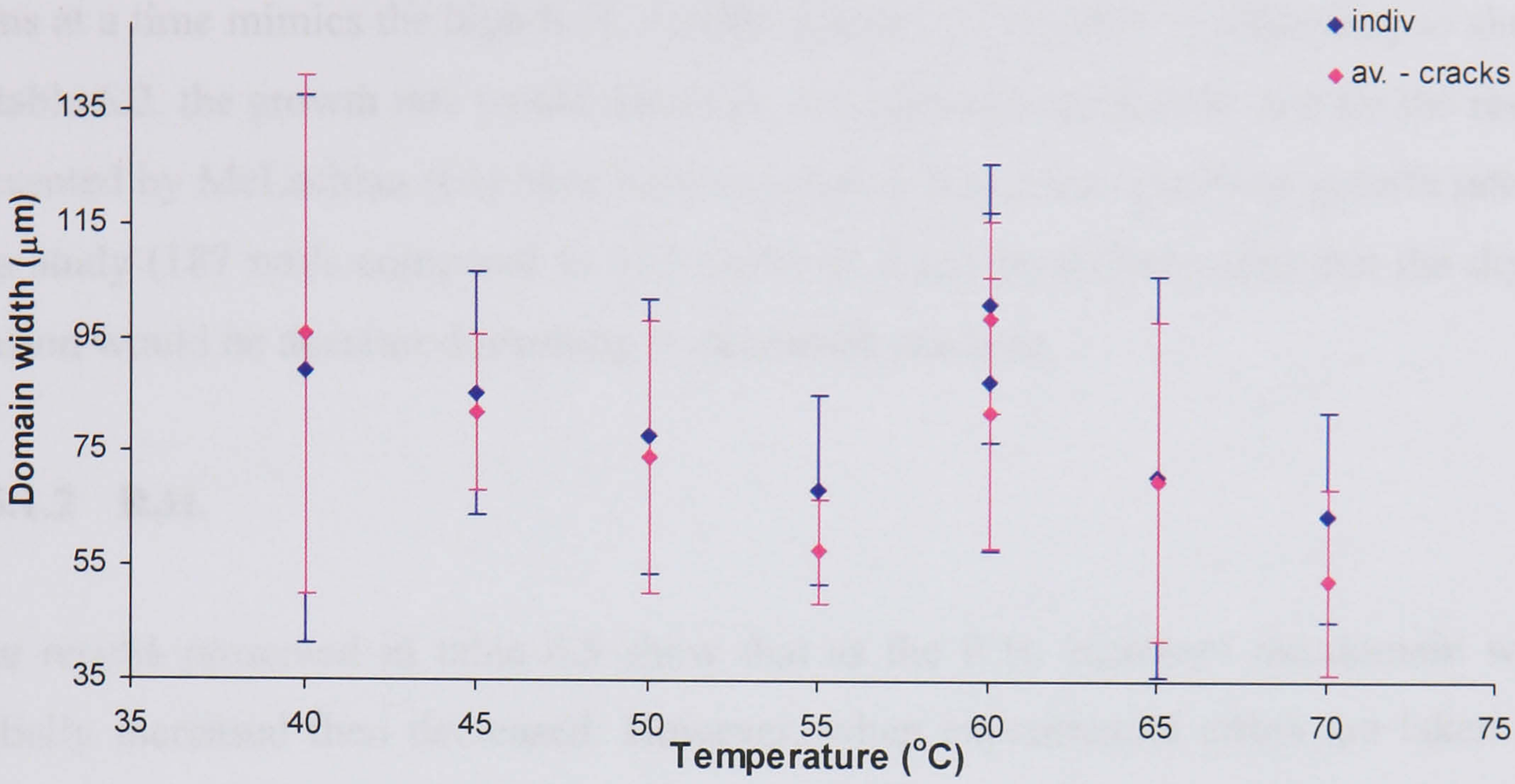


Figure 6.17 Variation of domain width with increasing growth temperature

As discussed previously in section 6.1 the cracks can be attributed to either shrinkage of the polystyrene spheres during the self-assembly procedure (36,122), or, to drying induced tension between neighbouring spheres as the solvent evaporates (6,126). It can therefore be hypothesised that as the growth temperature increases the shrinkage of the polystyrene spheres and the drying tension will increase and thus the surface of the films should become more cracked. This hypothesis agrees well with the results presented in table 6.5 and figure 6.17 and also follows the trend reported by Ye *et al* (45) where, as the growth temperature was increased, the distance between cracks decreased.

However, this proposed hypothesis does not explain why there is deviation from the trend around 60˚C, as shown in figure 6.17. The two films grown at 60˚C, 60 and 60(2), have different average domain widths. The domain width for the first growth at 60˚C growth is significantly higher than the calculated widths for the other temperatures and could therefore be an error. It could be argued that the domain width for the growth at 65˚C also does not fit the trend which may indicate that temperatures around 60-65˚C are optimum for thin film growth, which would be consistent with the literature (6,44).

The results from this study do not agree with the results reported by McLachlan *et al* (6), where as the temperature was increased from 25°C to 65°C the domain width increased from less than 50 μm to around 100-200 μm. However. the results reported by McLachlan *et al* (6,64) were grown using the procedure outlined in section 5.3, that is approximately ten films were grown at a time. As discussed in section 6.2.2 growing ten films at a time mimics the high R.H. condition used in this study and therefore as shown in table 6.2, the growth rate would decrease. The approximate growth rate for the results presented by McLachlan (64) have been calculated to be almost half the growth rate for this study (187 nm/s compared to 357 nm/s) so it can be hypothesised that the drying tension would be decreased resulting in decreased cracking.

6.5.1.2 R.H.

The results presented in table 6.5 show that as the R.H. increases the domain width initially increased then decreased. However, when experimental errors are taken into account the results are inconclusive and it could be argued that the domain width does not change with increasing R.H. The general assumption would be that increasing the R.H. lowers the growth rate, as shown in table 6.2, and therefore the domain width should increase. However the results do not support this hypothesis.

6.5.1.3 Colloidal concentration

The results presented in table 6.5 demonstrate that as the colloidal concentration is increased, the domain width increases, which is consistent with reports in the literature (64,122). As the colloidal concentration is increased it has been shown that the film thickness also increases (44,122). Therefore it can be hypothesised that an increase in film thickness enables more strain to be accommodated before it becomes energetically favourable for a crack to form. Thus as the colloidal concentration increases and the films grown become thicker, the domain width increases.

6.6 Film thickness

The influence of the growth parameters on the thickness of the films was also investigated. All thirteen films were cleaved using a clean scalpel blade and the thicknesses were then measured using the SEM and the ZYGO white light

interferometer. The two different techniques are described in section 5.4.4. The thicknesses obtained for all the films are summarised in table 6.6.

		SEM (μm)	ZYGO (μm)
Temp (°C)	40	20.28±0.56	18.98±2.58
	45	22.67±0.68	27.27±0.84
	50	19.20±0.33	21.53±1.53
	55	18.12±0.07	21.04±3.55
	60(2)	21.20±0.48	20.69±2.07
	65	15.63±0.27	23.55±1.89
	70	19.29±0.90	19.23±1.03
vol%	0.0533	6.95±1.34	4.57±1.90
	0.1065	9.02±0.32	12.03±1.70
	0.2130	16.97±0.48	23.57±1.60
R.H.	Low	16.97±0.48	23.57±1.60
	Medium	17.70±0.23	24.47±3.13
	High	19.26±0.59	21.56±0.50

Table 6.6 Thickness measurements for films grown at different temperatures

It is clear from a comparison of the SEM and ZYGO data that there are some discrepancies in the thicknesses obtained by the two techniques. As mentioned previously, section 5.4.4, when the thin films are cleaved using a scalpel blade it is probable that not all the layers of spheres down to the substrate are removed. Since the ZYGO uses white light, and can therefore not resolve individual spheres, it is unknown how many layers still remain on the substrate in the cleaved region. Therefore, the thickness measurements from the SEM have been taken as more reliable because the layers of spheres can be counted.

The results presented in table 6.6 suggest that the film thickness does not depend on the growth temperature. This is consistent with the observations reported by McLachlan *et al* (6) but contradicts those presented by Kuai *et al* (44) who demonstrate that for the three temperatures investigated in their study, the films grown at 60°C were the thickest. This was attributed to an optimum balance between the transfer of particles and assembly into the array.

The data shown in table 6.6 shows that the film thickness depends on colloid concentration which is also consistent with reports in the literature (44.122). As the colloidal concentration increases, there are more spheres to flux into the area of film formation resulting in an increase in film thickness.

The film thickness is shown to increase slightly as the R.H. increases, in agreement with the work by Kuai *et al* (44). The main step in the formation of a thin film is the convective transfer of spheres from the suspension to the thin wetting film. At low R.H. the film growth rate is fast, as shown in table 6.2, but if the transfer of particles is not correspondingly fast a thin film would be formed. As the R.H. is increased a balance is eventually reached between growth rate and the transfer of particles and this is where the thickest film would be formed (44).

It is interesting to note that, although the growth rates differ between the results presented in this study and those reported by McLachlan (64), at a colloidal concentration of approximately 0.2 vol% the thickness of the films grown at 65°C are comparable.

6.7 Why do cracks form?

It has been demonstrated in this study that the formation of drying cracks is unavoidable. Although previously hypothesised in section 6.1 that decreasing the temperature would reduce drying tension due to a slower growth rate and thus a decrease in cracking would be expected, the results presented table 6.5 show that at the lowest temperature investigated cracks are still formed. Although the domain widths may increase further at temperatures below 40°C, the quality of the films would be affected and the time taken for growth would be prohibitive.

The results reported in this chapter are consistent with the literature and demonstrate that crack free films cannot be formed using the self-assembly growth procedure. Therefore the best that can be done is to try and minimise the cracking that takes place. There have been many suggestions postulated for the reduction of cracking. Norris and co-workers (136) have demonstrated a method whereby silica spheres are sintered at 600°C before being used for the growth of self-assembled thin films. The implication is that the silica spheres behave as hard spheres (42), see section 1.6 for the definition of

hard spheres, and it is known that polystyrene colloids can also be modelled as hard spheres (137). However, although the films grown by Norris and co-workers showed no observable cracks this sintering protocol would not be suitable for polystyrene spheres since the decomposition of polystyrene starts to occur around 300°C (64.138). Jin *et al* (139) have shown that template-assisted colloidal self-assembly can eliminate cracks. In the method proposed by Jin *et al* (139) a (100) patterned template is formed by electron beam lithography and then self-assembly is carried out on this template. Crack free films of more than ten layers in thickness in an area 800x800 μm^2 have been reported to have been grown by this method (139). However, films grown by this method would not be suitable for the formation of macroporous thin films due to the presence of the (100) patterned template.

The results presented in table 6.5 and discussed in section 6.5.1.1 show that as the temperature increases the domain width, or crack spacing, decreases. It can therefore be hypothesised that crack spacing should depend on the solvent evaporation rate. However, the films grown in this study and those grown by McLachlan (64) at 65°C have different evaporation rates (357 nm/s compared to 187 nm/s) but comparable thicknesses and domain widths. This would indicate that the domain width is independent of solvent evaporation rate, or growth temperature, contradicting the data presented in table 6.5 and the hypothesis that domain width depends on solvent evaporation rate.

To explain this apparent contradiction it was hypothesised that there must be two different rates involved in thin film growth, (a) the growth rate and (b) the evaporation/drying rate (illustrated schematically in figure 6.18).

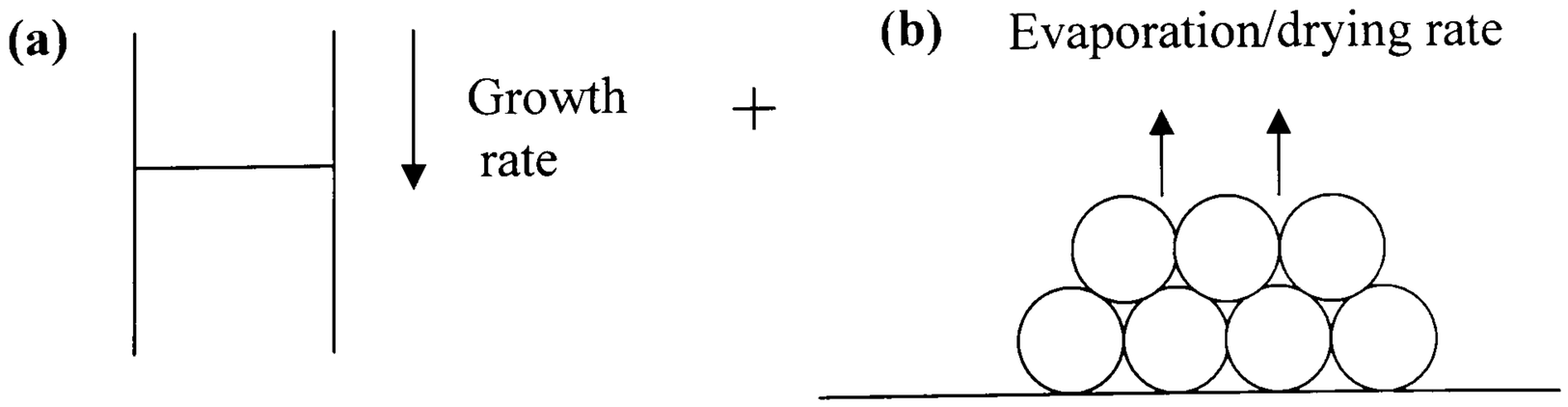


Figure 6.18 Illustration of hypothesised rates involved in thin film growth (a) growth rate (b) evaporation/drying rates

It has been established that the growth rate, or the drop of the meniscus, is proportional to the evaporation rate (figure 6.1). The evaporation/drying rate from the compacted region of spheres is also proportional to the evaporation rate but the constant of

proportionality is not the same as that in the growth rate. The results presented in tables 6.1-3 are a measure of the growth rate, or the drop in meniscus height. and are most likely independent of the drying rate from the compacted region. The evaporation of water from the compacted, semi-ordered, region of spheres is due to diffusion or percolation and can be compared to the percolation of water in drying mud (140).

As the meniscus falls, colloidal spheres are deposited on the substrate and as water evaporates from the system, the spheres become closer together until it becomes energetically favourable for those spheres to self-assemble into an fcc/hcp array. Koh and Wong (129) have recently demonstrated, through monitoring the PBG during colloidal self-assembly, that an fcc structure forms initially with interstitial water present. There is then a gradual reduction of the lattice parameter as more water evaporates from the system and the spheres become closer together. In this intermediate ordered state, the spheres are still mobile enough to remove point defects such as vacancies and dislocations. Zhao *et al* (126) have shown that the liquid bridge/capillary force, the force between two spheres of equal radius, plays a significant role in pulling the spheres together by driving the flow of solvent to the drying front.

Zeta potential measurements on the polystyrene colloids synthesised in this study, chapter 3, show that the spheres have negative surface charge. According to Coulomb's law, each charge generates an electric potential which will be compensated by opposite charges. The Derjaguin, Landau, Verwey, and Overbeek (DVLO) theory states that the total interaction between two particles in suspension is the sum of an attractive potential energy, due to van der Waals forces, and a repulsive potential energy from electrostatic or steric effects (93).

As the spheres become closer together it would be expected that, due to their negative surface charge, they would be repelled from each other. However, Juillerat *et al* (93) have shown that, for 75 nm silica spheres, the attractive capillary forces are at least four to five orders of magnitude greater than the interaction potentials calculated from DVLO theory. However, the capillary forces only act once the particles emerge from the solvent, which again indicates that the spheres are free to re-arrange till late on in the drying process.

Once enough water has evaporated, and the spheres are able to protrude from the solvent, the attractive capillary, or liquid bridge, forces pull the spheres together. A stress/strain is built up due to the low permeability of the ordered region which causes the tension in the liquid to be greater nearer the drying surface. The tension between the spheres builds up in the lateral direction, as illustrated in figure 6.19.

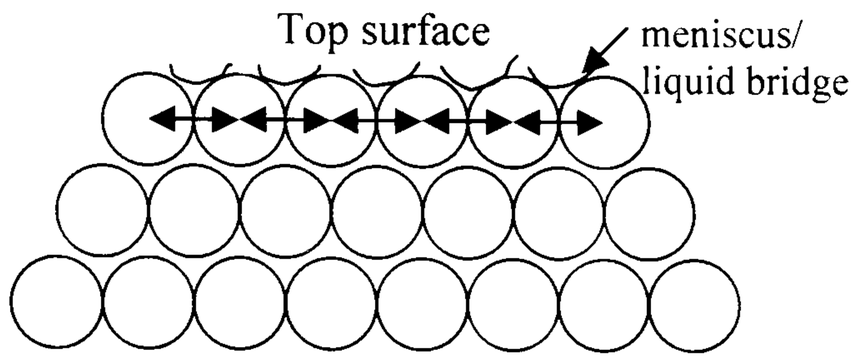


Figure 6.19 Illustration of the build up of strain between particles

Juillerat *et al* (93) have shown that for 80 nm silica spheres at 30˚C the maximal stress formed can be 17.5 MPa. When the stress between spheres exceeds the local tensile strength, it becomes energetically favourable for a crack to form (141). This crack relieves the stress locally along the sides of the crack but the stress is concentrated at the crack tip (141). The crack tip propagates in the direction of growth, perpendicular to the direction of maximum stress, until the stress is reduced below the local stress of the material (141). The total strain is constant only if the crack opening displacement is constant.

As the crack propagates through the ordered layers of spheres the menisci become smaller due to the water from this region having already flowed towards the top drying surface. It therefore becomes favourable for a crack to form in the horizontal direction. Juillerat *et al* (93) have shown that any crack nucleating at, or growing towards, a pre-existing crack will meet that crack perpendicularly. Thus pseudo-rectangular domains are formed. As the growth temperature is increased, the strain between spheres increases and therefore the domain widths get narrower.

At a given growth temperature the same 'amount' of strain can be accommodated between spheres, *i.e.* there should be the same number of cracks per unit area. For the results described by McLachlan (64) the evaporation rates, at a given temperature, are slower than those calculated in this study, as previously discussed. Thus the compacted region will be shorter, but there is no reason why the drying rate from the compacted region of spheres will not be the same in both cases, as it has been hypothesised that it is

independent of the growth rate. Therefore, before the meniscus can move down and deposit more spheres, the bottom layers of spheres are dry and it becomes favourable for a crack to form in the horizontal direction. Since, for the same unit area, cracks have formed in the horizontal direction accommodating some strain, the strain in the lateral direction can be accommodated for a slightly greater distance and thus the domains formed are wider. This would explain why the domains formed in McLachlan's work (64) are wider and shorter than the domains formed in this work.

6.8 Mechanism for cracking

There have been many proposed methods for the mechanism of cracking but the general consensus is that the crack spacing arises due to a balance between the elastic energy released and the surface energy consumed in crack formation. However, Routh and Lee (142) have proposed a new mechanism where hydrodynamics, specifically the distance a solvent can flow to relieve stress, controls the crack spacing.

Norris *et al* (35) have demonstrated that the flow of solvent plays an important role in the assembly of thin films. As discussed in the previous section capillary forces, or liquid bridge forces, play an important role in pulling the compacted spheres together by driving the flow of solvent to the drying surface. Evaporation arises at the small menisci between the spheres and creates capillary tension which pulls water through the compacted region to replace that lost by evaporation. This flow of solvent keeps the spheres wet and the water-air interface at the first layer of spheres (143). There must be a balance between the evaporation rate and fluid flow through the compacted region to keep the position of the air-water interface fixed. But as the compacted region grows, its resistance to flow increases, the small menisci between neighbouring spheres decreases and the evaporation/drying rate falls.

Since no further evaporation can occur to reduce the capillary pressure, a crack is formed to relieve the stress formed due to the difference in capillary and atmospheric pressure at the menisci. In the vicinity of the crack, reduction of water eliminates the capillary pressure, causing a flow of solvent towards areas of lower pressure in the grown film.

Many models have been proposed to explain crack spacing and suggest that the underlying model is a diffusive process. If fluid diffuses to the drying surface, there should be a smooth gradient in the water concentration from the compaction front to the drying edge. However, Dufresne *et al* (143) have shown by laser-scanning coherent anti-Stokes Raman scattering (CARS) that both the solid and fluid regions are wet, with the exception of the cracks and thus the diffusive model cannot be correct.

6.8.1 Hydrodynamic model

Routh and Lee (142) have hypothesised that it is the distance the solvent flows which determines the crack spacing and as such have determined a capillary or hydrodynamic length scale, X, over which the solvent is thought to flow to relieve the capillary pressure (equation 6.5).

$$X \approx \frac{20R(1-\phi)^2}{75\mu\phi^2}\left(\frac{3\eta_0\gamma^3}{E^3}\right)^{\frac{1}{4}} \qquad \textbf{Equation 6.5}$$

Where R is the particle radius, ϕ is the volume fraction, μ is the solvent viscosity, η_0 is the dispersion viscosity, γ is the water-air surface tension and E is the evaporation rate.

As discussed previously, the driving force for cracking is the capillary stress. A dimensionless group, P_{cap} (equation 6.6), which characterises the pressure distribution along the film surface between cracks, has been derived.

$$P_{cap} = \frac{20}{75}\left(\frac{3\gamma\eta_0}{E}\right)^{\frac{1}{2}}\frac{R(1-\phi)^2}{\mu\phi^2 H} \qquad \textbf{Equation 6.6}$$

Where all parameters have the same definition as in equation 6.5 and H is the film thickness.

A similar analysis has been carried out for the films investigated in this chapter, although in the experiments conducted by Routh and Lee (142) a Petri dish was used as the growth vessel to minimise the effects of horizontal drying fronts. The films were grown with spheres of diameter 387 nm, with an original dispersion of volume fraction (v.f.) 0.2134%. However, the v.f. of closest packing was taken to be 64%, a value which is between the 0.213 vol% colloidal volume fraction used and that at closest packing

(for fcc=74%). The evaporation rates are tabulated in tables 6.1-3 and the dispersion viscosity, η_0, was taken to be 1 Ns/m^2 for each dispersion (142). The film thicknesses were taken from the SEM values shown in table 6.6. Table 6.7 below summarises the water-air surface tension, γ, and the solvent viscosity, μ, at the seven temperatures investigated (134).

Temp. (°C)	μ ($\mu Pas/Nm^{-2}s$)	γ (mN/m)
40	653.2	69.60
45	600.1	68.77
50	547.0	67.94
55	506.8	67.09
60	466.5	66.24
65	435.3	65.36
70	404.0	64.47

Table 6.7 Water-air surface tension and solvent viscosity at increasing temperature

A plot of the crack spacing, y, shown in table 6.5, normalised by the hydrodynamic scaling factor, X, was plotted against the capillary pressure (P_{cap}). This graph is shown in figure 6.20 with a line representing the data fitted to the equation obtained by Routh *et al* (142) (shown in red).

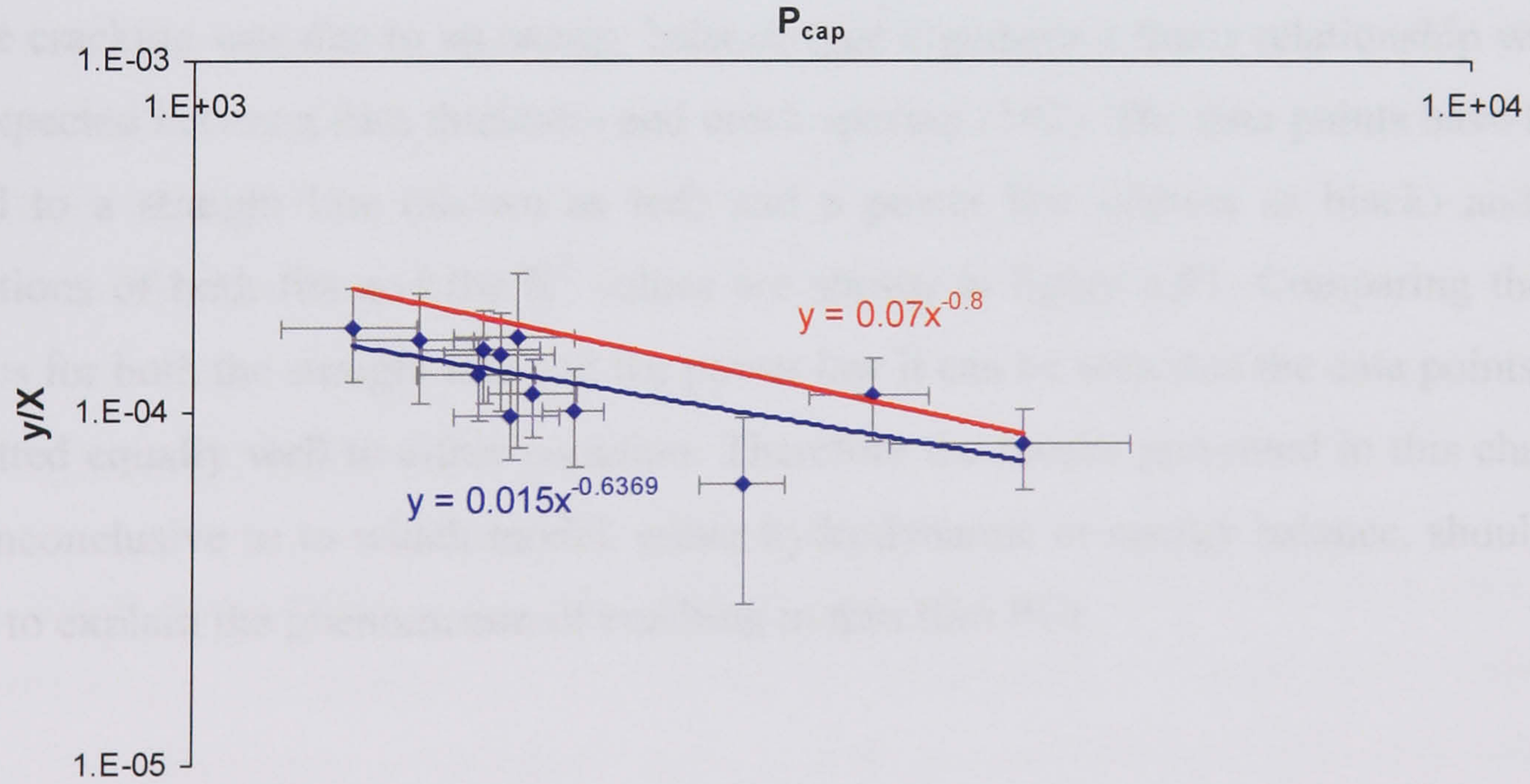


Figure 6.20 Collapse of crack spacing with hydrodynamic scaling

The results presented in figure 6.20 show that the data collapses to a single curve similar to the results shown by Routh and Lee. The collapse of the data follows the following power law, equation 6.7.

$$\frac{y}{X} = 0.015 P_{cap}^{-0.6369} \qquad \textbf{Equation 6.7}$$

Equation 6.7 indicates that the crack spacing scales with the film thickness to the power of 0.6369. This scaling factor is lower than the factor of 0.8 found by Routh and Lee (142) and may be due to the horizontal growth fronts present in our method for film growth and also the presence of the glass substrate.

In order to compare the data above with an energy balance type scaling, a graph of crack spacing versus film thickness was plotted (figure 6.21).

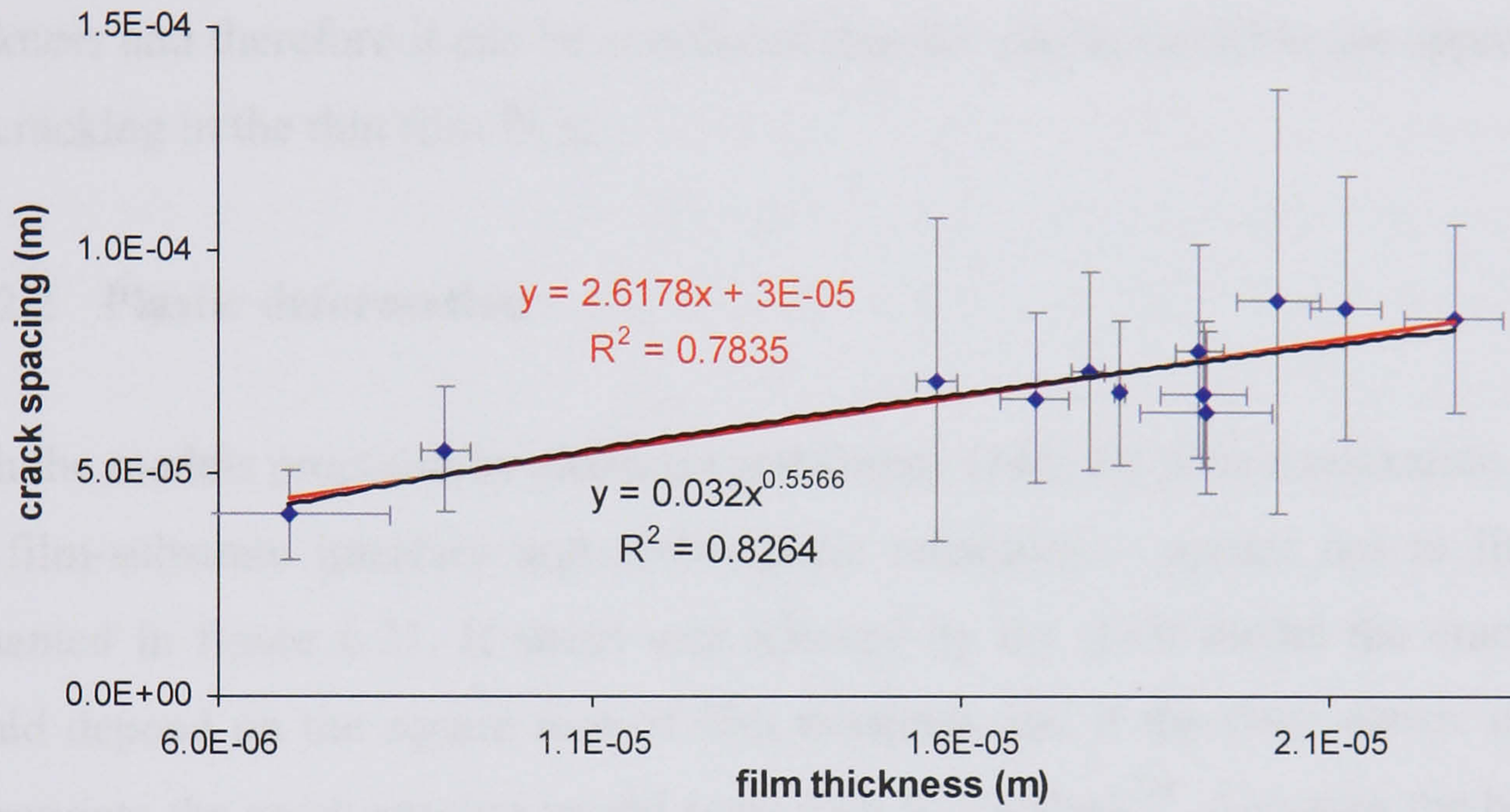


Figure 6.21 Crack spacing as a function of the film thickness

If the cracking was due to an energy balance type argument a linear relationship would be expected between film thickness and crack spacing (142). The data points have been fitted to a straight line (shown as red) and a power law (shown as black) and the equations of both fits and the R^2 values are shown in figure 6.21. Comparing the R^2 values for both the straight line and the power law it can be seen that the data points can be fitted equally well to either equation. Therefore the results presented in this chapter are inconclusive as to which model, either hydrodynamic or energy balance, should be used to explain the phenomenon of cracking in thin film PCs.

6.8.2 Other models

6.8.2.1 Elastic relaxation

Atkinson and Guppy (144) have considered the crack patterns that would form if the crack spacing arose from elastic relaxation. If the stress relaxation was elastic in nature then the stress should decay with distance from the crack over a characteristic length, approximately equal to the film thickness. This model would predict a crack spacing that decreases with film thickness, since the greater the strain to be relaxed the closer the cracks are (144). Figure 6.21 illustrates that the crack spacing increases with film thickness and therefore it can be concluded that the elastic model is not appropriate for the cracking in the thin film PCs.

6.8.2.2 Plastic deformation

Both the models proposed by Atkinson and Guppy (144) for plastic relaxation – shear at the film-substrate interface and visco-elastic relaxation – appear not to fit the data presented in figure 6.21. If stress was relieved by the shear model the crack spacing would depend on the square root of film thickness and if the visco-elastic model was appropriate the crack spacing would scale with $(\text{thickness})^{-3/4}$. Although the best fit line illustrated in figure 6.21 shows that the crack spacing is proportional to the film thickness raised to the power 0.5566, it is known that the cracks formed in the films do not go all the way to the substrate. Due to a strong sphere-substrate interaction at least one layer of spheres is left on the substrate when the film cracks, or delaminates, and thus the shear model would not fit with the results presented in this chapter.

6.9 Conclusions

This chapter summarises a series of experiments which were conducted in an attempt to determine the optimum growth parameters for the formation of good quality thin film PCs. The parameters investigated were growth temperature and R.H. and colloidal concentration.

Experiments to derive an overall growth rate indicated that temperature was the most important growth parameter, which agreed with reports in the literature (6,44,45,64). In

order to determine the optimum growth conditions the phenomenon of cracking was investigated, since if self-assembled PC films are to be feasible for technological applications they should possess the widest domains possible. Table 6.6 summarises the domain widths for the different growth parameters investigated. It has been demonstrated that the widest domains are formed at 60-65°C, a medium R.H. and a high colloidal concentration. Thus it can be seen that the films grown routinely, outlined in chapter 5, have been grown at approximately the optimum growth conditions. Although a high colloidal concentration forms films with wide domains, depending on the purpose of the films, thick films are not always beneficial.

Through investigating the process of cracking it was attempted to formulate a model for thin film growth, since it is clear from the literature that the fundamentals of self-assembly are not well understood. Although the results are only taken from a small data set, and therefore not conclusive, the results obtained indicated that the crack spacing, or domain width, does not simply originate from an energy balance type argument. As demonstrated by Routh and Lee (142), for a wide range of evaporation rates, particle sizes and materials, the elimination of pressure due to cracking must also be taken into account.

7 Three-Dimensionally Ordered Macroporous Films

7.1 Introduction

Since the proposal of photonic crystals (PCs) there has been much research interest in being able to fabricate a periodic structure possessing a full photonic band gap (PBG). The synthetic opal structure has been widely researched as a method for forming 3-D PBG materials. The synthesis, characterisation and optimisation of thin film synthetic opals has been discussed in the previous chapters. However, it is unlikely that synthetic opal structures will realise a full PBG due to the low refractive index contrast (RIC) between the constituents and symmetry considerations.

Work has been undertaken to increase the RIC found in synthetic opals by using spheres of higher refractive index or by filling with a second material of higher refractive index. Busch and John (23) have shown that for close packed structures, the RIC must be ≥ 2.8. Since the value for refractive index cannot be less than one, the highest RIC can be obtained by forming an ordered array of air voids surrounded by a material of high refractive index. In addition the filling fraction of the air voids must be greater than 80% (1).

A promising technique for forming a material with a PBG in the visible spectral region has been reported where the synthetic opal structure is used as a template to form a 3-D macroporous material (3-DOM) or inverse opal (see for example (15,71,112,138,145)). The easiest way to visualise the formation of a 3-DOM material is to first consider the structure of synthetic opal. In synthetic opal a cubic close packed array of spheres exists where each sphere touches its twelve nearest neighbours at point contacts. Since the spheres are arranged periodically the voids around the spheres are also arranged periodically. If the voids are filled with another material, *e.g.* by a sol-gel method (103), and then the spheres are removed leaving behind the material in the voids, a macroporous material is formed. This infilling method forms a close packed array of air voids surrounded by interconnected walls of the filling material. The wall material corresponds to the contact points of the spheres and the voids in the original template. This method is illustrated schematically in figure 7.1.

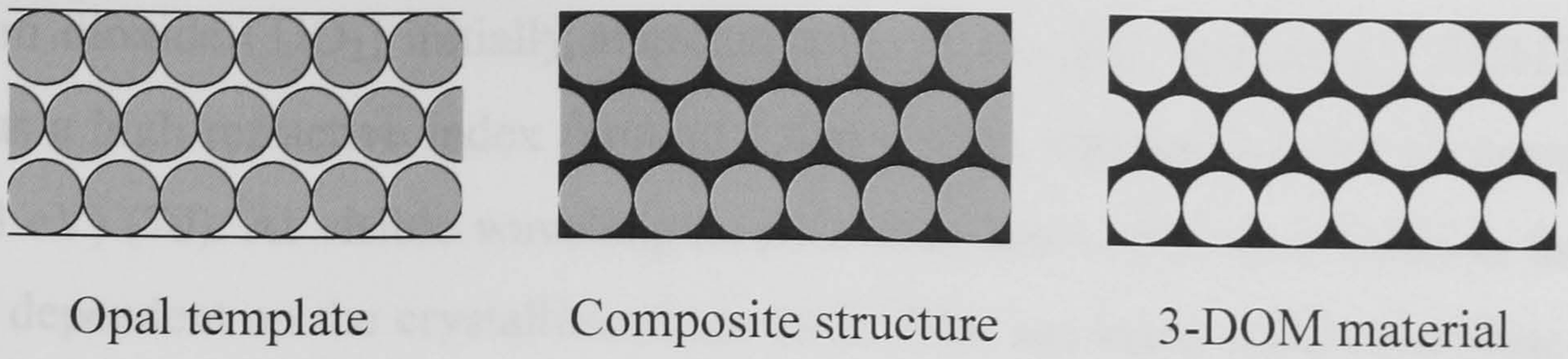


Figure 7.1 **Schematic illustration of the formation of a 3-DOM material from a synthetic opal template**

As discussed in chapter one the Brillouin zone of a face centred cubic (fcc) lattice is the most favourable for the formation of a PBG material (18). Since the spheres in the template are arranged in an fcc lattice then so must be the air voids in the inverse structure.

7.2 Applications

Macroporous materials have been proposed to have many applications in a wide variety of different fields. Separation processes and catalysis would benefit from the more uniform macroporous materials provided by the templating method (71). Other possible applications are thermal insulators and porous electrodes. In the field of PCs the fabrication of macroporous materials is predicted to have useful optical properties such as photon localisation, inhibition of spontaneous emission and the realisation of a complete PBG.

While the formation of a complete PBG material is still the goal for many research groups there is also interest in the formation of functional macroporous materials which do not exhibit a complete PBG. Functional macroporous materials will be discussed in chapter 8.

7.3 Literature associated with the formation of 3-DOM materials

The main requirement for the formation of inverse opal with a complete PBG in the visible spectral region is the choice of material used to infill the voids of the template. The material needs to have both a high refractive index and negligible absorption at optical wavelengths (146). It has proven extremely challenging to find materials which fulfil both criteria simultaneously.

Titanium dioxide (TiO_2) initially attracted a lot of research interest (21.71,112) since TiO_2 has a high refractive index (around 2.6 at λ=500 nm) and a large electronic band gap (~3 eV) (70). At visible wavelengths pure TiO_2 has a refractive index in the range 2.4-3.0 dependent on the crystalline phase (21). TiO_2 has many solid crystalline phases which depend on the temperature the material is crystallised at. Anatase is the low temperature phase which is stable at temperatures below 700°C and rutile is the stable phase formed above 700°C (112). The rutile phase has a higher refractive index than the anatase phase (~3 compared to ~2.4) and would therefore be the favourable phase to form in the hope of the formation of a PC with a complete PBG (16).

The most common method for the formation of macroporous TiO_2 is the infiltration of the synthetic opal template with Ti(IV) alkoxide precursors in an alcoholic solvent. The voids between the spheres are filled by precipitation from a liquid-phase chemical reaction (112). When the precipitation is complete the spheres from the template are removed either chemically or by heat treatment. Heat treatment is preferable than removal by chemical means because the alkoxides need to be crystallised to solid TiO_2.

After template removal the structure is composed of an ordered hexagonal pattern of spherical air holes surrounded by an interconnected crystalline TiO_2 backbone. Electron diffraction carried out in the TEM on TiO_2 crystallised at 575°C has shown that the TiO_2 backbone is polycrystalline in nature and the interplanar spacings measured from the diffraction patterns are consistent with the anatase form of TiO_2 (21). The results presented by Richel *et al* (21) are consistent with those reported by Wijnhoven and Vos (112) who used optical Raman spectroscopy to determine the anatase form of TiO_2. Since the refractive index of the rutile phase of TiO_2 is higher than anatase, and it would therefore be beneficial for the formation of a complete PBG material, attempts have been made to heat the macroporous TiO_2 to higher temperatures to form the rutile phase (16,147). However, the conversion of anatase TiO_2 to rutile leads to extensive grain growth resulting in disruption of the fragile periodic structure of the 3-DOM TiO_2.

In the search for a complete PBG material macroporous silica (147,148), metal oxides *e.g.* TiO_2, ZrO_2, Al_2O_3 (71,147) and metals (149), to name just a few, have been investigated.

Another group of materials which simultaneously exhibit high refractive indices and low absorption at optical wavelengths are semiconductors. Success has been achieved for macroporous silicon and germanium structures with PBGs around 1.5 μm and 2 μm (17). The 3-DOM silicon structure satisfies the two essential criteria for complete PBG formation – a high refractive index (3.45 at 1.5 μm) and the optical absorption edge of silicon occurs at a wavelength well below the PBG (9). Recently a method has been proposed which could be suitable for the development of tantalum(V) nitride inverse opal with a complete PBG in the visible region (48).

In the realisation that the formation of a complete PBG 3-DOM structure is challenging, due to the difficulty in finding a material with simultaneous high refractive index and low absorption at optical wavelengths, there is a continued interest in the formation of tunable, or multifunctional, 3-DOM materials.

Many of the reports in the literature discuss the formation of 3-DOM ferroelectric materials (50-52,103,150,151). Ferroelectric materials are a large class of complex metal oxides with tunable dielectric and optical properties which vary with external conditions and are therefore ideal starting materials for achieving tunable PCs (51). The two most studied ferroelectrics are barium titanate ($BaTiO_3$) and lead lanthanum zirconate titanate (PLZT). 3-DOM $BaTiO_3$ has a temperature tunable photonic stop-band (103,150). PLZT as Li *et al* (51) have reported has a photonic stop-band which is tuned by an external electric field.

7.4 Reported experimental methods

Regardless of the infiltration precursor, the template material or sphere removal method the critical point of the templating technique lies in the design of the fluid-solid transformation which takes place in the voids of the template (138). There are reports in the literature of the fluid being a pure liquid (22,70), a solution (138), nanoparticles (146,148), colloidal particles (16) and gases (15,146).

In order to obtain well ordered macroporous materials by the templating method three requirements have to be satisfied (138). Firstly the solvent should wet the template spheres well so that the fluid can penetrate the template array completely and eliminate any faults in the final 3-DOM structure produced by non-wetting regions. Secondly the

precursor should have high solubility in the solvent to allow maximum precursor loading, allowing the walls in the macroporous material to be strong enough to avoid collapse. Finally the precursor should not melt at a temperature where the latex softens and should have a higher melting point than the temperature at which the latex spheres are gasified and burnt.

7.4.1 Before infiltration

Many authors have reported the 'wetting', or soaking, of the template with ethanol prior to the infiltration of the precursor (21,22,31,71,138,147). As previously discussed the wetting of the template spheres enhances the penetration of the liquid precursor into the voids of the template.

It has been reported that for templates formed from SiO_2 spheres sintering takes place prior to infiltration (31,152,153). The sintering process forms small necks between the spheres which not only improves the mechanical strength of the template but aids the final removal of the template (153). When polymer templates are used the interaction between adjacent spheres are weak, typically van der Waals and dipole-dipole interactions. Due to the thermal degradation of polymers, sintering to high temperatures cannot be achieved without the polymer decomposing and oxidising. But it has been reported that stronger contact between the spheres can be achieved by heating to 80°C, *i.e.* below the glass transition temperature, for 30 minutes (54,153).

7.4.2 Infiltration methods

Depending on the precursor used there have been many reported methods of infiltration into the template. Some of the most common techniques are described below.

7.4.2.1 Sol-gel infiltration

Many of the reports in the literature rely on the process of self-assembly to form the template combined with a sol-gel method to fill the voids and form a 3-DOM material (56,153,154). The reagents for sol-gel syntheses are usually metal organic compounds, *e.g.* titanium alkoxides, which are usually covalent liquids mixed in the appropriate ratios (40). The sol is allowed to penetrate into the voids between the spheres of the

template. Gelation occurs when the sol-filled template is exposed to the atmosphere where water vapour hydrolyses the alkoxides. This hydrolysation is why many authors report the use of a nitrogen filled glove box when using Ti(IV) alkoxides as precursors.

7.4.2.1.1 Vacuum filtration

Initially the most common method for producing 3-DOM materials was by a vacuum infiltration technique (103,147,151,155). The dried latex template is placed in a Buchner funnel and then soaked with the precursor. The use of the vacuum ensures that the precursor is pulled through the voids in the latex template and therefore maximum filling is achieved.

7.4.2.1.2 Capillary infiltration

The simple method of vacuum infiltration cannot be used when the synthetic opal template is contained within a glass capillary. In this case the capillaries are opened at the bottom and placed into a solution of the precursor material (70.112). This method, which has been reported for TiO_2 precursors, relies on capillary forces to draw the precursor into the voids of the template.

7.4.2.1.3 Dip/Fill

The majority of the work which is reported in the literature concerning the formation of 3-DOM materials has the common feature that the template is free-standing or contained within a capillary. When considering a template attached to a substrate, restrictions are imposed on the methods of infiltration. However the formation of 3-DOM materials supported on a substrate are important for two main reasons. Firstly the 3-DOM structure is porous (~80% air) and extremely fragile and therefore the presence of a substrate provides mechanically strength. Secondly, if the 3-DOM material is functional it is likely that in order to test any properties a contact needs to be made to the structure. Due to the fragility of the 3-DOM material it would be much easier to make a contact to the substrate than attempt to contact the easily damaged film.

The majority of techniques employed to infill supported templates involve a dip-infiltrating process (50,54.148,153). In this technique the substrate with the attached template film is vertically immersed into the precursor solution where the solution is allowed to penetrate the voids between spheres by capillary forces. The template film is then slowly withdrawn, either manually or mechanically, from the solution and allowed to dry. This process is then repeated a number of times to ensure complete infiltration

depending on the template thickness, precursor concentration *etc*. During the lifting process the precursor solution slowly evaporates inducing a flowing movement of the solvent within the template (148). This flow of solvent allows the precursor to be drawn into the template where it can precipitate.

7.4.2.2 'One-pot' synthesis

Two authors (16,31) have reported a method whereby the template formation and infiltration occurs simultaneously, which has been reported to overcome many of the limitations of sol-gel infiltration methods. In the 'one-pot' synthesis described by Subramanian *et al* (16) a nanoparticle TiO_2 solution is mixed with a monodisperse colloidal suspension of polystyrene spheres. As the water slowly evaporates, the polystyrene spheres self-assemble and the ultrafine oxide particles pack into the voids between the spheres.

In the second method described by McComb *et al* (31) a solution of titanium ethoxide and dry ethanol was produced and the dried latex spheres were added. A quartz plate was added to this solution and placed in a temperature controlled environment and left for around one week, similar to the process for normal opal growth. When all the liquid had evaporated the plate was coated with a white deposit which was a composite latex-TiO_2 material.

7.4.2.3 Electrodeposition

3-DOM cadmium-selenium (156) and zinc oxide (157) have been reported formed by electrodeposition. In electrodeposition the opal template is either grown on a conductive substrate, *e.g.* ITO (157), or the free-standing template is placed on a conductive substrate (156) which acts as the cathode. The template is then placed in a bath of the precursor solution and an anode is added forming an electrochemical cell. The morphology and thickness of the 3-DOM film can be controlled by adjusting the current or voltage passed through the electrochemical cell. The biggest advantage of this filling technique is that is that a high filling fraction of precursor can be achieved because the filling occurs from the bottom of the template, *i.e*. the cathode, to the top (157).

7.4.2.4 Chemical Vapour Deposition

Another approach which has been successful in forming 3-DOM materials is chemical vapour deposition (CVD), although initial attempts failed to achieve homogeneous filling (146). The formation of inverse silicon (9) and germanium (158) have been reported, both of which have complete PBGs in the near IR spectral region. In the CVD method the template is placed in a high vacuum cell into which a gas precursor, disilane and digermane for silicon and germanium respectively, is introduced. The cell is then cooled allowing the gas precursor to condense. The cell is then heated and above a certain temperature, which is precursor dependent, the gas decomposes within the template. Miguez *et al* (158) have reported that germanium growth takes place layer by layer and that homogeneous filling throughout the entire template is achieved.

7.4.2.5 Atomic Layer Deposition

Atomic layer deposition (ALD) has been proposed as a promising route to forming 3-DOM materials and has recently been reported for the formation of 3-DOM zinc oxide (145) and aluminium oxide (15). ALD is a modified CVD growth method where the substrate is only exposed to one reactant at a time. After every available surface site has reacted with the first precursor the reactor can be purged before the second precursor is introduced eliminating any gas-phase reactions (15).

7.4.3 Sphere removal

Once the composite template-precursor material has been formed the spheres need to be removed in order to form the 3-DOM material. The most common method reported in the literature for the removal of the template is heating, or calcination, of the latex spheres (50,103,112,138,151,155). During the calcination process the latex spheres undergo several processes such as glass transition, decomposition and oxidation. Stein and co-workers have reported that the polystyrene starts to combust at temperatures above 310°C and that this is an extremely exothermic process (138). The calcination process is typically carried out at a slow heating rate and under flowing air in an attempt to minimise damage to the product structure caused by the exothermic combustion process of the polystyrene.

Although in the majority of publications polystyrene spheres are used as the template material it has been reported that the use of poly(methyl methacrylate) (PMMA) spheres can improve the quality of the 3-DOM material formed (159). PMMA has a better thermal degradation character because it decomposes by chain polymerisation. When PMMA degrades a smaller amount of carbon is left compared to polystyrene and milder heating conditions are required to remove the PMMA template. In addition PMMA spheres have better wettability than polystyrene spheres allowing the precursor solution to penetrate the PMMA template more effectively (159).

The main advantage of using heat treatment to remove the latex spheres is that the precursor material can be simultaneously crystallised. During the calcination process the hydrolysed precursor material starts to dehydrate and metal-oxide-metal bonds are formed causing a densification of the product (104). Since the heating process can be detrimental to the quality of the resulting 3-DOM material care has to be taken to ensure that the composite material is not subjected to needless high temperatures. Consequently XRD analysis is often completed on the precursor material to investigate its crystallisation profile so the correct heating profile can be selected (56,103,151).

However the main disadvantage of using heat treatment to remove the latex spheres is that shrinkage relative to the template occurs (21,56,103,112,160). There are two possible reasons for this shrinkage. Firstly the latex spheres of the template are mesoporous and probably decrease in diameter as the water vapour is released from the pores during heating (21). Secondly during the crystallisation process the precursor material densifies causing a contraction of the wall material. For the case of TiO_2 the density of titanium(IV) ethoxide is 1.088 gcm^{-3} compared the density of anatase equal to 3.9 gcm^{-3}. Depending on the infiltration method, the heating rate and the precursor material a wide range of shrinkages have been reported in the literature. The lowest reported shrinkage is 17.5% reported by Richel *et al* (21) for TiO_2 and the highest reported was 40% for $BaTiO_3$ (151). Wijnhoven and co-workers (70) have found the sphere/void shrinkage to be around 30% independent of the original sphere diameter. The shrinkages reported for supported 3-DOM materials are generally greater than free-standing materials because the isotropic compressive strain on the crystal incurred during heating cannot be accommodated as well with the presence of the substrate (31).

In order to overcome the heat induced shrinkage the one-pot synthesis route reported by Subramanian *et al* (16) uses colloidal particles of TiO_2 rather than the usual titanium alkoxide precursors. Using colloidal particles reduces the shrinkage because the particles tend to pack to high volume fraction in the voids and therefore there is less densification than alkoxides upon heating. A shrinkage of 6% was reported for 3-DOM TiO_2 using the one-pot synthesis method (16).

Another method which has been employed to remove the latex template is the use of solvents which should reduce the problem of shrinkage. The use of organic solvents, such as tetrahydrofuran, has been reported (70,112,147). However if the latex spheres swell before they dissolve the ordering of the resulting 3-DOM material is destroyed. The use of organic solvents for sphere removal is only suitable for precursor materials which are already crystalline since the sample does not get heated. If non-crystalline precursors are used, for example titanium alkoxides, heat treatment is required before or after sphere removal which will have a detrimental effect on the formed 3-DOM material.

There are reports of silica being used to form the templates since silica spheres have increased thermal and chemical stability compared to latex spheres (125,153,154). However the increased stability of the silica means that template removal becomes more difficult. To thermally remove silica spheres temperatures of at least 1000°C, a temperature at which most precursor materials would be damaged, are required. In addition most of the commonly used substrates for supported 3-DOM materials, *e.g.* glass or quartz, would be deformed at these temperatures. Consequently silica templates are removed by etching with strong acids, *e.g.* sulphuric acid (15), or strong bases, *e.g.* sodium hydroxide (153,154). Both of these chemical treatments are incompatible with many precursor material systems and the composite material still requires to be heated if crystallisation of the precursor is needed. As a result of the problems faced removing templates formed from silica the majority of work reported is carried out with templates formed from latex spheres.

7.5 Precursor Material

The ferroelectric material lead zirconate titanate (PZT) has been chosen as the precursor material in this project. PZT has a high refractive index (~2.4-2.7) and high band gap

energy (~3 eV) (57). Similar to the 3-DOM PLZT crystals, which have been reported by Li *et al* (51,56), 3-DOM PZT films may be potential candidates for tunable, or multifunctional PCs.

Lead titanate ($PbTiO_3$) is a ferroelectric material with a Curie temperature of 490°C. When some of the Ti^{4+} ions in $PbTiO_3$ are partially replaced with Zr^{4+} ions with a molar ratio x, a solid solution $xPbZrO_3$-$(1-x)PbTiO_3$ ($0<x<1$) is formed (40). This solid solution is called lead zirconate titanate, $Pb(Zr_xTi_{1-x})O_3$ or PZT and has the perovskite structure with Ti^{4+} and Zr^{4+} ions found at the B sites at random (refer to figure 1.7).The phase diagram for the PZT system is shown in figure 7.2.

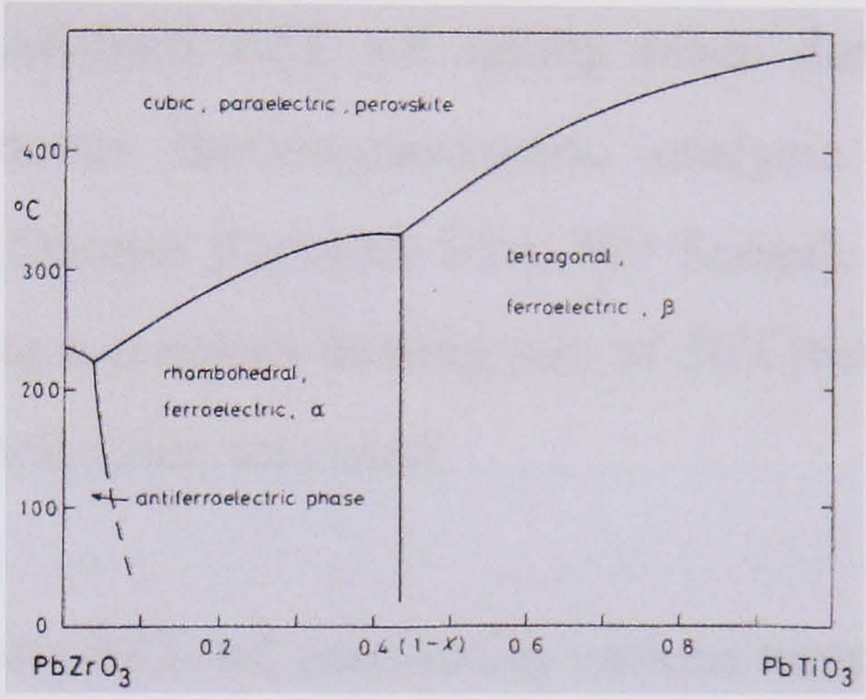


Figure 7.2 Phase diagram for the solid solution $PbZrO_3$-$PbTiO_3$ (40)

The phase diagram indicates that PZT behaves as a ferroelectric material at room temperature and when the solid solution contains more than 10% $PbTiO_3$ and its phase has a non-centrosymmetric structure *i.e.* tetragonal, rhombohedral or orthorhombic. A morphotropic phase boundary separates the rhombohedral phase (Zr rich) from the tetragonal phase (Ti rich) and at room temperature the boundary is at the Zr/Ti ratio 52/48. Below 10% $PbTiO_3$ content, PZT behaves antiferroelectrically similar to $PbZrO_3$ (40).

7.6 Experimental methods

7.6.1 Characterisation of PZT sol

The PZT source used in this project was a PZT sol of composition $Pb(Zr_{0.3}Ti_{0.7})O_3$ or PZT(30/70) synthesised by Cranfield University. The PZT(30/70) sol is prepared from the starting materials lead acetate, zirconium n-propoxide and titanium n-butoxide (161).

The lead acetate is dissolved in a methanol/methanol-amine mixture with gentle warming. The zirconium n-propoxide and titanium n-butoxide are mixed separately in the correct ratio and ethanol and a stiochiometric volume of acetic acid are added to the mixed solution. The Zr/Ti solution is stirred at room temperature for one hour and then the lead solution is added and the combined solution is stirred for a further two hours. Acetic acid is added to adjust the pH and the PZT concentration to 0.4 M. The resulting PZT solution is filtered through a 0.2 μm filter to remove any large aggregates and ethylene glycol is added to prevent cracking and to improve the surface smoothness of any films grown (162).

The reactions of the uncalcined PZT sol taking place during heat treatment were investigated by simultaneous thermogravimetric analysis (TGA) and differential thermal analysis (DTA) (Stanton Redcroft STA 780 Series). The analysis was carried out under flowing air using a constant heating rate of 20˚C/min from room temperature to 960˚C and an alumina reference was used.

The crystalline nature of the PZT sol calcined at various temperatures was investigated by X-ray diffraction (XRD). The PZT sol was dried and then calcined under the same conditions that the composite PZT-template material would be treated at. The PZT powders calcined at 490˚C and 530˚C were analysed by XRD using a Philips PW1700 series automated powder diffractometer with a secondary graphite crystal monochromator and Cu Kα radiation (λ=1.5406 Å).

In order to determine the exact composition of the PZT sol after calcination energy dispersive X-ray (EDX) analysis was carried out in the TEM (JEOL 2010). The electron beam was focussed on an area (~50 nm in diameter) of the sample and an EDX spectrum was recorded. Three different areas of the sample were analysed.

The final method used to characterise the PZT was Raman spectroscopy. The Raman data was collected at the University of Strathclyde by Mr D. Cunningham. The Raman data was collected using a Renishaw InVia spectrometer with a 0.1 mW Ar^+ 514.5 nm laser. A 5x objective lens was used and the accumulation time was fifteen seconds.

7.6.2 Template Film Growth

The polystyrene template films were grown as described in chapter 5. The films were grown at 65°C in a temperature stable incubator on pre-cleaned indium tin oxide (ITO) substrates. In the course of this study template films of varying thickness (5-10 μm) were produced by varying the concentration of the polystyrene colloid.

7.6.3 Heat treatment of the polystyrene template

Although it is well documented that the decomposition of polystyrene starts at around 300°C and that by 400°C the polystyrene has all decomposed (64,138) thermal analysis was carried out on a dried polystyrene sample (reference 09/08/04). The sample was heated in the temperature range 25-1000°C under flowing air at a rate of 10°C/min against an alumina reference.

The effect of heating the polystyrene templates prior to infilling was also investigated. The films were placed in a temperature controlled oven for thirty minutes at temperatures of 80°C and 100°C.

7.6.4 Infiltration of the PZT sol

Initially five different methods were investigated for infiltrating the PZT sol into the voids of the template film and the PZT was diluted with ethanol prior to infiltration. The five initial methods are summarised in table 7.1.

Method	Description
1	Dip in solution
2	Dip with glass coverslip
3	As 2 but remove coverslip to dry
4	Drop solution on from above, hold film horizontally
5	As 4 but hold film vertically

Table 7.1 Summary of the five initial methods investigated for infiltration

The effect of dipping the film in ethanol to wet the surface before the dipping in the PZT/ethanol solution was also investigated. The infilling process was repeated two to

three times depending on film thickness and PZT concentration to ensure that filling would occur through all the layers of the template film.

Method one was found to give optimum filling and the 3-DOM materials with the best ordering and was therefore used for all future experiments. In method one the film was simply immersed into the PZT/ethanol solution for thirty seconds and then slowly withdrawn manually and allowed to dry in the atmosphere. This method is similar to the technique published by Gu *et al* (148) but there was no mechanical control of the lifting speed. Figure 7.3 schematically illustrates the infiltration process.

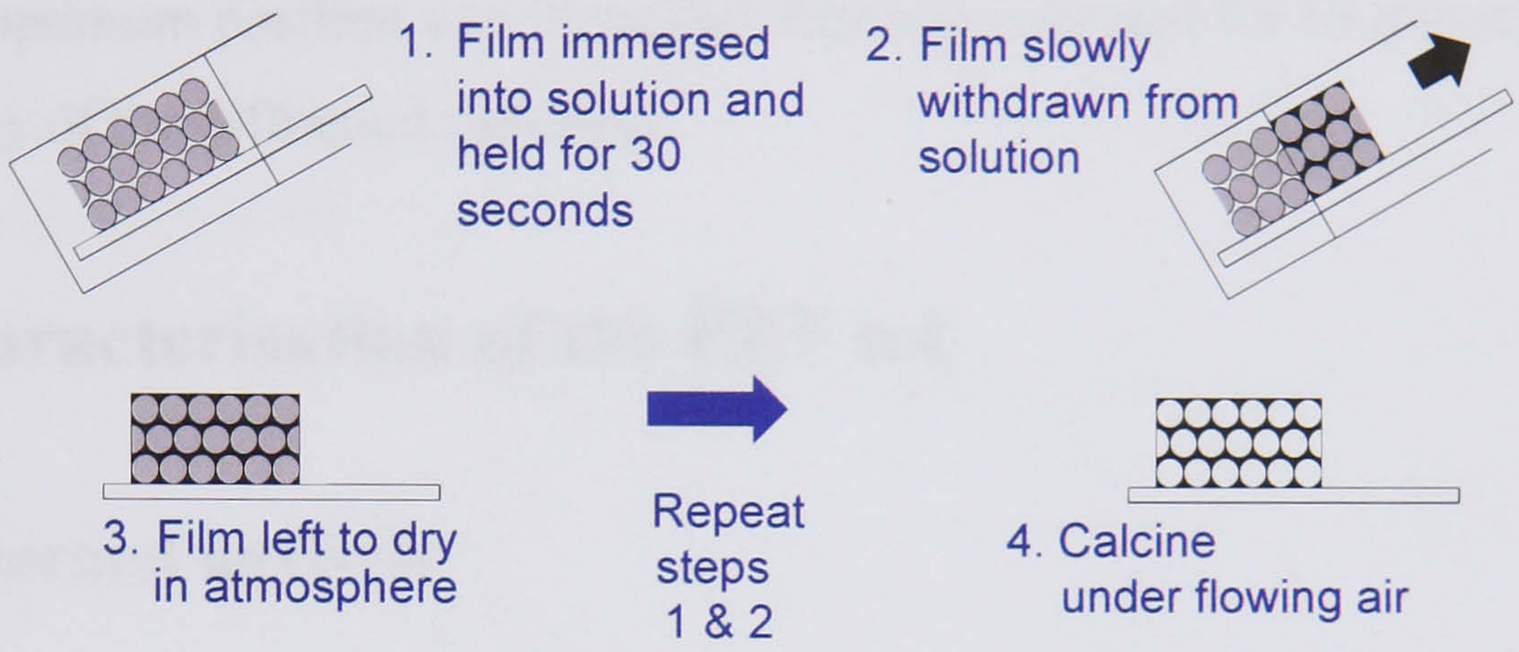


Figure 7.3 Schematic illustration of the optimum infiltration method

Since the experimental method for filling the voids of the polystyrene template with PZT had been optimised experiments were conducted investigating the effect of the thickness of the template and the PZT concentration.

7.6.5 Calcination conditions

The polystyrene template can be removed and the PZT crystallised in a single step heat treatment. A tube furnace, which was calibrated prior to use, was used to calcine the composite films. The composite films were heated at a rate of 1°C/min to 530°C, held at this temperature for six hours and then allowed to cool slowly to room temperature. A bubbler was connected to one end of the furnace tube and moist air was blown through the tube during the heating process to accelerate the decomposition reaction of the polystyrene spheres. Although the majority of composite films were calcined under the same conditions some experiments were conducted to investigate the effect of varying the heating rate and the air flow.

7.6.6 Analysis of the 3-DOM PZT films

The 3-DOM films of PZT formed in this chapter were analysed using reflectance spectroscopy and scanning electron microscopy (SEM). XRD analysis was carried out on both 3-DOM PZT scraped from the substrate surface and on supported 3-DOM PZT. The XRD analysis for the supported 3-DOM film was carried out on a Nonius PDS120 XRD diffractometer. Copper $K\theta_1$ (λ=1.5406Å) radiation was selected from the primary beam using a germanium (111) single-crystal monochromator, and horizontal and vertical slits were used to restrict the beam to a size of 0.24 by 5.0 mm respectively. When the optimum position was identified data was collected for 15 minutes to increase the intensity of the diffracted radiation.

7.7 Characterisation of the PZT sol

7.7.1 Thermal analysis

The TGA and DTA curves for the dried PZT sample are shown in figure 7.4.

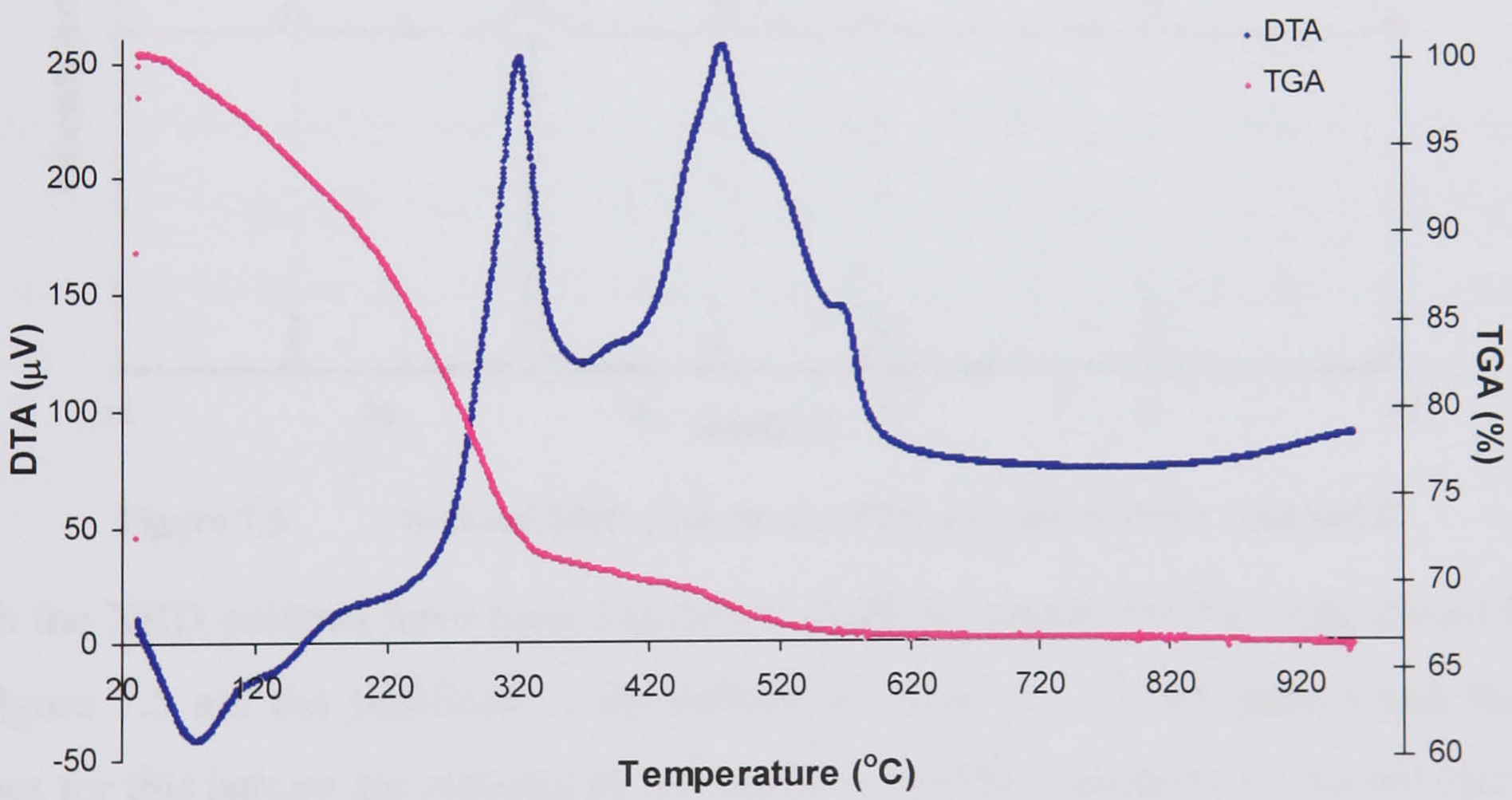


Figure 7.4 TGA and DTA curves for the PZT sol

The TGA analysis indicates that there is a major weight loss (~30%) between 20°C and 300°C followed by a further weight loss (10%) between 300°C and 500°C. These stages of weight loss can be attributed to the decomposition of any residual organics and the evaporation of water from the drying sol. In the temperature range 300-600°C the sample shows several large exothermic peaks in the DTA curve. The DTA peak centred around 320°C which corresponds to the large weight loss observed by TGA can

probably be attributed to the decomposition of organic species from the PZT sol (163). The large exothermic peak at 480˚C may be contributed to the formation of the amorphous phase of PZT since the TGA data shows that the weight loss was complete by ~500˚C (164). The smaller exothermic peaks at 520˚C and 570˚C may result from the crystallisation of the perovskite phase of the PZT which has been verified by XRD analysis (165).

7.7.2 XRD

The crystalline nature of the PZT sol calcined at various temperatures was investigated by X-ray diffraction (XRD). Powder XRD patterns of the PZT calcined at 490˚C and 530˚C are shown in figure 7.5.

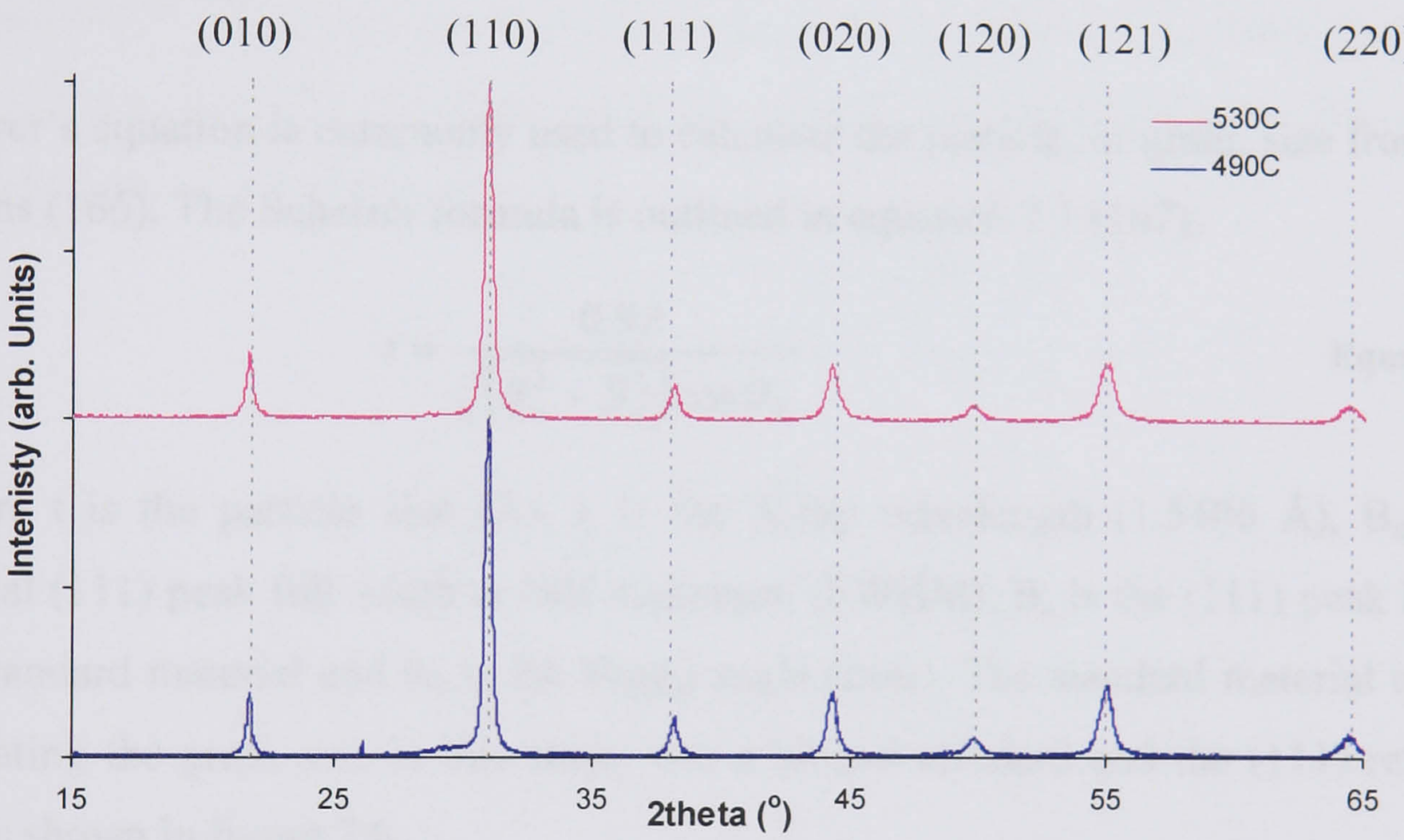


Figure 7.5 Indexed XRD patterns for PZT calcined at 490˚C and 530˚C

Both the XRD patterns have been indexed to JCPDS pattern 50-0346. The dotted lines in figure 7.5 are the positions of the reflections from the JCPDS pattern and the 2θ values for this pattern are outlined in Appendix 3. The XRD patterns for the sol calcined at both temperatures show that the PZT has crystallised and that the tetragonal phase has formed indicated by the presence of the (010) and (110) peaks. The tetragonal phase of PZT is the desirable phase, since with reference to figure 7.2, the PZT will behave ferroelectrically at room temperature. The slight shift in 2θ of the XRD patterns relative to the JCPDS pattern can be attributed to the difference in the composition of the PZT PZT(30/70) and PZT (44/56) respectively.

As the calcination temperature increases from 490˚C to 530˚C the XRD patterns become sharper and more intense indicating better crystallinity has been achieved. The XRD pattern for the PZT calcined at 490˚C shows slight peaks on either side of the (110) peak which can be attributed to the pyrochlore phase of PZT (165). The pyrochlore phase has an oxygen deficient cubic fluorite structure and, since the structure is non-centrosymmetric, does not possess any ferroelectric properties (166). Further heating of the PZT promotes the development of the perovskite phase so that after calcining at 530˚C the pyrochlore phase has been eliminated. Thus a temperature of 530˚C was selected to calcine the composite template films, since as discussed previously the lowest possible temperature should be selected to minimise the damage to the fragile 3-DOM film.

7.7.2.1 Grain size

Scherrer's equation is commonly used to calculate the particle, or grain, size from XRD patterns (166). The Scherrer formula is outlined in equation 7.1 (167),

$$t = \frac{0.9\lambda}{\sqrt{\left(B_m^2 - B_s^2\right)}\cos\theta_B} \qquad \textbf{Equation 7.1}$$

, where t is the particle size (Å), λ is the X-ray wavelength (1.5406 Å), B_m is the material (111) peak full width at half maximum (FWHM), B_s is the (111) peak FWHM of a standard material and θ_B is the Bragg angle (rads). The standard material used for calculating the grain size in this study was a silicon standard and the (111) reflection peak is shown in figure 7.6.

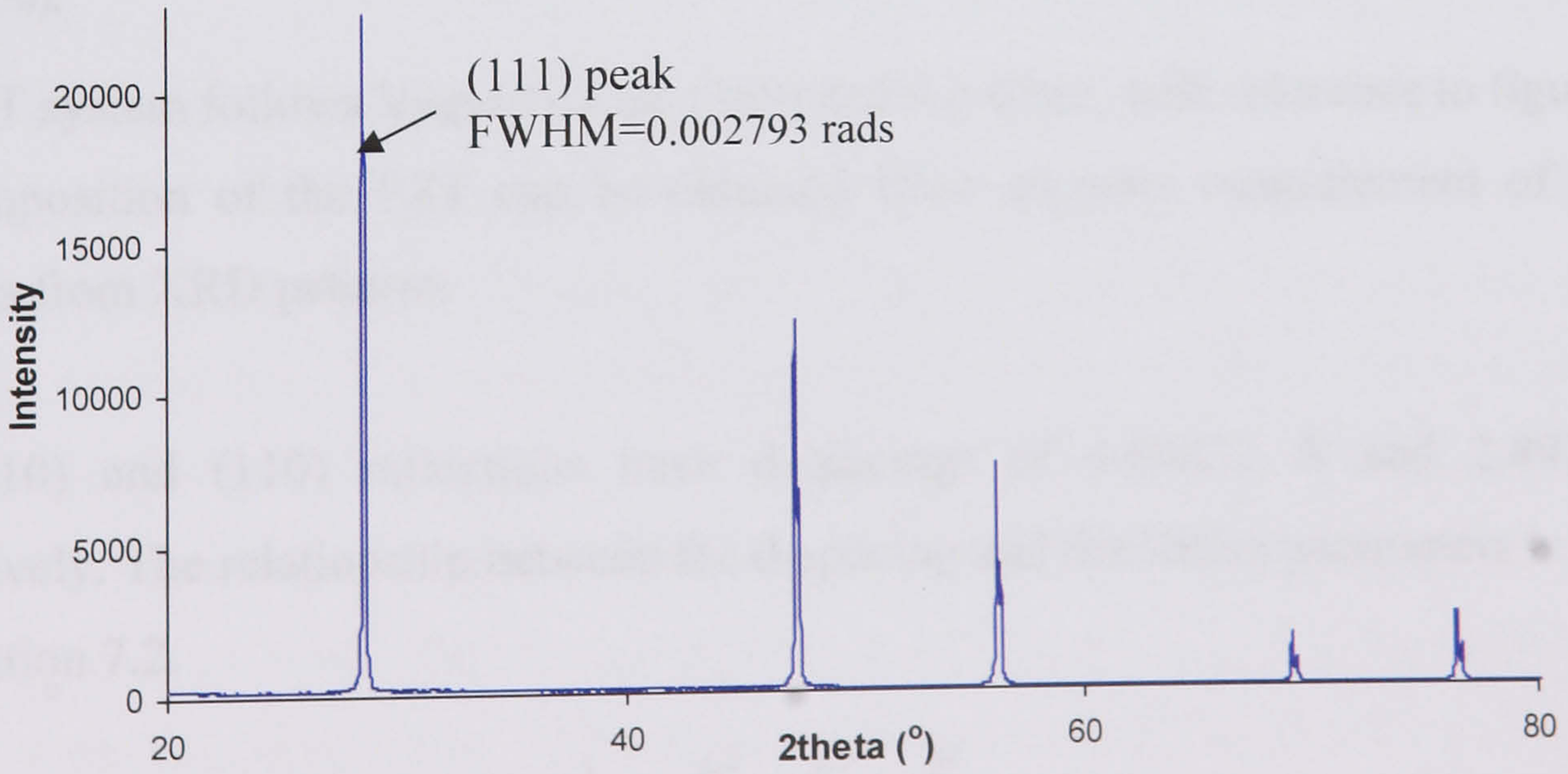


Figure 7.6 **XRD pattern for a silicon standard showing the FWHM of the (111) diffraction peak**

The FWHM of the peak is 0.16˚ or 0.002793 radians. For the PZT calcined at 530˚C the (111) peak is found at a Bragg angle of 31.08˚ (see figure 7.5) and has a FWHM of 0.54˚. Thus a particle or grain size of 22.5 nm can be calculated for the PZT calcined at this temperature.

7.7.2.2 Composition

As the composition varies across a solid solution the unit cell undergoes a small contraction or expansion depending on the relative size of the atoms/ions that are being replaced (167). This observation can be explained by Vegard's law where the unit cell parameters should vary linearly with composition and applies to solid solutions formed by random substitution or distribution of ions. In the solid solution $PbZrO_3$-$PbTiO_3$ the relative size of the ionic radii of the zirconium and titanium cations are 0.72 Å and 0.61 Å respectively (59). Therefore as the percentage of zirconium is increased in the solid solution there should be an expansion in the a and b unit cell parameters. This effect is shown in figure 7.7 for tetragonal PZT.

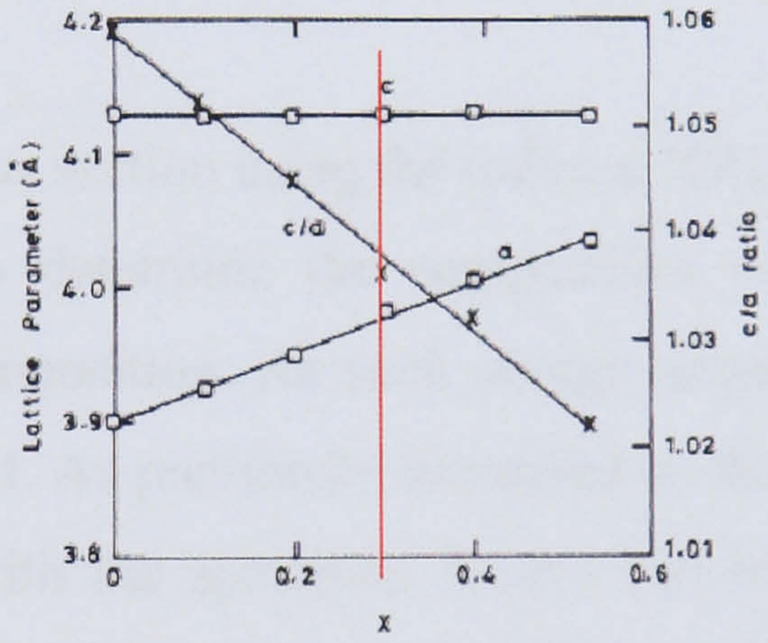


Figure 7.7 Variation in the lattice parameters a and c with the composition (where x is the percentage of Zr) (168). The red line indicates the composition PZT(30/70).

The PZT system follows Vegard's Law (169) and therefore, with reference to figure 7.7, the composition of the PZT can be obtained from accurate measurement of the d-spacings from XRD patterns.

The (010) and (110) reflections have d-spacings of 4.09832 Å and 2.89146 Å respectively. The relationship between the d-spacing and the lattice parameters is shown by equation 7.2.

$$\frac{1}{d_{hkl}^2} = \frac{h^2}{a^2} + \frac{k^2}{b^2} + \frac{l^2}{c^2} \qquad \textbf{Equation 7.2}$$

From equation 7.2 a lattice parameter of 4.0983 Å and 4.0890 Å can be calculated for the (010) and the (110) planes respectively. These calculated values for the lattice parameter, a, do not correspond with the value obtained from figure 7.7 (indicated by the red line) of ~3.98 Å. The lack of correlation between the calculated lattice parameters from XRD and those obtained from figure 7.7 may be due to a departure from Vegard's law. Departure from the behaviour predicted by Vegard's law has been observed in many metal solid solution series and there appears to be no systematic trend between the direction of the departure and structural features of the solid solutions (167). In addition no internal standard, *e.g.* KCl, with accurately known d-spacings was used in the collection of the XRD data. The use of an internal standard material allows a correction factor, which may vary with 2θ, to be obtained from the discrepancy between the observed and true d-spacing of the standard material. This internal calibration would therefore allow more accurate d-spacings to be calculated for PZT from the XRD patterns which may allow the composition to be determined.

7.7.3 EDX

As discussed in the previous section using the indexed XRD patterns, as shown in figure 7.5, and Vegard's law to determine the composition of the calcined PZT did not calculate the expected composition. As such energy dispersive X-ray (EDX) analysis was carried out in the TEM. As previously discussed in chapter 2 when the high energy electron beam interacts with the specimen X-rays can be produced (see figure 2.3). There are two types of X-rays emitted, characteristic X-rays that are element specific and Bremsstrahlung X-rays (76). The process of the emission of characteristic X-rays is outlined in figure 7.8. The high energy electron beam penetrates through the outer electron shells and interacts with the core electrons. The inner shell electron (K shell) can be ejected if a critical amount of energy is supplied by the electron beam and a hole is left in its place, as shown in figure 7.8. The atom is now described as being ionised (76). The ionised atom can return to its lowest energy state by filling the hole in the K shell by an electron from one of the outer electron shells (*e.g.* L shell). It is the transition of this electron from L to K, as shown in figure 7.8, which is accompanied by the emission of an X-ray. The energy of the emitted X-ray is equal to the difference in energy of the two shell levels which is atom dependent and thus the X-ray is element specific.

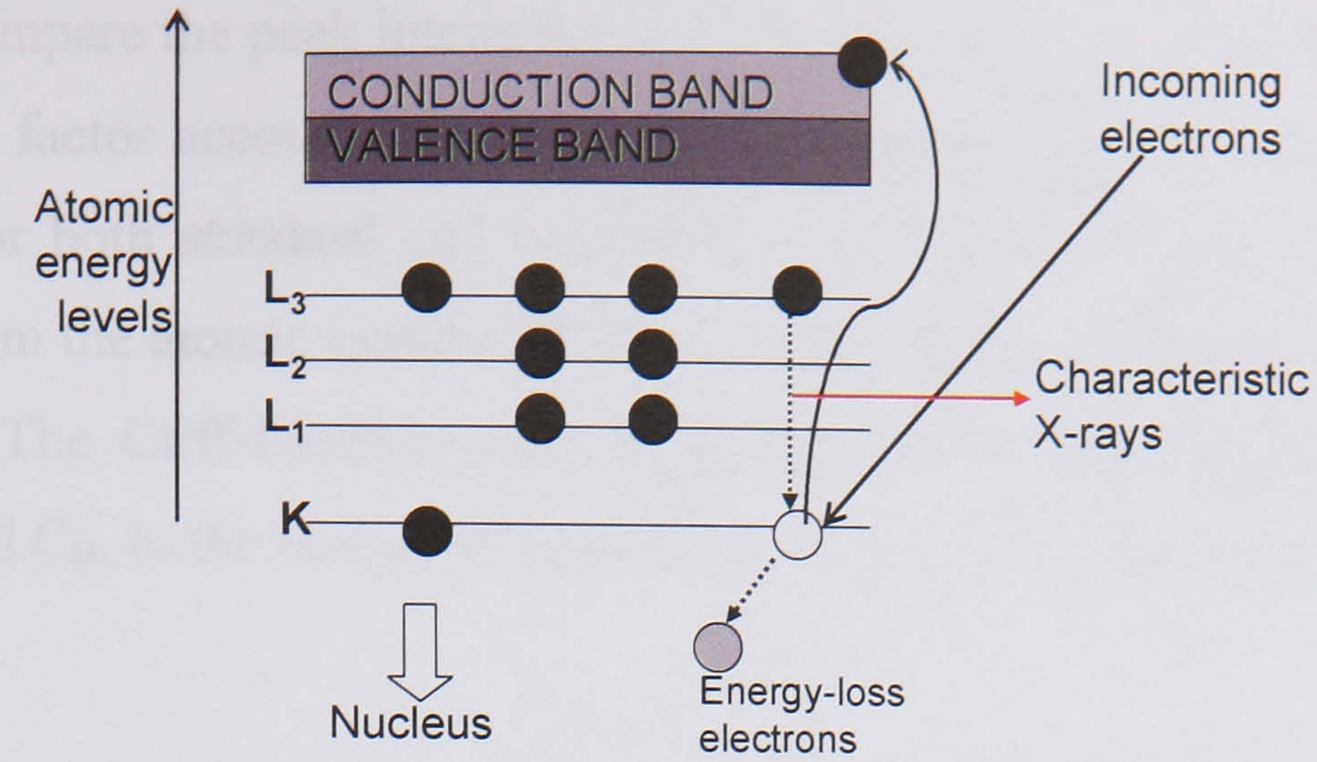


Figure 7.8 Schematic illustration of the process of characteristic X-rays

Bremsstrahlung X-rays are emitted when the electron beam penetrates completely through the electron shells and interacts inelastically with the nucleus (76). The Bremsstrahlung radiation is seen as a decreasing background in an EDX spectrum onto which the characteristic X-rays are superimposed. The characteristic X-rays appear as peaks in the EDX spectrum because they have a narrow energy range and the Bremsstrahlung intensity depends on the average atomic number of the specimen.

Experimentally an EDX spectrum was collected at three regions of a sample of PZT powder calcined at 530°C. An example of the typical EDX spectrum from one of the regions is shown in figure 7.9.

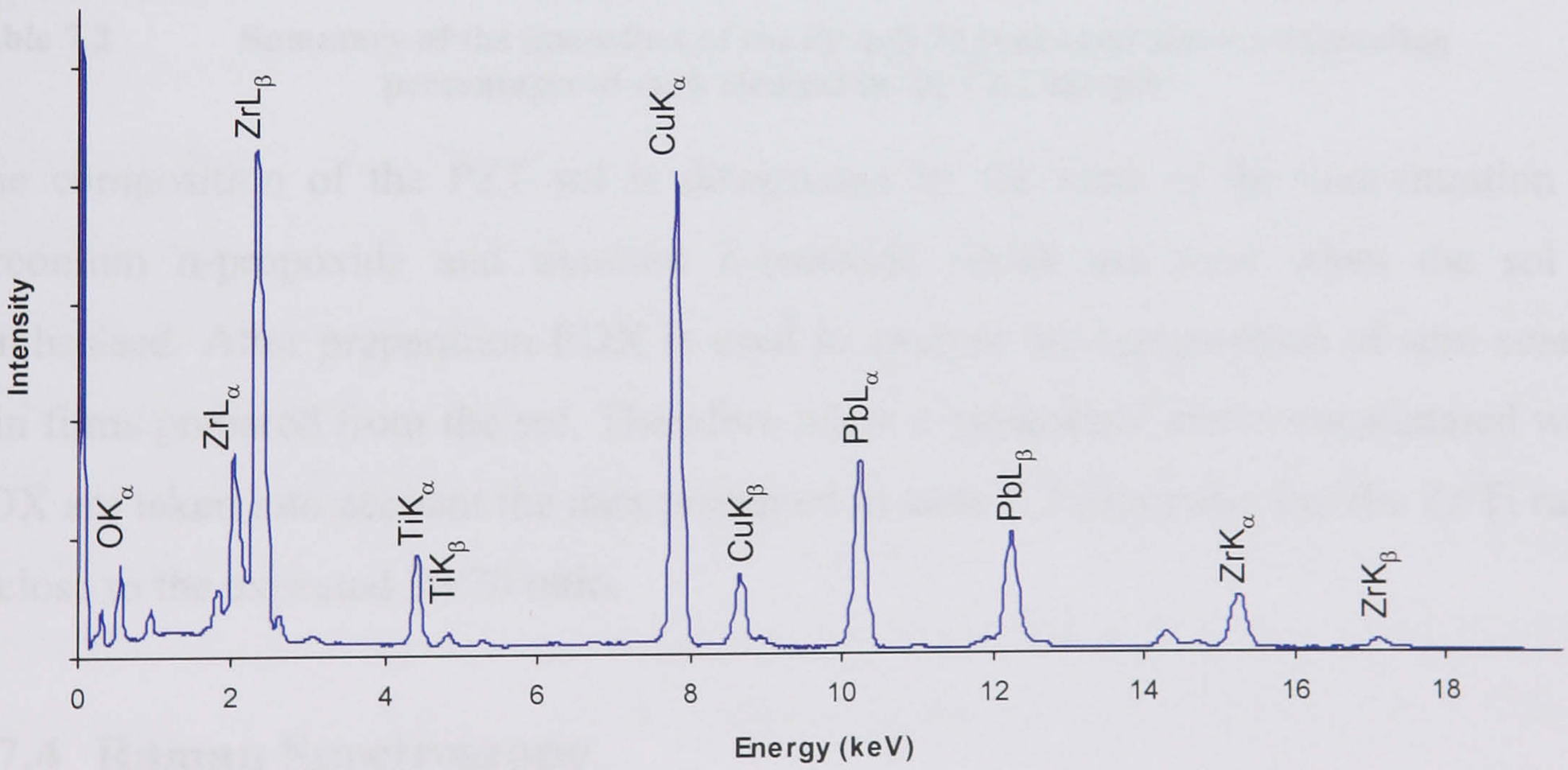


Figure 7.9 EDX spectrum collected from region 2 of the calcined PZT sample

The data presented in figure 7.9 shows that peaks for oxygen, titanium, lead and zirconium are found from the PZT and carbon and copper peaks are found from the TEM grid. In order to calculate the Zr/Ti ratio in the PZT sample the ratio of Zr and Ti K_α peak intensities were investigated.

However, to compare the peak intensities the k factor for the X-ray lines need taken into account. The k factor accounts for the difference between generated and measured X-ray intensity for both standard and unknown specimens (170). Contributions to the k factor come from the atomic number of the element and the absorption of X-rays within the specimen. The Cliff-Lorimer ratio technique relates the weight percent of each element, C_A and C_B, to the measured intensities, I_A and I_B, by equation 7.3.

$$\frac{C_A}{C_B} = k_{AB}\frac{I_A}{I_B} \qquad \textbf{Equation 7.3}$$

, where k_{AB} is the Cliff-Lorimer factor and is related to the atomic number (170). In a binary system $k_{AB} = \frac{k_{AC}}{k_{BC}}$. At 200 kV and with a silicon standard the Cliff-Lorimer factor for Zr/Ti k_α lines is 2.79. Table 7.2 summarises the relative intensities of the Zr and Ti k_α lines and the calculated Zr:Ti ratio.

Region	I(Zr)	I(Ti)	$\frac{C(Zr)}{C(Ti)}$	Zr (%)	Ti (%)
1	1847±198	9640±216	0.535	0.35±0.02	0.65±0.02
2	2725±198	12973±216	0.586	0.37±0.02	0.63±0.02
3	1945±166	7377±163	0.736	0.43±0.02	0.57±0.02

Table 7.2 Summary of the intensities of the Zr and Ti peaks and the corresponding percentages of each element in the PZT sample

The composition of the PZT sol is determined by the ratio of the concentration of zirconium n-propoxide and titanium n-butoxide which are used when the sol is synthesised. After preparation EDX is used to analyze the composition of spin coated thin films prepared from the sol. Therefore when experimental errors encountered with EDX are taken into account the data presented in table 7.2 illustrates that the Zr/Ti ratio is close to the expected 30/70 ratio.

7.7.4 Raman Spectroscopy

The unit cell of PZT is shown in figure 7.10.

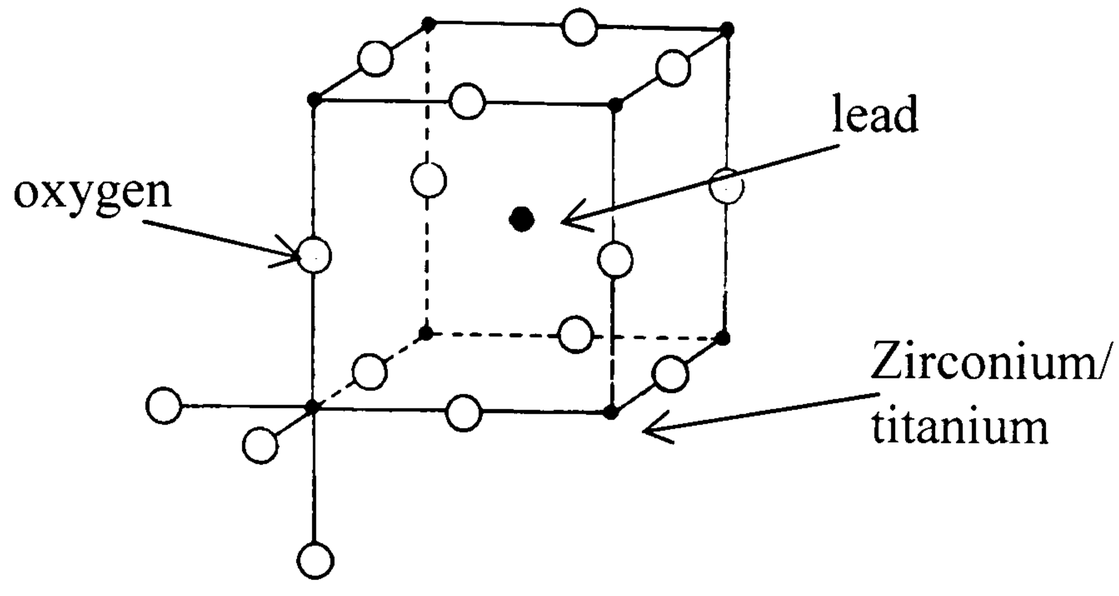


Figure 7.10 The coordination geometry of the perovskite structure of PZT (167)

From figure 7.10 it can be seen that the perovskite unit cell has five atoms as described below:

1 Pb at the centre	contributes 1 atom
8 Zr/Ti at the lattice corners	contributes 8x1/8=1 atom
12 O at the edge centres	contributes 12x1/4=3 atoms.

Therefore the cubic perovskite unit cell of PZT has fifteen vibrational modes (three acoustical and twelve optical) and only the optical modes can be IR active (171).

In the cubic, or paraelectric phase, the unit cell of PZT belongs to the O_h space group (Pm3m) and the twelve optical modes transform as the $3T_{1u}+T_{2u}$ irreducible representation (58). As mentioned previously below the Curie temperature ($T<430^{\circ}C$ for PZT(30/70)) the perovskite crystal changes from the cubic phase to the ferroelectric tetragonal phase. The tetragonal phase belongs to the less symmetric C_{4v} space group (P4mm) (59). This reduction in symmetry splits the three triply degenerate cubic T_{1u} and one triply degenerate T_{2u} modes to transform as $3A_1+3E$ and B_1+E irreducible representations of the C_{4v} point group (171). Due to the electric field all the modes are split into longitudinal optical (LO) and transverse optical (TO) components (168). The modes which arise from the three triply degenerate T_{1u} cubic modes are labelled in sequence 1,2,3 in order of increasing frequency (171). Table 7.3 shows the approximate frequencies of the Raman active phonon modes for PZT(30/70) (168). The A_1 symmetric mode is polarised along the [001] direction (the hard direction) and the E mode is polarised in a plane perpendicular to the [001] direction (the soft direction) (58).

E symmetry modes		A_1 symmetry modes	
Mode	**Frequency (cm^{-1})**	**Mode**	**Frequency (cm^{-1})**
E(1TO)	69	A_1(1TO)	140
E(1LO)	120	A_1(1LO)	160
E(2TO)	220	A_1(2TO)	-
E(2LO)	450	A_1(2LO)	440
E(3LO)	520	A_1(3LO)	610
E(3TO)	680	A_1(3TO)	780

Table 7.3 Approximate frequencies of the Raman active phonon modes for PZT(30/70) (168)

The lowest frequency mode *i.e.* E(1TO) is called the soft ferroelectric mode and corresponds to the motion of the B ion (Ti/Zr) against the oxygen octahedron (171). The second frequency mode corresponds to a vibration of the Pb ion against the BO_6 octahedra and the third frequency mode consists of the motion of the B and O(1) against the oxygen ions O(2) and O(3) which are located in the plane perpendicular to the direction of polarisation (168). The nomenclature of the three oxygen atoms is defined by Fontanant *et al* (172).

Figure 7.11 illustrates the Raman spectrum collected for the PZT sol calcined at 530˚C and the approximate positions of the vibrations outlined in reference (164) are added for comparison.

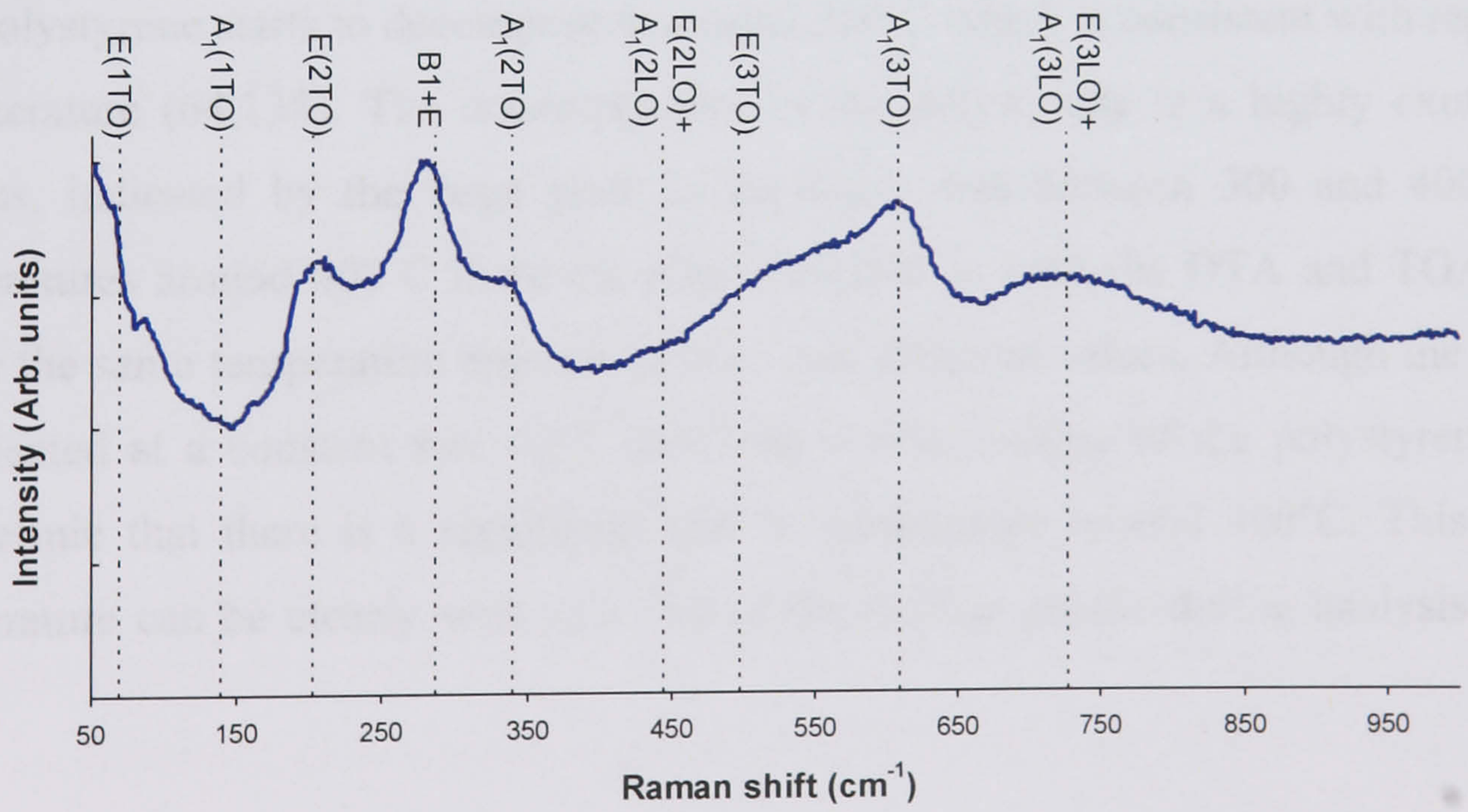


Figure 7.11 Raman spectrum collected for PZT calcined at 530˚C

The results presented in figure 7.11 show that only three of the expected vibrations are not found in the Raman spectrum for the PZT calcined at 530˚C. The presence of a

small peak near the E(1TO) mode, which corresponds to the movement of the Zr/Ti ion against the oxygen octahedron, indicates that the PZT is behaving ferroelectrically.

7.8 Formation of 3-DOM PZT films

7.8.1 Polystyrene template

The TGA/DTA data collected for a dried polystyrene sample (reference 09/08/04) is shown in figure 7.12.

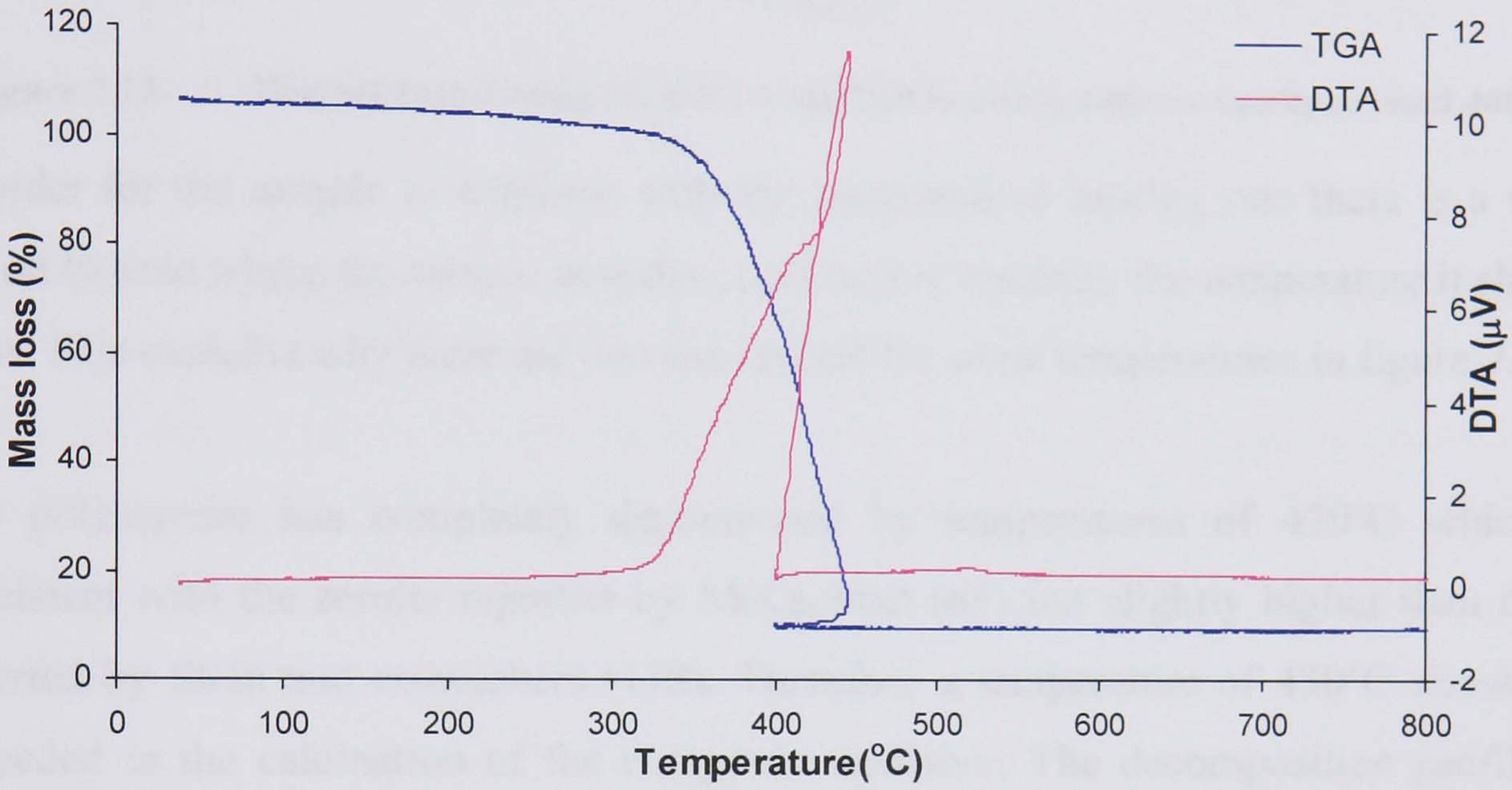


Figure 7.12 TGA and DTA data collected for polystyrene colloid (reference 09/08/04)

The polystyrene starts to decompose at around 300˚C which is consistent with reports in the literature (64,138). The decomposition of the polystyrene is a highly exothermic process, indicated by the large peak in the DTA data between 300 and 400˚C. At temperatures around 400˚C there are discontinuities in both the DTA and TGA plots, where the same temperature appears to have two different values. Although the sample was heated at a constant rate (10˚C/min) the decomposition of the polystyrene is so exothermic that there is a significant rise in temperature around 400˚C. This rise in temperature can be clearly seen in a plot of the heating profile during analysis (figure 7.13).

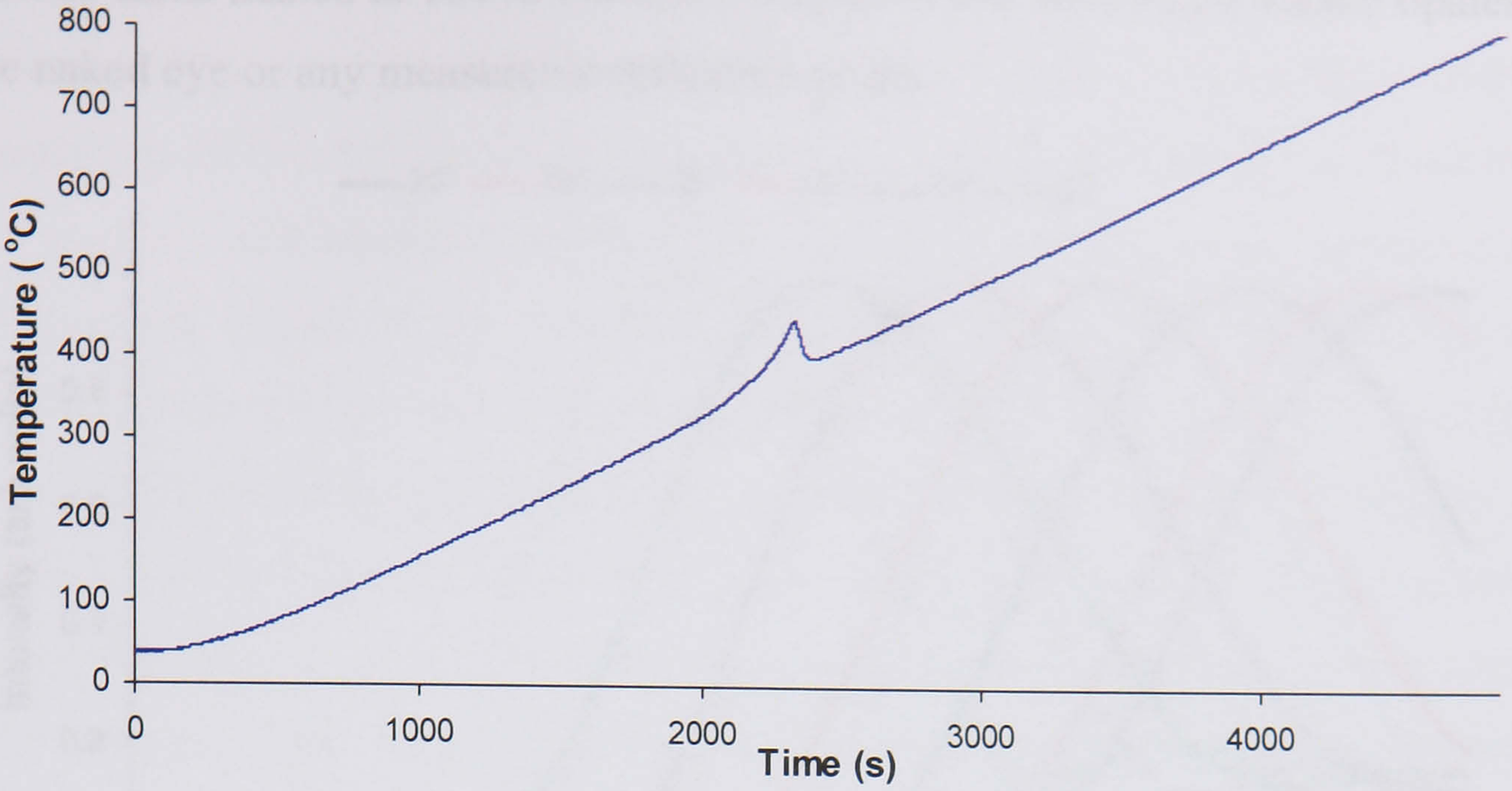


Figure 7.13 Heating rate during TGA/DTA analysis showing a discontinuity around 400°C

In order for the sample to continue with the programmed heating rate there is a short period in time where the sample actually cools before reaching the temperature it should be at. This explains why there are two data points for some temperatures in figure 7.12.

The polystyrene has completely decomposed by temperatures of 430°C which is consistent with the results reported by McLachlan (64) but slightly higher than those reported by Stein and co-workers (138). Therefore a temperature of 430°C should be exceeded in the calcination of the composite structure. The decomposition profile of polystyrene has only been investigated for one sphere size and monomer concentration but it has been reported that there is no variation in the TGA profile when samples of different sphere sizes or monomer concentrations are investigated (64).

When the template is formed from silica spheres it has been reported that sintering the spheres at ~600°C prior to infiltration improves the mechanical strength of the template and also aids the final removal of the template (153). Due to the thermal degradation of polystyrene (see figure 7.12), sintering to high temperatures cannot be achieved without the polymer decomposing and oxidising. However it has been reported that the connection between spheres can be enhanced by heating the template films to around 80°C, *i.e.* below the glass transition temperature, for 30 minutes (54,153). In an attempt to test this hypothesis films grown from polystyrene spheres of diameter 474 nm were heated at 80°C and 100°C for thirty minutes. Following the heat treatment the quality of the films was assessed by reflectance spectroscopy and SEM. Reflection spectra for a template film before and after heating at 80°C for thirty minutes are shown in figure

7.14. The films heated at 100˚C became transparent and showed no visible opalescence to the naked eye or any measurable reflection peaks.

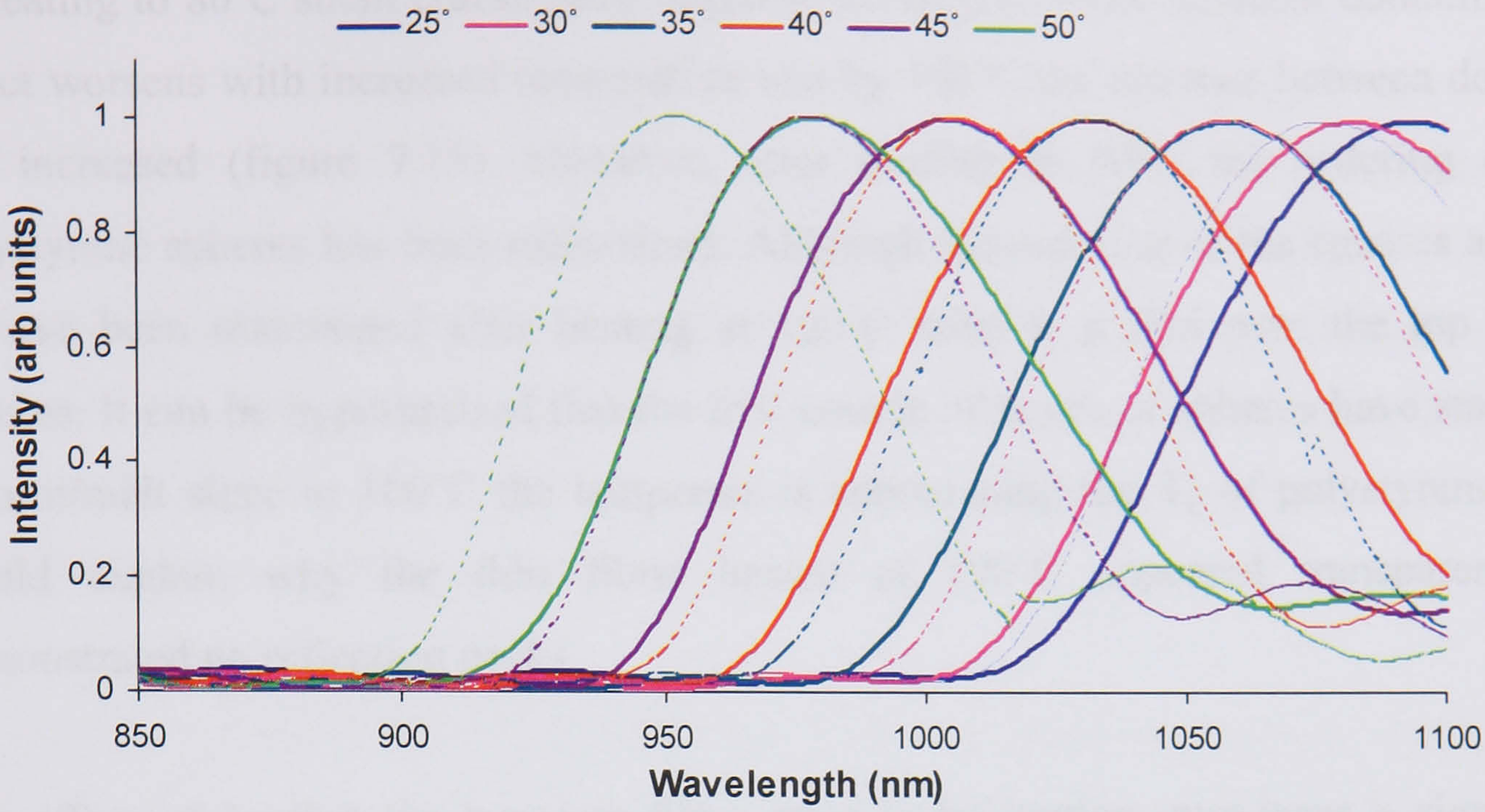


Figure 7.14 **Difference in reflectance spectra for a template film before (continuous line) and after heating at 80˚C for 30 minutes (dashed line)**

As can be seen in figure 7.14 heating the template film at 80˚C has had no effect on the definition of the reflection peaks. However, the reflection peaks have shifted to shorter wavelength after the heat treatment. This would indicate that shrinkage of the polystyrene spheres has occurred.

The SEM micrographs (figure 7.15) show the effects of heating the polystyrene templates on the domains and on the cracks between adjacent domains.

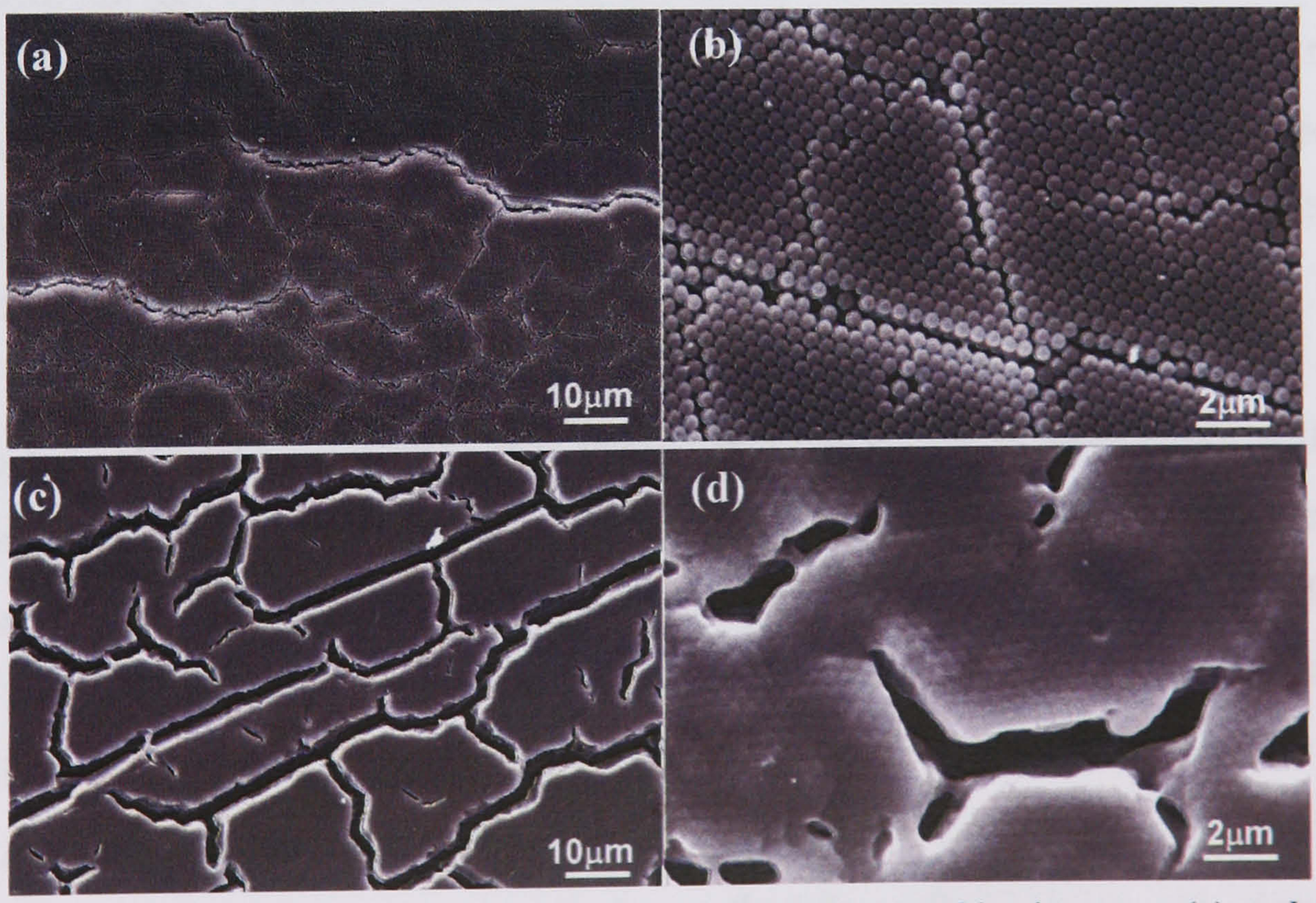


Figure 7.15 **SEM images of the template film after heating for 30 minutes at (a) and (b) 80˚C and (c) and (d) 100˚C**

It can be seen that even a short exposure to temperatures below the glass transition temperature (T_g) of polystyrene has a significant effect on the template films. In the case of heating to 80°C small cracks have began to develop between adjacent domains. This effect worsens with increased temperature and by 100°C the distance between domains has increased (figure 7.15). However, after heating at 80°C the ordering of the polystyrene spheres has been maintained. Although the ordering of the spheres appears to have been maintained after heating at 100°C there is a film over the top of the spheres. It can be hypothesised that the first couple of layers of spheres have started to deform/melt since at 100°C the temperate is approaching the T_g of polystyrene. This would explain why the thin films heated at 100°C appeared transparent and demonstrated no reflection peaks.

The effect of heating the template films prior to infiltration introduces a significant number of additional cracks into the already cracked films. Additional cracking of the template films is undesirable, since the quality of the 3-DOM material is dependent on the quality of the template, and thus the use of heat treatment to strengthen the films was not used in this study.

7.8.2 Methods of infiltration

As discussed previously a sol-gel synthesis was used for the formation of 3-DOM PZT films. The sol-gel synthesis starts with a viscous 'sol' of colloidal PZT mixed with ethanol which is allowed to permeate the template. As the ethanol evaporates the PZT oligomers remain within the voids of the template. Gelation occurs when the sol-filled template is exposed to the atmosphere and the sol dries. The voids within the template are then filled with an amorphous 'gel' of PZT oligomers.

When a sol-gel method is used to form a 3-DOM material from a precursor with two or more metals in a specific ratio the synthetic route must be refined to ensure chemical homogeneity of the formed 3-DOM material. The formation of 3-DOM $BaTiO_3$ has shown that while the sol may contain two molecular species in the correct ratio it is impossible to ensure that this ratio is maintained in the voids of the template material (151). A solution to this problem is to use a well defined hetero-metallic precursor to infiltrate the template. In this project the well defined PZT(30/70) sol (described in section 7.6.1) was used to infill the polymer template ensured that the

lead:zirconium:titanium ratio was correct throughout the template and that after calcination a single phase PZT material was formed with the correct stoichiometry.

The five methods investigated for infilling the polystyrene templates, summarised in table 7.1, were attempts to identify the optimum infiltration method. Although the presence of the substrate gives mechanical strength to the formed 3-DOM film it limits the methods which can be used for infiltration of the PZT sol. All five methods rely on capillary action to draw the PZT sol into the voids of the template. The PZT sol is diluted with ethanol to lower the viscosity of the sol and to increase the wettability of the PZT to ensure optimum penetration into the template.

The use of a coverslip has been reported as a method for the formation of 3-DOM TiO_2 (173) and has been shown to produce well ordered 3-DOM structures. It has been hypothesised that the use of a coverslip (methods 2 and 3) would aid the capillary action and ensure that the PZT sol is able to penetrate the template efficiently. This method also has the added advantage that the progression of the sol into the template could be monitored visually. However, unlike the reported results for TiO_2, the composite template-PZT films exhibited poor film coverage after the infiltration process had been completed. The poor film coverage was attributed to the difficulty in removing the top slide while keeping the composite film from delaminating from the substrate. The film coverage was worse when the top slide was removed immediately after the film had been dipped into the PZT sol.

In methods four and five the PZT/ethanol solution was dropped onto the template film surface from above using a pipette. The main problem with this technique was that upon addition of the PZT/ethanol solution the film was effectively submerged with fluid which caused the domains to delaminate from the substrate. This problem of delamination was slightly improved by holding the template film horizontally rather than vertically but the film coverage was still very poor.

The methods resulting in the best film coverage after drying were methods one and five, and as such they were investigated further. The technique in method five involved holding the template substrate vertically and dropping the PZT/ethanol solution, using a syringe, down the surface of the film. The idea was that as the solvent evaporated at the suspension-air interface, a flowing motion would be generated within the template,

allowing more oxide particles to pack into the voids. The best coverage was obtained when the film was held at about 45° from the vertical, but even then the film coverage was still only of the order of 50% when the film had dried.

In method one the template film was dipped into the PZT/ethanol solution and then slowly withdrawn manually. The process of withdrawing the film extremely slowly from the PZT/ethanol solution was hoped to aid the penetration of the PZT into the voids of the template. This infiltration technique has proven to be the optimum method for forming 3-DOM PZT and has therefore been used as the infiltration method for all the films discussed in this chapter. SEM micrographs of the composite material, *i.e.* after infiltration of PZT but before template removal are shown in figure 7.16.

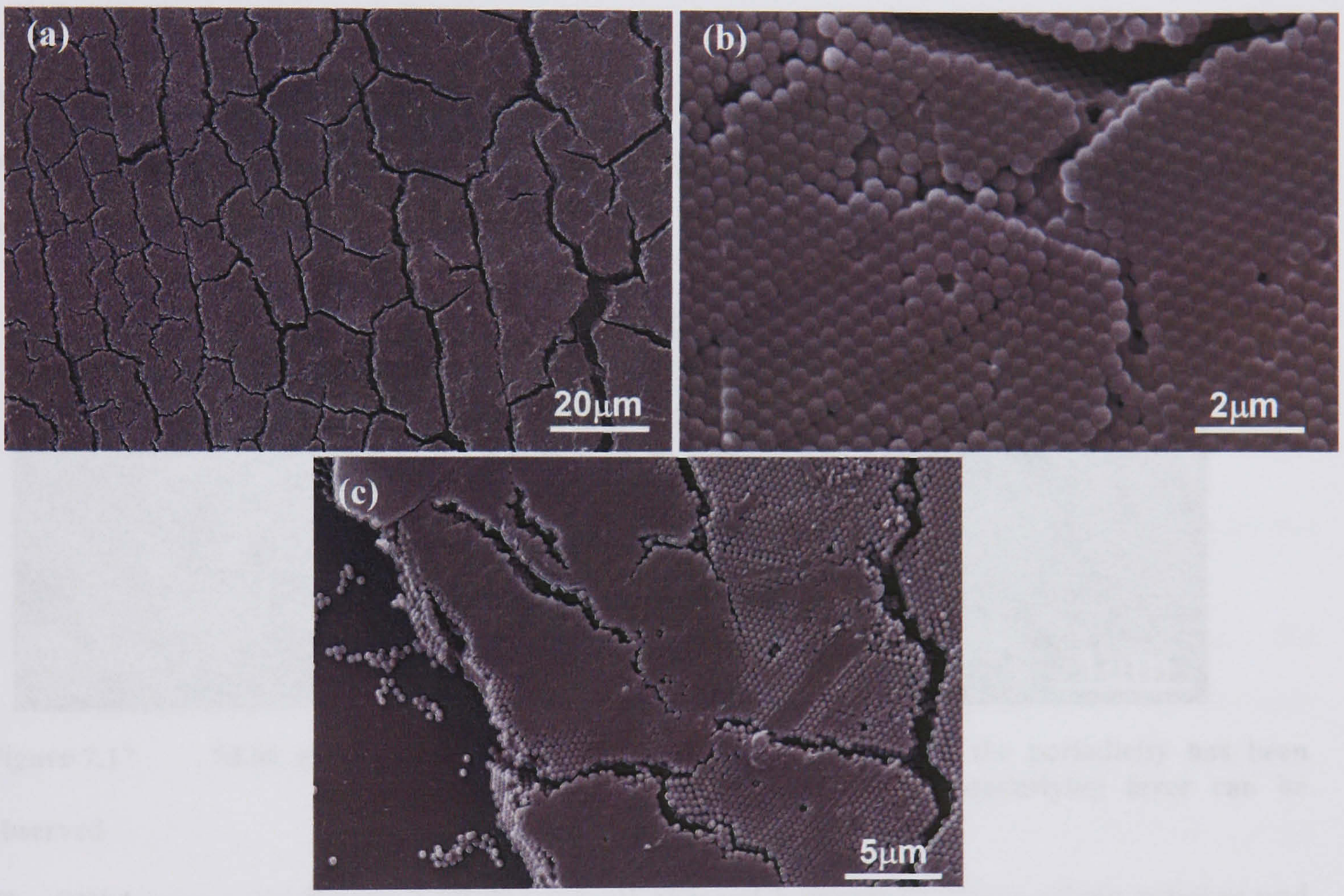


Figure 7.16 SEM micrographs showing the template film after infiltration with PZT but before sphere removal

The low magnification SEM micrograph (figure 7.16(a)) shows that the surface of the composite film is slightly more cracked than a typical thin film PC. This is most likely due to a contraction of the template caused by the PZT densifying upon drying from the sol to a 'gel'. The filling of the PZT has occurred through all the layers of the template to the substrate (figure 7.16(b)) and the ordering of the spheres has been maintained. However, as shown in figure 7.16(c), while the majority of the film has been infilled with PZT there are some regions which have not been infilled properly.

7.8.3 Calcination conditions

The polystyrene template is removed and the PZT crystallised in a one step heat treatment. XRD analysis has shown that the bulk PZT calcined at 530˚C has crystallised to the desirable tetragonal phase. Thus a temperature of 530˚C was chosen to calcine the composite films, which is sufficient to remove the polystyrene template (figure 7.12) and form a 3-DOM PZT film. The calcination of the composite films was carried out in a tube furnace under a flow of moist air and the heating rate was set to 1˚C/minute. It has been reported that the air flow accelerates the decomposition of the polystyrene and aids the transport of by-products formed by the heating of both the template and the precursor (138).

After calcination the 3-DOM PZT films exhibited regions of opalescence. SEM images of the surface of the 3-DOM PZT films (figure 7.17) show that the periodicity of the porous network has been maintained.

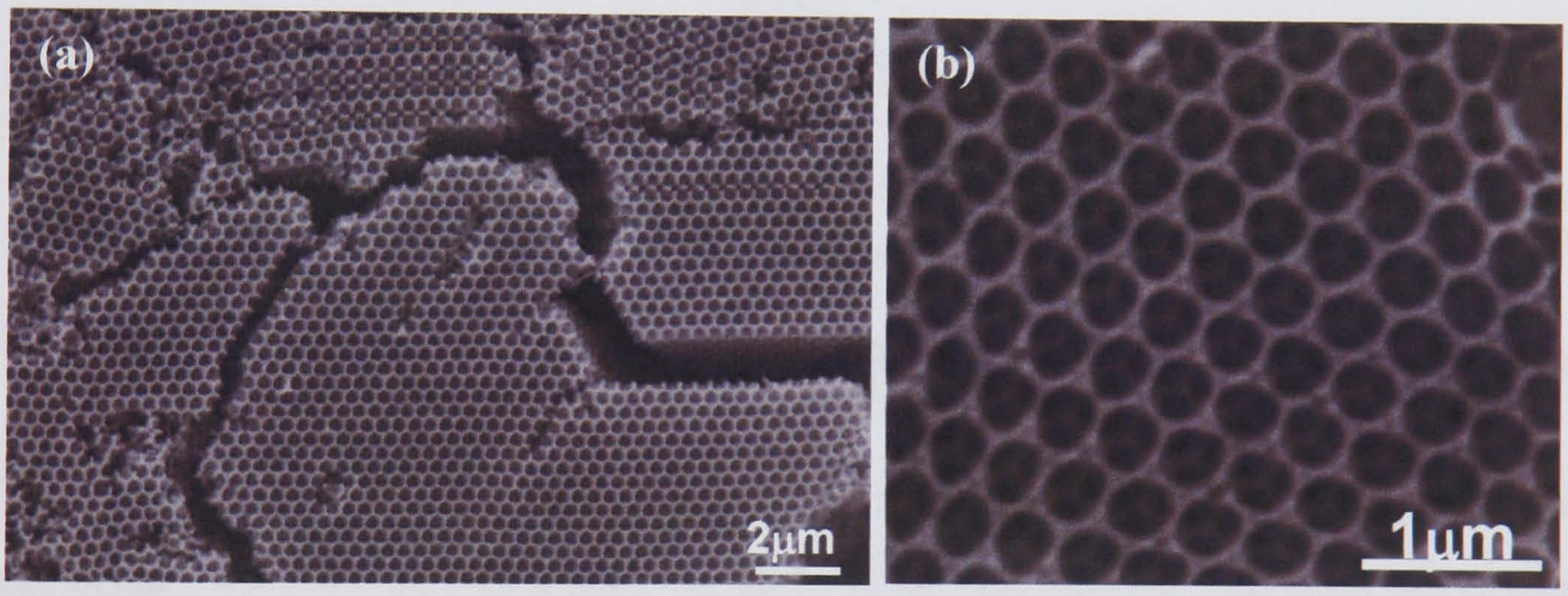


Figure 7.17 SEM micrographs of 3-DOM PZT films showing (a) the periodicity has been maintained and (b) the air spheres of the underlying layer can be observed

The SEM images in figure 7.17 show well ordered hexagonal arrays of air spheres and interconnected PZT walls. Connecting windows, shown as dark spots in figure 7.17(b) indicate that the air spheres are connected with the layers below. Figure 7.17(a) shows that the filling has occurred all the way through the template.

7.9 Characterisation of the 3-DOM PZT films

7.9.1 XRD

After calcination the 3-DOM films were investigated by XRD to ensure that the tetragonal phase of PZT had been formed. The XRD pattern taken from a 3-DOM PZT film on a glass substrate is shown in figure 7.18 with the XRD pattern from a blank glass substrate shown for comparison.

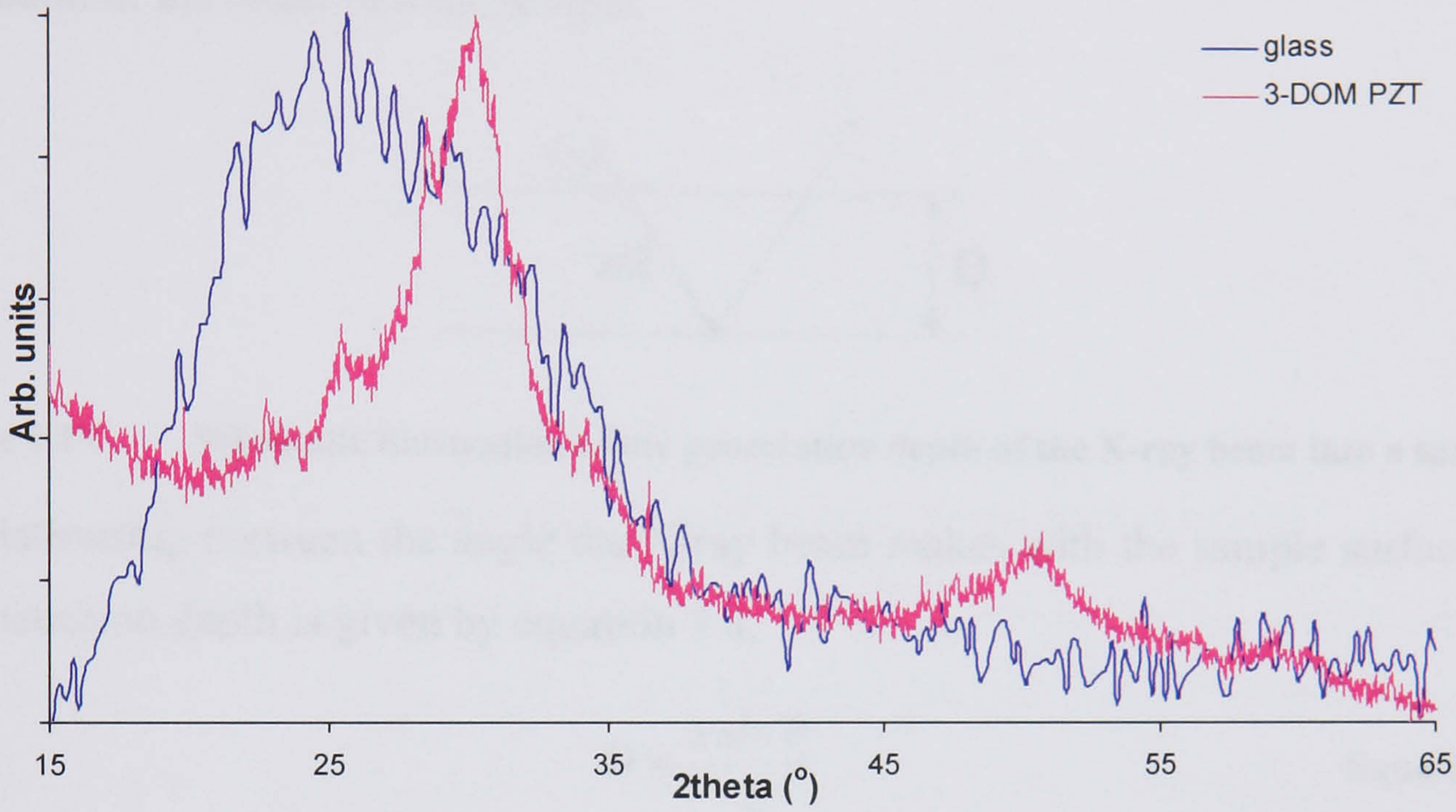


Figure 7.18 XRD pattern for a 3-DOM PZT film supported on glass. The XRD pattern for the substrate is also shown for comparison

Compared to the XRD patterns obtained from the bulk PZT the pattern for the supported 3-DOM film has a poor signal to noise ratio (SNR) and does not demonstrate any narrow diffraction peaks. There are two broad diffraction peaks visible in figure 7.18, at 2θ equal to 30° and 51°, which do not correspond with any diffraction peaks from the glass substrate. These peaks could be assigned to the (110) and (120) diffraction peaks respectively for tetragonal PZT. The broadness of the diffraction peaks can be attributed to the SNR and reflections for the amorphous glass substrate.

The fact that diffraction peaks are observed from the supported 3-DOM film indicates that the PZT is most likely crystalline. The XRD data presented in figure 7.17 was collected with a long acquisition time to improve sensitivity and reduce the SNR, yet the patterns collected are still very noisy. At ~8 μm thick the 3-DOM film is thick enough for XRD analysis but the problem lies with the porosity of the film *i.e.* the small amount of material present for analysis.

For a dense film an XRD pattern can be collected from a film ~1 μm thick. In order to calculate the volume of material required for a porous film the penetration depth for a porous 3-DOM PZT film was investigated. As the X-rays are scanned from small 2θ to larger values of 2θ, the length of the beam on the sample and the distance the beam penetrates the sample changes. At shallow angles the beam is diffuse and does not penetrate deep into the sample whereas as the angle increases the beam becomes narrower and penetrates deeper into the sample. Figure 7.19 schematically illustrates the penetration of the beam into the sample.

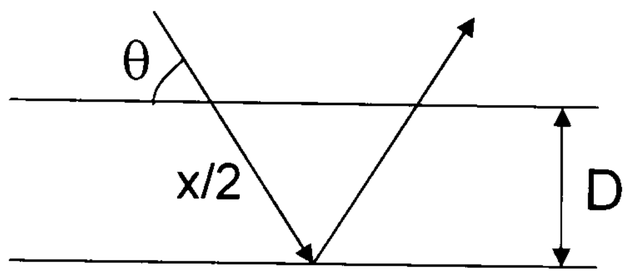


Figure 7.19 Schematic illustration of the penetration depth of the X-ray beam into a sample

The relationship between the angle the X-ray beam makes with the sample surface and the penetration depth is given by equation 7.4,

$$D = \frac{x \sin\theta}{2} \qquad \textbf{Equation 7.4}$$

, where D is the penetration depth, x is the path length of the X-ray and θ is the angle of the X-ray beam with respect to the sample surface.

If the penetration of the X-rays follows the Beer-Lambert law (174) the value of the path length can be calculated by equation 7.5,

$$I = I_0 \exp(-\rho\mu x) \qquad \textbf{Equation 7.5}$$

, where I is the intensity after the beam has passed through the sample, I_0 is the initial intensity of the beam, ρ is the density of the material, μ is the mass absorption coefficient and x is the path length. The mass absorption coeffficient for any chemical compound is given by equation 7.6 (175),

$$\mu = \sum_i w_i \mu_i \qquad \textbf{Equation 7.6}$$

, where w_i and μ_i are the weight fraction and the mass absorption coefficient of the ith constituent respectively. For a chemical compound the weight fraction can be calculated by equation 7.7 (175),

$$w_i = \frac{a_i A_i}{\sum_j a_j A_j}$$ **Equation 7.7**

, where A_i is the atomic weight of the ith element and a_i is the number of formula units.

Table 7.4 summarises the elemental mass absorption coefficients for the constituents of PZT at a wavelength of 1.55Å (176). Thus for the composition PZT(30/70) a value for μ of 171.5 cm^2/g can be calculated.

Element	μ (cm^2/g)
Pb	245
Zr	143.5
Ti	205
O	11.75

Table 7.4 Mass absorption coefficients for the elements of PZT

In order to calculate the density of the 3-DOM PZT it is assumed that the material is only ~10% PZT (ρ=7.8 gcm^{-3} (177)) and 90% air (ρ=0.0012 gcm^{-3} (178)), consistent with the literature for TiO_2 (70). A density of 0.7811 gcm^{-3} was calculated for the 3-DOM PZT. If 99% absorbance is assumed for the 3-DOM PZT sample a path length of 0.0344 cm can be calculated from equation 7.5.

To calculate the thickness of the sample required for XRD analysis a 2θ value of 35° was chosen, the mid-point of the angles investigated, and from equation 7.4, a sample thickness of ~50 μm was calculated. Therefore although XRD patterns can be obtained from samples as thin as 1 μm for dense films due to the porosity of the 3-DOM films the sample thickness would need to be at least 50 μm. Using the optimum infiltration method discussed previously, problems were encountered infiltrating thick films because the film tended to delaminate from the substrate.

Consequently an XRD pattern was collected from delaminated flakes of 3-DOM PZT formed from trying to infill a thick template film. Figure 7.20 shows the XRD pattern collected and figure 7.21 shows SEM micrographs proving the XRD data has been collected from 3-DOM PZT and not dense PZT.

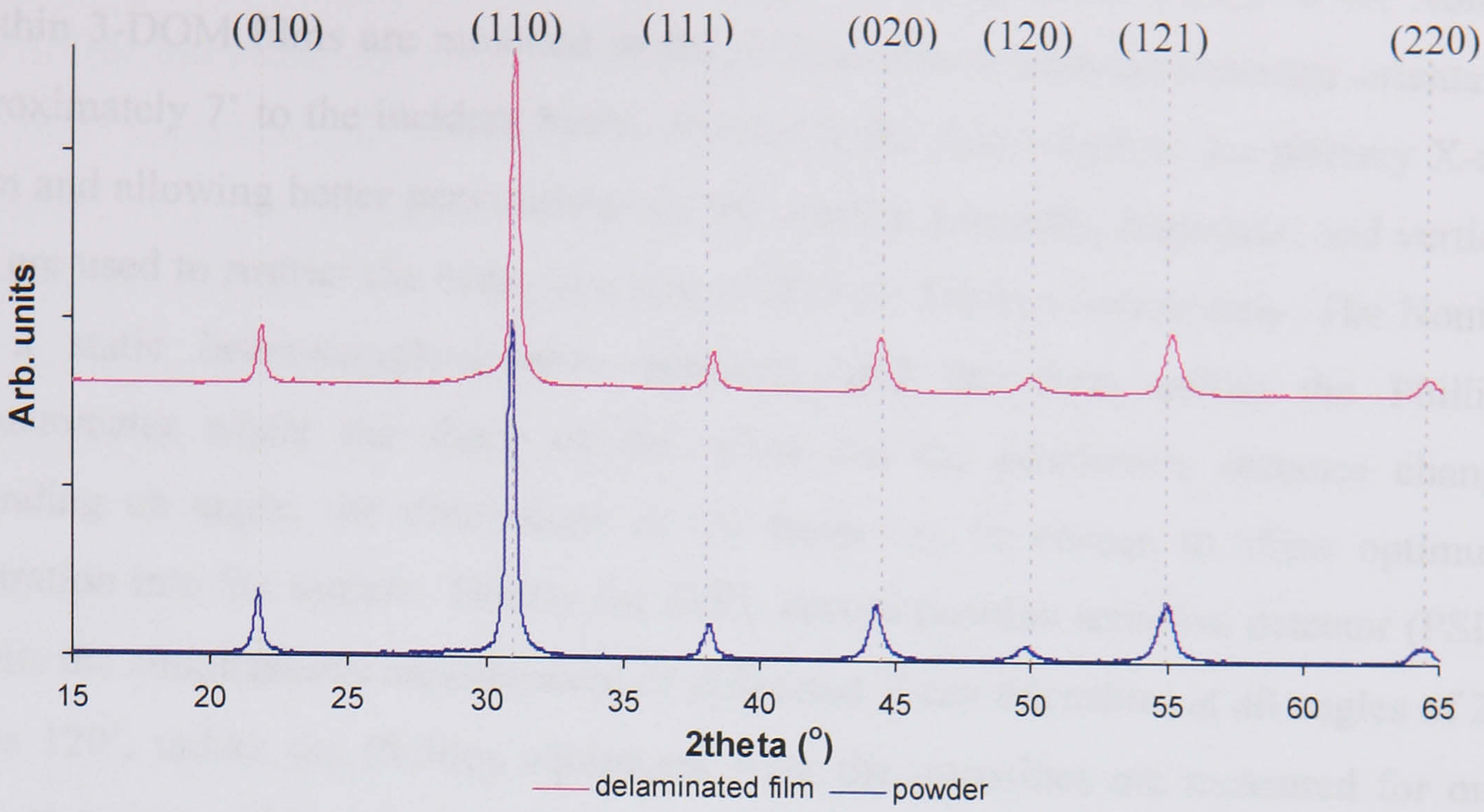


Figure 7.20 **Indexed XRD pattern collected from delaminated flakes of 3-DOM PZT compared to bulk PZT**

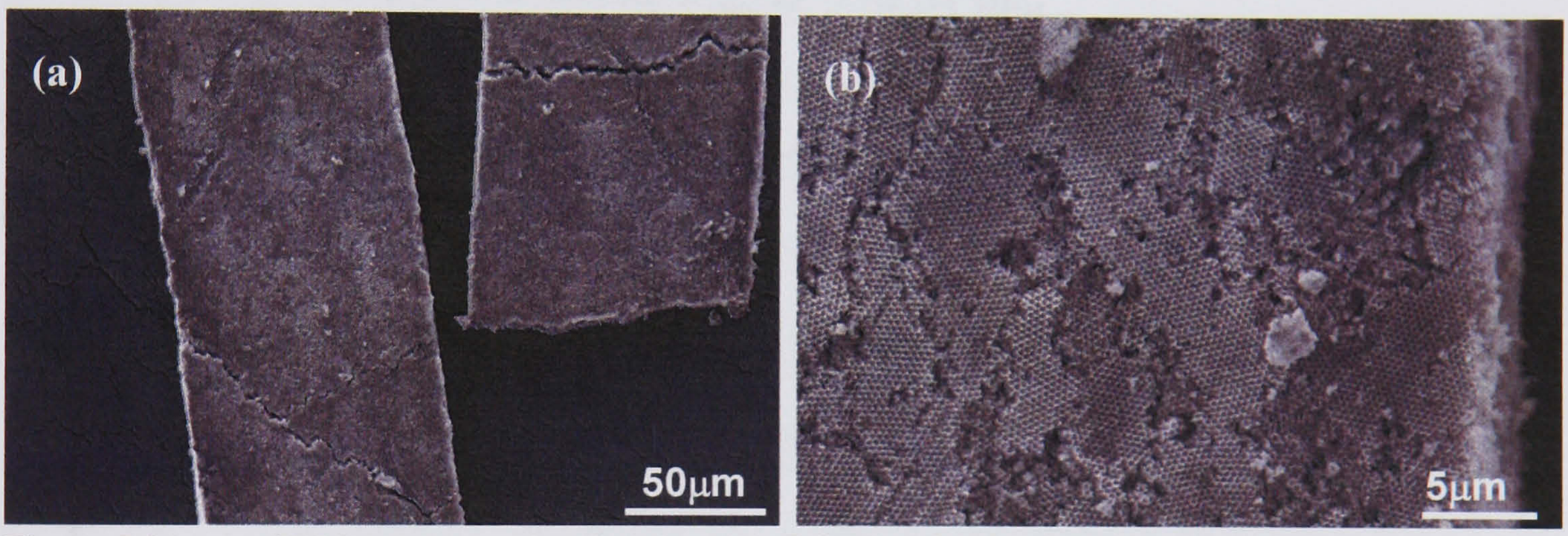


Figure 7.21 **SEM micrographs showing (a) flakes and (b) structure of the flakes of 3-DOM PZT**

The XRD analysis (figure 7.20) shows that the 3-DOM PZT, after calcination, has crystallised to the same ferroelectric perovskite phase as the bulk PZT treated at the same temperature. The SEM micrograph shown in figure 7.21(b) indicates that the XRD data was collected from 3-DOM PZT. Using the Scherrer formula and the method of analysis described previously (section 7.7.2.1) a grain size of 26 nm was calculated for the 3-DOM PZT, which is slightly larger than the grain size of 22.5 nm calculated for the bulk PZT.

There are few publications where XRD analysis is reported on supported 3-DOM films (179,180), probably due to the problems mentioned previously of the porosity of the samples. In order to obtain a diffraction pattern for a supported 3-DOM PZT film a different XRD diffractometer was used, a Nonius PDS120. There are four main differences between the Nonius and the Phillips diffractometers which allow the

acquisition of diffraction patterns from 3-DOM supported films. Firstly in the Nonius the thin 3-DOM films are mounted in the diffractometer with the substrate orientated approximately 7° to the incident beam, increasing the path length of the primary X-ray beam and allowing better penetration into the sample. Secondly, horizontal and vertical slits are used to restrict the beam to a size of 0.24 by 5.0 mm respectively. The Nonius has a static beam-sample-detector geometry and therefore, unlike the Phillips diffractometer where the shape of the beam and the penetration distance change depending on angle, the dimensions of the beam can be chosen to allow optimum penetration into the sample. Thirdly the INEL curved position sensitive detector (PSD) permits the simultaneous measurement of diffracted X-ray intensities at all angles of 2θ across 120°, unlike the Phillips equipment were the intensities are measured for one angle at a time. Although this reduces the resolution of the data collected from the Nonius it improves the SNR. Finally the sample can be rapidly repositioned to ensure the incident beam continues to interact with the 3-DOM film.

The XRD pattern collected for a supported 3-DOM PZT film ~8 μm thick is shown in figure 7.22.

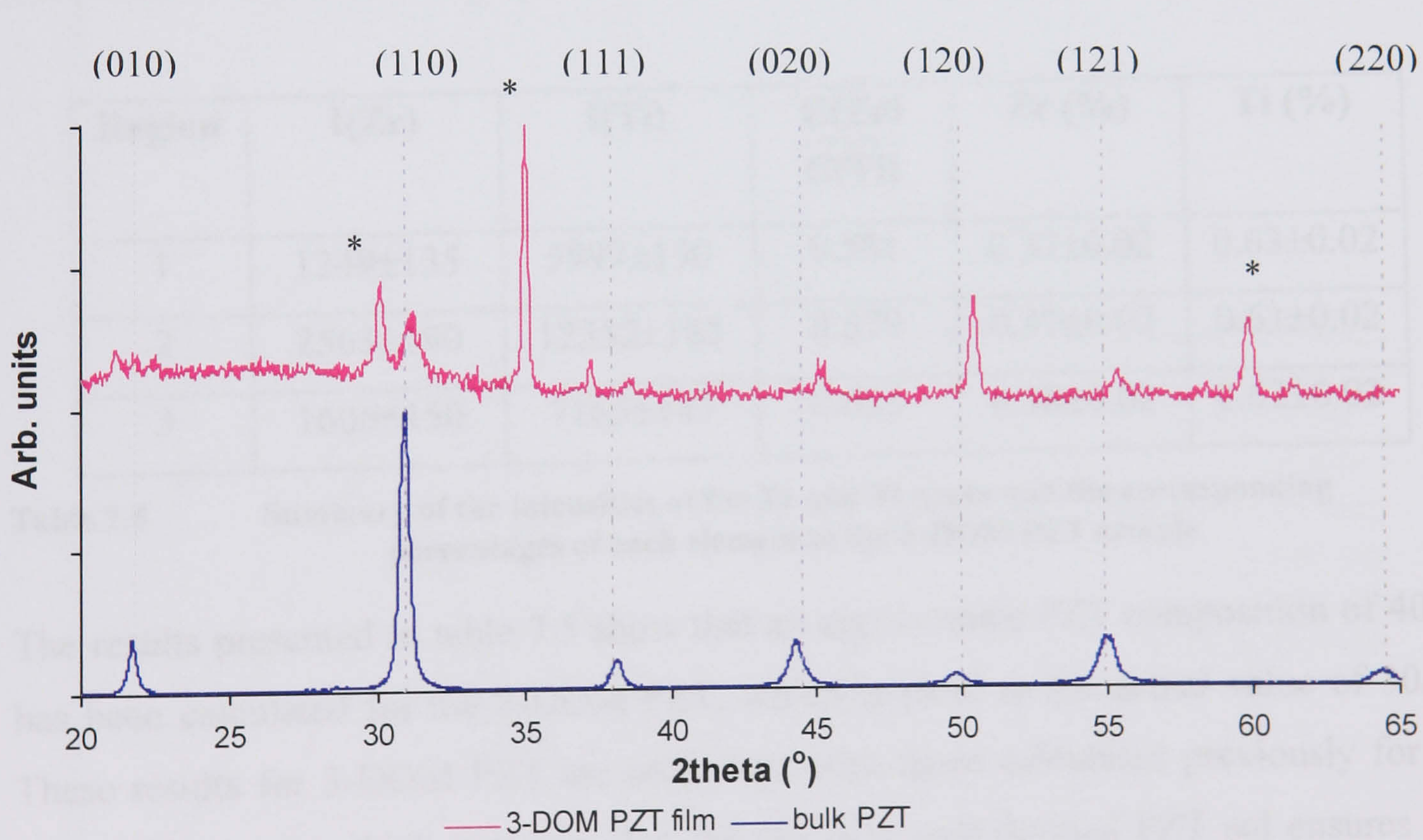


Figure 7.22 Indexed XRD pattern from a 3-DOM PZT film supported on an ITO substrate

The XRD analysis shows that the film, after calcination, has crystallised to the same ferroelectric perovskite phase as the bulk PZT treated at the same temperature. The peaks have been indexed using Stoe WinXPow, and the additional peaks have been assigned to the ITO substrate, shown as * in figure 7.22.

The diffraction peaks shown in figure 7.22, collected using the Nonius diffractometer, are much narrower and better defined than those obtained for the 3-DOM PZT film supported on a glass substrate (figure 7.18) measured using the Phillips diffractometer. This can be attributed to better penetration into the porous sample, due to the sample positioning, and the simultaneous measurement of diffracted X-ray intensities at all angles of 2θ across 120°, which improves the SNR.

7.9.2 EDX

As discussed in section 7.7.2.2 problems were encountered determining the composition of the calcined PZT from the indexed XRD patterns and Vegard's law. Therefore the EDX method was used to determine the composition of the 3-DOM PZT film and ensure that the composition had not changed during the infiltration and calcination processes. A small piece of the delaminated 3-DOM PZT film used for the XRD analysis, figure 7.20, was investigated in the manner described in section 7.7.3. The composition for the three regions investigated are summarised in table 7.5.

Region	I(Zr)	I(Ti)	$\frac{C(Zr)}{C(Ti)}$	Zr (%)	Ti (%)
1	1249±135	5997±130	0.581	0.37±0.02	0.63±0.02
2	2563±190	12352±185	0.579	0.37±0.02	0.63±0.02
3	1606±150	7165±143	0.625	0.38±0.02	0.62±0.02

Table 7.5 Summary of the intensities of the Zr and Ti peaks and the corresponding percentages of each element in the 3-DOM PZT sample

The results presented in table 7.5 show that an approximate PZT composition of 40/60 has been calculated for the 3-DOM PZT, which is close to the actual value of 30/70. These results for 3-DOM PZT are consistent with those calculated previously for the bulk PZT sample which indicates that the use of a well defined PZT sol ensures that correct metal ratio is maintained throughout the template and after subsequent calcination.

7.9.3 Optical spectroscopy

The advantage of using the non-destructive technique of optical spectroscopy is that information can be gained from the template film, the composite template-PZT film and finally the 3-DOM PZT film. Ozin and co-workers (103) have reported the use of in-situ reflectance spectroscopy to monitor the time dependence of the infiltration of a $BaTiO_3$ precursor inside the template. A similar analysis has been carried out for the infiltration of the PZT sol into the voids of a template film composed of 415 nm polystyrene spheres. The template film was infilled using the normal filling procedure and then reflectance spectra were collected at an incident angle of 10° one, five, ten, fifteen and twenty minutes after the template was withdrawn from the PZT sol. This process of dipping and collection of reflectance spectra was repeated twice and the corresponding spectra are shown in figure 7.23.

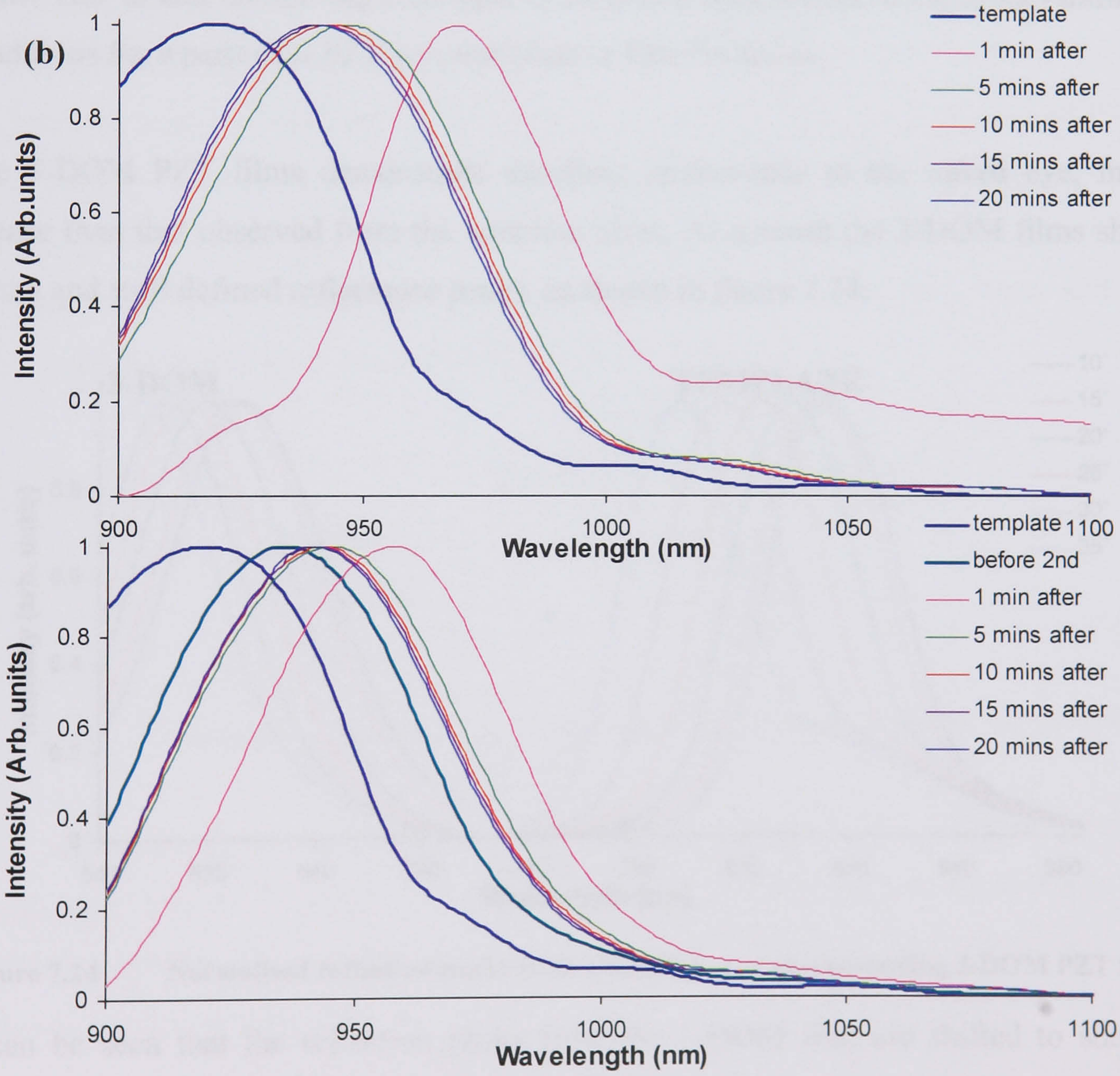


Figure 7.23 **Reflectance spectra collected during the infiltration process showing the Bragg peak at various times after infiltration (a) after first infiltration and (b) after second infiltration**

The reflection peak from the template film prior to infiltration of the sol is centred at a wavelength of 919 nm. After infiltration with the PZT sol the reflection peak shifted to 969 nm, as shown in figure 7.23(a). At times after the initial infiltration the reflection peak blue shifts. This can be explained in the following way. After infiltration the ethanol evaporates from the template allowing the PZT to be deposited on the surface of the spheres. Therefore some of the voids are re-instated, decreasing the overall refractive index resulting in the peak position moving to shorter wavelength. After a period of twenty minutes there is no further shift of the reflection peak indicating that the template has now dried.

Similar behaviour is observed when the template is infilled a second time although the initial red shift following infiltration is not as large (figure 7.23(b)). This is due to the refractive index having already been decreased as a result of PZT deposition within the voids. This in-situ monitoring technique is useful for establishing the optimum infilling conditions for a particular PZT concentration or film thickness.

The 3-DOM PZT films demonstrate excellent opalescence to the naked eye, more intense than that observed from the template films. As a result the 3-DOM films show strong and well defined reflectance peaks, as shown in figure 7.24.

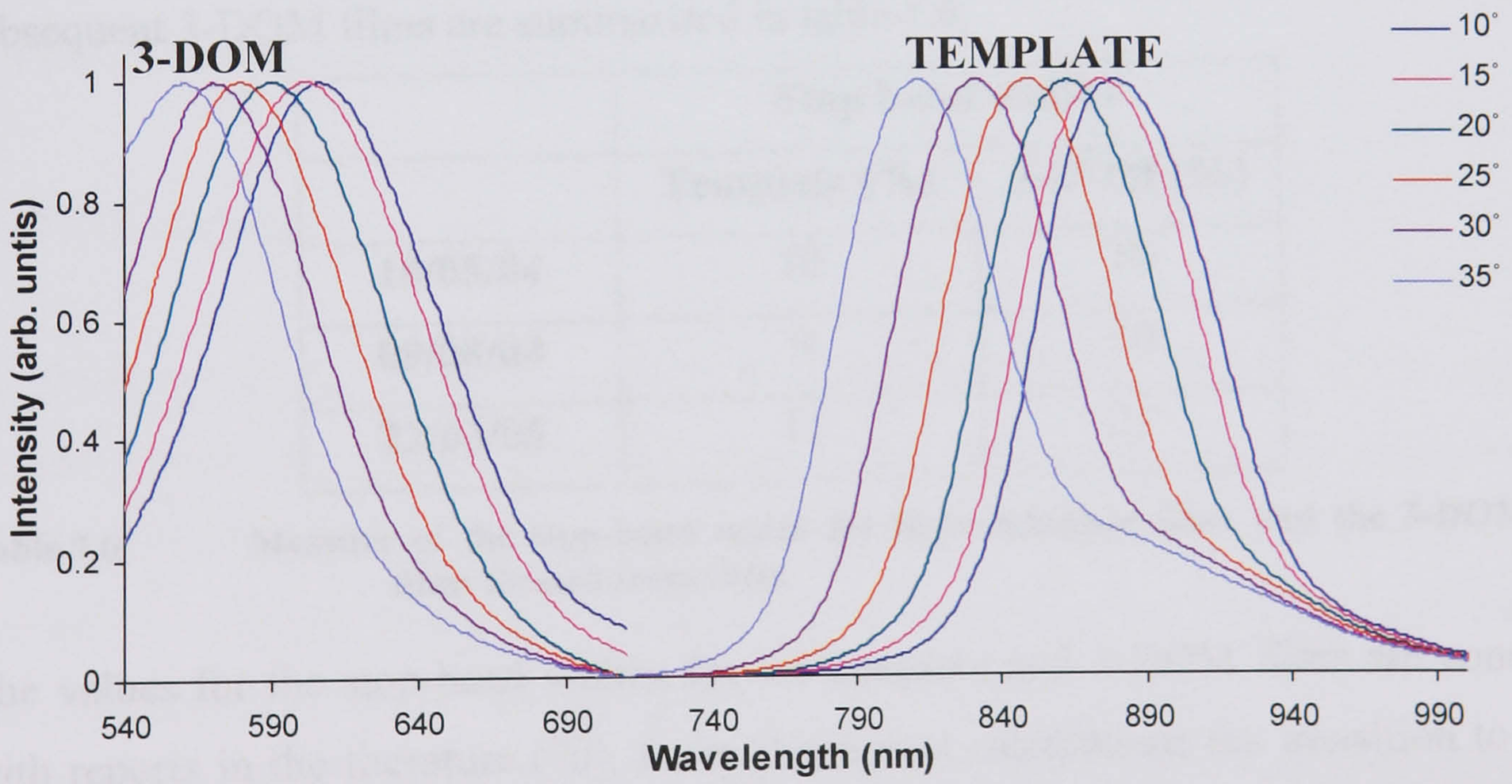


Figure 7.24 Normalised reflection peaks from a template and corresponding 3-DOM PZT film

It can be seen that the reflection peaks from the 3-DOM film are shifted to shorter wavelength compared to the reflection peaks from the template film which is indicative of a shrinkage. However, since well defined reflection peaks are formed, this shrinkage appears not to have affected the optical properties of the 3-DOM films.

To confirm that the stop-bands shown in the reflection spectra were not caused by absorption of the PZT, some of the PZT sol was spin coated onto a glass substrate and calcined under the same conditions as the composite films. This is similar to the method reported by Li *et al* (56) for 3-DOM PLZT samples. A reflection spectrum of the calcined spin coated PZT film showed a reflection peak centred around 400 nm which was not angle dependent. This peak corresponds to an energy value of ~3.1 eV which is close to the band gap energy of 3.6 eV reported by Moret *et al* (181) which is not composition dependent.

The reflectance measurements can also be used to give an idea of the width of the photonic stop-band (70,71). At normal incidence, the ratio of the width of the Bragg peak at half height to the position of the reflectance peak gives a normalised measure of the photonic stop-band (12). The full width at half maximum of the Bragg diffraction peaks is a quantity that can be unambiguously determined and therefore the use of this to infer the width of the stop-band is fully justified (12). Due to our optical set-up it is not possible for measurements to be taken at normal incidence, however, determining the stop-band widths for peaks at 10° or 15° incidence has been established as an alternative (12). The measured stop-band widths for three template films and their subsequent 3-DOM films are summarised in table 7.6.

	Stop band widths	
	Template (%)	**3-DOM (%)**
10/05/04	10	18
09/08/04	9	20
22/03/05	11	21

Table 7.6 **Measure of the stop-band width for three template films and the 3-DOM PZT films formed from them**

The values for the stop-band widths for the template and 3-DOM films are consistent with reports in the literature (70). From theoretical calculations the transition to a full PBG is expected for a stop-band width in the range 15-20% (112). The measure of the photonic stop-band can be considered as a measure of the coupling of the light and the photonic crystal, *i.e.* the photonic strength (112). Thijssen *et al* (12) have shown that the mapping between the stop-band widths and the widths of the frequency gaps in the band structure allows the broad reflection of the 3-DOM materials to be associated with broad frequency gaps in their band structure.

The reflectance spectra gathered from the 3-DOM films can be manipulated to gain information on the interplanar spacing and the effective refractive index. This data can be compared to the optical data collected from the original starting template and a value of the shrinkage which takes place during calcination can be calculated. When comparing the optical data it is only meaningful to compare the d_{111} values for the template and corresponding 3-DOM film. The d_{111} spacing is proportional to the sphere/void size in both cases but for the 3-DOM films the calculation for the void diameter would also include some of the wall material. Hence it is more accurate to compare d_{111} values. Table 7.7 summarises the d_{111} values and the effective refractive calculated from the spectra shown in figure 7.24.

	d_{111} (nm)	**n_{eff}**
Template film	342	1.422
3-DOM film	261	1.379

Table 7.7 Interplanar spacing and n_{eff} calculated from the spectra shown in figure 7.24

The results presented in table 7.7 show that the d_{111} spacing for the 3-DOM film is 24% smaller than that calculated for the template film before infiltration, *i.e.* there has been a shrinkage during infiltration and subsequent calcination. Reasons for this shrinkage will be discussed in the following section.

7.9.4 Shrinkage

The shrinkage of the domains found in 3-DOM materials compared to the original template material has been well documented, as discussed previously. Not only can this shrinkage be observed optically it can also be observed by SEM. The cracks which separated the adjacent domains in the template film remain in the 3-DOM films, but the separation between domains has increased (as shown in figure 7.25).

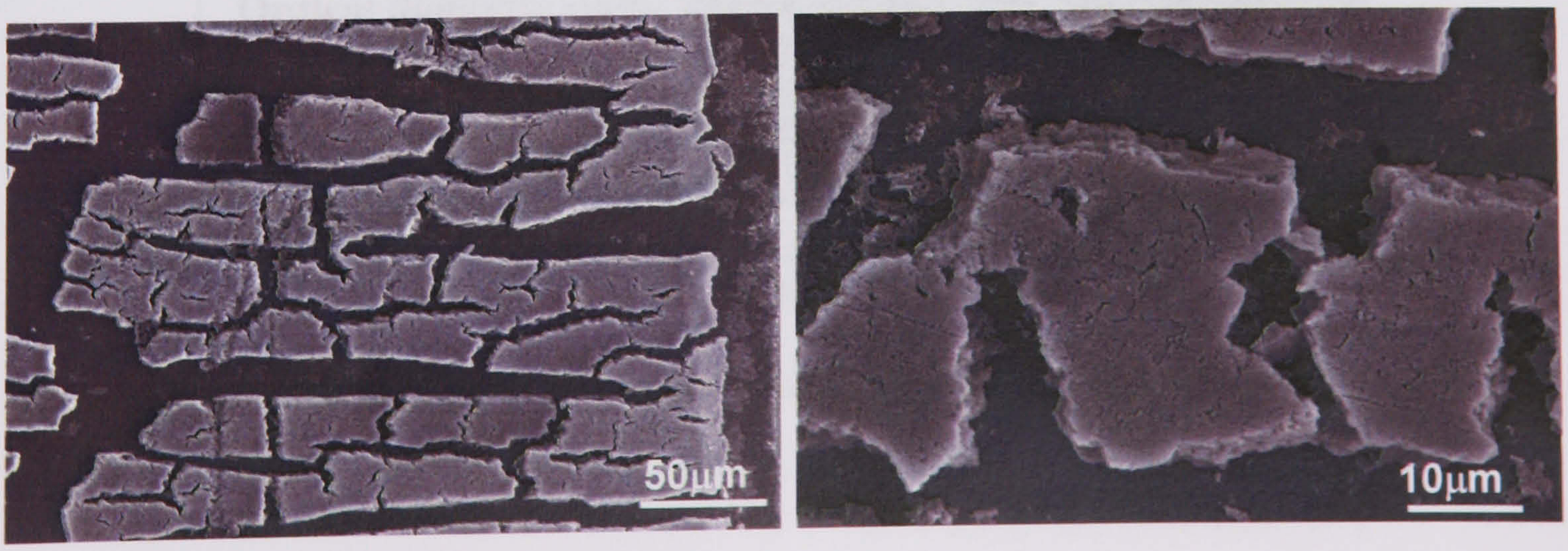


Figure 7.25 **SEM microgrpahs showing the domains present in 3-DOM PZT films. the separation between domanis has increased compared to the template film.**

The domains found in 3-DOM PZT films are typically of the order of 40-70 μm wide compared to 80-100 μm for the corresponding template films. Similarly the cracks between domains have also increased in the 3-DOM films which is indicative of a contraction of the domains which must take place during calcination.

It has been reported that the SEM can be used to measure the centre-to-centre distance of the air spheres in the 3-DOM structure and be used to calculate a value for the shrinkage (16,31). However, there is an error associated with this method since the centre-to-centre void diameter also includes the wall thickness. In this chapter the SEM diameter of the air voids has been calculated in the following manner. Using the measurement tool in the SEM the diameter of one and two air voids was measured to calculate an average wall thickness. A number of air voids was then measured allowing an average air void diameter to be calculated. On average the diameter of around fifty voids was measured. The optical and the SEM data from the 3-DOM films can be related back to the original starting polystyrene colloid which has been measured using SEM, TEM and optical methods. The results for three 3-DOM PZT films are summarised in table 7.8.

	TEMPLATE FILM		
	10/05/04	**09/08/04**	**22/03/05**
SEM diameter (nm)	392	470	388
TEM diameter (nm)	408	474	389
Optical diameter (nm)	410	483	426
	3-DOM FILM		
	10/05/04	**09/08/04**	**22/03/05**
SEM diameter (nm)	236	307	244
Optical diameter (nm)	229	294	296
% shrinkage (optical)	44.2	39.1	30.5
% shrinkage (SEM)	39.8	34.6	37.0

Table 7.8 **Summary of sphere diameter and n_{eff} of three template films and their corresponding 3-DOM films**

The results presented in table 7.8 are indicative of a considerable heat induced shrinkage which takes place during the calcination process and is larger than the percentage

shrinkage reported in the literature (22,70,138). There are two points in the calcination process where shrinkage can take place. Firstly the polystyrene spheres the template films are formed from are mesoporous and probably decrease in diameter as water vapour is released from the pores during heating (21). Secondly during the crystallisation process the precursor material densifies which will cause a contraction of the wall material. Large amounts of alcohol and water are produced when the PZT sol reacts with water in the atmosphere leading to only a small fraction of the oxide material within the voids of the template. During heating this water and alcohol are removed, resulting in shrinkage of the domains.

Depending on the heating rate, the infill method and material a wide range of shrinkages have been reported in the literature, from 17.5% for TiO_2 (21) to 40% for $BaTiO_3$ (151). The increase in the percentage shrinkage reported in this study could be due to the large difference in the density of the PZT sol (ρ=1.02 gcm^{-3} (161) and densified PZT (ρ~7.8 gcm^{-3} (177)) compared to the density of titanium(IV) ethoxide (1.088 gcm^{-3}) and anatase (3.9 gcm^{-3}) (173). In addition the shrinkages reported in the majority of publications are for unsupported 3-DOM materials and, as reported by McComb and co-workers, the shrinkage of a supported 3-DOM material is expected to be greater than an unsupported 3-DOM material (31).

Although it has been reported that the polystyrene spheres can be chemically removed this process has also been shown to damage the periodicity of the 3-DOM material (70,112,147). The PZT sol used in this project is not crystalline and requires to be heated to 530°C for crystallisation to occur. Therefore calcination of the composite film is the most sensible option for removing the template and crystallising in one step, rather than removing the spheres chemically and then heating the fragile 3-DOM PZT film. Since the shrinkage of the domain size in the 3-DOM PZT films is unavoidable the importance of being able to grow template films with large domain sizes is reinforced.

It is important to note that the cracks between domains in the 3-DOM PZT films have not been filled with densified PZT, as shown in figure 7.25. When the template film is immersed into the PZT/ethanol solution and then slowly withdrawn the cracks as well as the template will be filled with the sol. Evaporation of the solvent will occur from the entire surface of the composite film but will be greatest at the regions of largest surface area *i.e.* the infilled domains (173). As the composite domains dry, solvent from the

cracks is drawn by capillary action into the composite domains. Once within the composite domains the remaining solvent is drawn towards the surface of the domains where it can evaporate. Hence solvent is removed from the cracks and the PZT sol precipitates in the voids of the template.

7.9.5 Volume fraction

It is assumed that in the original template the polystyrene spheres are arranged in an fcc lattice (38,43). In the fcc unit cell 74% of the volume is occupied by polystyrene and the remaining 26% by air. Therefore it would be logical to assume that during the process of 3-DOM material formation the 26% of air in the template film could be potentially filled with PZT. The filling fraction of PZT in the 3-DOM films can be calculated provided the d_{111} spacing, the effective refractive index, and the position of several reflection peaks are known and the refractive index of PZT is taken as 2.6. Using the modified Bragg law n_{eff} can be calculated by equation 7.8:

$$n_{eff}^2 = \frac{\lambda^2}{4d_{111}^2} + \sin^2\theta \qquad \textbf{Equation 7.8}$$

Assuming the effective medium approximation holds the filling fraction of PZT can be calculated by equation 7.9:

$$f_{PZT} = \frac{n_{eff} - 1}{1.6} \qquad \textbf{Equation 7.9}$$

Table 7.9 summarises the calculated filling fraction from the optical data for the 3-DOM films described in table 7.8.

Sample	Filling fraction (%)
10/05/04	17.2
09/08/04	14.4
22/03/05	11.1

Table 7.9 Volume fraction of PZT back calculated from reflectance data using equations 7.8 and 7.9

The filling fractions summarised in table 7.9 agree with reports in the literature that the volume of material located in the voids of the 3-DOM material is less than the theoretical value of 26% (21,56,112,138,152). The majority of publications attribute the reduced filling fraction to a change in density between the precursor material and the crystalline material formed after calcination. The density of the PZT sol used to infill

the template is 1.02 gcm^{-3} (161) compared to the density of crystalline PZT of 7.8 gcm^{-3} (177). Thus if it is assumed that all the void volume, 26%, is filled with PZT sol upon gelation and subsequent crystallisation the volume of PZT would only occupy 13% of the original PZT volume. This would correspond to approximately 3% of the 3-DOM PZT film. The calculated values presented in table 7.9 are significantly higher than the 3% this hypothesis would suggest which can be attributed to multiple infiltrations of the template. The PZT will partly hydrolyse between infill cycles becoming denser and permitting the diffusion of more PZT sol on subsequent infiltrations.

Other authors attribute the reduced filling fraction to incomplete infiltration (70) and the presence of voids in this structure. This hypothesis has been supported for 3-DOM NiO where the calculated filling fraction is less than the predicted volume based on density alone and thus it should not be assumed that infiltration has been successful throughout the entire template (138), as shown in figure 7.16(c).

In some of the prepared 3-DOM films incomplete filling of the template is shown by the presence of small triangular voids at the intersections of the PZT walls, as shown in figure 7.26.

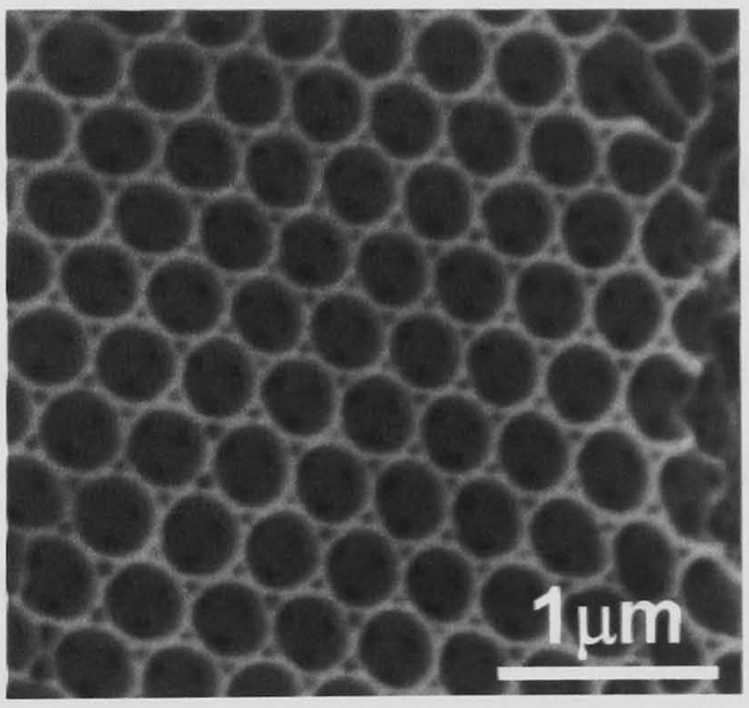


Figure 7.26 SEM micrograph showing small triangular voids at the intersection of the PZT walls

The triangular voids are located in positions corresponding to the octahedral and tetrahedral voids in the template film (21,145) where the spheres are in contact with the next layer (112). It has been suggested that the unfilled voids occur because the thin channels between spheres fill more rapidly than the octahedral and tetrahedral voids and thus when the PZT sol dries the voids are blocked from further filling (145). The formation of these voids indicates that, as discussed previously, the walls of PZT form due to capillary forces between the PZT sol and the polystyrene template (21). Although

the presence of these voids could potentially reduce the mechanical strength of the 3-DOM films they have been predicted to increase the width of the PBG (112.145).

7.10 Optimisation of the infiltration process

7.10.1 Infiltration process

Gu *et al* (148) have reported that the critical parameters for complete infiltration and good surface coverage of a 3-DOM film are the concentration of precursor, the number of times the template is filled and the lifting speed from the precursor solution. Essentially for complete infiltration a concentrated solution and a slow lifting speed should be used. For the experiments reported in this chapter there was no mechanical control of the lifting speed but it was ensured that the template films were withdrawn as slowly as possible to allow capillary forces to act.

The PZT sol is diluted with ethanol to lower the viscosity of the sol and also to improve the wetting properties of the sol (70). It has been reported that, although an increase in the concentration of the precursor solution or the number of dips will improve the filling fraction of the template it will also cause delamination of the film surface (148,154). In addition a 'crust' can be formed over the surface of the template domains. Before calcination this crust is precipitated precursor formed because all the voids in the template have been over filled. Upon drying/gelation of the precursor material there is a contraction of the crust due to an increase in density. This density change causes the top of the composite domains to curl upwards away from the substrate inducing delamination of the film (64,154).

Experiments have been conducted to find the optimum parameters for complete infiltration. The effect of film thickness was first investigated. As discussed in chapter 5 the thickness of the template films can be controlled by varying the colloidal concentration which also has the added benefit of increasing the template domain size (122).

However when thicker template films, >15 μm, were infilled serious delamination problems were encountered. Every time the template film is immersed in the PZT solution damage occurs and therefore to ensure complete infiltration of the template the

PZT concentration was increased. However this increased PZT concentration also caused damage to the film surface due to densification of the PZT upon drying. In some cases as much as 50% of the film delaminated from the substrate surface. SEM micrographs of 3-DOM films where delamination has occurred are shown in figure 7.27.

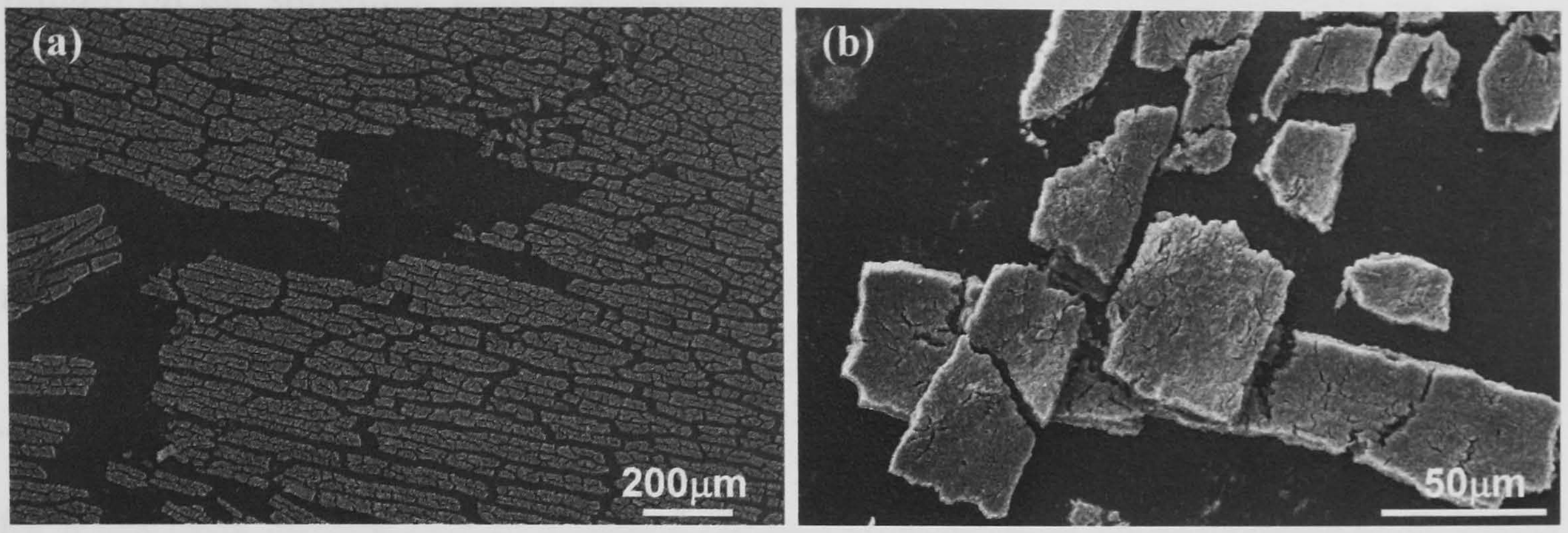


Figure 7.27 SEM micrographs showing the surface of 3-DOM PZT films where delamination has occurred (a) regions where there is no film coverage and (b) re-adhered delaminated domains

The surface of the 3-DOM films show large regions where there is no film coverage due to delamination (figure 7.27(a)). In some cases the delaminated domains have become re-adhered to the substrate, as shown in figure 7.27(b), but the re-location position is random. Further experiments indicated that an optimum template film thickness was ~8 μm.

Investigation of the images from the 3-DOM PZT films has given some insight into the way in which delamination occurs in the template films. Monolayers of inverse structured material are often located on the substrate near to 3-DOM domains, as shown in figure 7.28.

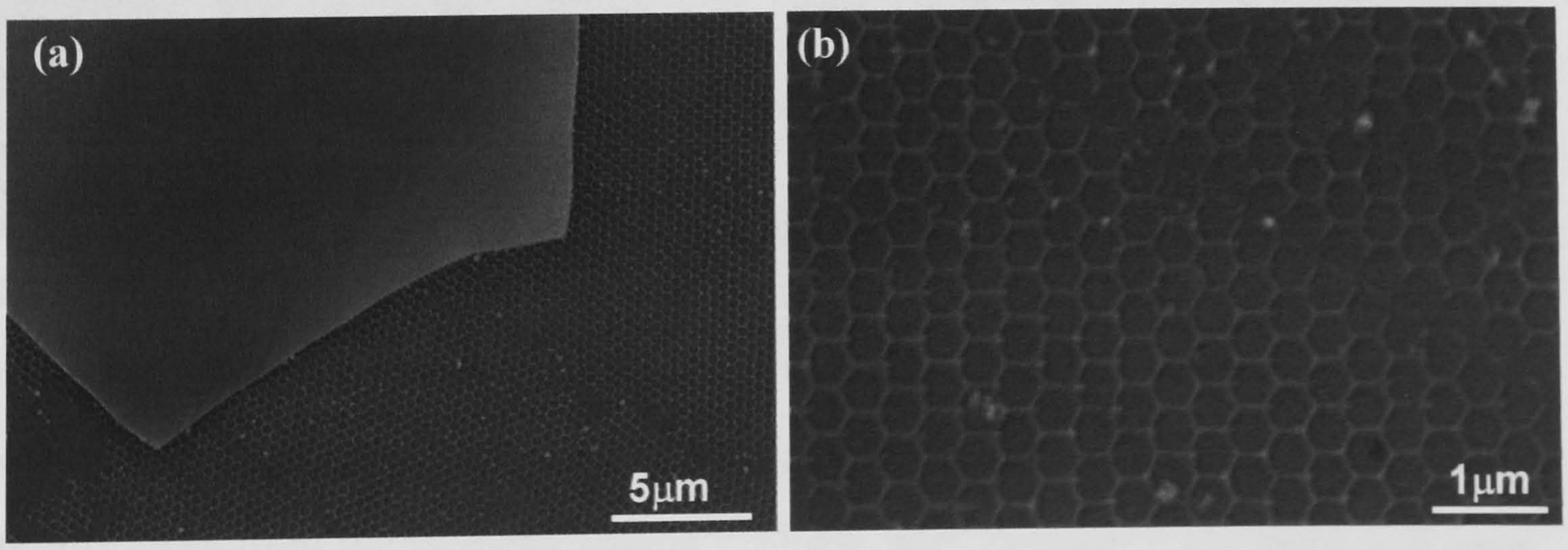


Figure 7.28 SEM micrographs showing (a) crusted inverse domain surrounded by an ordered monolayer and (b) ordered 2-DOM PZT

The presence of these regions of 2-DOM material would indicate that after delamination of the template domains, probably as a result of infilling, layers a few spheres thick remain on the substrate. It can therefore be hypothesised that delamination of the film tends to occur at a sphere/sphere interface rather than at the sphere/substrate interface. The interaction between adjacent spheres in the template are typically weak bonds, dipole-dipole or van der Waals (64), indicating that the sphere/substrate interaction must be stronger.

The effect of the concentration of PZT sol and the number of fillings was investigated for 8 μm thick template films. Experimentally it was found that an ethanol:PZT ratio of 3:1 and 2-3 successive dips of the template film resulted in the best quality and coverage of the 3-DOM PZT film after calcination. If the concentration of PZT was too high or the template filled to many times a crust of PZT was formed over the top of the 3-DOM PZT domains, as shown in figure 7.29.

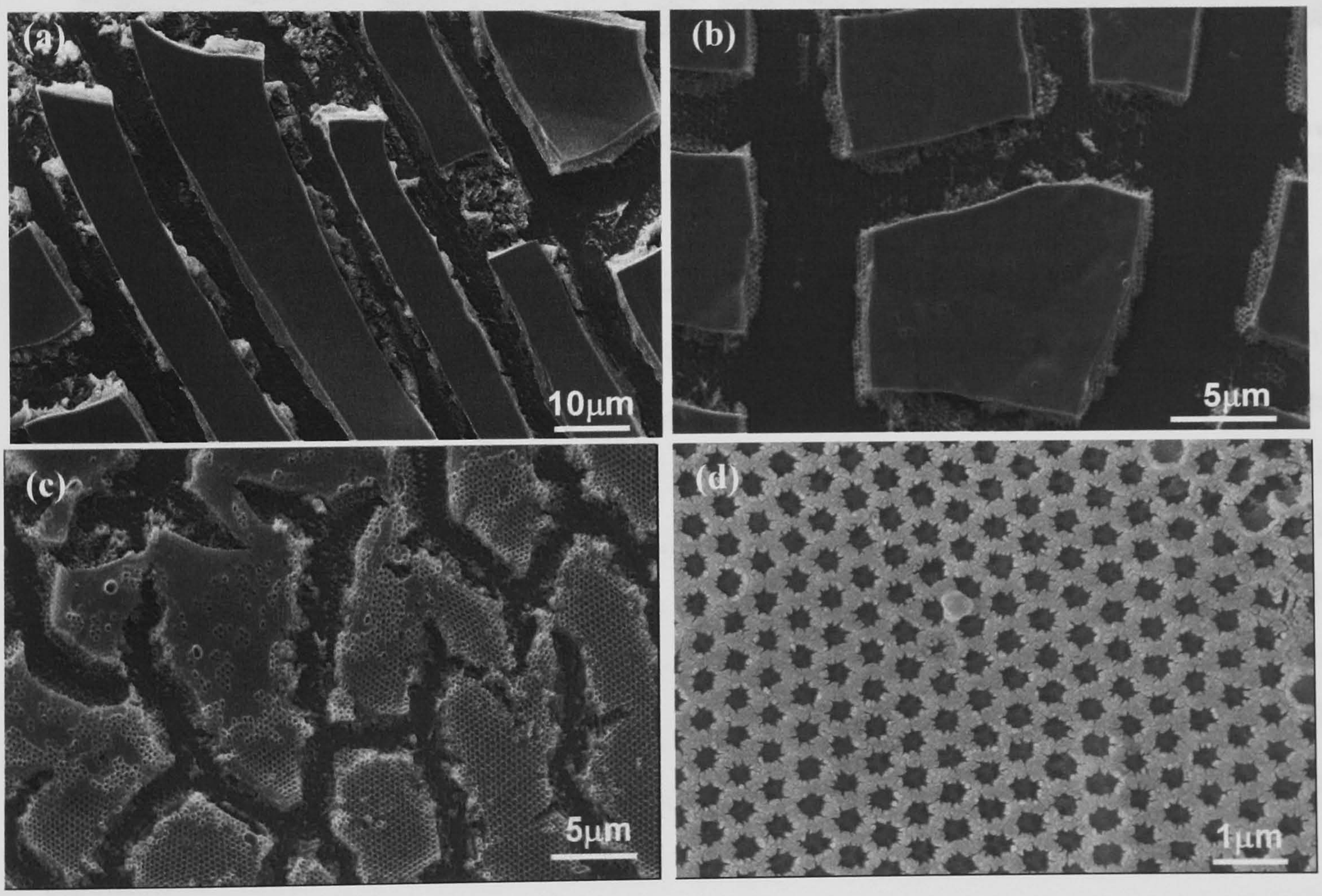


Figure 7.29 partial crust **SEM micrographs showing (a) large domains with a PZT crust on the top surface, (b) below the crust a 3-DOM PZT structure exists, (c) domains with formation and (d) voids surrounded by a thick PZT wall**

As discussed previously the crusted 3-DOM PZT domains can be observed curling upwards away from the substrate (figure 7.29(a)). The presence of this crust will limit any optical properties of the 3-DOM films since it covers the well ordered inverse structure below. Below the crust of PZT the filling of the domains is complete, as shown in figure 7.29(b). If the concentration of PZT or the number of dips is just too

high a partial crust is formed over the top of the domains, as shown in figure 7.29(c). The crust formation is the result of over filling the voids within the template film significantly. If the voids are only over filled slightly the result is that the thickness of the wall material increases. This effect is illustrated in figure 7.29(d) where the void diameter is decreased.

High resolution SEM images reveal differences in the microstructure of the 3-DOM films (figure 7.30).

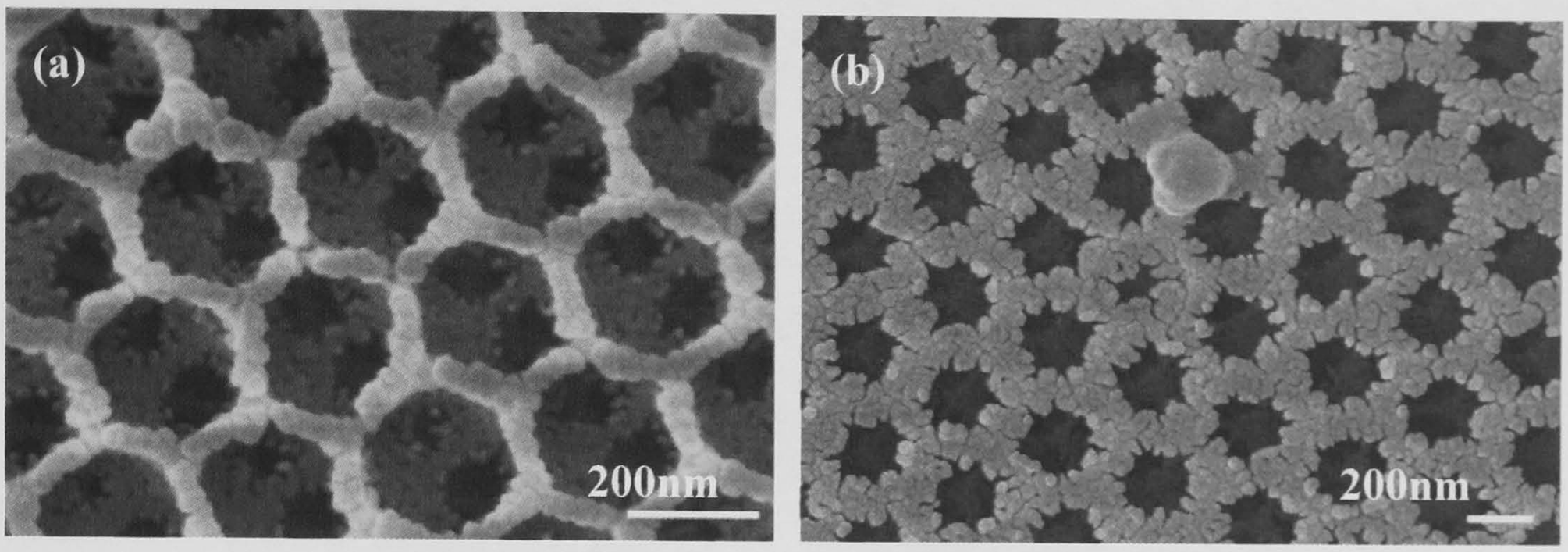


Figure 7.30 **High resolution SEM images reveal differences in the microstructure and allow the grain size to be measured (a) typical wall morphology and (b) walls composed of many grains**

The majority of the films have similar morphology to that shown in figure 7.30(a), although there are small regions which display morphology as shown in figure 7.30(b). Whilst the centre-to-centre distance between the air voids is the same in both images, approximately 200 nm, the wall thickness varies. In figure 7.30(a) the walls are ~50 nm thick and composed of grains 40-50 nm in size. In contrast the walls in figure 7.30(b) are ~150 nm thick, however, the grain size is still ~40-50 nm. The origin of the difference in wall thickness, which is only observed at small regions close to the edge of the films may be associated with differential rates of evaporation of the solvent at the edges of the substrate, or possibly temperature gradients across the substrate during calcination (182).

7.10.2 Calcination conditions

The calcination conditions of the composite film have an important effect on the quality of the 3-DOM material formed (138). At temperatures above 310°C there is an acceleration of the weight loss due to the decomposition of the polystyrene spheres (138). This combustion process is highly exothermic, as shown by the large exothermic

peak in the DTA analysis of polystyrene (figure 7.12), and can be detrimental to the structure of the 3-DOM material if excessive bubbling resulting from gas production during decomposition is allowed (138). The heating and the air flow during calcination also have an effect on the removal of the polystyrene template.

Experiments were conducted to investigate the effect of the heating rate and the air flow on the shrinkage of the 3-DOM films, the results of which are summarised in table 7.10 and 7.11.

Ramp rate	SEM shrinkage (%)
0.5°C/min	38
1°C/min	39
2°/min	40

Table 7.10 **Calculated shrinkage depending on the heating rate of calcination**

Air flow	SEM shrinkage (%)
No air flow	43
Normal air flow	39
Fast air flow	43

Table 7.11 **Calculated shrinkage depending on the air flow during calcination**

The results presented in table 7.10 indicate that as the heating rate of the calcination process is increased the shrinkage with respect to the original template film increases. A slower heating rate allows more even combustion of the polystyrene spheres avoiding excessive bubbling of the gaseous by-products which is detrimental to the structure of the 3-DOM film (figure 7.31(a)). However if the heating rate is too slow the film is held at elevated temperatures for prolonged periods of time which can also have a detrimental effect on the quality of the 3-DOM film. Thus a heating rate of 1°C/min was found to be optimum and is the rate used for the calcination of all composite films reported in this chapter.

The air flow during calcination accelerates the decomposition of the polystyrene spheres and aids the transport of the by-products of the combustion reaction (138). The results presented in table 7.11 show that the minimum amount of shrinkage was achieved when a normal air flow was used. If the decomposition of the polystyrene spheres occurs too quickly or slowly, *i.e.* under a fast or no air flow, the periodic structure of the 3-DOM material can be damaged. In addition since the tube furnace was calibrated under air flow, if there is no air flow present the effective temperature the composite films are

treated at is higher and thus more damage can be done to the fragile 3-DOM material (figure 7.31(b)).

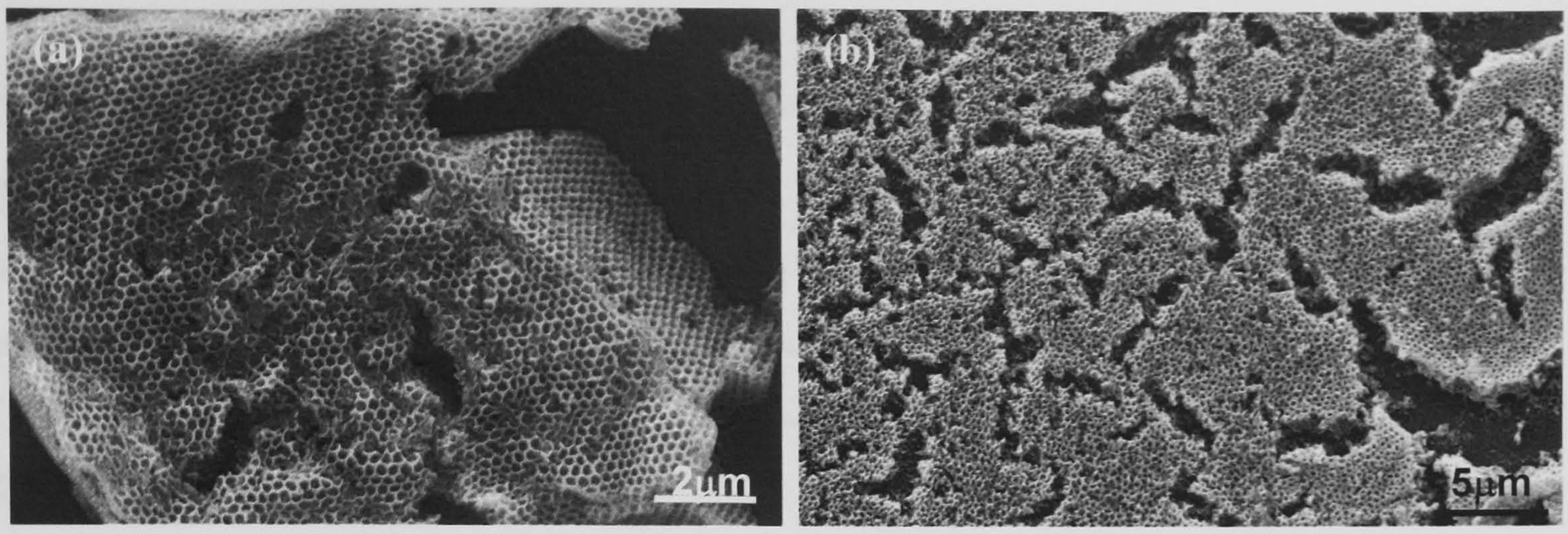


Figure 7.31 **SEM micrographs showing the detrimental effect on the 3-DOM material caused by (a) high heating rate and (b) fast air flow during calcination**

7.10.3 Optimum formation conditions

The SEM micrographs shown in figure 7.32 illustrate the quality of the 3-DOM films formed at the optimum conditions, *i.e.* an ethanol:PZT ratio of 3:1 and 2-3 successive dips, a 1˚C/minute heating rate and a normal air flow during calcination.

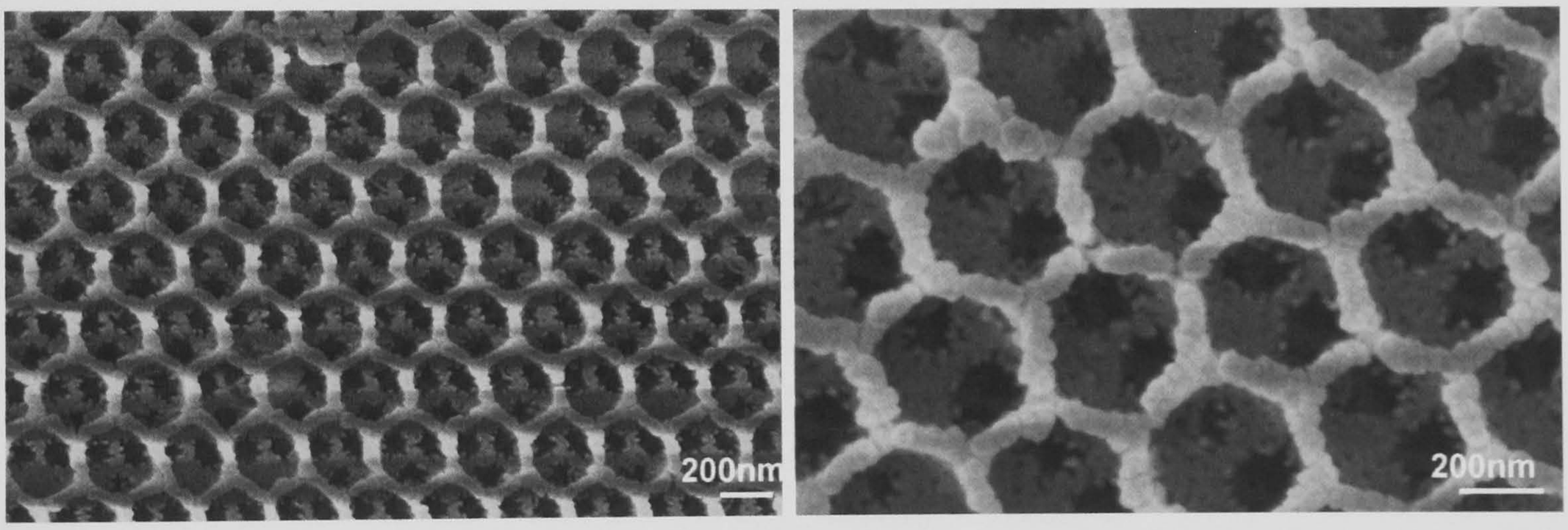


Figure 7.32 **High resolution SEM micrographs showing the surface of a 3-DOM PZT film formed at the optimum conditions**

7.11 Conclusions

Several routes have been investigated for the formation of 3-DOM PZT films from a polystyrene synthetic opal template. The most successful method for infiltration of a well defined PZT(30/70) sol is outlined in figure 7.3. The quality of the 3-DOM PZT films has been assessed by reflectance spectroscopy and SEM. Although there is a considerable shrinkage of the 3-DOM films with respect to the original template film,

~30%, this increased cracking has been shown not to affect the optical properties of the macroporous films.

The PZT sol and the 3-DOM PZT films were characterised by XRD and EDX. Analysis of the 3-DOM films by XRD analysis has confirmed that the desirable tetragonal phase has formed after calcination at 530˚C. In addition the 3-DOM films are as chemically homogeneous as the PZT sol used for infiltration as shown by EDX analysis in the TEM. This ensures that the chemical composition of the PZT is the same in the 3-DOM films as the starting PZT sol.

Although the refractive index of PZT is not high enough for the 3-DOM PZT films to have a complete PBG the formation of macroporous ferroelectric films may open the possibility for the films to be used as multifunctional or tunable PCs.

8 Towards a Multifunctional 3-DOM Material

8.1 Introduction

The previous chapter described the formation and characterisation of well ordered 3-DOM PZT films with a tetragonal phase. Although PZT has a high band gap and a refractive index of ~2.6, the refractive index contrast formed between the PZT and air in the 3-DOM structure is not great enough for a complete photonic band gap (PBG) to be realised. However, PZT is a ferroelectric material with tunable dielectric and optical properties due to phase transition, domain change and some coupling effects such as piezoelectric, pyroelectric and electro-optic properties (51). Therefore 3-DOM PZT films may be ideal materials for achieving a tunable or multifunctional photonic crystal (PC) and to the best of our knowledge 3-DOM PZT has not been reported in the literature.

A PC with a tunable stop-band is highly desirable because not only could it be used for simple on/off switching but in addition allows external control of the photonic properties. There have been reports in the literature of 3-DOM materials tuned by an electric field (50,51,56) and by temperature (103,150). The most promising tunable PCs may be based on application of an electric field due to the technical compatibility of the PC components with current electronic or optoelectronic technology (51).

The first class of electrically tunable PCs was proposed by Busch and John in 1999 (49). In this publication a nematic liquid crystal was infiltrated into the voids of a 3-DOM silicon material. By applying an electric field, which rotates the axis of the nematic molecules relative to the 3-DOM silicon backbone, the 3-D PBG can be opened or closed. More recently Li *et al* (51) have reported the formation of 3-DOM PLZT which can be electrically tuned. It has been reported that for a voltage increase of 700 V there was a corresponding change in refractive index of 0.035 resulting in a red shift of the reflection peak at normal incidence.

In this chapter the initial results will be reported for attempts to electrically tune the photonic stop-band of 3-DOM PZT films. As reported by Li *et al* (51) the change in the

refractive index of the 3-DOM PLZT crystals is due to the electro-optic effect where the applied electric field, or voltage, induces birefringence.

8.2 Birefringence

Birefringence is defined as double refraction of light in a transparent molecularly ordered material which is manifested by the existence of orientation-dependent differences in the refractive index (183).

Electromagnetic (EM) radiation propagates through space with oscillating electrical and magnetic field vectors, which are perpendicular to one another and to the direction of wave propagation. An EM wave propagates through a material by exciting atoms within the medium, electrons are driven by the field and re-radiate (97). These secondary wavelets re-combine and the resultant refracted wave moves on. The speed of the wave, or the refractive index, is determined by the difference between the frequency of the electric field and the natural frequency of the atoms – the dielectric constant. The vectorial relationship between an EM wave and a material is controlled by the orientation of the lattice vectors and the direction of the electric component of the EM wave.

The laws of electromagnetism proposed by Maxwell demonstrated that the velocity of light through a material, c`, could be described by equation 8.1,

$$c` = \frac{c}{\sqrt{\varepsilon\mu}} \qquad \textbf{Equation 8.1}$$

, where c is the speed of light in a vacuum, ε is the dielectric constant and μ is the magnetic permeability. Generally the materials used for PCs can be considered as non-magnetic and consequently μ can be set to unity (7). The refractive index of a material, n, can be calculated by equation 8.2.

$$n = \frac{c}{c`} \qquad \textbf{Equation 8.2.}$$

Thus if equations 8.1 and 8.2 are combined the relationship between the dielectric constant and the refractive index can be found (equation 8.3)

$$n = \sqrt{\varepsilon} \qquad \textbf{Equation 8.3}$$

Many crystalline materials are optically anisotropic. Anisotropic crystals have crystallographically distinct axes and interact with EM radiation by a mechanism which is dependent upon the orientation of the crystalline lattice with respect to the incident radiation angle. Crystals which have hexagonal, tetragonal or trigonal systems are optically anisotropic, *i.e.* EM radiation propagating in some general direction will encounter an asymmetric structure (97). The optic axis (typically the c or z axis) corresponds to the direction about which the atoms are arranged symmetrically – for the tetragonal system there is only one such direction and hence tetragonal crystals are termed uniaxial.

In an anisotropic material the precise geometrical ordering of the atoms is not symmetric with respect to the crystalline axes and the electrical properties vary depending on the direction from which they are probed. Thus, since the refractive index is related to the dielectric constant (equation 8.3), the refractive index also varies with direction when EM radiation is passed through the material. When anisotropic crystals refract light the incoming wave is split into two components which take different paths through the crystal and emerge as separate waves (184), schematically illustrated in figure 8.1.

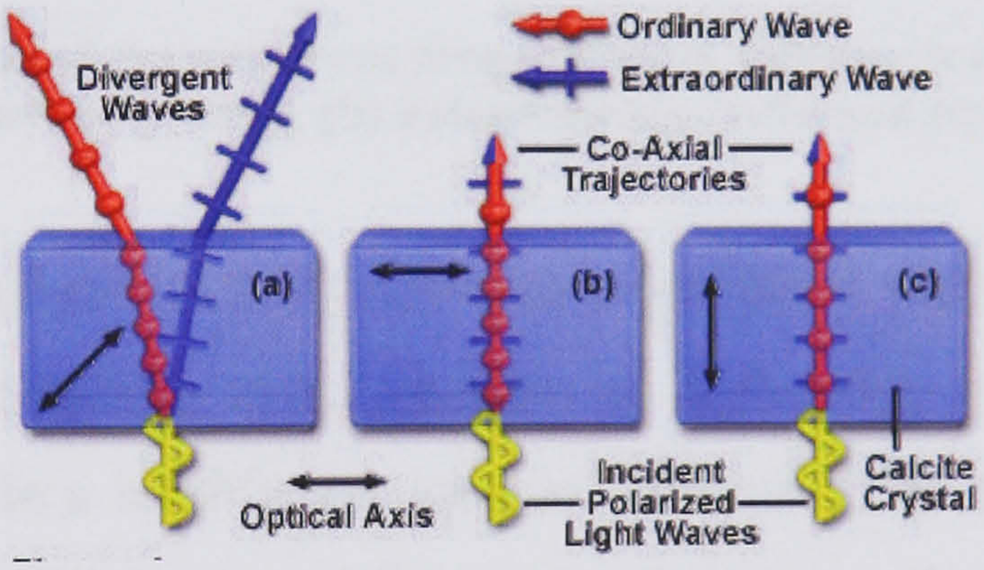


Figure 8.1 **Schematic illustration of the separation of light waves by a birefringent calcite crystal (185)**

The light polarised perpendicularly to the plane containing the propagation vector and the optic axis obeys normal refraction (183). This wave has ordinary polarisation, hence called the ordinary ray, and experiences a refractive index n_o. The light polarised in the plane containing the propagation vector and the optic axis travels with a velocity dependent on the propagation direction within the crystal (183). This ray has extraordinary polarisation, is termed the extraordinary ray, and has a refractive index n_e which depends on the angle between the optic axis and the propagation vector. The ordinary and extraordinary rays leave the crystal as linearly polarised rays with their electric field vectors vibrating in mutually perpendicular planes (184).

The difference in the refractive index of the ordinary and extraordinary rays is defined as the birefringence (Δn or B) (equation 8.4) (97)

$$B = \Delta n = \left| n_e - n_o \right| \qquad \textbf{Equation 8.4}$$

In a birefrigent crystal the ordinary ray can be described in terms of a spherical wavefront based on Huygen's principle of wavelets emanating from a point source of light in a homogeneous medium (illustrated in figure 8.2(a)) (97). The refractive index experienced by the wavelets is uniform and therefore the waves propagate with constant velocity. However, the extraordinary waves encounter variations in the refractive index as a function of direction and the wavelets can be described by the surface of an ellipsoid of revolution (97). The ellipsoidal wavefront of the extraordinary wave is illustrated in figure 8.2(b).

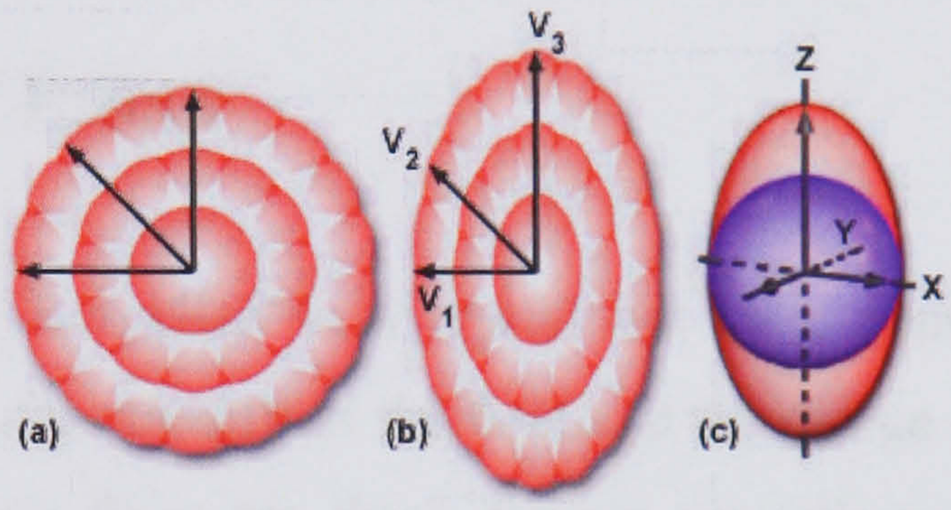


Figure 8.2 Illustration of the wavefront propagation in anisotropic crystals for the (a) ordinary wave, (b) extraordinary wave and (c) refractive index ellipsoid (185)

The 'index ellipsoid' (figure 8.2(c)) provides a graphical method of visualising and calculating how the refractive index changes as a function of the propagation and polarisation directions in a birefringent material in terms of n_o and n_e. The axes of the shaded ellipse in figure 8.3 lie in the directions of the two allowed polarisations – the ordinary and extraordinary waves.

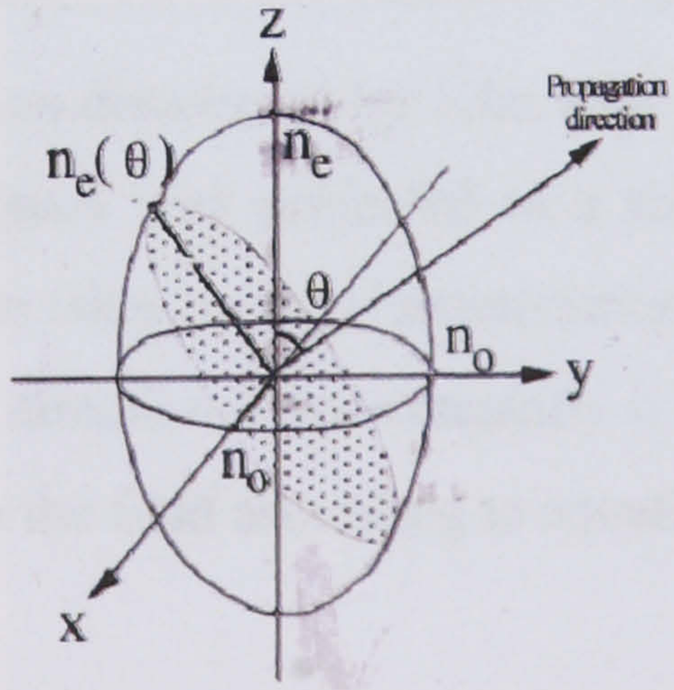


Figure 8.3 Illustration of the index ellipsoid showing the relationship between the ordinary and extraordinary waves

The length of the semi-minor axis of the shaded ellipse is n_o and the length of the semi-major axis is $n_e(\theta)$, the refractive index seen by the extraordinary wave. The relationship between $n_e(\theta)$, n_e and n_o is shown by equation 8.5:

$$\frac{1}{n_e(\theta)^2} = \frac{\sin^2\theta}{n_e^2} + \frac{\cos^2\theta}{n_o^2} \qquad \textbf{Equation 8.5.}$$

The index ellipsoid, or the indicatrix, is a geometric representation of the second order tensor which describes the optical properties of a crystal (186). In a general coordinate system, x, y and z, the equation of the index ellipsoid has the general form (equation 8.6),

$$\left(\frac{1}{n^2}\right)_1 x^2 + \left(\frac{1}{n^2}\right)_2 y^2 + \left(\frac{1}{n^2}\right)_3 z^2 + 2\left(\frac{1}{n^2}\right)_4 yz + 2\left(\frac{1}{n^2}\right)_5 xz + 2\left(\frac{1}{n^2}\right)_6 xy = 1 \qquad \textbf{Equation 8.6}$$

8.3 Electro-optic Effect

When an electric field is applied to a crystal the ionic constituents move to new locations determined by the strength of the field and the charge of the ions (187). In an anisotropic crystal, where there are three distinct crystallographic axes, the applied electric field causes a change in anisotropy. These changes can be described in terms of a modification of the index ellipsoid as illustrated schematically in figure 8.4.

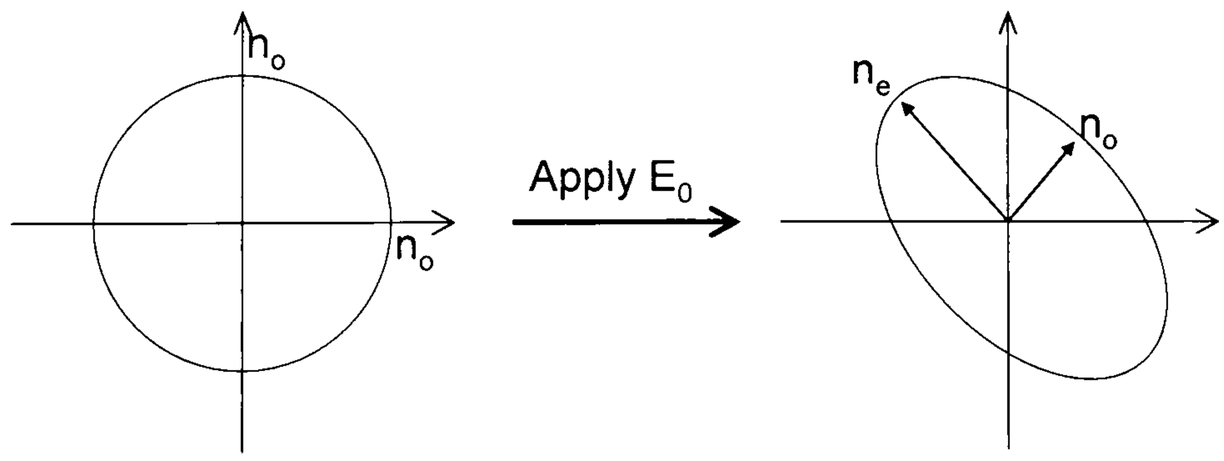


Figure 8.4 Schematic illustration of the effect of an electric field on the index ellipsoid

The first electro-optic effect was discovered by John Kerr in 1875. He found that when an isotropic transparent substance was subjected to a strong electric field it became birefringent (188). The medium takes on the characteristics of a uniaxial crystal with the optic axis parallel to the field direction. Experimentally it was found that the refractive index varies quadratically with the field according to equation 8.7 (57).

$$\Delta n(E) = -\frac{1}{2} R n^3 E^2 \qquad \textbf{Equation 8.7}$$

, where R is the quadratic/Kerr electro-optic coefficient, n is the refractive index and E is the applied field. The Kerr effect is generally exhibited by ferroelectrics in the paraelectric phase and typically has a coefficient of the order $x10^{-18}$ m^2/V^2.

The linear electro-optic effect was named after the German physicist, Pockel, who studied this effect in 1893. In the Pockels effect the refractive index, n, varies linearly with the applied electric field according to equation 8.8 (57),

$$\Delta n(E) = -\frac{1}{2} r n^3 E \qquad \textbf{Equation 8.8}$$

, where all parameters have the same meaning as in equation 8.7 and r is the linear or Pockels coefficient. The linear electro-optic response is only observed over a limited applied field range that does not lead to domain switching (57) and can only be observed for crystal systems that do not possess a centre of symmetry (183,187).

The linear electo-optic effect results from an anharmonic response of the valence electrons to intense light. The applied electric field changes each of the $\left(\frac{1}{n^2}\right)_i$ coefficients in equation 8.6 in a way that is linearly dependent on the E_x, E_y and E_z components of the field (187). The change in the coefficients is described by the electro-optic tensor, r, (184) through the relationship (equation 8.9),

$$\Delta\left(\frac{1}{n^2}\right)_i = \sum_{j=1}^{3} r_{ij} E_j \qquad \textbf{Equation 8.9}$$

, where $E_1=E_x$, $E_2=E_y$ and $E_3=E_z$.

Equation 8.9 can be represented in matrix form by equation 8.10 (183):

$$\begin{pmatrix} \Delta\left(\frac{1}{n^2}\right)_1 \\ \Delta\left(\frac{1}{n^2}\right)_2 \\ \Delta\left(\frac{1}{n^2}\right)_3 \\ \Delta\left(\frac{1}{n^2}\right)_4 \\ \Delta\left(\frac{1}{n^2}\right)_5 \\ \Delta\left(\frac{1}{n^2}\right)_6 \end{pmatrix} = \begin{pmatrix} r_{11} & r_{12} & r_{13} \\ r_{21} & r_{22} & r_{23} \\ r_{31} & r_{32} & r_{33} \\ r_{41} & r_{42} & r_{43} \\ r_{51} & r_{52} & r_{53} \\ r_{61} & r_{62} & r_{63} \end{pmatrix} \begin{pmatrix} E_x \\ E_y \\ E_z \end{pmatrix} \qquad \textbf{Equation 8.10}$$

The form of the matrix, r_{ij}, describing the electro-optic tensor depends on the symmetry of the crystal. For tetragonal PZT the crystal has the space group C_{4v} or P4mm and r_{ij} can be can be represented in tensor form as equation 8.11

$$r_{ij} = \begin{pmatrix} 0 & 0 & r_{13} \\ 0 & 0 & r_{13} \\ 0 & 0 & r_{33} \\ 0 & r_{51} & 0 \\ r_{51} & 0 & 0 \\ 0 & 0 & 0 \end{pmatrix} \qquad \textbf{Equation 8.11.}$$

The application of the electric field introduces cross terms so that x, y and z are no longer appropriate principal axes and the index ellipsoid has been changed in shape and rotated in space (187), as shown schematically in figure 8.4.

In order to explain the origin of the electro-optic effect, DiDomenco and Wemple presented a unified theory of the optical properties of oxygen-octahedra ferroelectrics based on electronic band structure calculations (189). This theory stressed the fundamental importance of the BO_6 octahedra building block. As previously discussed the structure of an ABO_3 type ferroelectric can be considered as composed of a network of oxygen octahedra. At the centre of the octahedra lies a transition metal ion, in the case of PZT a zirconium or titanium ion. From a band structure point of view the BO_6 octahedra govern the low lying conduction bands and the upper valence bands (189). This is because if the bonding is purely ionic the d-orbitals of the B cation and the 2p orbitals of the oxygen anion are the major contributors to the energy bands of interest. The O (2p) levels form a filled valence band and the lowest lying conduction band

derives from the d-orbitals of the B ion. The d-orbitals are split into t_{2g} and e_g sub-bands, as illustrated in figure 8.5.

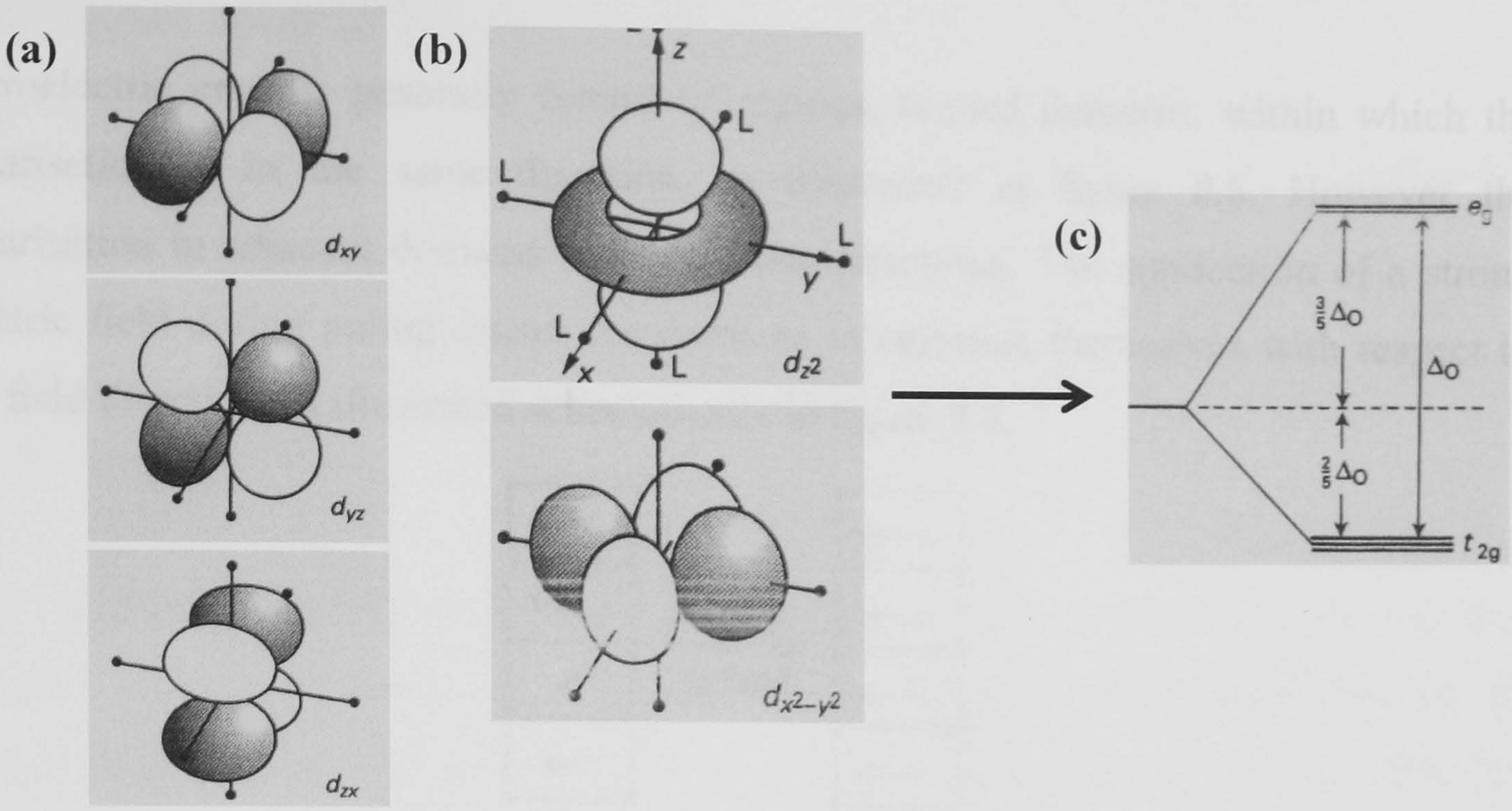


Figure 8.5 The orientation of the 5d-orbitals with respect to the ligands of an octahedral complex (a) the t_{2g} triplet, (b) the e_g pair and (c) the relative energies of the d-orbitals in an octahedral crystal field (41)

The B ion is located in a regular octahedron of anions. In this configuration the t_{2g} orbitals are directed between the anions (figure 8.5(a)) and overlap the p-orbitals of the oxygen anions. The e_g orbitals are directed towards the anions (figure 8.5(b)), experiencing a repulsive electrostatic interaction, and therefore lie at slightly higher energy (see figure 8.5(c)).

When an electric field is applied to the PZT crystal the electronic polarisation of the crystal lattice perturbs the electronic energy bands. The major contributors to the electronic polarisation are the O (2p) orbitals. The polarisation can be viewed as arising from a displacement and distortion of the 2p orbitals which have lobe axes normal to the polarisation axes (189). The perturbation of the p-d π-overlap energy overlap is analogous to the perturbation produced by displacement of the B cation towards the O anion.

8.3.1 Electro-optic Coefficient for PZT

Currently the electro-optic properties have only been evaluated for a small number of ferroelectric thin films with PZT and PLZT being the most widely studied materials

(57). Before the electro-optic coefficients can be calculated the films are generally poled by applying a strong electric field at elevated temperatures (56,162,190).

Ferroelectric crystals generally consist of regions, termed domains, within which the polarisation is in the same direction, as illustrated in figure 8.6. However the polarisation in adjacent domains is in different directions. The application of a strong electric field during poling causes the domains to orientate themselves with respect to the field direction, as illustrated schematically in figure 8.6.

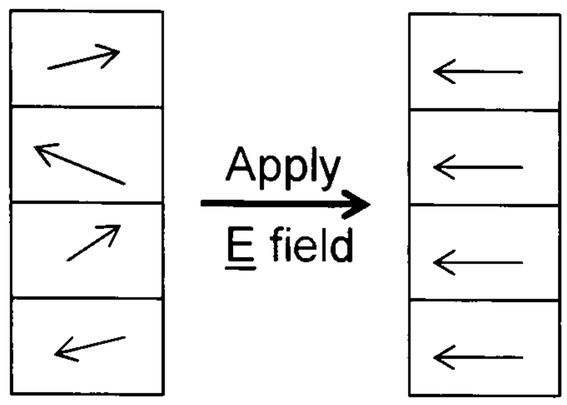


Figure 8.6 Schematic illustration of the effect of poling on the domains of a ferroelectric film

The poling of the films causes the ferroelectric films to become anisotropic on a macroscopic scale with the poling direction being the optical axis (57). Therefore in the poled state the films are optically uniaxial.

However it has been reported that ferroelectric films deposited on a substrate often possess a self-polarisation that may be as high as that produced by subsequent poling (59,190). Kholkin *et al* (190) investigated the self-polarisation effect of $PbZr_xTi_{1-x}O_3$ films of variable composition (x=0.1-0.7). The degree of self-polarisation was found to increase with increasing titanium content implying that the effect of poling in titanium-rich compositions is marginal. The self-polarisation effect can be explained in terms of stress developed during crystallisation and subsequent cooling through the Curie temperature (59,190).

Generally the common methods used to determine the electro-optic coefficient of bulk ferroelectric crystals cannot be used for thin films (191). Ellipsometry (57,162) and two-beam polarisation interferometry (192,193) have been reported as successful methods for measuring the electro-optic coefficient for PZT films.

In the ellipsometry technique a beam of light is passed through the sample and an electric field is applied perpendicularly to the incident light (194). After passing through the sample, the light has an elliptical polarisation and is passed through a $\lambda/4$ plate to

become linearly polarised again. The shift in the polarisation angle corresponds to the magnitude of the optical anisotropy created by the electric field. The shift in birefringence $\Delta(\Delta n)$ can be expressed as equation 8.12,

$$\Delta(\Delta n) = \frac{\lambda_0 \Delta\delta}{2\pi d} \qquad \textbf{Equation 8.12}$$

, where λ_0 is the wavelength of incident light, $\Delta\delta$ is the phase retardation shift and d is the thickness of the film. The electro-optic coefficient can then be calculated using equations 8.7 and 8.8.

The basic concept of the two-beam polarisation technique is to use the electric field induced phase shift between the s and p polarised beams transmitted through the ferroelectric film and reflected back from the opposite surface of the thin film. The phase shift between the s and p polarised waves, $\delta_{\psi 2sp}$, is outlined in equation 8.13.

$$\delta_{\Psi 2sp} = \left(\frac{2\pi d r_e E_m}{\lambda}\right)\left(\frac{n^2 \sin^2\theta}{\sqrt{\left(n^2 - \sin^2\theta\right)}}\right) \qquad \textbf{Equation 8.13}$$

, where d is the thickness of the film, r_e is the electro-optic coefficient, E_m is the electric field, λ is the wavelength of the light, n is the refractive index of the material and θ is the angle of incidence.

Table 8.1 summarises some of the linear/Pockels coefficients calculated for PZT films of different compositions.

Film	E-O coefficient (pm/V)	Reference
PZT (60/40)	24	(162)
PZT (40/60)	65	(192)
PZT (52/48)	46	(195)
PZT (53/47)	50	(196)
PZT (52/48)	165	(193)
PZT (50/50)	40	(197)
PZT (60/40)	20	(197)
PZT (50/50)	40	(198)

Table 8.1 Summary of the linear, or Pockels, coefficient for PZT of different compositions

The electro-optic response for ferroelectric thin films can be smaller than the response found from bulk ceramics or single crystals due to clamping stresses (57). In addition,

internal clamping stresses which occur during domain re-orientation due to the anisotropy of the unit cell can reduce the field induced birefringence.

8.4 Experimental methodology

The methodology for the experimental procedure for electrically testing the 3-DOM PZT films was similar to that reported by Li *et al* (51) for 3-DOM PLZT. In this publication the 3-DOM PLZT sample was mounted as shown schematically in figure 8.7.

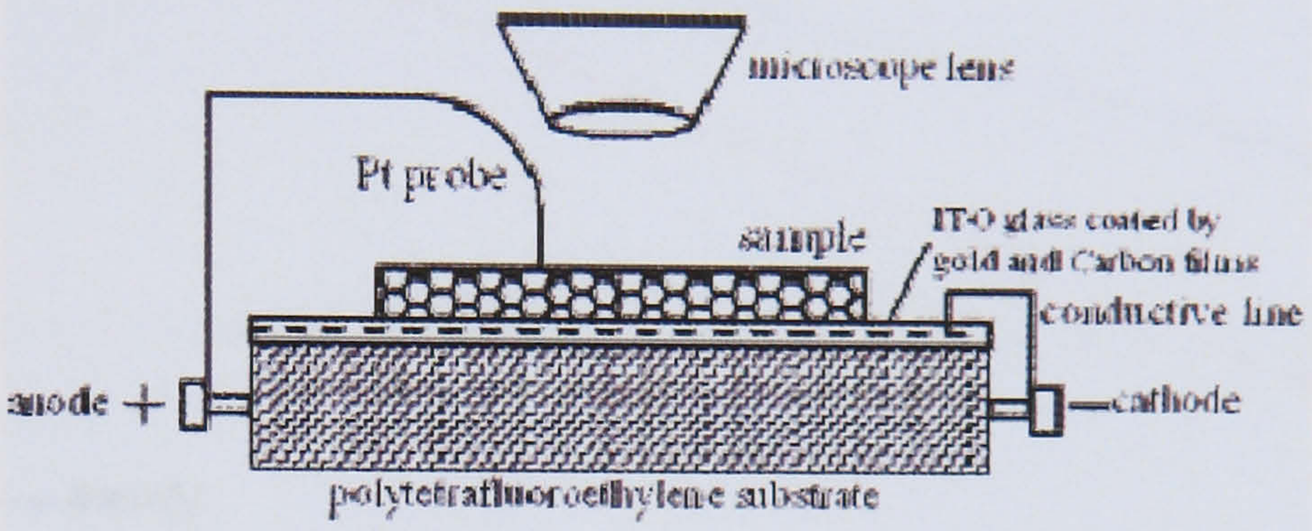


Figure 8.7 Schematic illustration of the method used to electrically test 3-DOM PLZT (51)

The Pt probe contacts the upper face, *i.e.* the (111) plane of the 3-DOM sample and the reflection spectra were measured at the edge of the Pt probe. With an increase in applied voltage the PBG red shifted suggesting that the refractive index at normal incidence increased with voltage/electric field. The 3-DOM PLZT crystals are in the cubic perovskite phase, due to the temperature the composite material is sintered at, and therefore, although not stated in the publication, the shift in refractive index must be attributed to the electro-optic Kerr effect. From the refractive index change of 0.030 corresponding to an applied voltage of 700 V an electro-optic coefficient of $\sim 2 \times 10^{-17}$ m^2/V^2 can be calculated from equation 8.7 which is of the correct order of magnitude for the electro-optic Kerr effect.

The linear electro-optic coefficient depends on the both the composition of PZT which is investigated and the method of film deposition, as illustrated in table 8.1. No values for the composition used in this project, PZT(30/70), could be found in the literature. In order to investigate the electric field induced birefringence of the 3-DOM PZT films calculations were conducted for electro-optic coefficients of 40 and 65 pm/V. These values were chosen because their corresponding PZT compositions were closest to the composition used in this study. Since the electric field, E, is equal to the voltage divided

by the distance the voltage is applied across, the largest electric fields are generated when the voltage is passed through a small distance, *i.e.* the 3-DOM film thickness. The change in refractive index, Δn, can be calculated using equation 8.8. Figure 8.8 summarises the calculations carried out for a 3-DOM PZT film ~8 μm thick in the applied voltage range 0-700 V. The refractive index of PZT(30/70) was taken as 2.6 (calculated from the method presented in (181)).

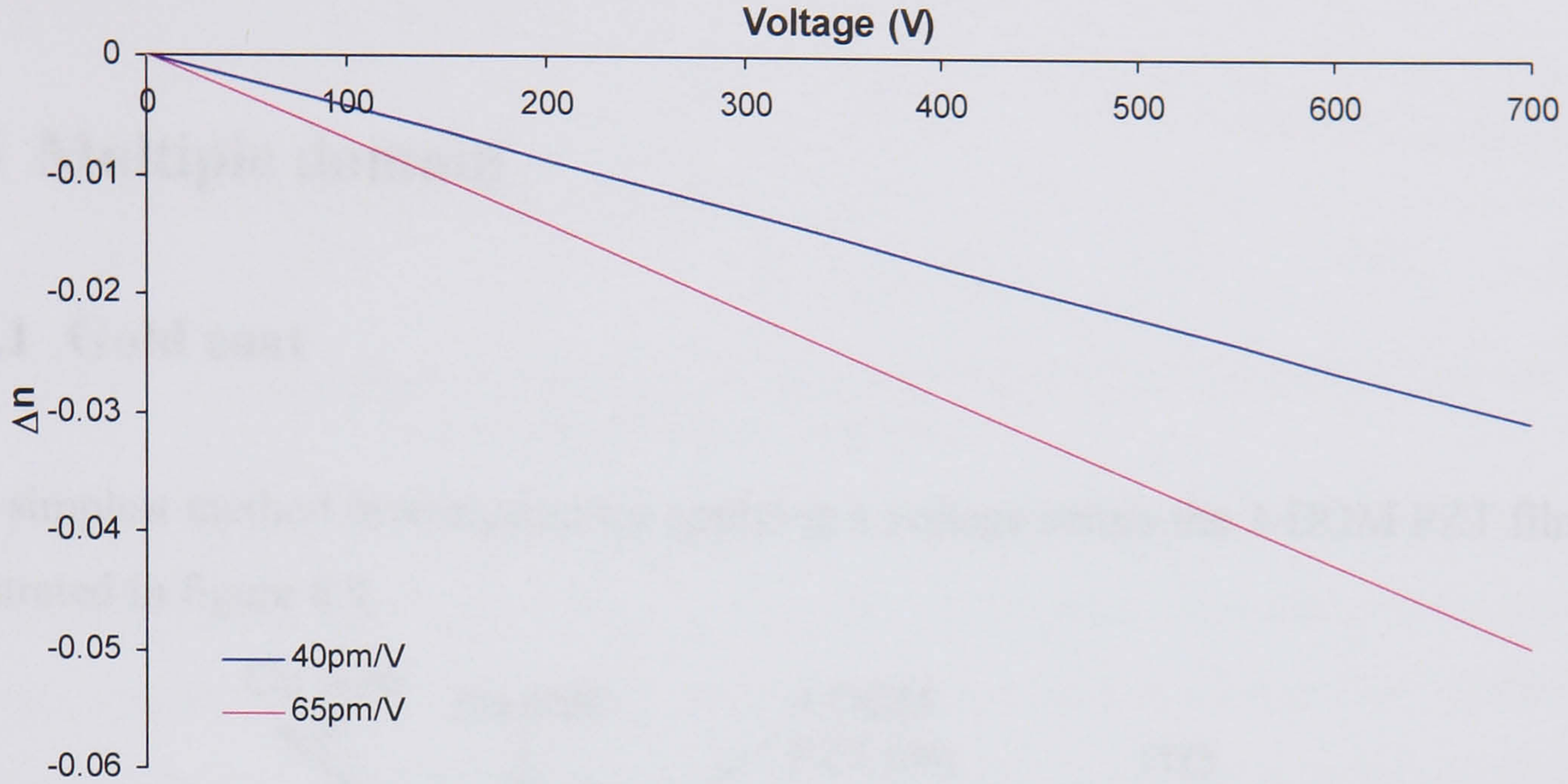


Figure 8.8 The calculated change in refractive index for PZT with different Pockels coefficients for applied voltages in the range 0-700 V

The results presented in figure 8.8 show that only a small change in refractive index can be induced by passing a high voltage across the 3-DOM PZT films. This small change in refractive index will correspond to a maximum shift in the reflection peaks of only 2 nm which will be challenging to observe using the optical set-up available.

In the experimental method described by Li *et al* (51) it is not clear whether the 3-DOM PLZT material is supported on a substrate and, if it is, there is no indication what the substrate material is. The 3-DOM PLZT is then mounted onto an ITO coated glass to act as a cathode. From previous work, see chapters 5 and 7, the 3-DOM PZT films are not continuous. The domains found in the 3-DOM films are typically 40-70 μm wide separated by cracks up to 10 μm. This unavoidable cracking found in the 3-DOM PZT films presents a problem when a voltage is passed across the ITO substrate because shorting may occur.

Two methods were investigated for passing a voltage across the 3-DOM PZT films. The first method investigated was similar to that reported by Li *et al* (51) since it was not

reported that any adverse effects, such as shorting, were experienced. In the second method a single domain electrical measurement was attempted. In both the multiple domain and single domain experiments the films were not poled. As discussed previously poling requires a high voltage to be applied at elevated temperature. Due to the porosity and cracking of the 3-DOM PZT films conventional sample preparation for poling, *e.g.* sputtering a set of Au/Cr electrode dots onto the film surface (161), would be problematic.

8.5 Multiple domain

8.5.1 Gold coat

The simplest method investigated for applying a voltage across the 3-DOM PZT films is illustrated in figure 8.9.

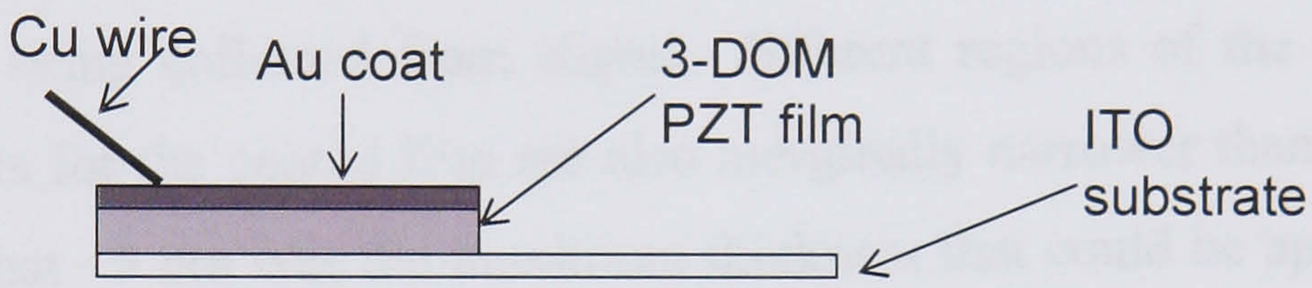


Figure 8.9 Schematic illustration of the simplest method for forming a contact on the 3-DOM film

As illustrated in figure 8.9 the entire surface of the 3-DOM film was gold coated. The uncoated part of the ITO substrate could act as one electrode and a copper wire was attached to the gold coated film region with conductive silver paint to act as the second electrode.

The first challenge with this method was to determine if gold coating could be applied which was thin enough to allow optical measurements to be obtained but thick enough to act as a conductive material. The thickness of the sputtered gold depends on both the deposition rate and the deposition current. The spectra shown in figure 8.10 were obtained from a film before and after coating with a gold layer approximately 5 nm thick.

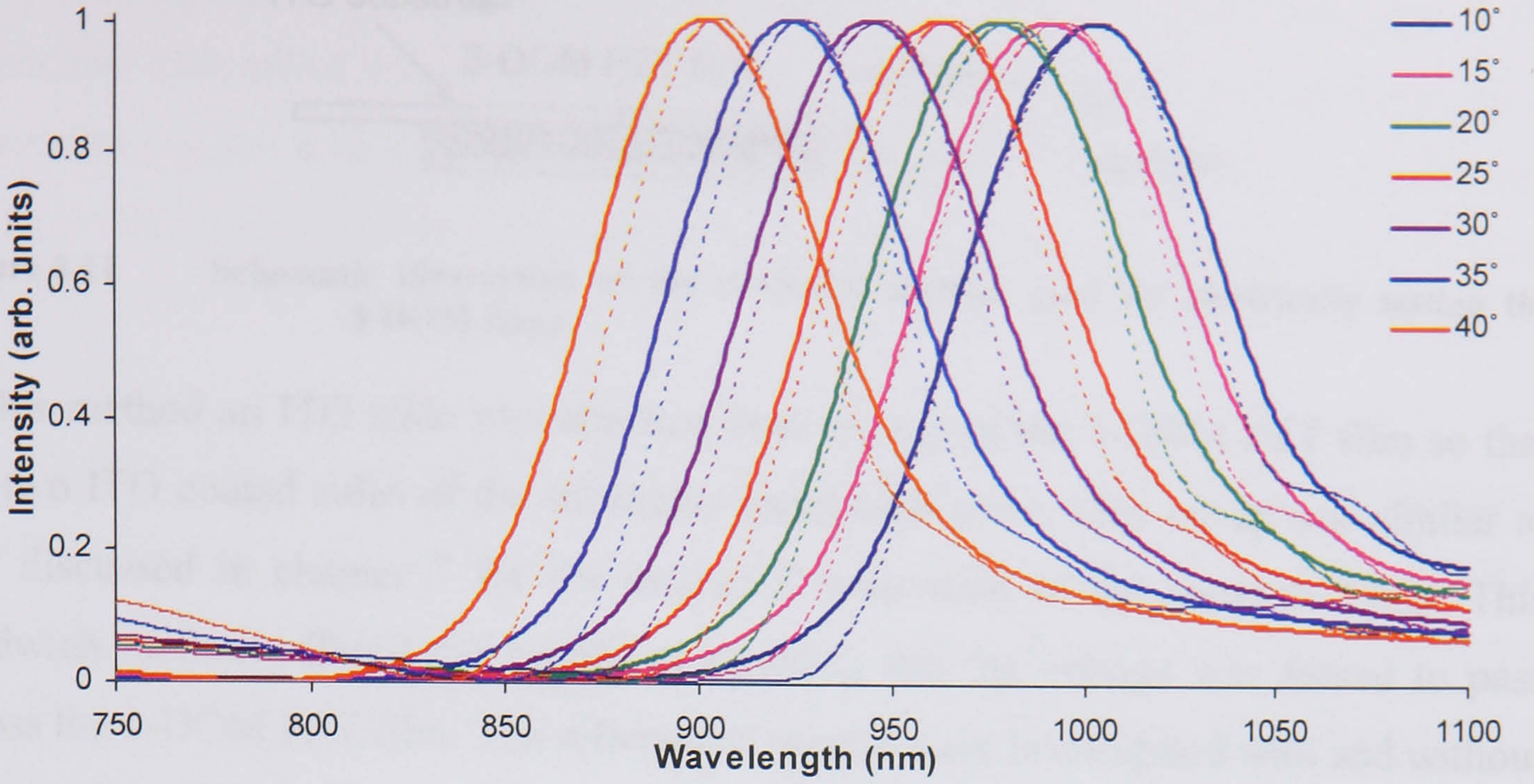


Figure 8.10 **Normalised reflection spectra for a 3-DOM PZT film (continuous line) and a gold coated 3-DOM film (dashed line)**

The spectra presented in figure 8.10 show that the position of the reflection peaks are shifted only a few nanometres after the film was gold coated. This shift can be attributed to the spectra being collected from slightly different regions of the film surface. The reflection peaks for the coated film are also marginally narrower than the original film. It was found that ~5 nm was the maximum thickness that could be applied before there was a significant change in the optical properties.

The experimental set-up was then tested to investigate if a voltage could be passed across the supported 3-DOM film. When the voltage reached ~40 V the power supply started to alarm and displayed a short circuit warning. This is because the easiest path for the current to take is across the top surface of the film, *i.e.* not penetrating the 3-DOM sample at all. If this method is to be successful the voltage must be passed across the 3-DOM film to the ITO electrode below. One way in which to achieve this will be discussed in the electrical testing of single 3-DOM domains section.

8.5.2 Sandwich Films

The second method investigated for electrically testing the 3-DOM PZT films is illustrated schematically in figure 8.11.

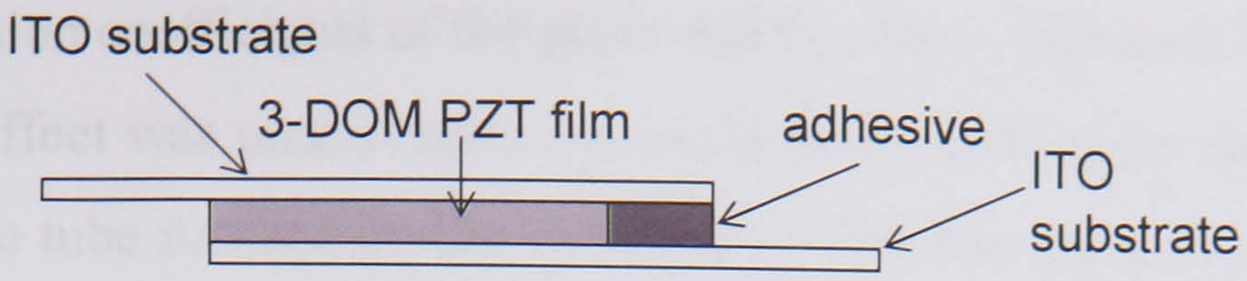


Figure 8.11 **Schematic illustration of the sandwich method used for electrically testing the 3-DOM films**

In this method an ITO slide was attached over the top of the 3-DOM PZT film so that the two ITO coated sides of the substrates faced each other. This set-up was similar to that discussed in chapter 7 for the sandwich infiltration of the template films. This sandwich method offered the benefit of ensuring that the voltage was forced to pass across the 3-DOM PZT film. The reflectance spectra were investigated with and without the top ITO slide to ensure that good reflectance peaks could be obtained with the top ITO slide in place (figure 8.12).

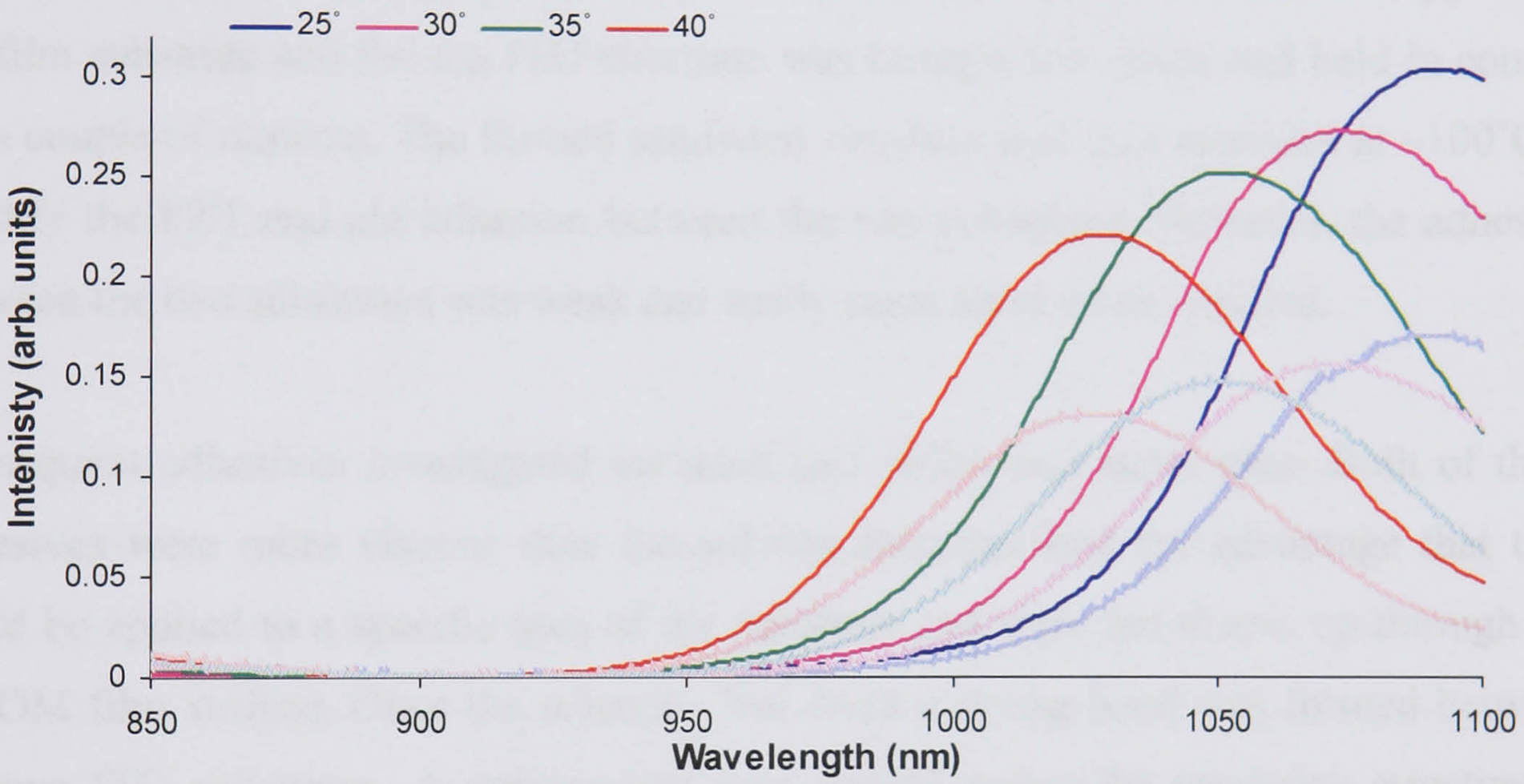


Figure 8.12 **Difference in reflectance spectra for 3-DOM PZT film without (continuous line) and with (dotted line) a top ITO substrate**

The reflectance spectra shown in figure 8.12 illustrate that good optical properties can still be measured from the 3-DOM films with a top ITO substrate present. The small shift in the reflectance peaks can be attributed to a slightly different position on the film being probed after the top ITO slide had been attached. However the presence of the top ITO substrate decreases the intensity of the reflection peaks and the peaks therefore have a lower signal to noise ratio (SNR).

During the calcination and subsequent crystallisation of the 3-DOM PZT films the ITO substrates bend slightly which made forming the sandwich structure described above difficult. This bending, which occurred during heating, was attributed to the difference

in thermal expansion coefficients of the glass and the thin (~100 nm) ITO coating on the substrates. This effect was unavoidable but could be minimised by altering the position of the films in the tube furnace during calcination. The best case scenario was that just the tip of the substrate bent which could then be removed without damaging the 3-DOM film.

The second challenge was the choice of adhesive used to form the sandwich structure. The adhesive had to be insulating, able to withstand high voltages and able to be applied thinly enough that the two substrates were in good contact. Care also had to be taken that the adhesive would not be drawn into the 3-DOM PZT film region by capillary action.

The first adhesive investigated was the PZT sol. A thin layer of the sol was applied to the film substrate and the top ITO substrate was brought into place and held in contact for a couple of minutes. The formed sandwich structure was then annealed at ~100˚C to solidify the PZT and aid adhesion between the two substrates. However, the adhesion between the two substrates was weak and easily came apart when handled.

Subsequent adhesives investigated included nail polish and super glue. Both of these adhesives were more viscous than the sol and therefore had the advantage that they could be applied to a specific area of the substrate and were not drawn up through the 3-DOM film surface. Once the adhesive had dried a strong bond was formed between the two ITO substrates. A voltage was then passed across the sandwich structure to ensure a proper circuit had been formed. At voltages above ~30 V the adhesive started to spark and burn, as shown in figure 8.13.



Figure 8.13 Sandwich structure after a voltage of 30 V had been applied. A black region (labelled) shows where the film started to spark

The observed sparking could be attributed to a gap or an air bubble between the ITO substrates and the adhesive. However, the contact between the substrates was maximised by subjecting the sandwich structure to a weight while the adhesive dried. Since, as discussed previously, a voltage of ~700 V requires to be applied to the 3-DOM

PZT films to observe a measurable change in refractive index the nail polish and super glue are not suitable adhesives to use.

The next adhesive to be investigated was silicone adhesive. Silicone adhesive is reported to have excellent insulating and sealing properties and prevents arcing on EHT connections. However the same sparking described above was observed for the sandwich structures formed with the silicone adhesive.

The final method investigated to attach the substrates together was UHU® White Tack. A very thin piece of the tack was placed onto the bottom substrate and the top substrate placed over the top. A weight was then applied to the sandwich structure for a period of at least twelve hours to ensure optimum contact between the two substrates was achieved. A voltage in excess of 200 V could be passed across the sandwich structure without any observed sparking or burning.

The final challenge that had to be met before the 3-DOM PZT films could be electrically tested was to ensure that the voltage was passing through the PZT and not just across the ITO substrate. The resistance of a blank sandwich structure, *i.e.* no PZT film present, was ~100 Ω for an applied voltage of 20 V. When the same experiment was conducted on a 3-DOM PZT sandwich structure the calculated resistance was ~4000 Ω. The increase in measured resistance was attributed to the voltage passing through the PZT film. This test was conducted for all 3-DOM PZT sandwich structures before electrical testing to ensure that the voltage was passing through the PZT rather than just across the ITO substrate.

8.5.3 Electrical Testing

To test the electro-optic Pockels effect the 3-DOM PZT sandwich structures needed to be placed in the optical bench in order for reflectance spectra to be collected as a voltage was applied across the films. The optical bench set-up is shown in figure 8.14.

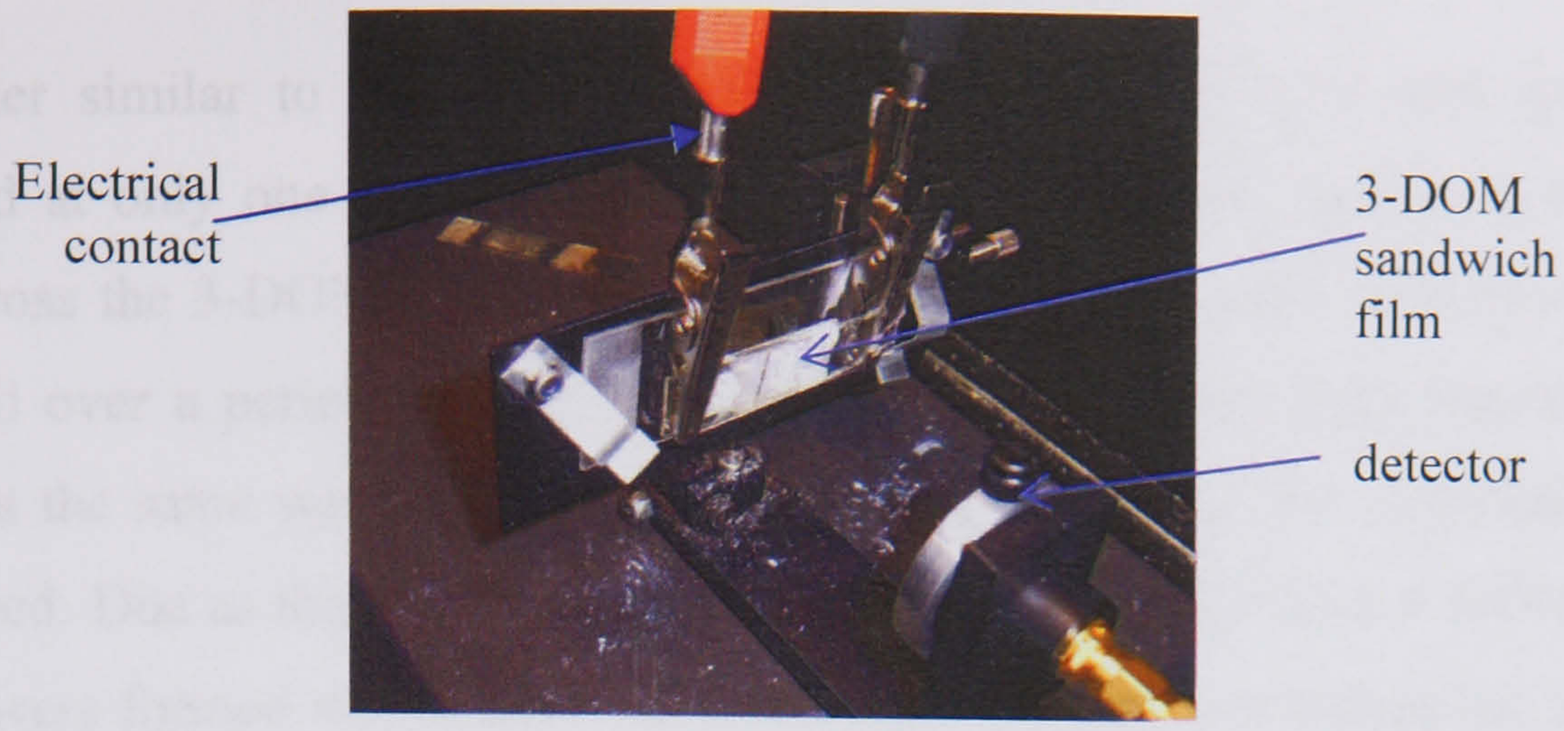


Figure 8.14 **The optical bench set-up for the electrical measurements**

The 3-DOM sandwich structure was held in place by two crocodile clips which were mounted on a microscope slide. This construction was then held in place on the optical bench sample stage using the normal sample holders. The use of the microscope slide ensured that the 3-DOM sandwich film would be held securely during testing and offered an easy way to attach the voltage supply through the crocodile clips.

Before a voltage was applied to the 3-DOM film reflectance spectra were collected from the film at angles of incidence 10-40° to ensure that a well ordered region of the 3-DOM film had been selected and that the presence of the top ITO slide was not inhibiting the optical properties of the film (figure 8.15).

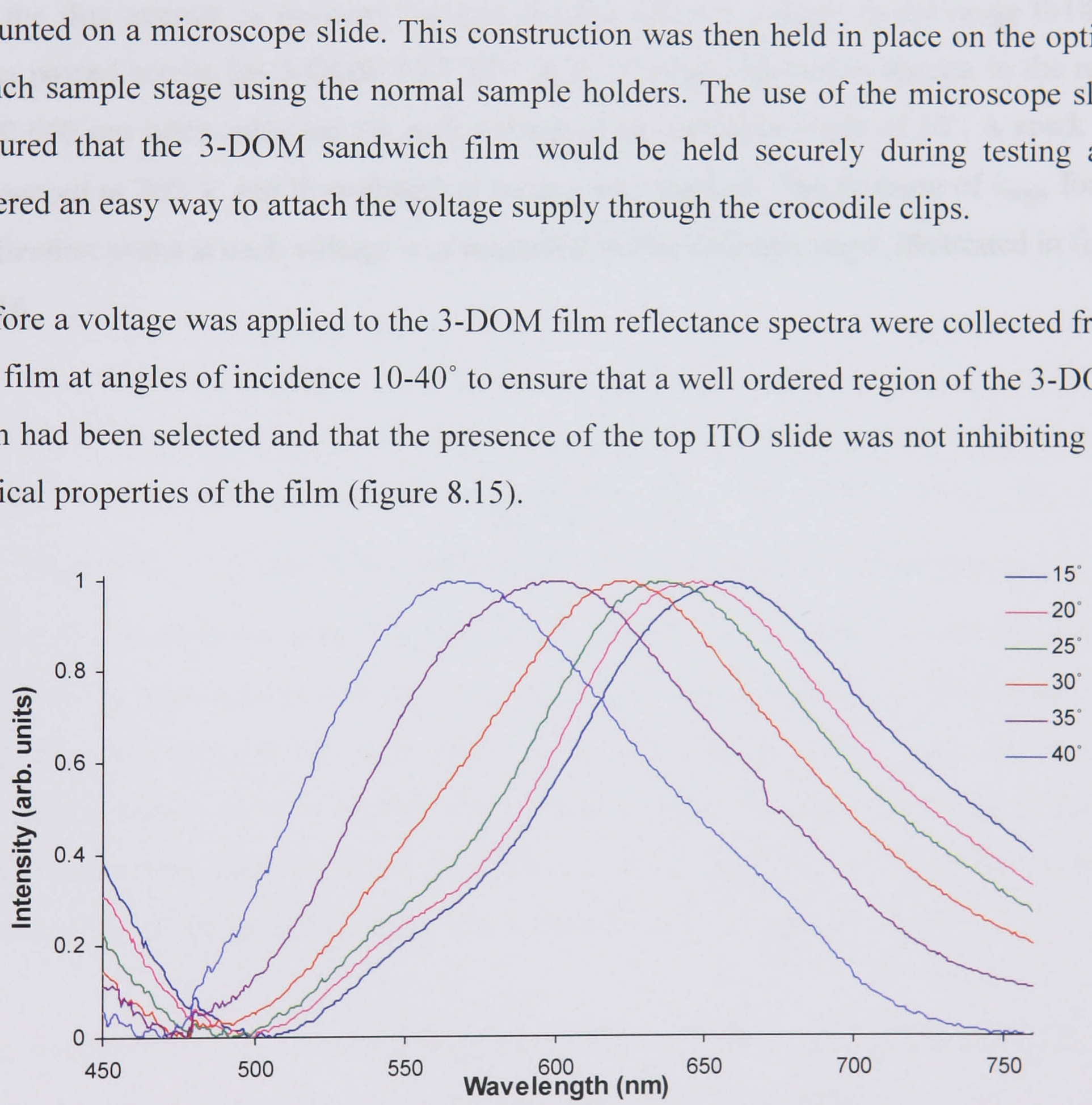


Figure 8.15 **Normalised reflection spectra for 3-DOM PZT film used for test 3**

The spectra presented in figure 8.15 have a poorer SNR than those generally obtained from 3-DOM PZT films, see for example figure 7.24. As discussed previously the weaker signals were attributed to the presence of the top ITO substrate and the decrease in SNR was attributed to both the top substrate and also the optical bench set-up which was more susceptible to vibration and movement in the lab.

In a manner similar to that reported by Li *et al* (51) the reflection spectra were investigated at only one angle, typically 10° or 15° incidence. Before a voltage was applied across the 3-DOM PZT sandwich structure the reflection peak of interest was investigated over a period of time to ensure that the reflection peak maximum (λ_{max}) remained at the same wavelength. Once this had been verified the electrical test could be conducted. Due to the problems mentioned previously only three 3-DOM sandwich structures were formed which could withstand high voltages and where the voltage was passed through the PZT film and not just across the ITO substrate.

In the first attempt to measure the electro-optic effect a voltage in the range 0-180 V was passed across the 3-DOM PZT film in 20 V steps. Reflection spectra in the range 600-660 nm were collected for each voltage at an incidence angle of 10°. A spark was observed at 200 V and thus electrical testing was stopped. The position of λ_{max} for the reflection peaks at each voltage was measured in two different ways, illustrated in figure 8.16.

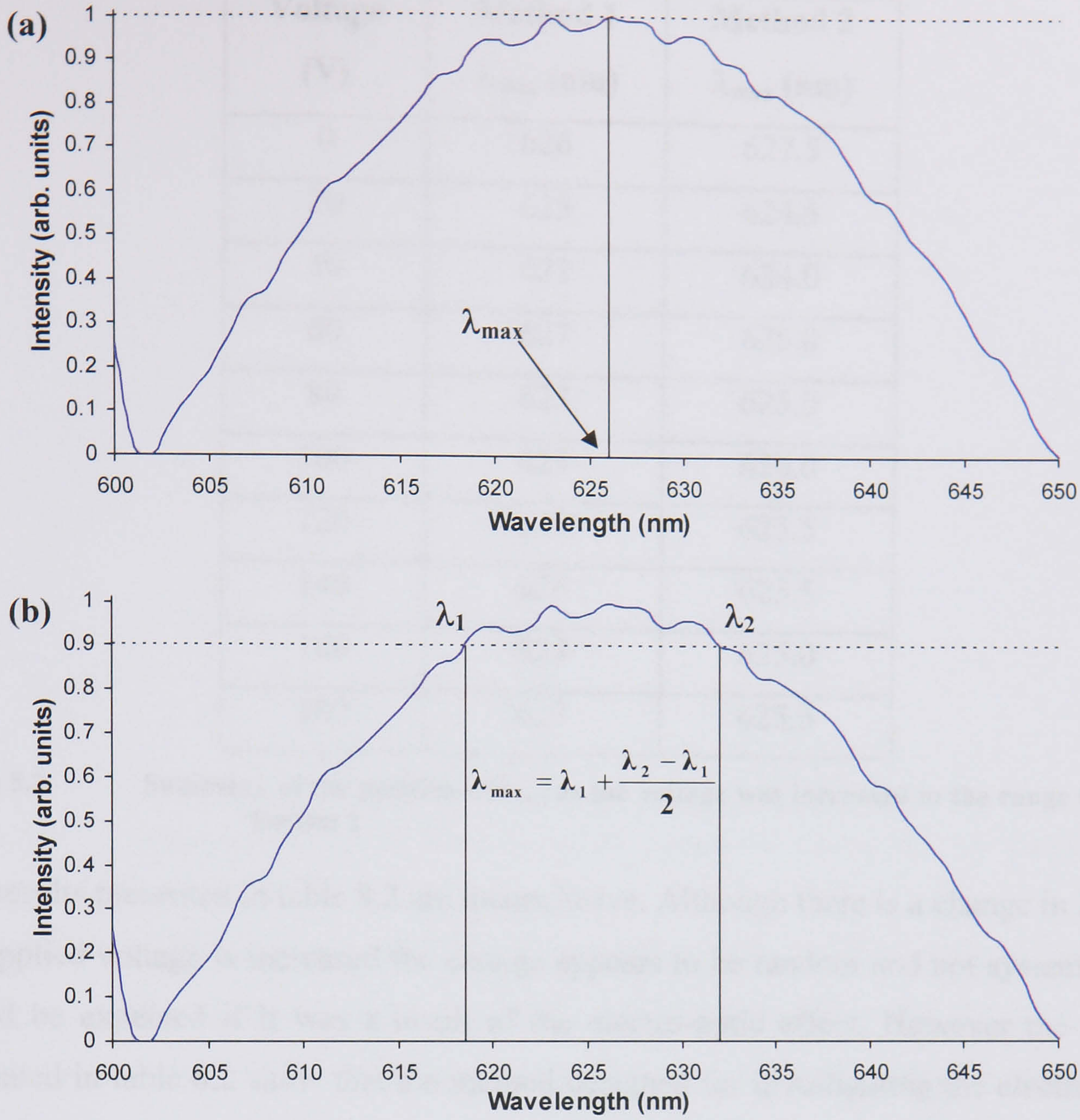


Figure 8.16 Graphical illustration of the two different methods used to calculate λ_{max}

In the first method the reflection peak was normalised to one and λ_{max} was taken when the intensity was equal to one (figure 8.16(a)). The second method was employed to try and take into account the poor SNR of the peaks which could skew the absolute maximum signal. In this method the reflection peak was again normalised but the wavelength at an intensity of 0.9 on either side of the maximum of the peak was noted and then the midpoint of this range was chosen to be λ_{max} (figure 8.16(b)).

The positions of λ_{max} for the first attempt at electrically testing a 3-DOM PZT film calculated by the two different methods are summarised in table 8.2.

Voltage (V)	Method 1 λ_{max} (nm)	Method 2 λ_{max} (nm)
0	626	627.5
20	625	624.5
40	623	624.0
60	627	625.0
80	623	625.0
100	625	626.0
120	627	625.5
140	626	625.5
160	623	625.0
180	623	625.5

Table 8.2 **Summary of the position of λ_{max} as the voltage was increased in the range 0-180 V for test 1**

The results presented in table 8.2 are inconclusive. Although there is a change in λ_{max} as the applied voltage is increased the change appears to be random and not systematic as would be expected if it was a result of the electro-optic effect. However the results presented in table 8.2 show that the method designed for investigating the electro-optic effect is suitable and that high voltages can be applied to the 3-DOM PZT sandwich structures for a period long enough to collect reflection data while not damaging the PZT film.

For the second electrical test a voltage in the range 0-200 V was passed across another 3-DOM PZT film in 20 V steps. The reflectance spectra were collected at 15° incidence in the wavelength range 570-670 nm. In this test three spectra were collected at each voltage in order for an average λ_{max} to be calculated. λ_{max} was evaluated in the same way as described previously and the average values calculated from both methods are summarised in table 8.3.

Voltage (V)	Method 1 λ_{max} (nm)	Method 2 λ_{max} (nm)
0	621.67	623.50
20	621.33	624.00
40	627.00	625.17
60	622.33	623.67
80	622.00	623.17
100	620.67	624.00
120	621.67	623.00
140	621.00	623.33
160	623.00	623.33
180	621.33	623.17
200	621.00	623.17

Table 8.3 **Summary of the position of λ_{max} as the voltage was increased in the range 0-200 V for test 2**

The maximum difference between the positions of λ_{max} calculated by method 2 is ~2 nm which is smaller than the maximum difference presented in table 8.2. This would indicate that repeating the reflectance measurements and calculating an average has improved the reproducibility of the experiment. Similar to the results presented in table 8.2, the data for the second test indicates that the random change in λ_{max} cannot be attributed to the electro-optic effect.

In the final electrical test a voltage of 300 V was reached which should be high enough to measure an observable change in λ_{max}. Reflectance spectra were collected in the wavelength range 615-725 nm at angle of incidence of 10°. The results for both methods of finding λ_{max} are summarised in table 8.4.

Voltage (V)	Method 1 λ_{max} (nm)	Method 2 λ_{max} (nm)
0	680.67	678.83
20	677.67	678.33
40	676.33	678.50
60	679.33	678.17
80	678.00	678.33
100	679.33	680.50
120	674.67	677.17
140	674.00	675.83
160	675.00	676.33
180	676.67	677.17
200	677.33	678.33
220	679.00	678.50
240	680.33	679.50
260	678.76	677.17
280	680.67	681.00
300	679.00	678.67

Table 8.4 Summary of the position of λ_{max} as the voltage was increased in the range 0-300 V for test 3

The data presented in table 8.4 shows the same random variation in λ_{max} which was observed in the first two attempts at measuring the electro-optic effect was also observed for the final electrical test.

In order to analyse the experimental data further the raw data was smoothed to remove some of the effects of the poor SNR of the reflection peaks. The raw data points were plotted using Origin and the data was smoothed using a Savitsky-Golay filtering technique for nine data points. This filtering technique performs a local polynomial regression to determine the smoothed data for each data point. A parabola was then fitted to the smoothed data points and the best fit equation of the parabola was noted. This smoothing and parabola fitting procedure was carried out for each set of raw data and then an average equation for the best fit parabola was calculated for each voltage.

The wavelengths the raw data were collected at were then fitted to the average best fit parabolas for each voltage. The resulting graphs for the final electrical test are shown in figure 8.17.

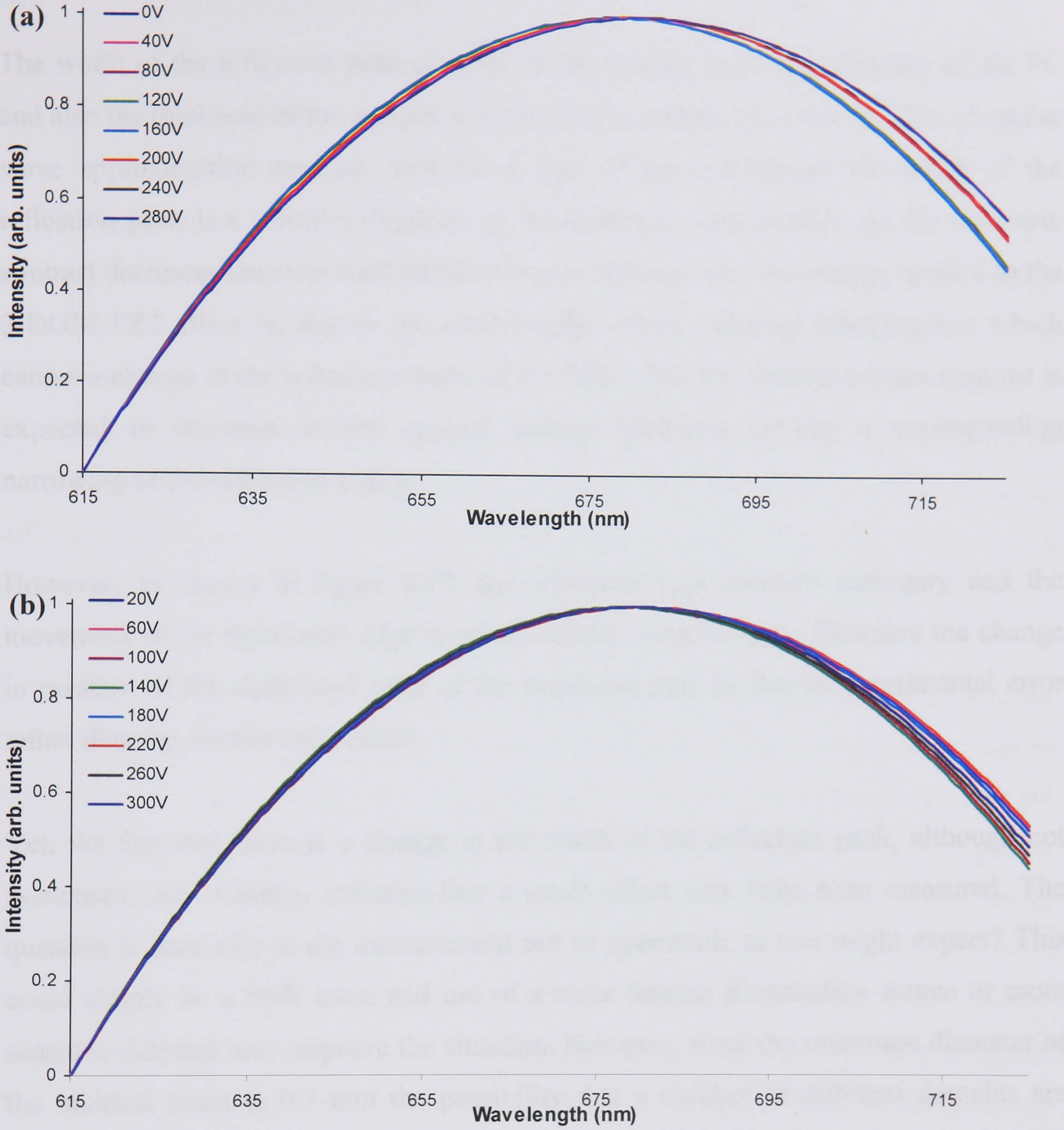


Figure 8.17 Fitted parabolas for smoothed data points for test 3 (a) 0-280 V in 40 V steps and (b) 20-300 V in 40V steps

The curves plotted in figure 8.17 show that, once the raw data has been smoothed, there is no significant shift in the position of λ_{max} but there does appear to be a change in the peak width. For some voltages the right-band edge of the stop-band is shifted to longer wavelength. However this change in peak width does not systematically vary with applied voltage. Although the data presented by Li *et al* (51) shows a systematic shift in the right-band edge of the PBG to longer wavelength as the applied voltage is increased

further investigation of both the left and right-band edges showed that the peak width remains constant. The shift in position of the band edges is due to the shift in mid-gap position due to the electro-optic effect.

The width of the reflection peak depends on the quality and dimensionality of the PC and also the thickness of the sample. Colvin and co-workers have shown, through scalar wave approximation analysis, that for a film of given thickness the width of the reflection peak is a sensitive function of the dielectric contrast (62). As the dielectric contrast decreases the stop-band width is expected to narrow. The voltage applied to the 3-DOM PZT films is, due to the electro-optic effect, inducing birefringence which causes a change in the refractive index of the PZT. Thus the refractive index contrast is expected to decrease as the applied voltage increases causing a corresponding narrowing of the reflection peaks.

However, as shown in figure 8.17, the left-band edge remains stationary and the movement of the right-band edge is not systematic with voltage. Therefore the change in position of the right-band edge of the stop-band may be due to experimental error rather than the electro-optic effect.

Yet, the fact that there is a change in the width of the reflection peak, although not systematic with voltage, indicates that a small effect may have been measured. The question is then why is the measurement not as systematic as one might expect? This could simply be a SNR issue and use of a more intense illumination source or more sensitive detector may improve the situation. However, since the minimum diameter of the incident beam is 0.7 mm the possibility that a number of different domains are simultaneously probed needs to be considered. Therefore, if this is the case then the optical signal measured will be an average over 10-20 domains. If the contact between each domain and the top ITO electrode is identical this 'averaging' would have no effect on the measurement. While we have confidence that the infiltration process results in high quality 3-DOM PZT films we cannot be certain that the heights of adjacent domains are identical. Thus, the top electrode may not be in contact with all of the domains that are being optically probed. Hence the measured reflectance spectrum will have contributions from domains that have an applied voltage and others that do not. This would lead to broadening of the features in the reflectance spectra and dilution of the electro-optic effect.

The reasoning presented in the previous paragraph would indicate that, if the electro-optic effect is being measured but being 'washed' out due to averaging, a measurement of a single 3-DOM PZT domain would be one way to observe the Pockels effect in the hope of forming a multifunctional PC.

8.6 Single domain

In this section electrical contact to a single 3-DOM domain will be discussed. A contact to a single domain was proposed for two main reasons. Firstly, as discussed previously, there was concern that a short circuit could be formed when a voltage was applied to the 3-DOM PZT because the films are not continuous and have regions where the ITO substrate, or bottom electrode, is exposed. Although this problem was not discussed by Li *et al* (51) for 3-DOM PLZT and no indication of a short circuit was observed in the multiple domain experiments discussed in the previous section. Secondly, testing over a single domain ensures that the voltage was definitely being applied to the 3-DOM PZT.

The formation of an electrical contact to a single 3-DOM PZT domain was attempted using the focussed ion beam (FIB). The use of the FIB has the advantage that, because simultaneous imaging of the sample can be carried out, a large well ordered 3-DOM PZT domain can be selected. The basic concept was to use the FIB to deposit a pad of platinum onto the 3-DOM PZT domain onto which a wire could be attached to act as the second, or top, electrode.

Platinum is deposited in the FIB in the following way. The main gas jet delivers an organometallic platinum precursor gas to the sample. The ion beam cracks the precursor molecule and because the platinum is non-volatile the platinum is deposited on the surface of the sample and the carbon atoms move into the vacuum (199). The deposited platinum has some carbon from the precursor gas and gallium from the ion beam as impurities. Platinum pads were deposited onto large 3-DOM PZT domains demonstrating good order (figure 8.18) to ensure that the ion beam did not damage the 3-DOM film.

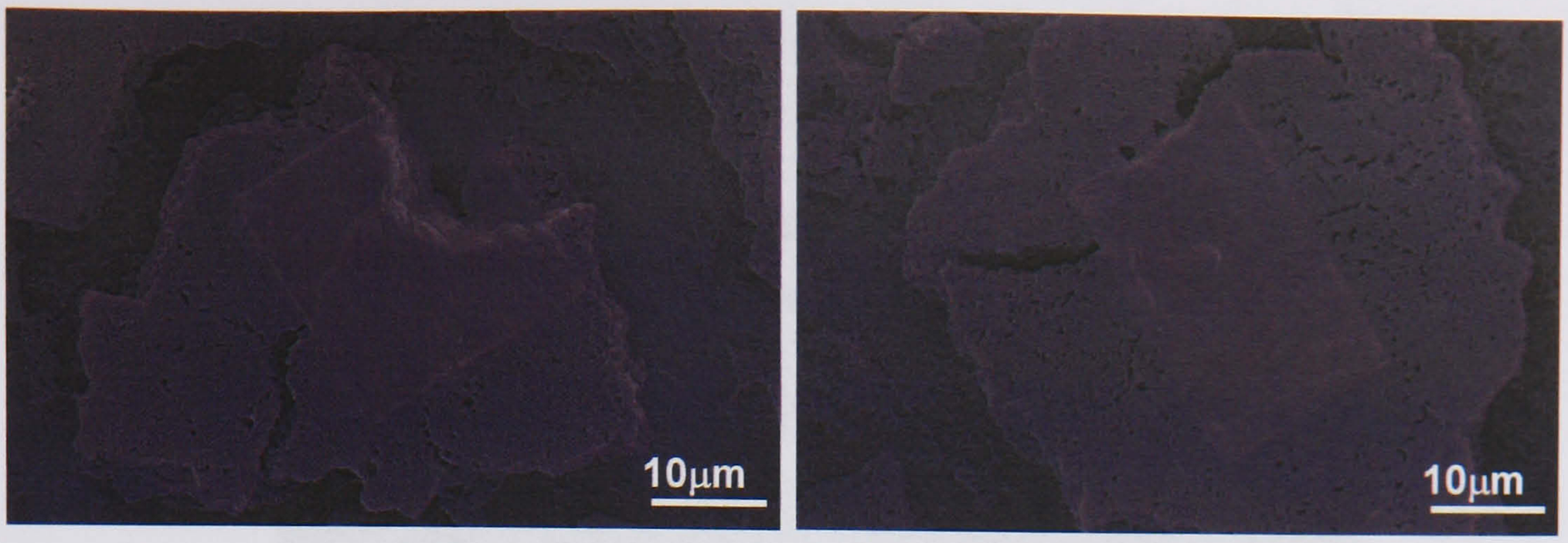


Figure 8.18 **SEM images of FIB deposited platinum pads of diferent dimensions**

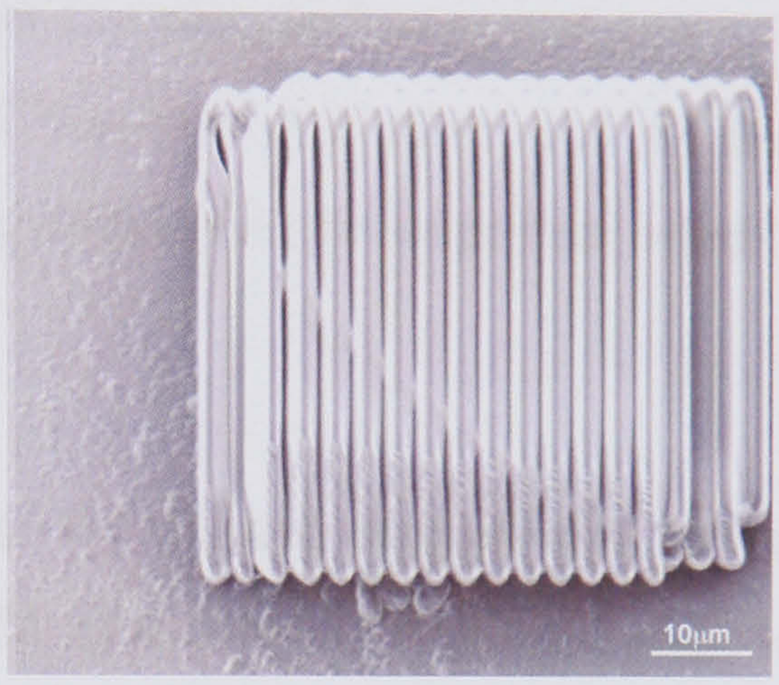


Figure 8.19 **High magnification FIB image showing a well defined platinum pad**

The SEM images show that the FIB deposited platinum pads have a well defined shape and appear not to be diffuse (see figure 8.19) which had been a concern. The dimensions of the pads and the deposition beam current can be selected by the user. A high beam current is beneficial because platinum of the lowest resistivity is deposited (200) and therefore a beam current in the range 300-500 pA was used. The length and the width of the pad were chosen to best fit the 3-DOM domain selected and the depth was in the range 1-2 μm to ensure the platinum would not penetrate through the thickness of the film and contact the ITO substrate.

Once the platinum pads had been deposited attempts were made to attach a wire onto the surface of the pads. A copper wire was chosen for the electrical contact because copper has a high conductivity (~60 MS/m (178)) and is relatively cheap. The smallest diameter of copper wire available was ~0.1 mm which was too large to contact the platinum pads (see figure 8.18).

An electrochemical etching technique was used to reduce the thickness of the tip of the copper wire. An electrochemical cell was constructed with the copper wire as the anode and orthophosphoric acid (H_3PO_4) was used as the electrolyte. The 0.1 mm copper wire

was electrochemically etched at a current of 2 A for one minute. Figure 8.20 shows an image of the copper wire before etching and after etching.

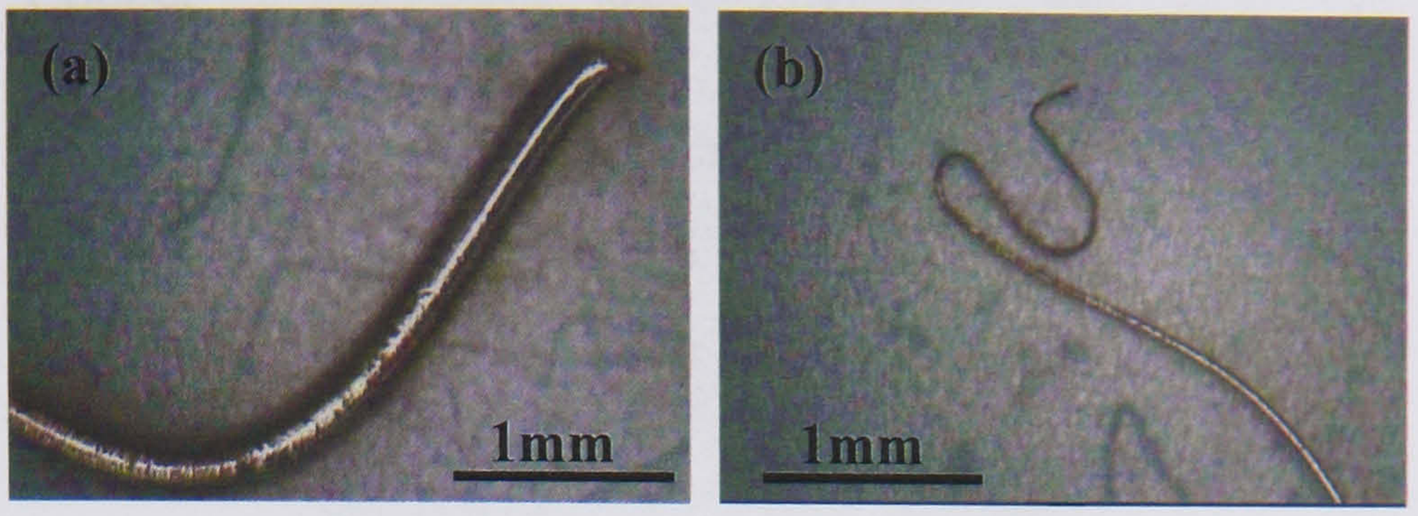


Figure 8.20 Optical microscope images of copper wire (a) before etching and (b) after 1 minute etching in H_3PO_4

After etching the diameter of the wire had been reduced to ~15 μm. The advantage of using this thinning method was that the other end of the wire remained the same thickness as prior to etching which will be important when a voltage is required to be passed through the wire.

The idea was then to 'weld' the thinned copper wire to the large deposited platinum pads. Before the 3-DOM PZT film with the deposited pads was placed into the vacuum chamber of the FIB the pre-thinned copper wire was attached to the substrate, as shown in figure 8.21, and the thin end of the wire was wound round the in-situ manipulator.

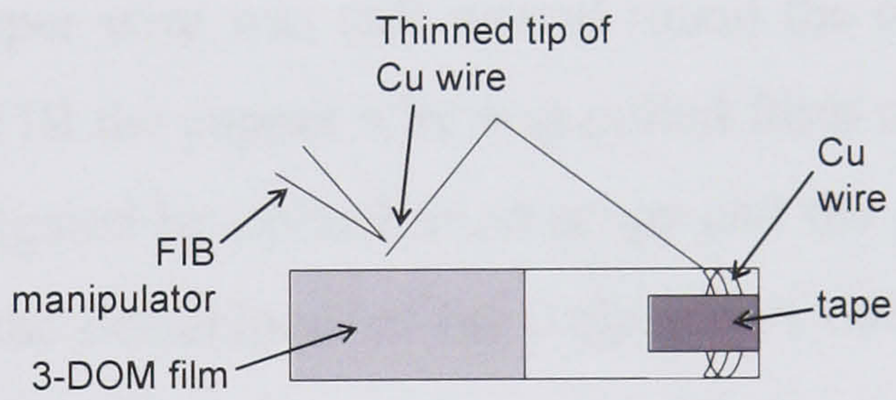


Figure 8.21 Schematic illustration of the set-up of the 3-DOM film before being placed into the FIB

Once in the FIB one of the large platinum pads was located and the tip of the copper wire was brought into contact with it using the manipulator. Once it was determined that the copper wire was in contact with the platinum pad on the 3-DOM domain, platinum was deposited to attach the wire to the initial large platinum pad. Three trapezoids of platinum were deposited to try and attach the wire to the surface, as shown in figure 8.22.

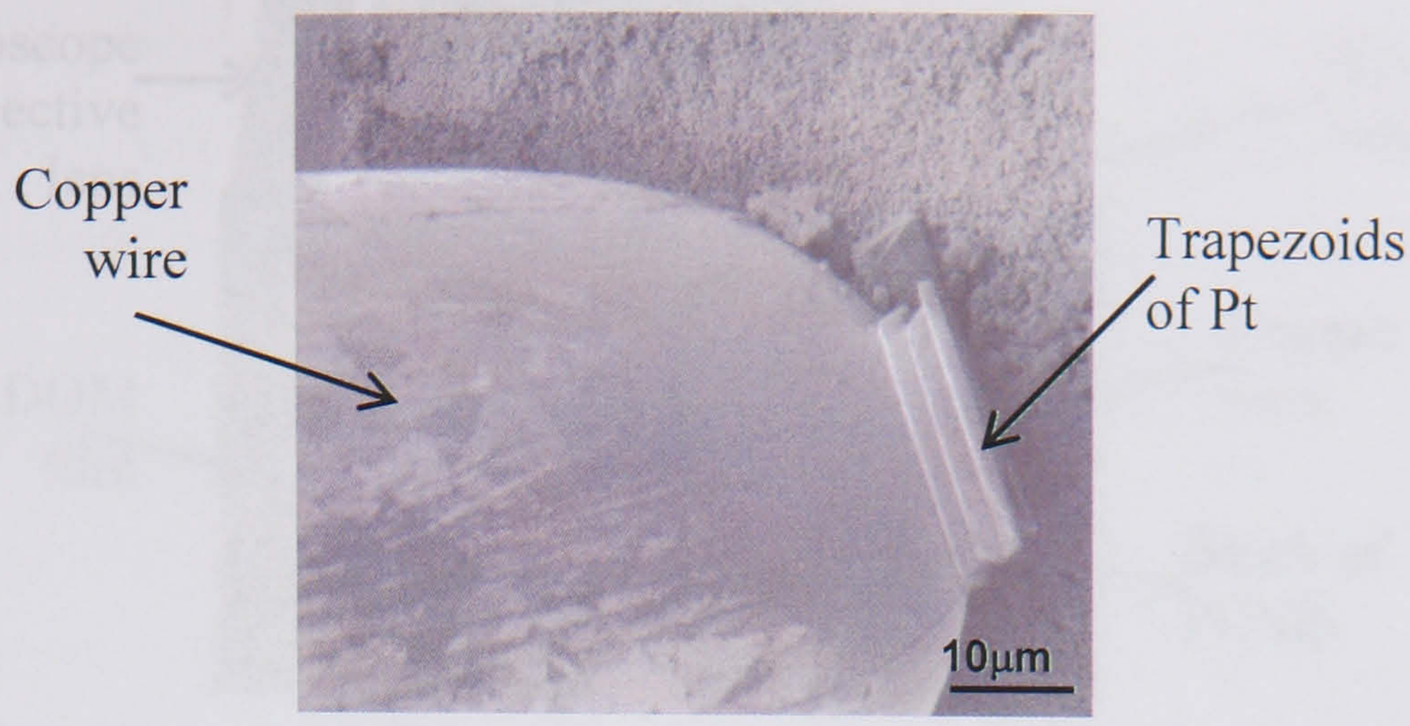


Figure 8.22 FIB image of the copper wire attached to the 3-DOM film surface with 3 trapezoids of platinum

The image in figure 8.22 is convincing that the wire is held in place on the film surface by the three small trapezoids of platinum. While it appears that the platinum weld has successfully attached the copper wire to the surface, the wire was attached at an angle which would weaken the bonding of the wire to the film. It would be beneficial if the wire could meet the film vertically so that the smallest dimension of the wire is in contact with the surface and in theory platinum could be deposited all the way round the base of the wire thus strengthening the contact between wire and 3-DOM film.

However difficulties were encountered when the film was removed from the vacuum chamber. Since the copper wire was still wound round the manipulator when the film was removed from the FIB the copper wire was pulled from the surface of the film. The film surface was investigated by optical microscopy and the platinum pad could not be located indicating that the detachment of the copper wire had pulled the entire 3-DOM PZT domain from the substrate.

The main problem with attaching a pre-thinned wire to a single domain was trying to support the weight of the wire on the surface without damaging the fragile 3-DOM film. As such an experiment investigating supporting the wire was carried out using the optical microscope. The experimental set-up is shown in figure 8.23.

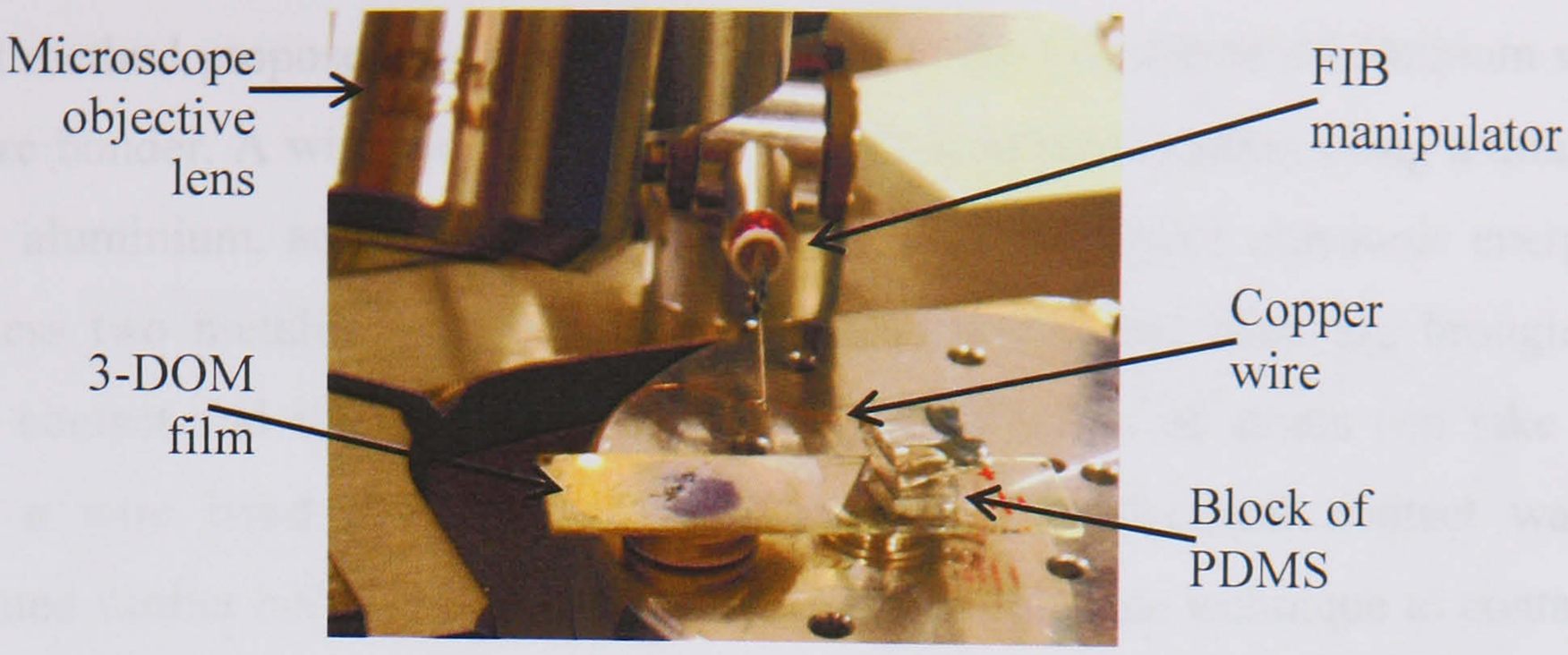


Figure 8.23 **Picture of the set-up for attempting to attach the copper wire on the open bench using the optical microscope**

A block of PDMS was stuck to the end of the substrate and the non-thinned end of the copper wire was stuck to this. The film substrate was then placed under the optical microscope where the surface could be viewed. One of the mechanical FIB manipulators was then used to guide the copper wire to above the 3-DOM domain with deposited platinum. However the stress in the wire kept causing the wire to bounce off the tip of the manipulator. To overcome this problem a position further up the wire away from the tip was soldered onto the manipulator tip to hold the wire in place. The copper wire was moved to just past the 3-DOM domain with the deposited platinum pad (figure 8.24(a)).

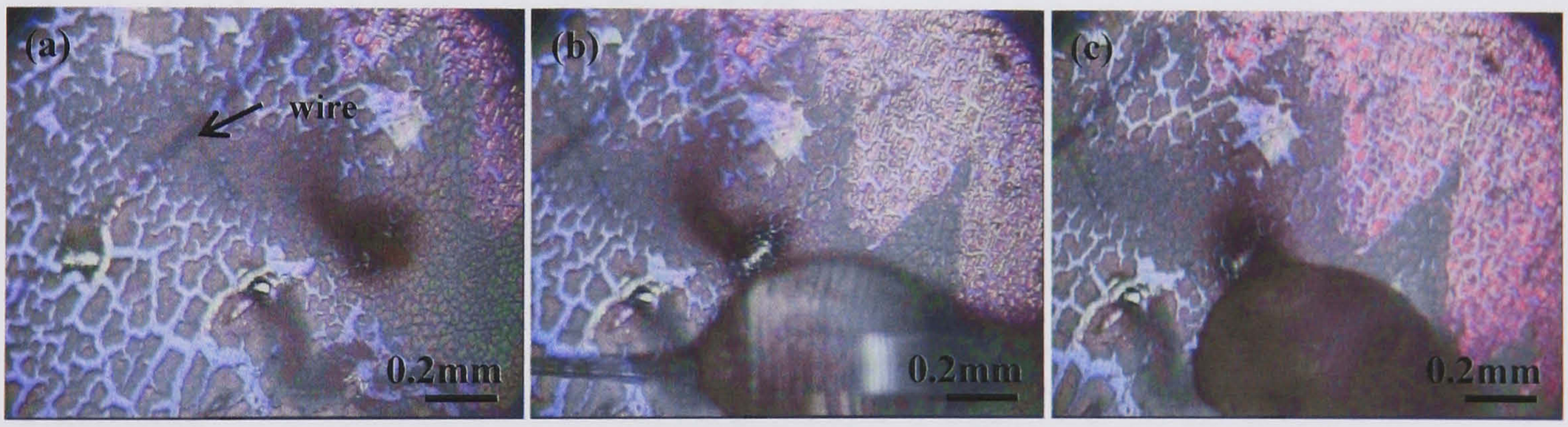


Figure 8.24 **Optical microscope images showing (a) copper wire just past deposited platinum pad, (b) blob of epoxy on the end of the glass capillary and (c) blob of epoxy on the 3-DOM film surface**

A glass capillary was drawn and placed into the ex-situ FIB manipulator. The smallest possible blob of epoxy was put onto the tip of the glass capillary (figure 8.24(b)). The copper wire was then brought into place on the 3-DOM domain and the glass capillary was brought above the wire. Under gravity the blob of epoxy fell onto the film surface (figure 8.24(c)). The copper wire was firmly attached to the 3-DOM PZT surface by the epoxy but due to the size of the blob it was unclear as to where exactly the copper wire was attached. Although a good strong contact between the wire and the film surface was formed this method of forming an electrical contact on a single domain was decided unsuitable.

The next method proposed for attaching a contact to the FIB deposited platinum was to use a wire bonder. A wire bonder forms an electrical interconnection using a thin wire, typically aluminium, and a combination of heat, pressure and/or ultrasonic energy. In the process two metallic materials, *i.e.* the platinum pad and wire, are brought into intimate contact and then electron sharing or interdiffusion of atoms can take place forming a wire bond (201). However this method of electrical contact was not investigated further because the wire bonder uses an ultrasonic technique to contact the wire to the platinum pad which would most likely damage the fragile 3-DOM film surface.

When the platinum pads are deposited using the FIB a 'halo' of platinum is formed round the user defined deposition region. Although this halo of platinum was not observed by the SEM (figure 8.18) it was clear when the regions were investigated with an optical microscope with a large objective lens. This halo of platinum round the defined platinum pads may contact the underlying substrate thus forming a short circuit.

The final idea proposed was to isolate a well defined 3-DOM domain which could then be contacted to a larger platinum pad which an electrical contact could be made to. This idea is sketched schematically in figure 8.25.

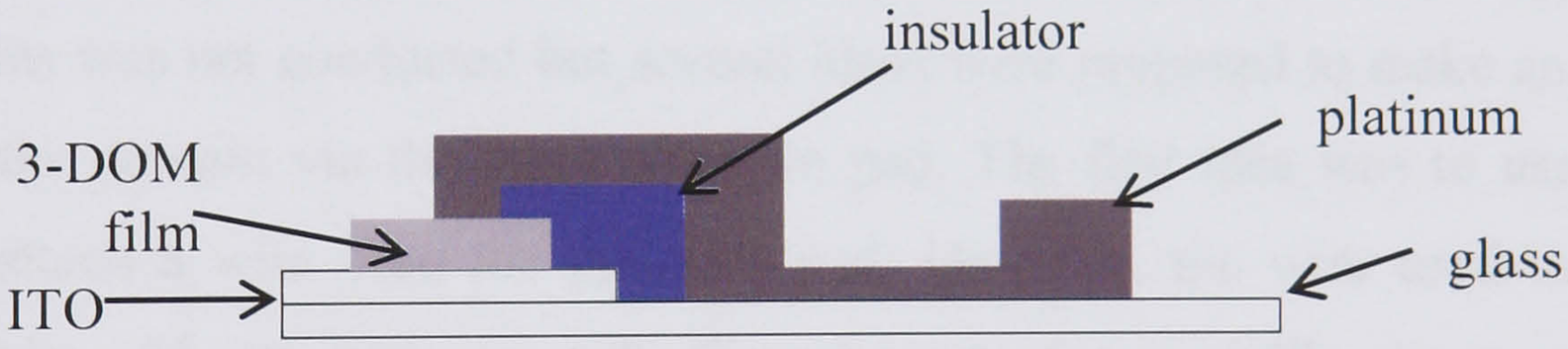


Figure 8.25 Labelled schematic diagram of the second method proposed to form an electrical contact to the 3-DOM films

The following experiment to isolate a single 3-DOM PZT domain was carried out at SciVenture, Maidenhead, by Dr. J. Walker. A large (~60x30 μm) well ordered 3-DOM domain was selected and the end of the domain was etched away to make a straight edge. A pad of SiO_x (27x3 μm) was then deposited onto the etched end of the domain to act as an insulator (figure 8.26(a)). Around this pad of insulating material platinum was deposited. In the next step a large platinum pad (95x68 μm) was deposited on a bare region of the ITO substrate and a strap of platinum (45x9 μm) was deposited to join the large platinum pad to the area of insulator (figure 8.26(b)). An area around the large platinum pad and strap was etched away to isolate the deposited platinum from the underlying ITO substrate (figure 8.26(c)). Finally the area around the 3-DOM domain

was etched away except for a region where connection with the ITO substrate could be made (figure 8.26(d)). These last two steps were to counteract the 'halo' of platinum which is deposited around the defined deposition shape.

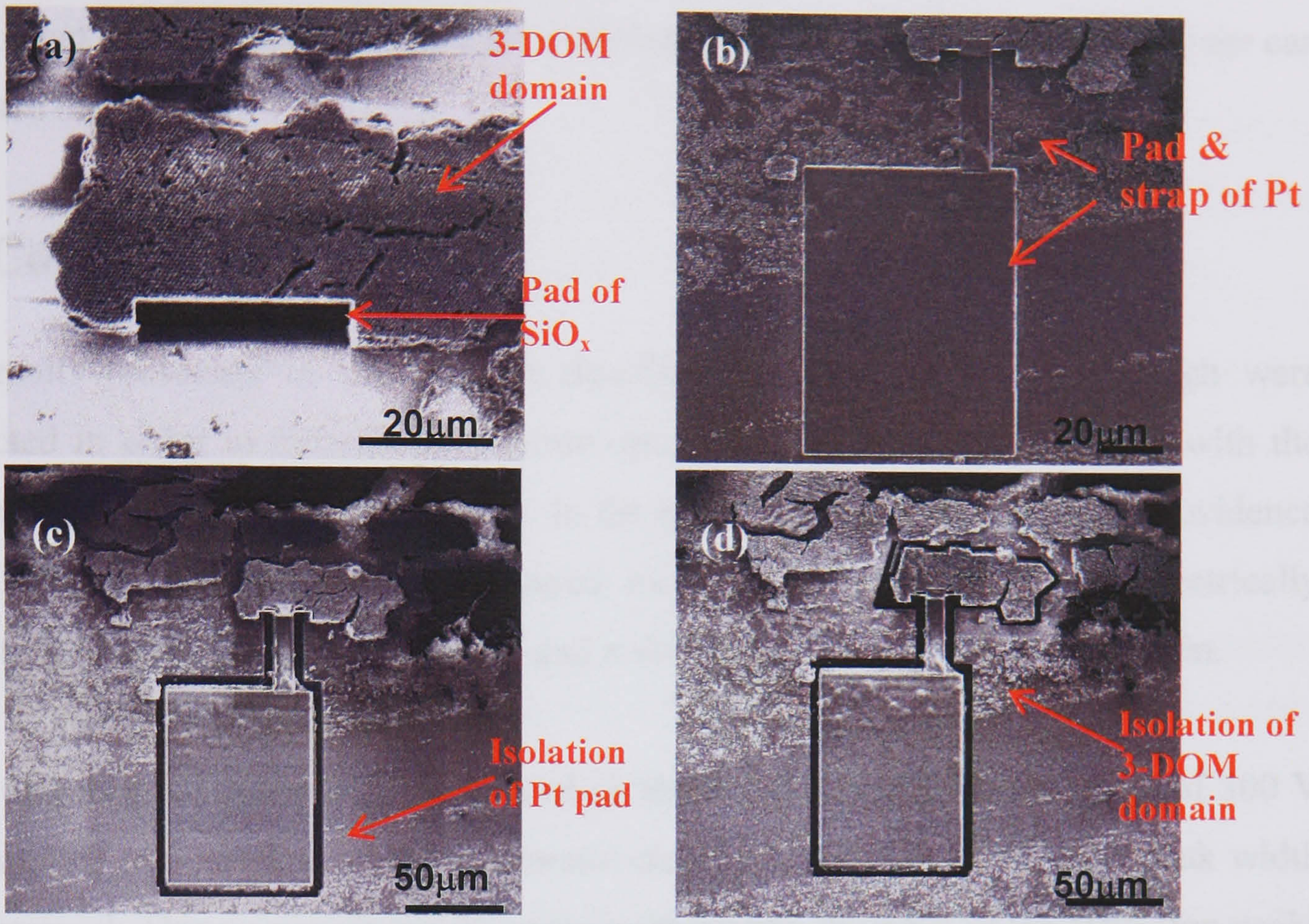


Figure 8.26 FIB images of the process used to isolate a 3-DOM domain and attach to a large pad of platinum. Each image is described in the text.

Unfortunately due to time constraints electrical testing of the isolated single 3-DOM PZT domains was not conducted but several ideas were proposed to make an electrical contact to the domain via the large platinum pad. The first idea was to use the wire bonder to attach a wire onto the platinum pad. However, the wire used in the wire bonder is thin, ~25 μm, and very soft. Thus the use of a crocodile clip to contact the wire, similar to that reported for the testing of the entire 3-DOM film, would not be suitable.

The most suitable method for electrically testing the single 3-DOM domain is illustrated schematically in figure 8.27.

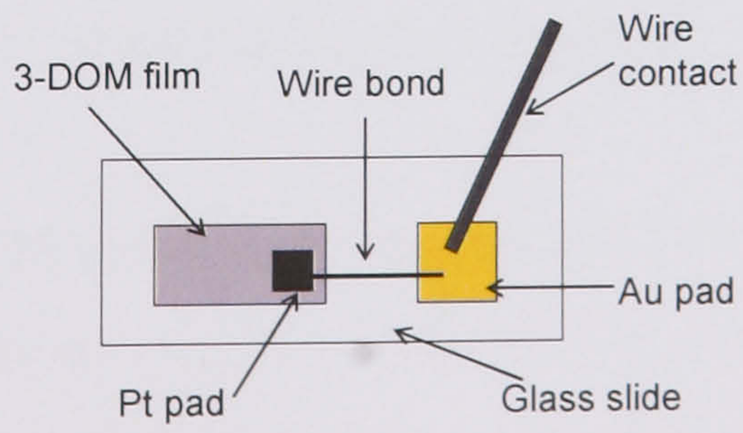


Figure 8.27 Schematic illustration of the most suitable proposed method for contacting the isolated 3-DOM domain

In the method illustrated in figure 8.27 the 3-DOM PZT with the isolated single domain connected to a large pad of platinum is attached to a glass slide. Using the wire bonder the platinum pad is bonded to a large pad of gold on the glass substrate. A large wire/contact can then be attached, *e.g.* by soldering, to the gold pad which a voltage can be passed through.

8.7 Conclusions

The results presented in this chapter describe the initial experiments which were conducted in order to measure the electro-optic effect in 3-DOM PZT films with the ultimate goal of forming a tunable PC. In the course of these experiments no evidence of the electro-optic effect was measured but success was achieved in electrically contacting both the entire 3-DOM film and a single, well ordered 3-DOM domain.

In the electrical measurements conducted on the entire 3-DOM film voltages of 300 V were applied and no measurable systematic change in the peak position or peak width was observed. This was attributed to experimental error, the SNR of the reflection peaks and the simultaneous measurement of many domains which may mask the weak electro-optic effect measured. This would indicate that the way forward may be to electrically test a single domain. Success was achieved in isolating a large 3-DOM domain and connecting it to a large platinum pad which can then be electrically contacted. This method of testing a single isolated domain ensures that the second electrode is not in contact with the bottom electrode, *i.e.* the ITO substrate.

9 Conclusions

9.1 Outline of chapter

In this thesis results have been presented and discussed at the end of each chapter. In this final chapter the key results and conclusions are summarised and their significance is highlighted. At the end of this chapter suggestions for future work are discussed.

9.2 Conclusions

9.2.1 Thin film growth

The three-dimensional (3-D) photonic crystal (PC) thin films prepared in this project were used as templates for the formation of macroporous materials. A self-assembly method was used to form the template films on both glass and ITO substrates.

The position of the photonic stop-band can be varied by changing the diameter of the polystyrene spheres used to form the template films. This has been achieved by carrying out controlled and reproducible synthesis of sub-micron polystyrene spheres. An emulsifier-free emulsion polymerisation technique was investigated to produce spheres with a narrow size distribution (<3%) which is ideal for the growth of thin film PCs.

Since the position of the photonic stop-band is directly related to the diameter of the colloidal spheres used for the growth of the thin films it is crucial that the sphere diameter can be measured accurately. Routinely the diameter of the spheres is measured using a TEM method but during the course of this project two alternative methods were investigated. Both of these methods use a light scattering technique and offered fast, non-destructive analysis of a large population of spheres. However, the results presented in chapter 4 indicate that for confidence in the measured diameters the TEM method, although tedious and time consuming, should be used.

The thin film PCs were characterised by optical microscopy, reflectance spectroscopy and SEM to ensure that films suitable for the use as templates for macroporous films could be formed. The films were shown to have good long range order, to exhibit close packing and to have controllable thickness. In addition reflectance spectroscopy was

verified as an acceptable method for calculating the sphere diameter used to form the template films.

9.2.2 Towards a method for thin film growth

It became apparent during the course of this project that, although widely used to form thin film photonic crystals, the self-assembly growth process is not well understood. Chapter 6 reports the systematic study conducted to determine the optimum temperature, relative humidity and colloidal concentration for template film growth. Through monitoring the self-assembly process in-situ the overall rate for film growth indicated that temperature was the most important growth parameter.

Although high quality 3-D PC thin films can be formed using the self-assembly growth procedure, all the films grown in this project and reported in the current literature show cracks between domains. If self-assembled films are to be used successfully as templates for the formation of high quality macroporous materials the films should demonstrate the largest domains widths possible. Experimentally the widest domains were formed at 60-65˚C, a medium relative humidity (~15%) and a high colloidal concentration. However, as described in chapter 7, template films grown at a high colloidal concentration are not always suitable for the formation of macroporous materials.

From the results presented in chapter 6 it was shown that even at the optimum growth parameters the formation of cracks was unavoidable when using the self-assembly procedure. Through investigating the process of cracking a model for film growth was hypothesised. The general model for film formation is based on the evaporation of water from the meniscus region which draws colloidal spheres into the area of film formation where they self-assemble into close packed arrays. From the results presented in this study it was proposed that there are two rates involved in film growth – the growth rate (which was measured experimentally) and the drying/evaporation rate from the compacted region of spheres. This hypothesis was able to explain how stress between spheres in the compacted region originated and how cracks were initiated.

There have been many methods proposed for the mechanism of cracking but the results presented in chapter 6 indicate that the crack spacing, or domain width, does not simply

originate from an energy balance argument. It became clear that the elimination of pressure in the assembled region of spheres must be taken into account.

9.2.3 3-D macroporous films

Since the proposal of PCs there has been much research interest in being able to fabricate a periodic structure possessing a complete photonic bad gap (PBG). It has been shown that macroporous materials formed from 3-D PC templates would be one way to achieve this elusive complete PBG and this is the ultimate goal for many research groups. However, this was not an objective of this project.

In this project the formation of 3-DOM films from the functional ferroelectric material lead zirconate titanate (PZT) was investigated for the potential use as a multifunctional PC. The knowledge gained regarding 3-DOM film formation from simple binary precursor materials, *e.g.* TiO_2, has allowed the infiltration and inversion process to be better understood. Large, high quality, optically active areas of 3-DOM PZT could be formed partly due to the quality of the template films.

In this project supported 3-DOM PZT is formed on a substrate. Although the presence of the substrate restricts the methods of infiltration it provides mechanical strength and allows detailed and accurate characterisation of the fragile 3-DOM films to be carried out.

The quality of the 3-DOM PZT films were assessed and although there is considerable, and unavoidable, shrinkage with respect to the original template film no detrimental effects on the optical properties were observed. The additional cracking enforces the importance of minimising the cracking present in the template films. Analysis of the 3-DOM PZT films has confirmed that the desirable tetragonal phase has been formed and that the correct metal ratio is present, *i.e.* the PZT films are chemically homogeneous.

9.2.4 Towards multifunctional PCs

The refractive index of PZT is not high enough for the 3-DOM PZT films to have a complete PBG but the 3-DOM films may be ideal materials for achieving a multifunctional PC.

Ferroelectric materials are suitable candidates for multifunctional 3-DOM materials because the position of the photonic stop-band can be tuned by an electric field. The electric field, or the applied voltage, induces birefringence in the ferroelectric material which causes a change in the refractive index of the 3-DOM material.

The results presented in chapter 8 describe initial experiments conducted to electrically tune the photonic stop-band of 3-DOM PZT films. Success was achieved in electrically contacting the entire 3-DOM PZT film. Voltages of 300 V were applied across the entire 3-DOM film but no evidence of a systematic shift in the stop-band position was observed. This was attributed to experimental error, the signal to noise ratio of the reflection peaks and the possibility that multiple domains were being measured.

Success was achieved in isolating a large, well-ordered 3-DOM domain and contacting it to a large platinum pad which can be electrically contacted. It would be interesting to electrically test this isolated domain because one can be confident that the voltage is passing though the 3-DOM PZT.

9.3 Possibilities for further work

The thin film PC template films formed in this project have been grown at the optimum growth conditions to ensure minimum cracking. A model for crack formation has been proposed for the small data set presented. It would be interesting to further investigate the cracking mechanism in order to formulate a more comprehensive model for the self-assembly growth process.

Firstly further growth rate experiments should be conducted for a wider range of growth parameters and sphere sizes. Attempts could then be made to fit this larger data set to various different models for crack formation, *e.g.* energy balance, hydrodynamic. Since the model for thin film growth proposed by investigating crack initiation highlighted the importance of the solvent flow in the semi-ordered region of spheres the scenario becomes similar to the percolation of water from drying earth. It would be fascinating to see if the mathematical modelling for a natural phenomenon, like cracking mud, could be used to model the process of the growth of thin film PCs by colloidal self-assembly.

Through the growth rate experiments it became clear that even for growths conducted at the optimum parameters the problem of cracking could not be eliminated using the self-assembly growth process alone. However, although outwith the scope of this project one of the areas which it will be interesting to investigate in the future would be directed self-assembly. This could be approached in one of two different ways. one micromaching and one chemical, both of which would cause the self-assembly of the spheres to occur in certain regions of the growth substrate.

Jin *et al* (139) have reported the use of electron beam lithography to pattern a (100) template onto a growth substrate which can be used for colloidal self-assembly. The purpose of this experiment was to grow a PC which was assembled in a different orientation to normal thin film PCs. Since substrates patterned by electron beam lithography have been shown to be suitable substrates for self-assembly this technique could be used to form trenches in a substrate where the growth of spheres is prohibited.

Aizenberg *et al* (202) have reported the method of microcontact printing (μCP) of charged alkanethiols onto a gold coated substrate. If a combination of positive and negative alkanethiols are used the gold surface can be patterned with negative and positive regions. Since the polystyrene spheres have a negative surface charge, verified by the zeta potential measurements in chapter 3, they will be repelled by the negative regions and/or attracted to the positive regions. Therefore, if an appropriate μCP stamp can be fabricated, a gold coated substrate could be patterned with areas where the spheres were able to assemble and blank regions the spheres repelled from. Another chemical way of patterning a substrate would be by hydrophobic/hydrophilic interactions.

The basic concept with either of the aforementioned methods is that the pattern dimensions are chosen to be roughly the dimensions of the biggest domain possible, *e.g.* ~100 μm. Then since the region the spheres can assemble in is limited the maximum stress built up between spheres will be able to be accommodated over the length the spheres are allowed to order in. Thus no energy will need to be dissipated and cracking will not occur. One major challenge with this method is the thickness of crack-free film that can be grown. In the electron beam lithography technique the thickness will be the same as the trench depth and for the chemically patterned substrate since the

electrostatic interactions will only be weak it is thought unlikely that thick films will be able to be grown.

It has been reported in chapter 7 that good quality 3-DOM PZT films could be formed in the hope of forming a multifunctional PC. Success was achieved passing a high voltage across an entire 3-DOM PZT film. However, as reported in chapter 8, initial attempts at measuring the electro-optic effect for the entire 3-DOM PZT were unsuccessful for one of many reasons. Although the method discussed in chapter 8 was similar to that reported by Li *et al* (51) for the measurement of 3-DOM PLZT, there were many problems ensuring proper contact between the top and bottom electrode before the voltage could be applied.

One method which would be exciting to investigate for measuring the electro-optic effect over an entire 3-DOM PZT film would be to form a composite material. If the voids of the 3-DOM PZT film could be back filled with a polymer, *e.g.* PVA, which is then cured a composite material can be formed. A large electrode could then be evaporated onto the surface of this composite material since the infilled polymer will act as an insulator preventing the top electrode from touching the ITO substrate, *i.e.* the bottom electrode. This method has the advantage that a material that can be easily electrically tested is formed but also comes with additional problems. Due the fragility of the 3-DOM films the process of back filling has a high probability of damaging the structure. Hence much work will be required to find the optimum back filling conditions and the best polymer to use.

Alternatively, as also discussed in chapter 8, the electro-optic effect could be measured from a single 3-DOM PZT domain. During the course of the project a large well defined PZT domain was isolated using the FIB. However due to time constraints an electrical contact and electrical testing was not carried out on this sample. There are two ways which have been considered for electrically contacting the isolated domain.

As outlined in chapter 8 the first idea proposed for contacting the isolated domain was to use a wire bonder to attach a wire to the large platinum pad the isolated domain was attached to. However, the wire bonder uses a thin, ~25 μm, aluminium wire which is very soft. Thus the wire would not withstand the use of a crocodile clip to pass the voltage through the film, as had been used in the entire 3-DOM film experiments.

Moving on from this concept the idea sketched in figure 8.27 was proposed and it would be interesting to investigate if this method would prove successful. In this proposed method the 3-DOM PZT sample with the isolated domain is adhered to a glass slide to which a large pad of gold has been evaporated onto. The wire bonder could then be used to form a thin wire contact between the large pad of platinum the isolated domain is attached to and the gold pad. A larger wire contact could then be attached to the gold offering a more robust way to contact the single domain. However, it will have to be investigated if the fine wire between the platinum and gold pads will be able to withstand the high voltages required to observe a measurable shift in the stop-band position due to the electro-optic effect.

An alternative method which could be investigated if the wire bond proved to be unable to endure the high voltages is the following. Rather than forming a wire contact to the platinum pad to allow electrical testing a probe could be touched to the suface of the 3-DOM PZT and the ITO substrate to pass the voltage. However, this method will not be straightforward because when the 3-DOM film is placed in the optical set-up an optical microscope will be required to ensure that the tip of the probe is contacting the surface of the platinum pad. It will also be important to make certain that the point of the probe is small enough to contact the platinum pad and that the pad is deep enough so that the probe point cannot penetrate the platinum and contact the ITO substrate below. Finally care would have to be taken to guarantee the probe does not block either the incident light beam or the detector when the reflectance measurements are conducted.

Whichever method for contacting the isolated domain proves to be most successful the size of the incident beam of light will need to be reduced. As mentioned previously the size of the optical beam is 0.7 mm which, since the domain of interest is only ~60-30 μm, will illuminate many domains. Decreasing the diameter of the incident light source will not be a trivial matter, and will involve using a combination of lenses after the light has left the exit slit of the optical bench, but will ensure that all the intensity of the beam goes onto the domain of interest.

However, it may be the case that due to the low Pockel's coefficient for PZT it will not be possible to measure the electro-optic effect with the apparatus described in chapter 2. Another area of future work would be the formation of other functional 3-DOM materials using the developments made during this project. If a 3-DOM film of a

material possessing a higher electro-optic coefficient than PZT, *e.g.* PLZT. could be formed then the application of a similar magnitude of voltage would produce a larger change in the refractive index. Hence the shift in the photonic stop-band would be more pronounced and easier to measure.

During the course of this project well ordered, optically active 3-DOM PZT films have been successfully fabricated. Using the methods developed as a basis for future studies the ultimate goal of forming a multifunctional 3-DOM PC for technological applications becomes closer.

Appendix 1

Throughout the course of this project 'best' fit straight lines have been used routinely to calculate the sphere diameter and n_{eff} from reflectance measurements and for comparison of different methods used to measure the diameter of the polystyrene spheres (see chapter 4).

Microsoft Excel or Origin was used to plot the data and the technique used to fit a trendline to the raw experimental data uses the method of least squares or linear regression. In linear regression a relationship of the form

$$y=mx+c$$

is assumed between the variables, where m is the gradient and c is the y-intercept of the line. The aim is then to find the best values of the constants m and c.

The method of least squares estimates the equation of the straight line passing through the data points for which the sums of the squares of the deviations of these points from the line are a minimum (203). Given a set of n data points (x_i,y_i) the gradient, m, the y-intercept, c, and the correlation coefficient, R, can be calculated by the following equations:

$$m = \frac{n\sum(xy) - \sum x \sum y}{n\sum(x^2) - (\sum x)^2}$$

$$c = \frac{\sum y - m\sum x}{n}$$

$$R = \frac{\sigma_{xy}}{\sigma_x \sigma_y}$$

where σ_x and σ_y are the standard deviations of the x and y data sets respectively and σ_{xy} is the covariance between the two data sets.

Excel quotes an R^2 value, which is the square of the correlation coefficient (R). The R value is a number between -1 and 1 which reveals how closely the estimated values for the fitted trendline correspond to the raw data set. The closer to zero the R factor is the less points fall on a straight line.

Appendix 2

Date	[monomer] ($molL^{-1}$)	[initiator] ($molL^{-1}$)	Diameter (nm)	St. Dev. (nm)	% deviation
10/05/04	0.4365	0.0296	408	8	1.7
11/05/04	0.2180	0.0296	387	9	2.4
13/05/04	0.1090	0.0296	200	4	1.8
04/08/04	0.4360	0.0296	651	14	2.2
09/08/04	0.3274	0.0296	474	8	1.7
10/08/04	0.2180	0.0296	440	10	2.2
12/08/04	0.2180	0.0296	359	10	2.9
16/08/04	0.1090	0.0296	237	7	2.9
19/08/04	0.0436	0.0296	158	5	2.9
08/03/05	0.326	0.0297	336	21	6.1
09/03/05	0.326	0.0297	277	5	2.0
11/03/05	0.326	0.0297	304	9	2.8
12/03/05	0.326	0.0297	300	5	1.7
14/03/05	0.087	0.0297	192	5	2.6
15/03/05	0.175	0.0297	254	4	1.6
16/03/05	0.262	0.0297	327	6	1.8
18/03/05	0.349	0.0297	334	5	1.6
21/03/05	0.436	0.0297	389	5	1.3
22/03/05	0.524	0.0297	415	9	2.2

Appendix 3

JCPDS pattern 50-0346

Lead Zirconium Titanium Oxide, PZT(44/56).

Tetragonal unit cell – a=b=4.0172 Å and c=4.1391 Å

d (Å)	Relative Intensity	hkl
4.1406	16	001
4.0195	18	100
2.8829	100	101
2.8424	37	110
2.3424	24	111
2.0689	10	002
2.0090	18	200
1.8398	5	102
1.8065	4	201
1.7972	3	210
1.6724	13	112
1.6480	21	211
1.4413	7	202
1.4206	3	220
1.3794	1	003
1.3569	2	212
1.3431	1	221
1.3390	<1	300
1.3047	4	103
1.2740	4	301

References

1. Joannopoulos, J. D., Meade, R. D., and Winn, J. N., Photonic Crystals: Moulding the Flow of Light, Princeton University Press, 1995
2. Yablonovitch, E. and Hwang, K. S., *Physical Review Letters*, **58**(20), 2059-2062. 1987
3. John, S., *Physical Review Letters*, **58**(23), 2486-2489, 1987
4. Yablonovitch, E., *Scientific American*, **285**(6), 46-53, 2001
5. Almeida, R. M. and Portal, S., *Current Opinion in Solid State & Materials Science*. **7**(2), 151-157, 2003
6. McLachlan, M. A., Johnson, N. P., De La Rue, R. M., and McComb, D. W., *Journal of Materials Chemistry*, **14**, 144-150, 2004
7. Mizeikis, V., Juodkazis, S., Marcinkevicius, A., Matsuo, S., and Misawa, H., *The Journal of Photochemistry and Photobiology C*, **2**, 35-69, 2001
8. Pendry, J. B., *Current Science*, **76**(10), 1311-1316, 1999
9. Blanco, A., Chomski, E., Grabtchak, S., Ibisate, M., John, S., Leonard, S. W., Lopez, C., Meseguer, F., Miguez, H., Mondia, J. P., Ozin, G. A., Toader, O., and van Driel, H. M., *Nature*, **405**, 437-439, 2000
10. Myers, H. P., Introductory Solid State Physics, Taylor & Francis Ltd, 1997
11. Kittel, C., Introduction to Solid State Physics, (7th ed.), John Wiley & Sons, 1996
12. Thijssen, M. S., Sprik, R., Wijnhoven, J. E. G. J., Megens, M., Narayanan, T., Lagendijk, A., and Vos, W. L, *Physical Review Letters*, **83**(14), 2730-2733, 1999
13. Romanov, S. G., Fokin, A. V., and De La Rue, R. M., *Journal of Physics: Condensed Matter*, **11**, 3593-3600, 1999
14. Ozin, G. A. and Yang, S. M., *Advanced Functional Materials*, **11**(2), 95-104, 2001
15. Sechrist, Z. A., Schwartz, B. T., Lee, J. H., McCormick, J. A., Piestun, R., Park, W., and George, S. M., *Chemistry of Materials*, **18**(15), 3562-3570, 2006
16. Subramanian, G., Manoharan, V. N., Thorne, J. D., and Pine, D. J., *Advanced Materials*, **11**(15), 1261-1265, 1999
17. Meseguer, F., Blanco, A., Miguez, H., Garcia-Santamaria, F., Ibisate, M., and Lopez, C., *Colloids and Surfaces A: Physicochemical and Engineering Aspects*, **202**, 281-290, 2002
18. Yablonovitch, E., *Journal of the Optical Society of America B*, **10**(2), 283-295, 1993
19. Ho, K. M., Chan, C. T., and Soukoulis, C. M., *Physical Review Letters*, **65**(25), 3152-3155, 1990
20. Haus, J. W., Sözüer, H. S., and Inguva, R., *Journal of Modern Optics*, **39**(10), 1991-2005, 2006
21. Richel, A., Johnson, N. P., and McComb, D. W., *Applied Physics Letters*, **76**(14), 1816-1818, 2000
22. Johnson, N. P., McComb, D. W., Richel, A., Treble, B. M., and De La Rue, R. M., *Synthetic Metals*, **116**(1-3), 469-473, 2001
23. Busch, K. and John, S., *Physical Review E*, **58**(3), 3896-3908, 1998
24. Jiang, P., Bertone, J. F., Hwang, K. S., and Colvin, V. L., *Chemistry of Materials*, **11**, 2132-2140, 1999
25. Kim, B. G., Parikh, K. S., Ussery, G., Zakhidov, A., Baughman, R., Yablonovitch. E., and Dunn, B. S., *Applied Physics Letters*, **81**(23), 4440-4442, 2002
26. Campbell, M., Sharp, D. N., Harrison, M. T., Denning, R. G., and Turberfield, A. J. *Nature*, **404**, 53-56, 2000
27. Turberfield A.J., *MRS bulletin*, **26**(8), 632-636, 2001
28. Sanders, J. V. and Darragh, P. J., *Mineralogical Record*, **2**(6), 261-268, 1971
29. Brazilian Opal www.theimage.com/gemstone/opal/320brazopel.jpg
30. SEM image of the internal order of natural opal www.adelaide.edu.au/microscopy/services/instrumentation/gallery.html

31. McComb, D. W., Treble, B. M., Smith, C. J., De La Rue, R. M., and Johnson, N. P., *Journal of Materials Chemistry*, **11**, 142-148, 2001
32. Vukusic, P., Sambles, J. R., Lawrence, C. R., and Wootton, R. J., *Proceedings of the Royal Society of London B*, **266**, 1403-1411, 1999
33. Vukusic, P. and Sambles, J. R., *Nature*, **424**, 852-855, 2003
34. Filho, D. A., Hisano, C., Bertholdo, R., Schiavetto, M. G., Santilli, C., Ribeiro, S. J. L., and Messaddeq, Y., *Journal of Colloid and Interface Science*, **291**(2), 448-464, 2005
35. Norris, D. J., Arlinghaus, E. G., Meng, L., Heiny, R., and Scriven, L. E., *Advanced Materials*, **16**(16), 1393-1399, 2004
36. Gu, Z. Z., Kubo, S., Fujishima, A., and Sato, O., *Chemistry of Materials*, **14**, 760-765, 2002
37. Im, S. H., Kim, M. H., and Park, O. O., *Chemistry of Materials*, **15**, 1797-1802, 2003
38. Woodcock, L. V., *Nature*, **385**, 141-143, 1997
39. Bolhuis, P. G., Frenkel, D., Mau, S. C., and Huse, D. A., *Nature*, **388**, 235-236, 1997
40. West, A. R., Basic Solid State Chemistry, (2nd ed.), John Wiley & Sons Ltd, 2000
41. Shriver, D. F., Atkins, P. W., and Langford, C. H., Inorganic Chemistry, (2nd ed.), Oxford University Press, 1994
42. Míguez, H., Meseguer, F., López, C., Mifsud, A., Moya, J. S., and Vázquez, L., *Langmuir*, **13**, 6009-6011, 1997
43. Cheng, B., Ni, P., Jin, C., Li, Z., Zhang, D., Dong, P., and Guo, X., *Optics Communications*, **170**, 41-46, 1999
44. Kuai, S.-L., Hu, X.-F., Haché, A., and Truong, V.-V., *Journal of Crystal Growth*, **267**, 317-324, 2004
45. Ye, Y.-H., LeBlanc, F., Haché, A., and Truong, V.-V., *Applied Physics Letters*, **78**, 52-54, 2001
46. Ma, X., Lu, J. Q., Brock, R. S., Jacobs, K. M., Yang, P., and Hu, X. H., *Physics in Medicine and Biology*, **48**, 4165-4172, 2003
47. Mark, H. F., Bikales, N. M., Overberger, C. G., and Menges, G., Encyclopaedia of Polymer Science and Engineering, (2nd ed.), Wiley - Interscience Publications, 1988
48. Rugge, A., Park, J. S., Gordon, R. G., and Tolbert, S. H., *Journal of Physical Chemistry B*, **109**(9), 3764-3771, 2005
49. Busch, K. and John, S., *Physical Review Letters*, **83**(5), 967-970, 1999
50. Huang, S, Li, A.-D., Gao, Y., and Wu, D., *International Journal of Modern Physics B*, **19**(15-17), 2769-2774, 2005
51. Li, B., Zhou, J., Li, L., Wang, X. J., Liu, X. H., and Zi, J., *Applied Physics Letters*, **83**(23), 4704-4706, 2003
52. Xiang, A., Gao, J. P., Chen, H. K., Yu, J. G., and Liu, R. X., *Chinese Chemical Letters*, **15**(2), 228-230, 2004
53. Kee, C.-S., Kim, J. E., Park, H. Y., Park, I., and Lim, H., *Physical Review B*, **61**(23), 15523-15525, 2000
54. Kubo, S., Gu, Z. Z., Takahashi, K., Fujishima, A., Segawa, H., and Sato, O., *Journal of the American Chemical Society*, **126**(26), 8314-8319, 2004
55. Kuai, S.-L., Bader, G., and Ashrit, P. V., *Applied Physics Letters*, **86**(22), 221110-1-3, 2005
56. Li, B., Zhou, J., Hao, L., Hu, W., Zong, R., Cai, M., Fu, M., Gui, Z. L., Li, L., and Li, Q., *Applied Physics Letters*, **82**(21), 3617-3619, 2003
57. Dimos, D., *Annual Review of Materials Science*, **25**, 273-293, 1995
58. Burns, G. and Scott, B. A., *Physical Review Letters*, **25**(17), 1191-1194, 1970

59. Yakovlev, S., PhD Thesis, *Lanthanide Ions Doping Effects on Structural, Electrophysical and Functional Properties of Sol-gel Fabricated $PbTiO_3$ Thin Films*, University of Kiel, 2004
60. Allard, M., Sargent, E. H., Kumacheva, E., and Kalinina, O., *Optical and Quantum Electronics*, **34**, 27-36, 2002
61. Romanov, S. G., Maka, T., Sotomayor-Torres, C. M., Müller, M., Zentel, R., Cassagne, D., Manzanares-Martinez, J., and Jouanin, C., *Physical Review E*, **63**, 056603-1-5, 2001
62. Bertone, J. F., Jiang, P, Hwang, K. S, Mittleman, D. M., and Colvin, V. L., *Physical Review Letters*, **83**(2), 300-303, 1999
63. Romanov, S. G., Maka, T., Sotomayor Torres, C. M., Muller, M., and Zentel, R., *Journal of Lightwave Technology*, **17**(11), 2121-2127, 1999
64. McLachlan, M. A., PhD Thesis, *Synthesis and Characterisation of Thin Film Photonic Crystals*, University of Glasgow, 2005
65. Lopez, J. F. G. and Vos, W. L., *Physical Review E*, **66**, 036616-1-5, 2002
66. Bogomolov, V. N., Gaponenko, S. V., Germanenko, I. N., Kapitonov, A. M., Petrov, E. P., Gaponenko, N. V., Prokofiev, A. V., Ponyavina, A. N., Silvanovich, N. I., and Samoilovich, S. M., *Physical Review E*, **55**(6), 7619-7625, 1997
67. Miguez, H., Lopez, C., Meseguer, F., Blanco, A., Vazquez, L., Mayoral, R., Ocana, M., Fornes, V., and Mifsud, A., *Applied Physics Letters*, **71**(9), 1148-1150, 1997
68. Comoretto, D., Grassi, R., Marabelli, F., and Andreani, L. C., *Materials Science and Engineering C*, **23**, 61-65, 2003
69. Norris, D. J., Vlasov, Y. A., and Deutsch, M., *Applied Physics Letters*, **76**(12), 1627-1629, 2000
70. Wijnhoven, J. E. G. J., Bechger, L., and Vos, W. L., *Chemistry of Materials*, **13**(12), 4486-4499, 2001
71. Holland, B. T., Blanford, C. F., and Stein, A., *Science*, **281**, 538-540, 1998
72. Tarhan, I. I. and Watson, G. H., *Physical Review B*, **54**, 7593-7597, 1996
73. Bressona, F., Chen, C.-C., Chi, G.-C., and Chen, Y.-W., *Applied Surface Science*, **217**, 281-288, 2003
74. Slayter, E. M. and Slayter, H. S., Light and Electron Microscopy, (1st ed.), Cambridge University Press, 1992
75. Watt, I. M., The Principles and Practice of Electron Microscopy, (2nd ed.), Cambridge University Press, 1997
76. Williams, D. B. and Carter, C. B., Transmission Electron Microscopy - A Textbook for Materials Science Basics I, Springer Science+Business Media Inc., 1996
77. Gabriel, B. L., SEM: A Users Manual for Materials Science, American Society for Metals, 1985
78. Goldstein, J. I., Newbury, D. E., Echlin, P. E., Joy, D. C., Fiori, C., and Lifshin, E., Scanning Electron Microscopy and X-Ray Microanalysis, (1st ed.), Plenum Press, 1981
79. Goodhew, P. J., Humphreys, J., and Beanland, R., Electron Microscopy and Analysis, (3rd ed.), Taylor & Francis, 2001
80. Chescoe, Dawn and Goodhew, Peter J., The Operation of Transmission and Scanning Electron Microscopes, Oxford University Press, 1990
81. Bentham Manual - TMc300 Monochromator (Issue 3.00), Bentham Instruments Ltd., 2000
82. Asher, C., Reese, E., and Sanford, A., *Journal of Colloid and Interface Science*, **248**, 41-46, 2002
83. Madaeni, S. S. and Ghanbarian, M., *Polymer International*, **49**, 1356-1364, 2000
84. Young, R. J. and Lovell, P. A., Introduction to Polymers, (2nd ed.), Chapman & Hall, 1991
85. Goodall, A. R., Wilkinson, M. C., and Hearn, J., *Journal of Polymer Science: Polymer Chemistry Section*, **15**, 2193-2218, 1977

86. Goodall, A. R., Hearn, J., and Wilkinson, M. C., *The British Polymer Journal*, **10**, 141-150, 1978
87. Munro, D., Goodall, A. R., Wilkinson, M. C., Randle, K., and Hearn, J., *Journal of Colloid and Interface Science*, **68**(1), 1-13, 1979
88. Cowie, J. M. G., Polymers: Chemistry & Physics of Modern Materials, (2nd ed.), Blackie Academic & Professional, 1991
89. Harkins, W. D., *Journal of the American Chemical Society*, **69**, 1428-1447, 1947
90. Wang, Q., Fu, S., and Yu, T., *Progress in Polymer Science*, **19**, 703-753, 1994
91. Brinker, C. J. and Scherer, G. W., Sol-Gel Science, (1st ed.), Academic Press Ltd., 1990
92. HPPS Operation Manual (Man0314), Malvern Instruments Ltd., 2001
93. Juillerat, F., Bowen, P., and Hofmann, H., *Langmuir*, **22**(5), 2249-2257, 2006
94. ISO 13321:1996 *Particle size analysis -- Photon correlation spectroscopy*, 1996
95. Malvern Instruments, High Performance Particle Sizer - The First to Combine High Sensitivity with a High Concentration Capability, Malvern Instruments Ltd., 2000
96. Rawle, A., PCS in 30 minutes, Malvern Instruments, 1990
97. Hecht, E., Optics, (4th ed.), Addison Wesley, 2002
98. ISO 13320-1:1999 *Particle size analysis -- Laser diffraction methods -- Part 1: General principles*, 1999
99. Mastersizer Manual, Getting Started (Man0101, Issue 1.3), Malvern Instruments Ltd., 1997
100. Rawle, A., Basic Principles of Particle Size Analysis, Malvern Instruments, 2001
101. Yablonovitch, E. and Gmitter, T. J., *Physical Review Letters*, **67**(17), 2295-2298, 1991
102. Fleming, J. G., Lin, S. Y., El-Kady, I., Biswas, R., and Ho, K. M., *Nature*, **417**, 52-55, 2002
103. Soten, I., Miguez, H., Yang, S. M., Petrov, S., Coombs, N., Tetreault, N., Matsuura, N., Ruda, H. E., and Ozin, G. A., *Advanced Functional Materials*, **12**(1), 71-77, 2002
104. Bechger, L. and Vos, W. L., *Chemistry of Materials*, **16**, 2425-2432, 2004
105. Noda, S., Tomoda, K., Yamamoto, N., and Chutinan, A., *Science*, **289**, 604-606, 2000
106. Subramania, G., Constant, K., Biswas, R., Sigalas, M. M., and Ho, K. M., *Synthetic Metals*, **116**, 445-448, 2001
107. Mayoral, R., Requena, J., Moya, J. S., López, C., Cintas, A., Miguez, H., Meseguer, F., Vázquez, L., Holgado, M., and Blanco, A., *Advanced Materials*, **9**, 257-260, 1997
108. Li, Q., Dong, P., Guo, X., Cheng, B., Ni, P., and Zhang, P., *Colloids and Surfaces A: Physicochemical and Engineering Aspects*, **216**, 123-128, 2003
109. Burmeister, F., Schafle, C., Keilhofer, C., Bechinger, C., Boneberg, J., and Leiderer, P., *Langmuir*, **13**(11), 2983-2987, 1997
110. Holgado, M., Garcia-Santamaria, F., Blanco, A., Ibisate, M., Cintas, A., Miguez, H., Serna, C. J., Molpeceres, C., Requena, J., Mifsud, A., Meseguer, F., and Lopez, C., *Langmuir*, **15**(14), 4701-4704, 1999
111. Rogach, A. L., Kotov, N. A., Koktysh, D. S., Ostrander, J. W., and Ragoisha, G. A., *Chemistry of Materials*, **12**(9), 2721-2726, 2000
112. Wijnhoven, J. E. G. J. and Vos, W. L., *Science*, **281**, 802-804, 1998
113. Bardosova, M., Hodge, P., Pach, L., Pemble, M. E., Smatko, V., Tredgold, R. H., and Whitehead, D., *Thin Solid Films*, **437**(1-2), 276-279, 2003
114. Shimmin, R. G., DiMauro, A. J., and Braun, P. V., *Langmuir*, **22**, 6507-6513, 2006
115. Bardosova, M. and Tredgold, R. H., *Journal of Materials Chemistry*, **12**, 2835-2842, 2002
116. Denkov, N. D., Velev, O. D., Kralchevsky, P. A., Ivanov, I. B., Yoshimura, H., and Nagayama, K., *Langmuir*, **8**(12), 3183-3190, 1992

117. Dimitrov, A. S. and Nagayama, K., *Langmuir*, **12**, 1303-1311, 1996
118. Dimitrov, A. S. and Nagayama, K., *Chemical Physics Letters*, **243**, 462-468, 1995
119. Goldenberg, L. M., Wagner, J., Stumpe, J., Paulke, B. R., and Gornitz, E., *Materials Science and Engineering C*, **22**, 233-237, 2002
120. Burmeister, F., Schafle, C., Keilhofer, C., Bechinger, C., Boneberg, J., and Leiderer, P., *Advanced Materials*, **10**(6), 495-497, 1998
121. Galisteo-López, J. F., Palacios-Lidón, E., Castillo-Martínez, E., and López, C., *Physical Review B*, **68**, 115109_1-8, 2003
122. McLachlan, M. A., Johnson, N. P., De La Rue, R. M., and McComb, D. W., *Journal of Materials Chemistry*, **15**(3), 369-371, 2005
123. Goldenburg, L. M., Wagner, J., Stumpe, J, Paulke, B. R., and Görnitz, E., *Langmuir*, **18**(8), 3319-3323, 2002
124. Teh, L. K., Tan, N. K., Wong, C. C., and Li, S., *Applied Physics A*, **81**, 1399-1404, 2005
125. Vlasov, Y. A., Bo, X.-Z., Sturn, J. C., and Norris, D. J., *Nature*, **414**, 289-293, 2001
126. Zhou, Z., Li, Q., and Zhao, X. S., *Langmuir*, **22**(8), 3692-3697, 2006
127. Technical Note 007B, Duke Scientific Corporation, 1996
128. Muir, L. E, Electron and Ion Microscopy and Microanalysis Principles and Applications, (2nd ed.), Marcel Dekker, 1991
129. Koh, Y. K. and Wong, C. C., *Langmuir*, **22**(3), 897-900, 2006
130. Zhou, Z. and Zhao, X. S., *Langmuir*, **21**, 4717-4723, 2005
131. Cong, H. and Cao, W., *Langmuir*, **19**, 8177-8181, 2003
132. Cross, G. H., Reeves, A., Brand, S., Swann, M., Peel, L. L., Freeman, N. J., and Lu, J. R., *Journal of Physics D: Applied Physics*, **37**, 74-80, 2004
133. Rakers, S., Chi, L. F., and Fuchs, H., *Langmuir*, **13**(26), 7121-7124, 1997
134. Lide, D. R., Handbook of Chemistry and Physics, (85th ed.), CRC Press, 2005
135. Atkins, P. W., Physical Chemistry, (6th ed.), Oxford University Press, 1998
136. Chabanov, A. A., Jun, Y., and Norris, D. J., *Applied Physics Letters*, **84**(18), 3573-3575, 2004
137. Lurio, L. B., Lumma, D., Sandy, A. R., Borthwick, M. A., Falus, P., Mochrie, S. G. J., Pelletier, J. F., Malik, A., and Stephenson, G. B., *Physical Review Letters*, **84**(4), 785-788, 2000
138. Yan, H., Blanford, C. F., Holland, B. T., Smyrl, W. H., and Stein, A., *Chemistry of Materials*, **12**, 1134-1141, 2000
139. Jin, C., McLachlan, M. A., McComb, D. W., De La Rue, R. M., and Johnson, N. P., *Nano Letters*, **5**(12), 2646-2650, 2006
140. King, J. R. and Wattis, J. A., 'Mud-cracking' in a Latex Paint Film, European Study Group with Industry 1997, University of Bath, 1997
141. Shorlin, K. A., de Bruyn, J. R., Graham, M., and Morris, S. W., *Physical Review E*, **61**(6), 6950-6957, 2000
142. Routh, A. F. and Lee, W. P., *Langmuir*, **20**(23), 9885-9888, 2004
143. Dufresne, E. R., Corwin, E. I., Greenblatt, N. A., Ashmore, J., Wang, D. W., Dinsmore, A. D., Cheng, J. X., Xie, X. S., Hutchinson, J. W., and Weitz, D. A., *Physical Review Letters*, **91**(22), 4501-1-4501-4, 2003
144. Atkinson, A. and Guppy, R. M., *Journal of Materials Science*, **26**, 3869-3873, 1991
145. Scharrer, M., Wu, X., Yamilov, A., Cao, H., and Chang, R. P. H., *Applied Physics Letters*, **86**, 151113_1-3, 2005
146. Norris, D. J. and Vlasov, Y. A., *Advanced Materials*, **13**(6), 371-376, 2001
147. Holland, B. T., Blanford, C. F., Do, T., and Stein, A., *Chemistry of Materials*, **11**(3), 795-805, 1999
148. Gu, Z. Z., Kubo, S., Fujishima, A., and Sato, O., *Applied Physics A*, **74**, 127-129, 2002
149. Yan, H., Blanford, C. F., Holland, B. T., Parent, M., Smyrl, W. H., and Stein, A., *Advanced Materials*, **11**(12), 1003-1006, 1999

150. Zhou, J., Sun, C. Q., Pita, K., Lam, Y. L., Zhou, Y., Ng, S. L., Kam, C. H., Li, L. T., and Gui, Z. L., *Applied Physics Letters*, **78**(5), 661-663, 2001
151. Harkins, P., Eustace, E., Gallagher, J., and McComb, D. W., *Journal of Materials Chemistry*, **12**(5), 1247-1249, 2002
152. Ni, P., Dong, P., Cheng, B., Li, X., and Zhang, D., *Advanced Materials*, **13**(6), 437-441, 2001
153. Kuai, S. L., Hu, X. F., and Truong, V.-V., *Journal of Crystal Growth*, **259**(4), 404-410, 2003
154. Kuai, S.-L., Truong, V.-V., Haché, A., and Hu, X.-F., *Journal of Applied Physics*, **96**(11), 5982-5986, 2004
155. Blanford, C. F., Schroden, R. C., Al-Daous, M., and Stein, A., *Advanced Materials*, **13**(1), 26-29, 2001
156. Braun, P. V. and Wiltzius, P., *Nature*, **402**, 603-604, 1999
157. Yeo, K. H, Teh, L. K., and Wong, C. C., *Journal of Crystal Growth*, **287**, 180-184, 2006
158. Miguez, Hernan, Meseguer, Fransisco, Lopez, Cefe, Lopez-Tejeira, Fernando, and Sanchez-Dehesa, Jose, *Advanced Materials*, **13**(6), 393-396, 2001
159. Yan, H., Blanford, C. F., Smyrl, W. H., and Stein, A., *Chemistry Communications*, 1477-1478, 2000
160. Matsuura, N, Yang, S., Sun, P., and Ruda, H. E., *Applied Physics A*, **81**, 379-384, 2005
161. Zhang, Q. and Whatmore, R. W., *Journal of Physics D: Applied Physics*, **34**(22), 2296-2301, 2001
162. Yi, G., Wu, Z., and Sayer, M., *Journal of Applied Physics*, **64**(5), 2717-2724, 1988
163. Tipakontitikul, R. and Ananta, S., *Materials Letters*, **58**(3-4), 449-454, 2004
164. Pontes, F. M., Leite, E. R., Nunes, M. S. J., Pontes, D. S. L., Longo, E., Magnani, R., Pizani, P. S., and Varela, J. A., *Journal of the European Ceramic Society*, **24**, 2969-2976, 2004
165. Lakeman, C. D. E and Payne, D. A., *Journal of the American Ceramic Society*, **75**(11), 3091-3096, 1992
166. Kwok, C. K. and Desu, S. B., *Journal of Materials Research*, **9**(7), 1728-1733, 1994
167. West, A. R., Solid State Chemistry and its Applications, John Wiley & Sons Ltd., 1984
168. Sivasubramanian, V., Murthy, V. R. K., Viswanathan, B., and Sieskind, M., *Journal of Physics: Condensed Matter*, **8**, 2447-2456, 1996
169. Bellaiche, L. and Vanderbilt, D., *Physical Review B*, **61**(12), 7877-7882, 2000
170. Williams, D. B. and Carter, C. B, Transmission Electron Microscopy: A Textbook for Materials Science Spectrometry IV, Springer Science+Business Media Inc., 1996
171. Verardi, P., Dinescu, M., and Craciun, F., *Applied Surface Science*, **154-155**, 514-518, 2000
172. Fontanat, M. D., Metrat, G., Servoin, J. L., and Gervais, F., *Journal of Physics C: Solid State Physics*, **16**, 483-514, 1984
173. McLachlan, M. A., Barron, C. C. A., Johnson, N. P., De La Rue, R. M., and McComb, D. W., *Formation of Large Area Three Dimensionally Ordered Macroporous Thin Films via a confined Crystallization Approach*, submitted to Journal of Materials Chemistry October 2006
174. Silbey, R. J. and Alberty, R. A, Physical Chemistry, (3rd ed.), John Wiley and Sons, 2001
175. Çevik, U., Baltas, H., Çelik, S., Karaca, I., and Kopyal, A. I., *Superconductor Science and Technology*, **18**, 101-106, 2005
176. Jenkins, R. and De Vries, J. L., Practical X-ray Spectrometry, (2nd ed.), Springer-Verlag, 1974

177. Schwarzer, S. and Roosen, A, *Journal of the European Ceramic Society*. **19**(6-7). 1007-1010, 1999
178. Young, H. D. and Freedman, R. A., University Physics. (10th ed.). Addison Wesley. 2000
179. Liu, Z., Jin, Z., Li, W., Liu, X., Qiu, J., and Wu, W., *Materials Letters*. **60**(6). 810-814, 2006
180. Liu, Z., Jin, Z., Li, W., Qiu, J., Zhao, J., and Liu, X., *Applied Surface Science*. **252**(14), 5002-5009, 2006
181. Moret, M. P., Devillers, M. A. C., Worhoff, K., and Larsen, P. K, *Journal of Applied Physics*, **92**(1), 468-474, 2002
182. Barron, C. C. A., McLachlan, M., Zhang, Q., and McComb, D. W., *Ferroelectric Three-Dimensionally Ordered Macroporous Thin Films*, submitted to Ferroelectrics 2006
183. Boyd, R. W., Nonlinear Optics, Academic Press, 1992
184. Yariv, A., Quantum Electronics, (3rd ed.), John Wiley & Sons, 1989
185. Optical Birefringence http://micro.magnet.fsu.edu/primer/lightandcolor/birefringenceintro.html
186. Camatini, E., Progress in Electro-Optics, Plenum Press, New York, 1975
187. Davis, C. C., Lasers and Electro-Optics, Cambridge University Press, 1996
188. Jenkins, F. A. and White, H. E., Fundamentals of Optics, (4th ed.), McGraw-Hill International, 1981
189. DiDomenico, M. and Wemple, S. H., *Journal of Applied Physics*, **40**(2), 720-734, 1969
190. Kholkin, A. L., Brooks, K. G., Taylor, D. V., Hiboux, S., and Setter, N., *Integrated Ferroelectrics*, **22**(1-4), 525-533, 1998
191. Akazawaa, H. and Shimada, M., *Journal of Applied Physics*, **98**, 113501-1-5, 2005
192. Kang, H.-S. and Lee, W.-J., *Journal of Vacuum Science and Technology A*, **20**(4), 1498-1504, 2002
193. Lee, C., Spirin, V., Song, H., and No, K., *Thin Solid Films*, **340**, 242-249, 1999
194. Adachi, H., Kawaguchi, T., Setsune, K., Ohji, K., and Wasa, K., *Applied Physics Letters*, **42**(10), 867-868, 1983
195. Nashimoto, K., Nakamura, S., Morikawa, T., Moriyama, H., Watanabe, M., and Osakabe, E., *Applied Physics Letters*, **74**(19), 2761-2763, 1999
196. Busch, J. R., Ramamurthi, S. D., Swartz, S. L., and Wood, V. E., *Electronics Letters*, **28**(17), 1591-1592, 1992
197. Uhlmann, D. R., Teowee, G., Boulton, J. M., Motakef, S., and Lee, S. C., *Journal of Non-Crystalline Solids*, **147-148**, 409-423, 1992
198. Land, C. E., *Journal of the American Ceramic Society*, **72**(11), 2059-2064, 1989
199. Rotkina, L., Lin, J.-F., and Bird, J. P., *Applied Physics Letters*, **83**(21), 4426-4428, 2003
200. Tao, T., Ro, J. S., Melngailis, J., Xue, Z., and Kaesz, H. D., *Journal of Vacuum Science and Technology B*, **8**(6), 1826-1829, 1990
201. Lai, Z. and Liu, J., Chapter A: Wire Bonding, Nordic Electronics, 2006
202. Aizenberg, J., Braun, P. V., and Wilzius, P., *Physical Review Letters*, **84**(13). 2997-3000, 2000
203. Tebbutt, P., Basic Mathematics for Chemists, (2nd ed.). John Wiley & Sons Ltd., 1998